

# Highly Miniaturized Antennas and Filters for Wireless Applications

by

**Reza Azadegan**

A dissertation submitted in partial fulfillment  
of the requirements for the degree of  
Doctor of Philosophy  
(Electrical Engineering)  
in The University of Michigan  
2004

Doctoral Committee:

Professor Kamal Sarabandi, Chair  
Assistant Professor Michael P. Flynn  
Professor John W. Halloran  
Professor Gabriel M. Rebeiz  
Professor John L. Volakis

© Reza Azadegan 2004  
All Rights Reserved

## ABSTRACT

### Highly Miniaturized Antennas and Filters for Wireless Applications

by

Reza Azadegan

Chair: Kamal Sarabandi

A novel approach to miniaturize antennas and microwave filters for wireless systems is presented. This approach is based on a proper choice of a miniature topology, which at the same time offers minimal loss. The proposed topology has been used to design a miniaturized slot antenna structure whose dimensions are as small as  $0.05\lambda_0 \times 0.05\lambda_0$  with a gain of  $-3$  dBi. A number of similar miniaturized topologies, including a miniaturized folded-slot, its complementary and self-complementary pairs have also been designed to provide miniaturized antennas with enhanced bandwidths.

Based on the same premise, miniaturization of direct-coupled and cross-coupled filters are demonstrated. Although miniaturization is expected to adversely affect the  $Q$  of a filter, the proposed filters exhibit a comparable  $Q$  to that of standard size microstrip filters due to the inherent higher  $Q$  of a slot-line.

Finally, a high-impedance miniaturized antenna is proposed, followed by a radar cross-section (RCS) measurement technique to extract its input impedance. Such a high-impedance antenna may be a suitable candidate for emerging high-impedance low-power micro- and nano-devices used in future wireless systems.

To my mother Batool (Akhtar), my father Jahangir,  
my wife Zeinab, and my son Mohammad-Hosein

## ACKNOWLEDGEMENTS

I would first like to thank my advisor, Professor Kamal Sarabandi for his strong support and encouragement. I should commend him for two things in particular. First is the enormous amount of time he spends with his students providing them with advice and thoughtful comments. Second is his exemplary courage to embark on novel research avenues.

I also thank my dissertation committee, Prof. Michael P. Flynn, Prof. John Halloran, Prof. Gabriel M. Rebeiz, and Prof. John L. Volakis. for their support and feedback. I should acknowledge Prof. Volakis for his input on the different aspects of the numerical simulation of antennas.

Special thanks are due to Prof. Liepa, Prof. Senior, and Prof. Tai for numerous technical conversations that we have had regarding different topics in electromagnetics. On a personal level, Dr. Liepa has been a very kind friend to me as well as an outstanding expert on electromagnetic measurements.

I would like to acknowledge breadth and depth of help I have received from my friends at the Radiation Laboratory of The University of Michigan. The spirit of perseverance and cooperation in the RADLAB produces a unique environment that nurtures academic excellence.

This acknowledgment would be incomplete without referring to my Iranian friends at The University of Michigan whose presence made my stay in Ann Arbor a more pleasant experience. Special thanks to my very good friend Mr. Alireza Tabatabaenejad with whom I had long conversations on a variety of issues, and to many others.

Mrs. Susan Charnley and Mr. Masoud Agah deserve a special mention. Dr. Charnley has kindly helped me in editing a considerable portion of this manuscript for style while it was developing. Masoud was kind enough to read my dissertation in its entirety and provide helpful suggestions.

Finally, I would like to express my sincere gratitude to my family whose emotional support has been essential in fulfilling this endeavor; to my mother for being my inspiration; to my father for his rationality; to my wife for her continued love and patience, and to my son for being so sweet.

# TABLE OF CONTENTS

|  |      |
|--|------|
| <b>DEDICATION</b> . . . . .                                    | ii   |
| <b>ACKNOWLEDGEMENTS</b> . . . . .                              | iii  |
| <b>LIST OF TABLES</b> . . . . .                                | viii |
| <b>LIST OF FIGURES</b> . . . . .                               | ix   |
| <b>CHAPTER</b>   |      |
| 1 Introduction . . . . .                                       | 1    |
| 1.1 Motivation and Background . . . . .                        | 1    |
| 1.2 Thesis Overview . . . . .                                  | 8    |
| 2 A Compact Quarter-wavelength Slot Antenna Topology . . . . . | 12   |
| 2.1 Introduction . . . . .                                     | 12   |
| 2.2 Compact Spiral Antennas . . . . .                          | 14   |
| 2.3 A Miniature Quarter-wave Topology . . . . .                | 16   |
| 2.4 Realization and Measurements . . . . .                     | 22   |
| 2.5 Conclusion . . . . .                                       | 29   |
| 3 Miniaturization of Slot Antennas . . . . .                   | 30   |
| 3.1 Introduction . . . . .                                     | 30   |
| 3.1.1 Background . . . . .                                     | 30   |
| 3.1.2 Fundamental Limitations of Small Antennas . . . . .      | 31   |
| 3.1.3 Approaches for Antenna Miniaturization . . . . .         | 31   |
| 3.2 Miniaturized Antenna Geometry . . . . .                    | 34   |
| 3.2.1 Slot Radiator Topology . . . . .                         | 34   |
| 3.2.2 Antenna Feed . . . . .                                   | 37   |
| 3.3 Design Procedure . . . . .                                 | 38   |
| 3.4 Full-Wave Simulation and Tuning . . . . .                  | 40   |
| 3.4.1 Equivalent-Circuit Model . . . . .                       | 43   |
| 3.4.2 Antenna Matching . . . . .                               | 45   |
| 3.5 Antenna Simulation and Measurements . . . . .              | 48   |
| 3.6 Conformability to Curved Platforms . . . . .               | 54   |

|       |   |     |
|-------|---|-----|
| 3.7   | Conclusion . . . . .  | 60  |
| 4     | Bandwidth Enhancement of Miniaturized Slot Antennas Using Folded, Complementary and Self-Complementary Realizations . . . . . | 61  |
| 4.1   | Introduction . . . . .  | 61  |
| 4.2   | Miniaturized Folded Slot Antenna . . . . .  | 64  |
| 4.3   | Miniaturized Folded Printed Wire Antenna . . . . .  | 71  |
| 4.4   | Miniaturized Self-Complementary Folded Antenna . . . . .  | 77  |
| 4.4.1 | Impedance Matching . . . . .  | 78  |
| 4.5   | Self-Complimentary H-Shaped Antenna . . . . .   | 84  |
| 4.6   | Conclusion . . . . .  | 92  |
| 5     | RF Filter Miniaturization Using a High- $Q$ Slot-line Resonator . . . . .   | 94  |
| 5.1   | Introduction . . . . .  | 94  |
| 5.2   | Miniaturized Slot-line Resonator Topology . . . . .   | 97  |
| 5.3   | Direct-Coupled 4-Pole Filter . . . . .  | 104 |
| 5.3.1 | Coupling Structures . . . . .   | 104 |
| 5.3.2 | External Coupling . . . . .   | 109 |
| 5.3.3 | Examples . . . . .  | 110 |
| 5.4   | Cross Coupled Miniature Filters . . . . .   | 113 |
| 5.5   | Conclusions . . . . .   | 123 |
| 6     | RCS Measurement Technique to Extract the Input Impedance of High-Impedance Miniaturized Slot Antennas . . . . .               | 125 |
| 6.1   | Introduction . . . . .  | 125 |
| 6.2   | Methodology . . . . .   | 127 |
| 6.3   | Formulation . . . . .   | 129 |
| 6.3.1 | Scattering from an Electric-Dipole Antenna . . . . .  | 129 |
| 6.3.2 | Scattering from a Magnetic Dipole Antenna . . . . .   | 132 |
| 6.3.3 | Radar Cross-Section of an Aperture Antenna . . . . .  | 133 |
| 6.4   | Analytical Results . . . . .  | 136 |
| 6.5   | Numerical Simulation . . . . .  | 137 |
| 6.5.1 | Center-fed Slot Antenna . . . . .   | 138 |
| 6.5.2 | High-impedance Miniaturized Slot Antenna . . . . .  | 141 |
| 6.6   | Measurement of High-Impedance Antenna . . . . .   | 145 |
| 6.7   | Conclusion . . . . .  | 147 |
| 7     | Conclusions and Recommendations for Future Work . . . . .   | 149 |
| 7.1   | Summary . . . . .   | 149 |
| 7.2   | Contributions . . . . .   | 150 |
| 7.2.1 | Antenna Miniaturization . . . . .   | 150 |
| 7.2.2 | Bandwidth Enhancement of Miniaturized Antennas . . . . .  | 150 |
| 7.2.3 | Microwave Filter Miniaturization . . . . .  | 151 |
| 7.2.4 | High-Impedance Antenna Measurement . . . . .  | 151 |
| 7.3   | Future Work . . . . .   | 152 |

|                        |     |
|------------------------|-----|
| APPENDIX . . . . .     | 155 |
| BIBLIOGRAPHY . . . . . | 169 |

## LIST OF TABLES

**Table**

|     |  |     |
|-----|--|-----|
| 2.1 | Resonant frequencies, gains, and ground plane sizes of the three miniaturized slot antennas of Fig. 2.7. . . . .   | 25  |
| 3.1 | Slot-line characteristics for two different values of slot width $w$ , and the dielectric constant of $\epsilon_r = 2.2$ and thickness of $h = 0.787(\text{mm})$ and $f = 300 \text{ MHz}$ . . . . . | 38  |
| 3.2 | The parameters of the Genetic Algorithm optimizer. . . . .   | 45  |
| 3.3 | The equivalent circuit parameters of the microstrip fed slot antenna. . . . .  | 45  |
| 3.4 | The physical length of the $50 \Omega$ microstrip line needed for realizing the termination susceptance, where the dielectric material properties are as specified in Table 3.1. . . . .             | 47  |
| 3.5 | Antenna characteristics as a function of two different size ground planes compared with the simulated results for the same antenna on an infinite ground plane. . . . .                              | 51  |
| 4.1 | Comparison among characteristics of miniaturized slot, miniaturized folded slot, and miniaturized printed folded dipole antennas. . . . .  | 76  |
| 5.1 | The effect of the slot to strip width ( $s/w$ ) on the unloaded $Q$ of the miniaturized slot-line resonators. . . . .  | 100 |

# LIST OF FIGURES

**Figure**

|      |  |    |
|------|--|----|
| 2.1  | The geometry of resonant spiral antennas: (a) equiangular spiral, and (b) cornu spiral. . . . .  | 15 |
| 2.2  | The magnetic current distribution on the UHF miniaturized slot antenna at the resonance frequency (600 MHz). The figure shows the ground-plane side of the antenna and the meshing configuration used in the method of moments calculations. . . . . | 17 |
| 2.3  | Electric current distribution on the microstrip feed of the slot antenna at the resonant frequency. . . . .  | 18 |
| 2.4  | Simulated reflection coefficient of the miniaturized UHF antenna with an infinite ground plane. (a) Smith chart representation. (b) Magnitude of $ S_{11} $ in logarithmic scale. . . . .  | 21 |
| 2.5  | Measured reflection coefficient of three miniaturized UHF slot antennas, described in Table 2.1 and shown in Fig. 2.7, all having the same size and geometry, but with different ground plane sizes. . . . .   | 23 |
| 2.6  | Simulated Gain of the UHF miniaturized antenna on an infinite substrate with $\epsilon_r = 4.0(1 - j \tan \delta)$ . . . . .   | 24 |
| 2.7  | A photograph of three miniaturized UHF antennas, all having the same topology and dimensions but with different ground plane sizes. . . . .  | 24 |
| 2.8  | Identification of the principle E and H planes of the proposed miniaturized quarter-wave antenna under test. . . . .   | 26 |
| 2.9  | Simulated radiation pattern of the miniaturized quarter-wave antenna for both E- and H- planes. . . . .  | 27 |
| 2.10 | The co- and cross-polarized pattern of the miniaturized UHF antenna in (a) E-plane and (b) H-plane. . . . .  | 28 |
| 3.1  | Magnetic current distribution on a half wavelength and inductively terminated miniaturized slot antenna. . . . .   | 35 |
| 3.2  | Transmission line model of a slot antenna (a) Half wave slot antenna; (b) Inductively terminated slot antenna; (c) Two series inductive terminations. . . . .  | 36 |

|      |   |    |
|------|---|----|
| 3.3  | Proposed antenna geometry fed by a two-port microstrip feed. This two-port geometry is used to find out the exact resonant frequency of the inductively loaded slot. . . . .  | 37 |
| 3.4  | S-parameters of the two-port antenna shown in Fig. 3.3. . . . .   | 41 |
| 3.5  | Topology of the equivalent circuit for the two-port antenna. . . . .  | 42 |
| 3.6  | Y-parameters of the two-port antenna after deembedding the microstrip feed lines. . . . .   | 44 |
| 3.7  | Comparison between the full-wave simulated S-parameters of the antenna and that of the equivalent circuit. . . . .  | 46 |
| 3.8  | The required terminating admittance for the second port of the two-port model in order to match the antenna to a $50\ \Omega$ line. . . . .   | 46 |
| 3.9  | The geometry of the antenna and its feed designed to operate at 300 MHz. . . . .  | 48 |
| 3.10 | Measured and simulated return loss of the miniaturized antenna. . . . .   | 49 |
| 3.11 | A photograph of the fabricated miniaturized slot antenna at 300 MHz. . . . .  | 50 |
| 3.12 | Simulated radiation pattern of the miniaturized antenna. . . . .  | 52 |
| 3.13 | Measured radiation patterns of the antenna with a small ( $0.2\lambda_0 \times 0.2\lambda_0$ ) and a larger ( $0.5\lambda_0 \times 0.5\lambda_0$ ) Ground Plane (GP): (a) H-plane pattern, (b) E-plane pattern. . . . .   | 53 |
| 3.14 | A photograph of the miniaturized slot antenna conformed into a curved surface along the H-plane. . . . .  | 55 |
| 3.15 | Comparison between the measured radiation pattern of the conformed miniaturized slot antenna of Fig. 3.14 with that of its planar counterpart having a large ground plane (GP) with dimensions of ( $0.5\lambda_0 \times 0.5\lambda_0$ ): (a) H-plane pattern, (b) E-plane pattern. . . . . | 57 |
| 3.16 | A photograph of the miniaturized slot antenna conformed into a curved surface along the E-plane. . . . .  | 58 |
| 3.17 | Comparison between the measured radiation pattern of the conformed miniaturized slot antenna of Fig. 3.16 with that of its planar counterpart having a large ground plane (GP) with dimensions of ( $0.5\lambda_0 \times 0.5\lambda_0$ ): (a) H-plane pattern, (b) E-plane pattern. . . . . | 59 |
| 4.1  | The layout and the the simulated input impedance of the miniaturized slot antenna around its resonance. . . . .   | 64 |
| 4.2  | The layout and the simulated input impedance of the miniaturized folded slot antenna around its resonance. . . . .  | 66 |
| 4.3  | Miniaturized folded-slot antenna fed by a capacitively coupled CPW line. . . . .  | 67 |
| 4.4  | Simulated and measured input return loss of the miniaturized folded slot antenna of Fig. 4.3. . . . .   | 68 |
| 4.5  | Measured radiation pattern of the miniaturized folded slot antenna of Fig. 4.3. (a) H-plane pattern, (b) E-plane pattern. . . . .   | 70 |
| 4.6  | Layout of the miniaturized folded printed wire antenna, and the real and imaginary parts of its input admittance. . . . .   | 72 |
| 4.7  | Merchand balun architecture. . . . .  | 73 |

|      |   |    |
|------|---|----|
| 4.8  | The miniaturized folded printed wire antenna with balanced feed and fine tuning setup. . . . .  | 74 |
| 4.9  | Simulated and measured input return loss of the miniaturized antenna in Fig. 4.8. . . . .   | 74 |
| 4.10 | E- and H-plane measured radiation patterns of the miniaturized folded printed wire of Fig. 4.8. . . . .   | 75 |
| 4.11 | The simulated radiation pattern of the miniaturized folded printed wire antenna without a balun. . . . .  | 75 |
| 4.12 | The miniaturized self-complementary folded antenna fed by a two-port self-complementary asymmetric CPW-line. . . . .  | 78 |
| 4.13 | The two-port simulated S-parameters of the miniaturized self-complementary folded antenna of Fig. 4.12 to be used for obtaining a proper loss-less matching network. . . . .  | 79 |
| 4.14 | The equivalent circuit of the required matching network to a $50 \Omega$ line. . . . .  | 80 |
| 4.15 | The geometry of the miniaturized self-complementary folded antenna along with the distributed-element realization of the matching network of Fig. 4.14. . . . .   | 80 |
| 4.16 | The measured, simulated, input return losses of the antenna of Fig. 4.15, as well as that of the equivalent circuit model of Fig. 4.14. . . . .   | 81 |
| 4.17 | Comparison between the measured and simulated radiation patterns of the miniaturized self-complementary antenna on three different planes of (a): $\phi = 0^\circ$ , (b): $\phi = 45^\circ$ , and (c): $\phi = 90^\circ$ . . . . .        | 83 |
| 4.18 | The topology of a self-complementary H-antenna fed by a short-circuited microstrip line. . . . .  | 85 |
| 4.19 | Measured and simulated return losses of the H-antenna in Fig. 4.18, as well as that of the same structure without dielectric ( $\epsilon_r = 1.0$ ). . . . .  | 85 |
| 4.20 | Comparison between the measured and simulated gains of the self-complementary H-antenna as a function of frequency. . . . .   | 86 |
| 4.21 | Comparison between the measured and simulated gain of the self-complementary H-antenna as a function of frequency. . . . .  | 87 |
| 4.22 | Comparison between the measured and simulated radiation patterns of the self-complementary H antenna at 1.5 GHz for three cuts of $\phi = 0^\circ$ , $\phi = 45^\circ$ , $\phi = 90^\circ$ ; (a): measurements, (b): simulations. . . . . | 88 |
| 4.23 | Comparison between the measured and simulated radiation patterns of the self-complementary H antenna at 2.0 GHz for three cuts of $\phi = 0^\circ$ , $\phi = 45^\circ$ , $\phi = 90^\circ$ ; (a): measurements, (b): simulations. . . . . | 89 |
| 4.24 | Comparison between the measured and simulated radiation patterns of the self-complementary H antenna at 2.5 GHz for three cuts of $\phi = 0^\circ$ , $\phi = 45^\circ$ , $\phi = 90^\circ$ ; (a): measurements, (b): simulations. . . . . | 90 |
| 4.25 | Comparison between the measured and simulated radiation patterns of the self-complementary H antenna at 3.0 GHz for three cuts of $\phi = 0^\circ$ , $\phi = 45^\circ$ , $\phi = 90^\circ$ ; (a): measurements, (b): simulations. . . . . | 91 |

|      |  |     |
|------|--|-----|
| 5.1  | A weakly coupled miniaturized slot-line resonator at 300 MHz with symmetrical inductive loadings. . . . .  | 97  |
| 5.2  | Photograph of the proposed miniaturized resonator capacitively coupled at 400 MHz with asymmetric end-loadings. . . . .  | 98  |
| 5.3  | Smith chart representation of the measured input admittance of the weakly coupled miniaturized resonator at 400 MHz. . . . .   | 99  |
| 5.4  | The miniaturized slot-line resonator topology with different ratios of slot to stirp width ( $s/w$ ) . . . . .   | 101 |
| 5.5  | Photograph of the optimized miniature resonator at 2.45 GHz. . . . .   | 102 |
| 5.6  | Equivalent circuit model of coupled miniaturized resonators exhibiting: (a) Electric coupling, (b) magnetic coupling, and (c) mixed coupling. . . . .  | 105 |
| 5.7  | Extracted coupling coefficients for a back-to-back coupling configuration (A) as a function of the horizontal separation $\Delta x$ for two different values of vertical offsets $\Delta y$ . . . . .  | 107 |
| 5.8  | Extracted coupling coefficients for configuration (B) (face-to-face arrangement) as a function of horizontal separation $\Delta x$ for two different values of vertical offsets $\Delta y$ . . . . .   | 107 |
| 5.9  | Comparison between dominantly magnetic: configuration (A), and dominantly electric: configuration (B), for the same overall coupling coefficient. (Note the locations of zeros.) . . . . .   | 108 |
| 5.10 | Two different methods for external coupling: (a) Electric coupling; (b) Magnetic coupling. . . . .   | 110 |
| 5.11 | The photograph and schematic of the miniaturized four-pole Chebyshev filter at 400 MHz. . . . .  | 111 |
| 5.12 | Comparison between the simulated and measured S parameters of the filter in Fig. 5.11. . . . .   | 112 |
| 5.13 | Layout of a four-pole miniaturized filter, with inline resonators at 400 MHz, as well as the comparison between its simulated and measured S parameters. . . . .   | 113 |
| 5.14 | Schematic of a low-pass prototype quasi-elliptic filter with series elements. . . . .  | 114 |
| 5.15 | Rational function ( $f(\omega)$ ) of the fourth order ( $n = 4$ ) with single attenuation pole corresponding to a transmission zeros. This function is used as a shape function for the synthesis of the quasi elliptic filter of Fig. 5.14. . . . . | 115 |
| 5.16 | Extracted coupling coefficients for configuration (A), as a function of resonators separation $\Delta x$ for different values of vertical offsets $\Delta y$ at 2.4 GHz. . . . .   | 117 |
| 5.17 | Topology of the modified coupling structure B, and the effect of the width of slot incision ( $w$ ) in the type and magnitude of coupling for the case of $h = 8\text{mm}$ . . . . .   | 118 |
| 5.18 | Extracted coupling coefficients for the coupling configuration shown in Fig. 5.17, as a function of incision width and height (in millimeter), at 2.4 GHz. . . . .   | 119 |

|      |   |     |
|------|---|-----|
| 5.19 | Extracted coupling coefficients for coupling configuration (C), as a function of the horizontal offset between the resonators $\Delta x$ for different values of vertical distances $\Delta y$ at 2.4 GHz. . . . .  | 119 |
| 5.20 | Photograph and schematic layout of a miniaturized quasi elliptic filter at 2.4 GHz with dimensions of $0.09\lambda_0 \times 0.14\lambda_0$ . . . . .  | 120 |
| 5.21 | Comparison between the lumped-element prototype, full-wave simulated, and measured S parameters of the quasi elliptic filter of Fig.5.20.   | 121 |
| 5.22 | The lumped-element prototype of a normalized quasi-elliptic bandpass filter in which, the cross-coupling term $k_{14}$ is realized by a mixed coupling where the difference between the two electric and magnetic coupling components is constant. . . . .                            | 122 |
| 5.23 | The variation of the location of transmission zeroes of a normalized quasi elliptic filter of Fig. 5.20 for different values of the ratio of the magnetic component to the electric component of the cross-coupling term $\eta = k_m/k_e$ , given that $k_{14} = k_e - k_m$ . . . . . | 123 |
| 6.1  | Illustration of Babinet's principle for three receiving antennas (a): an aperture antenna in a PEC screen, (b): the complimentary PEC strip, (c): the dual case of PMC strip. . . . .   | 128 |
| 6.2  | The input impedance of the PEC strip ( $Z_e$ ) with $\ell=55$ mm around its first resonance. . . . .  | 131 |
| 6.3  | the maximum back-scattering cross-section of the printed dipole as a function of load resistance $Z_{Le}$ . . . . .   | 132 |
| 6.4  | The radar cross-section of a slot antenna with the length of $\ell = 55$ mm, and ground plane size of $2\lambda \times 2\lambda$ , when the load impedance is changed as a parameter; (a) total RCS, (b) RCS after coherent subtraction. . . . .                                      | 137 |
| 6.5  | The layout of a center-fed slot antenna with $\ell = 55$ mm, and ground plane size of $14 \text{ cm} \times 14 \text{ cm}$ . . . . .  | 138 |
| 6.6  | The simulated total RCS of the slot antenna of Fig. 6.5 as a function of frequency for different values of load resistance ( $R_{La}$ ). . . . .  | 139 |
| 6.7  | Incoherent subtraction of the scattered power of the ground plane (background) from the total back-scattered power shown in Fig. 6.6. . . . .   | 140 |
| 6.8  | Coherent subtraction of the scattered field of the ground plane (background) from the total back-scattered field coming from the aperture and the ground. . . . .   | 140 |
| 6.9  | The layout of a center-fed miniaturized slot antenna with dimensions of about $0.05\lambda_0 \times 0.05\lambda_0$ , and ground plane size of $35.5 \text{ cm} \times 35.5 \text{ cm}$ . . . . .  | 142 |
| 6.10 | The simulated input impedance of the miniature antenna of Fig. 6.9 when fed at the center. . . . .  | 143 |
| 6.11 | The simulated total RCS of the slot antenna of Fig. 6.5 as a function of frequency for different values of load resistance ( $R_{La}$ ). . . . .  | 143 |
| 6.12 | Incoherent subtraction of the scattered power of the ground plane (background) from the total back-scattered power shown in Fig. 6.11. . . . .  | 144 |

|      |  |     |
|------|--|-----|
| 6.13 | Coherent subtraction of the scattered field of the ground plane (background) from the total back-scattered field of the miniaturized antenna of Fig. 6.9. . . . .  | 145 |
| 6.14 | High-impedance measurement setup for measuring the input impedance of the miniaturized slot antenna of Fig. 6.9. . . . .   | 146 |
| 6.15 | The input impedance of the high impedance miniaturized slot antenna of Fig. 6.9 measured using the setup of Fig. 6.14. . . . .   | 146 |
| 6.16 | Schematics of the equivalent circuit of the high-impedance antenna of Fig. 6.9 extracted by the impedance analyzer along with the line deembedding scheme. . . . .   | 147 |
| 6.17 | The measured input impedance of the high-impedance miniaturized slot antenna of Fig. 6.9 after deembedding the effect of the microstrip-line. . . . .  | 148 |
| A.1  | Slot antenna in a perfectly conducting ground plane center fed by a two-wire transmission line. . . . .  | 157 |
| A.2  | The geometry of a standard slot antenna along with its principle E- and H-planes. . . . .  | 161 |
| A.3  | The simulated radiation pattern of a slot antenna on air with an infinite ground plane using IE3D with magnetic current discretization. . . . .  | 163 |
| A.4  | The simulated radiation pattern of a slot antenna with an infinite ground plane over an infinite extent dielectric substrate with $\epsilon_r = 2.2$ and thickness of 0.7874 mm using IE3D with magnetic current discretization. . . . . | 164 |
| A.5  | Comparison between the simulated radiation patterns of a finite ground plane slot with no dielectric substrate, obtained from IE3D (electric current discretization) and HFSS. . . . .   | 165 |
| A.6  | The simulated radiation pattern of a slot antenna with a finite ground plane on a dielectric substrate using IE3D. . . . .   | 166 |
| A.7  | The simulated radiation pattern of a slot antenna with a finite ground plane and finite dielectric substrate obtained from HFSS. . . . .   | 167 |

# CHAPTER 1

## Introduction

### 1.1 Motivation and Background

Antennas are among the most important components of a wireless network, and as far as efficiency and size are concerned, they may impose stringent restrictions on the size and performance of any wireless system. With recent advances in solid-state devices and MEMS technology, construction of high performance miniaturized transmit and receive modules are now realizable. Although significant efforts have been devoted towards achieving low-power miniaturized electronic and RF components, issues related to design and fabrication of efficient, miniaturized, and easily integrable antennas have been overlooked. This remains true not only for antennas but also for all passive distributed microwave components such as resonators, filters and couplers whose dimensions are comparable or larger than a wavelength. This wavelength dependence stems from the fact that all of the aforementioned distributed components are composed of one or more resonant structures. The main objective of this dissertation is to embark on the challenging issue of antenna and microwave filter miniaturization to ultimately realize the holy grail of the next generation of wireless systems; that is, the idea of integrating antennas on a chip with the rest of the transceiver circuitry.

In addition to the need for miniaturization, low-power characteristics of such transmit/receive modules are extremely important and require highly efficient low-loss miniaturized components. In order to reach minimum power consumptions in the micro-circuits, high-impedance solid-state devices are preferred since they are less-expensive due to their smaller size. As the size of micro/nano-devices decreases, the bias current and DC power consumption are reduced. Meanwhile, the impedance of these devices increases drastically. For example, the motional resistance of MEMS resonators is on the order of a few kilo-ohms, which necessitates at least an order of magnitude larger input and output termination impedances so that their superb performance can be fully exploited and accurately measured. Obviously, if a miniaturized antenna is sought for integration with MEMS transceivers, it should demonstrate very high input impedance characteristics so as to be compatible with the MEMS circuitry. Therefore, a *high-impedance* miniature antenna is desired for such applications.

The use of high-impedance miniature antennas is not limited to the front-end of microsystems. These antennas may also be used in conjunction with nano-scale devices such as Carbon Nano Tube (CNT) transistors or nano-scale MOSFETs. CNT transistors are emerging as new high-speed low power nano-scale transistors. It is predicted that these devices would be extremely fast due to the ballistic transport of electrons inside the nano-tube, and that they demonstrate very low parasitic capacitances (in the order of several aF<sup>1</sup>). Yet, there is no report on the high-frequency operation of these devices. One reason is that they have a very high-impedance ( $\approx 5k\Omega$ ), and thus, they are extremely difficult to test and measure at RF. One way of utilizing these high-impedance devices is to use them in conjunction with high-impedance miniature antennas developed in this research. By doing so, we can also make these nano devices of practical use in new arenas. It is also important to have a compact and high-impedance antenna that can be matched directly to small size

---

<sup>1</sup> $10^{-18} F$

(minimum feature size) transistors to keep power consumption at a minimum.

In the context of the above examples, the design and fabrication of highly-efficient miniaturized antennas and microwave filters are of a great interest. By adding the high-impedance feature to miniature antenna characteristics, one of the major issues of nano-scale devices, especially at higher frequencies, can be resolved. Thus, these miniaturized components, together with micro/nano-scale sensors and transducers, may find numerous applications in industry, medicine, and the military.

The subject of small antennas is not new. The literature addressing this subject dates back to the early 1940's. The early studies of small antennas, however, were restricted to the establishment of the fundamental limitations of this class of antennas, where features such as bandwidth, gain, and efficiency have analytically been related to the antenna size [1, 2, 3]. Using a multi-pole expansion and a clever equivalent circuit model, Chu was able to derive the  $Q$  factor of the equivalent circuit for each spherical mode in terms of the normalized radius ( $a/\lambda$ ) of the smallest sphere enclosing the antenna structure. Also, it is shown that the  $Q$  of the lowest order mode is a lower bound for the  $Q$  of a single resonant antenna. Qualitatively, these studies show that for single resonant antennas, the smaller the maximum dimension of an antenna, the higher its  $Q$ , or equivalently, the lower its bandwidth. Nevertheless, no discussion is provided in the above literature about small antenna topologies, and its impedance matching.

In recent years, practical aspects of antenna miniaturization have received significant attention. Most successful designs rely on the use of high-permittivity ceramics, which are not suitable for monolithic integration. Moreover, this approach is prone to surface-wave excitation at higher frequencies. Another approach for antenna miniaturization, reported in the literature, is to use meandered-line antennas, in which a half wavelength antenna is made compact by meandering the line. In general, meandered antennas have considerable ohmic losses, and hence, must be fabricated on

high-temperature superconductive films.

Another approach for designing small antennas is to find a miniaturized topology with a minimal ohmic loss and an appropriate characteristic impedance. In accordance with this premise, a novel class of miniaturized slot topology is introduced. Variation of this topology has been extensively employed to design a variety of efficient miniaturized antennas, high- $Q$  microwave filters, and resonators. The proposed miniature slot topology, when used for antenna design, demonstrates a much less ohmic loss, and thus, higher efficiency than meandered microstrip structures. When used for resonator/filter miniaturization, the application of miniaturized slot-line topology leads to a much higher  $Q$ , or equivalently, lower insertion loss than that of microstrip filters. This miniaturized topology also demonstrates the high-impedance property required for some micro- and nano-devices.

Miniature antennas, as alluded to briefly in the earlier discussion, are inherently narrow band, where the bandwidth is subject to a fundamental limit. At the first glance, the bandwidth limit might seem to be intractable, whereas is not the case for planar antennas. In other words, the fundamental limit introduces a loose upper bound on the bandwidth of a planar antenna. For three dimensional antennas, in contrast, the attainable bandwidth can get closer to the fundamental limit. As a result, a considerable improvement in the bandwidth of planar antennas might be still possible without violating the fundamental limit.

The bandwidth of miniaturized antennas can be improved more effectively if we understand the causes of their narrow bandwidth. The radiation conductance of a slot antenna is an equivalent quantity, whose dissipated power models the radiated power by the antenna. Likewise, the radiation resistance of wire and printed antennas is defined. The radiation resistance does not contribute to the overall loss of the antenna. Instead, it indicates how effectively an antenna may perform. Moreover, radiation resistance/conductance determines the radiation quality factor, defined as

$Q_{rad} = 1/\Delta$ , where  $\Delta$  is the fractional bandwidth of the antenna. For the slot structure, radiation conductance is proportional to the length of the slot line. As the miniaturization increases, the radiation conductance decreases, and thus, it leads to a higher  $Q_{rad}$  and a lower antenna bandwidth. If the physical aperture of a slot antenna is increased in such a way that its overall dimensions remain the same, the radiation conductance as well as the bandwidth increases. Based on the above premise, a miniaturized *folded-slot* topology is introduced whose radiation conductance is four times as much as that of an unfolded miniaturized slot topology, while having almost the same dimensions.

Another factor limiting the bandwidth of small antennas is the required matching network, which turns out to be narrow-band by itself. As mentioned earlier, the radiation conductance of a miniaturized slot is very small, where it translates into a very high input impedance. Matching such a high-impedance to a standard  $50\Omega$  line is rather difficult and should be done off-resonance. At an off-resonant frequency, however, the reactance slope of the antenna impedance is very high, and therefore, matching would be narrow band. To alleviate this problem, namely, rapid variation of the input resistance and reactance with respect to frequency, the idea of self-complementarity may be tried. The input impedance of a self-complementary antenna, in an ideal case, is a frequency-independent real quantity. A few conditions must be satisfied by a self-complementary structure. The first condition is that the structure should be of an infinite extent. Obviously, this condition is contradictory to the notion of miniaturization and will be treated so that an economical compromise may be reached.

Another major thrust of this research pertains to the design and miniaturization of passive microwave resonators and filters. A few approaches in the literature address filter miniaturization, among which are the use of lumped-element filters, high-temperature super conducting (HTS) filters, and slow-wave distributed resonators

[4, 5]. Although filters designed using lumped-elements can be made very small, their insertion loss becomes prohibitively large at UHF and beyond. The power handling capability of lumped-element filters may also be very poor at high frequencies. To cope with the insertion loss and probably power handling problems, high-temperature super-conducting filters (HTS) have been proposed, which can play an important role in communication systems if the cost issue is resolved [6]. In addition to the cost and complexity associated with the HTS circuits, superconductivity has not yet been demonstrated at room temperature. Cooling systems and their power requirements make the current HTS technology inapplicable for mobile wireless systems [7]. Distributed element approaches in miniaturized filter design, such as coupled transmission-line resonators, exhibit far superior performance with regard to the insertion loss and power handling capabilities compared to lumped-element filters. On the other hand, size and complexity are two major drawbacks of distributed element filters.

The prevalent idea throughout this dissertation is to implement a novel and efficient miniaturized topology suitable to design miniaturized distributed microwave resonators and filters. The building block of the proposed topology for miniature resonators is similar to the one used for miniaturized antennas. The miniature resonators, on one hand, are conducive to the design of miniaturized antennas when the impedance of these resonators are matched to that of the standard transmission-line. On the other hand, the appropriate coupling between these miniaturized resonators, through adjusting their distance and orientation with respect to each other, would lead to miniaturized direct-coupled bandpass filters. Additionally, the proposed resonators allow for both electric and magnetic coupling –also referred to as negative and positive coupling– and thus, enabling the design of elliptical and quasi-elliptical filters. Quasi-elliptical filters are very compact, and at the same time, provide a very sharp out of band rejection due to the existence of two out-of-band transmission zeros.

Having successfully introduced novel miniaturized topologies for antenna, resonator, and filter applications, issues related to the integration of these components to the active electronics and circuitry must be addressed. As mentioned earlier, one of the restrictions in the integration process is the ultra high impedance of the electronics as well as micro- and nano-devices. The standard characteristic impedance adopted for RF applications is  $50\Omega$ , which makes it impossible to be matched directly to low-power high-impedance electronics with the use of ordinary matching networks. Conversely, significant effort has been devoted to modifying the electronic devices so as to reduce their input impedance level. In doing so, the size and cost of such a device, as well as its power consumption, would increase considerably. Another difficulty in dealing with high-impedance structures is that their performance cannot be accurately measured at RF since microwave measurement instruments are also designed to work well for impedances in the same order of magnitude as the standard impedance. All of the above ramifications remain true for micro- and nano-scale devices. Thus, the high-impedance miniature antenna introduced in this research may find numerous applications in the area of micro- and nano-systems.

In the future, this research can be pursued in a number of different directions, some of which are immediate extensions, while others can be a part of a longer term plan. A few of the short term extensions of this work include the use of the proposed miniaturized topology in almost any application, in which a resonant structure such as antenna, resonator, and filter is required. Array configuration of miniaturized antennas for automotive and radar applications, frequency selective surfaces, and lenses can lead to much smaller wireless and radar systems. Multi-functional and reconfigurable miniaturized and tunable antennas and resonators are among other areas where the contribution of this thesis may find prospective applications. In the long run, the high-impedance feature of the proposed miniature antenna can find numerous applications in conjunction with the emerging high-impedance nano-scale

devices in interfacing, impedance matching, and testing.

## 1.2 Thesis Overview

The primary objective of this thesis is to introduce a power efficient miniaturized solution for mobile wireless systems. This task has been divided into three main thrusts. The first thrust addresses issues related to the design and fabrications of miniaturized antennas. A great amount of attention is devoted to different aspects of this task, such as miniaturizing the antenna topology, enhancing the antenna bandwidth, and introducing the complementary and self-complementary realization of the same topology (Chapters 2,3,4). The second thrust addresses the design of miniaturized high- $Q$  resonators and RF filters, which will be presented in Chapter 5. The last piece of this work touches on the interfacing of the miniaturized antennas to the high-impedance electronics, MEMS, and nano-devices (Chapter 6). In more details, the outline of this thesis is as follows.

In Chapter 2, a UHF miniaturized planar antenna is introduced. This antenna consists of a quarter-wavelength resonant slot-line. The resonance is established by means of an open- and a short-circuit at both ends of the slot-line. Short-circuit termination for a slot-line is readily realizable due to the presence of the ground plane. The open-circuit termination, however, can only be realized using distributed elements by employing two coiled quarter-wave short-circuited slot lines. Further miniaturization is made possible through additional modification of the antenna topology so as to use the two dimensional area more efficiently. As a result, a miniaturized UHF planar slot antenna with dimensions of  $0.12\lambda_0 \times 0.12\lambda_0$  is achieved.

Chapter 3 demonstrates a novel approach for the miniaturization of slot antennas. The antenna design in Chapter 2 was based on the realization of an open and a short boundary condition at each end of the slot-line, which can only provide a quarter-wave

antenna. The basic premise of this chapter is to implement variable reactive boundary conditions instead of open-circuit or short-circuit terminations. The advantages of reactive boundary conditions are twofold. One advantage is that the symmetry of the antenna structure is preserved; the other is that much smaller antennas than a quarter-wavelength are feasible. The overall area occupied by this antenna can be precisely controlled by adjusting reactive boundary conditions at both ends of the slot-line. The application of such loads is shown to reduce the size of the resonant slot antenna for a given resonant frequency, without imposing any stringent condition on its impedance matching. The matching procedure is based on an equivalent circuit model for the antenna and its feed structure. The corresponding equivalent circuit parameters are extracted using a full-wave forward model in conjunction with a Genetic Algorithm (GA) optimizer. These parameters are employed to find a proper matching network to a  $50\ \Omega$  line. It is shown in this chapter that for a prototype slot antenna with approximate dimensions of  $0.05\lambda_0 \times 0.05\lambda_0$ , the impedance match is obtained with a fairly high gain of  $-3\ \text{dBi}$ , for a very small rectangular ground plane ( $\approx 0.20\lambda_0 \times 0.20\lambda_0$ ).

Chapter 4 delineates methodologies to enhance the bandwidth of miniaturized antennas. These methods include the application of folded and self-complementary structures, both of which are shown to be very effective for bandwidth improvement. The miniaturized folded-slot topology is demonstrated to enhance the bandwidth of the miniaturized slot antenna of Chapter 3 by more than 100%. The radiation conductance of a miniaturized folded-slot topology is four times larger than that of a miniaturized slot antenna, and thus, it is much easier to match to a  $50\ \Omega$  line. Furthermore, the higher the radiation conductance, the lower the  $Q$  and the higher bandwidth can be expected.

Another methodology described in this chapter is to utilize the concept of self-complementarity to achieve a wider bandwidth. In theory, self-complementary struc-

tures must be of infinite extent in order to behave as a frequency independent antenna. Nevertheless, a compromise can be made between the size (truncation) and the bandwidth. In the first example of self-complementary design, a self-complementary miniaturized folded antenna is presented, where it shows more than 20% bandwidth increase over the folded-slot of the same size. The next example of this chapter deals with an H-shaped self-complementary antenna, in which the miniaturization criterion has been relaxed in favor of bandwidth. The H-shape antenna demonstrates a very wide -10 dB return loss bandwidth of 2.3:1 and a fairly constant gain of slightly above 1 dBi over the entire band of operating frequency. The dimensions of this antenna are  $0.13\lambda_0 \times 0.24\lambda_0$  at the lowest frequency of operation.

The focus of the second thrust of this thesis is RF filter miniaturization, which is the topic of Chapter 5. In this chapter, both miniaturized slot-line and folded-slot resonators are used to design different types of direct- and cross-coupled filters. Coupling between the adjacent resonators is extracted using the pole-splitting method with the aid of a full-wave EM simulator. Having extracted the coupling coefficients, design curves can be generated, and the filter theory may be employed to design different bandpass filters. The size of introduced miniaturized filters is shown to be very small compared to that of conventional transmission-line filters, without compromising their insertion loss drastically. The  $Q$  of the proposed slot-line filters is demonstrated to be considerably higher than that of microstrip resonators of the same size. Also in this chapter, a rigorous study will be conducted on the effect of resonator parameters such as size and impedance on the unloaded  $Q$  of the structure.

The third part of this thesis deals with the interfacing of miniature antennas and high-impedance electronics, micro and nano-devices for wireless communication systems. Chapter 6 is an effort to address the issue of high-impedance antenna matching, which seems to be critical for nanotechnology, especially at high frequencies. The approach adopted in this chapter is to control the impedance of the miniaturized an-

tenna so that it can be matched directly to a high-impedance load without a need to any type of external matching network. This load can be an input stage of an LNA, a bank of MEMS filters, or a CNT transistor. Having designed a high-impedance miniature antenna, the impedance of the antenna needs to be measured. Available microwave measurement instruments are designed to work with the standard  $50\Omega$  systems. Nevertheless, an alternative measurement technique is required for high-impedance antennas. Chapter 6 introduces a new technique to measure the radiation resistance of high-impedance antennas. In this technique, first a relationship is established between the terminating impedance of a miniature antenna and its radar cross section (RCS). Also, the condition on RCS for the matched impedance is derived. Then, an antenna under test is terminated with a set of terminating impedances, and its RCS is measured. The antenna impedance can be identified when the RCS satisfies the condition for that of a matched antenna. This technique is, then, employed to measure the input impedance of the high-impedance miniature slot antenna presented in this research.

Finally, Chapter 7 summarizes the contributions presented in this thesis and submits recommendations for the future work.

## CHAPTER 2

# A Compact Quarter-wavelength Slot Antenna Topology

### 2.1 Introduction

With the advent of wireless technology and ever increasing demand for high data rate mobile communications, the number of radios on military mobile platforms has reached to a point that the real estate for these antennas has become a serious issue. Similar problems are also emerging in the commercial sector where the number of wireless services planned for future automobiles, such as FM and CD radios, analog and digital cell phones, GPS, keyless entry and etc., is on the rise. To circumvent the aforementioned difficulties to some extent, antenna miniaturization and/or compact multi-functional antennas must be considered. Such architectural antennas are, therefore, of great importance in mobile communication systems where low visibility and high mobility are required. Slot radiating elements, having a planar geometry and being capable of transmitting vertical polarization when placed nearly horizontal, are specifically appropriate for these applications. Moreover, slot antennas have another useful property so far as impedance matching is concerned. Slot dipoles can easily be excited by a microstrip line and can be matched to arbitrary line impedances

simply by moving the feed point along the slot. Slot structure seems to satisfy most requirements of mobile communication systems, and consequently, it is chosen as a suitable candidate to design miniaturized antennas.

The subject of antenna miniaturization is not new. The literatures concerning this subject date back to the early 1940's [8, 1]. To our knowledge the fundamental limitations of small antennas was first addressed by Chu in 1948 [1]. Using a multipole expansion and a clever equivalent circuit model, Chu was able to derive the  $Q$  factor of the equivalent circuit for each spherical mode in terms of the normalized radius ( $a/\lambda$ ) of the smallest sphere enclosing the antenna. In [1] it is also shown that the  $Q$  of the lowest order mode is a lower bound for the  $Q$  of a single resonant antenna. This subject was revisited by Wheeler [9], Harrington [3], and Collins [10]. In [10] a similar procedure is used for characterization of a small dipole antenna using cylindrical wave functions. Then, a cylindrical enclosing surface is used which produces a tighter lower bound for the  $Q$  of small antennas with large aspect ratios such as dipoles and helical antennas. Qualitatively, these studies show that for single resonant antennas, the smaller is the maximum dimension of an antenna, the higher is its  $Q$  or equivalently the lower is its bandwidth [2]. However, in these papers no discussion is provided about the miniaturization methods, antenna topology, or impedance matching.

Considering the wave propagation issues where line-of-sight communication is an unlikely event, such as in an urban environment or over irregular terrain, carrier frequencies at HF-UHF band are commonly used. At these frequencies there is considerable penetration through vegetation and buildings, wave diffraction around obstacles, and wave propagation over curved surfaces. However, at these frequencies the size of efficient antennas are relatively large and therefore a large number of such antennas may not fit in the available space without the risks of mutual coupling and co-site interference. Efficient antennas require dimensions of the order of half a wavelength

for single frequency operation. To cover a wide frequency range, broadband antennas may be used, however, dimensions of these antennas are comparable to or larger than the wavelength at the lowest frequency. Besides, depending on the applications, the polarization and the direction of maximum directivity for different wireless systems operating at different frequencies may be different and hence a single broadband antenna may not be sufficient. It should also be noted that any type of broadband antenna is highly susceptible to electronic warfare jamming techniques. Variations of monopole and dipole antennas in use today are prohibitively large and bulky at HF through VHF, and therefore, efforts to achieve miniaturized antennas are inevitable.

In subsequent sections, the topology of an efficient, miniaturized, resonant slot antenna is presented, and then, its input impedance, bandwidth, and radiation characteristics are investigated. This class of antennas can exhibit simultaneous band selectivity and anti-jam characteristics in addition to possessing a planar structure and low profile, which is easily integrable with other RF and microwave circuits.

## 2.2 Compact Spiral Antennas

Equiangular and Archimedean spiral antennas [11] are commonly used as broadband antennas. These antennas usually have arm length larger than a wavelength. Not much has been reported about the performance of spiral antennas when the arm length is half of the guided wavelength (a resonance condition). One obvious reason is that slot spiral antennas are usually center-fed where at the first resonance the input impedance is very high, and impedance matching becomes practically impossible. However, if we allow the feed point to be moved to one end of the arm, impedance matching to transmission lines with typical characteristic impedances seems possible.

First an equiangular spiral slot, as shown in Fig. 2.1(a), was considered. Using electrostatic analysis, the guided wavelength of a slot-line with finite ground plane

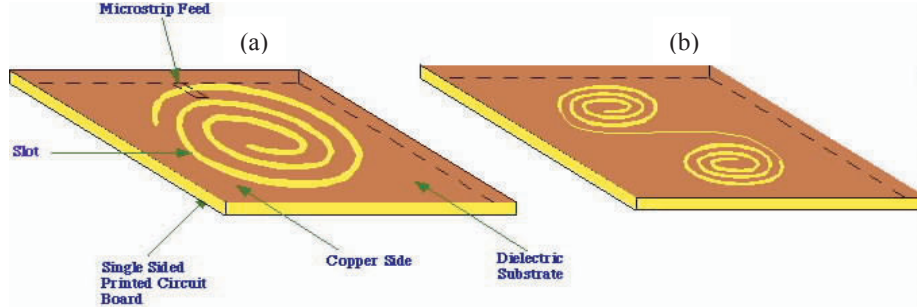


Figure 2.1: The geometry of resonant spiral antennas: (a) equiangular spiral, and (b) cornu spiral.

was calculated. The calculated guided wavelength was used to design an arm length of  $\lambda_g/2$ . The spiral was fed from the outer end using a microstrip line. The location of the feed point along the arm was found by trial and error until a good match was achieved. Also a slot dipole ( $\lambda/2$ ) coil around two center points (cornu spiral), as shown in Fig. 2.1(b), was considered. For this antenna, the microstrip feed was coiled around one arm on the other side of the substrate (over the ground plane) in order to feed the slot near an end point. Again by trial and error, the location of the feed point for best impedance match was found. A return loss of better than 20 dB for these antennas was obtained. However, gain measurement of these antennas showed poor radiation efficiencies (less than -10 dB). The efficiency of the cornu spiral was higher than the simple spiral antenna, nevertheless, neither showed an acceptable level of antenna efficiency. Far-field pattern and gain measurements at 60 MHz were carried out in an outdoor slant range using a boom truck and two antenna positioners.

The main problem in these designs seems to stem from the fact that the far-field generated by opposing equivalent magnetic currents along a resonant spiral antenna tend to cancel. To investigate whether ohmic losses are solely responsible for the low antenna efficiency, a similar antenna having the same geometry and substrate dielectric constant were constructed using a different dielectric quality factor and copper thickness. It was found that ohmic losses were not responsible for the lack of antenna efficiency to the degree observed in our measurements. By putting absorbers around

the feed cable and antenna positioner, it was found that these antennas produce a very strong near-field which can excite current on the nearby objects, such as the cable feeding them and the antenna positioner. The current induced on these objects in turn radiated the input power, but not necessarily in the direction of the maximum antenna radiation pattern. Thus, it can be discerned that the observed impedance match is owing to the near-field coupling to the feeding cable. Obviously, when the cable is shielded, the matching is deteriorated. This conclusion is consistent with our expectation that the antenna should be hard to match mainly due to the presence of opposing equivalent magnetic currents on the spiral.

### 2.3 A Miniature Quarter-wave Topology

A different topology for a miniaturized resonant slot is sought that does not have the drawbacks of the previously discussed spiral and cornu-spiral geometries. A major reduction in size is achieved by noting that a slot dipole can be considered as transmission line resonator where at the lowest resonant frequency the magnetic current (transverse electric field in the slot) goes to zero at each end of the dipole antenna. As mentioned before, at this frequency the antenna length is equal to  $\lambda_g/2$  where  $\lambda_g$  is the wavelength of the quasi-TEM mode supported by the slot-line.  $\lambda_g$  is a function of the substrate thickness, dielectric constant, and slot width, which is shorter than the free-space wavelength. In view of transmission line resonators, one can also make a quarter-wave resonator by creating a short circuit at one end and an open circuit at the other end. Creating a physical open circuit, however, is not practical for slot-lines.

The new design borrows the idea of the non-radiating tightly-coiled slot spiral from the previous design. Basically, a spiral slot of a quarter wavelength and short-circuited at one end behaves as an open circuit at the resonant frequency. Therefore, a quarter-wave slot-line, that is short-circuited at one end and terminated by the non-radiating

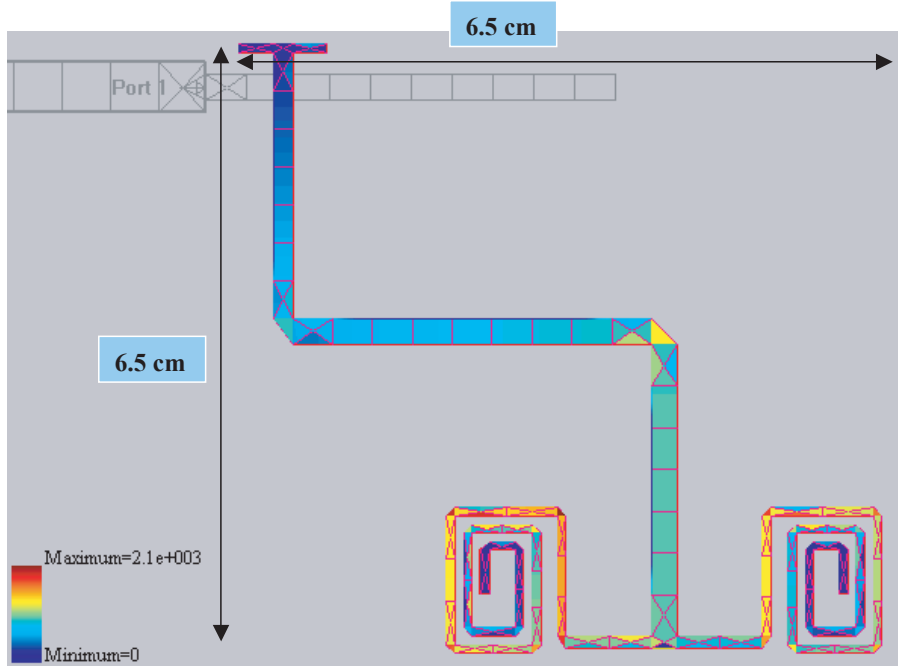


Figure 2.2: The magnetic current distribution on the UHF miniaturized slot antenna at the resonance frequency (600 MHz). The figure shows the ground-plane side of the antenna and the meshing configuration used in the method of moments calculations.

quarter-wave spiral at the other end, should resonate and radiate electromagnetic waves very efficiently. With this topology, the size of the slot dipole can be reduced by approximately 50%. Further size reduction can be accomplished by bending the radiating section. This bending procedure should be done so that no section of the resulting line geometry carries a magnetic current opposing the current on any other sections.

Fig. 2.2 shows the geometry of a typical  $\lambda_g/4$  compact resonating slot antenna. The radiating section is terminated with two identical quarter-wave non-radiating spiral slots to maintain the symmetry. It was found that by splitting the magnetic current at the end into equal and opposing magnetic currents, the radiation pattern is enhanced. Since the magnetic current distribution attains its maximum at the end of the quarter-wave line, the magnetic current in the beginning segments of a single (unbalanced) quarter-wave spiral reduces the radiation of the radiating section. But

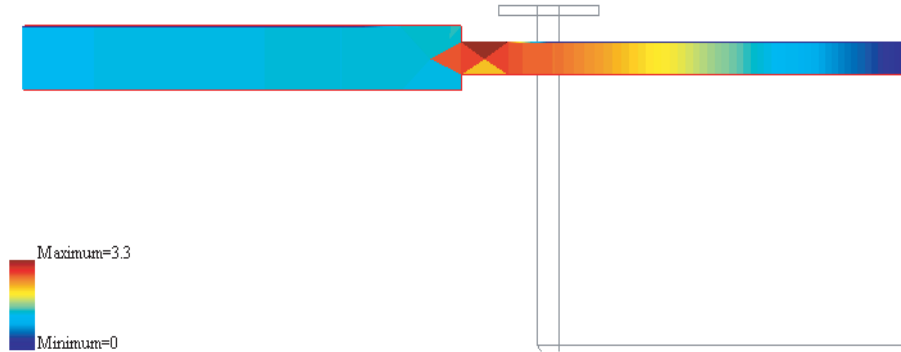


Figure 2.3: Electric current distribution on the microstrip feed of the slot antenna at the resonant frequency.

the opposite magnetic currents on two such spirals simply cancel the radiated field of each other, and as a result, the radiated field of the radiating section remains intact.

Additional miniaturization can also be achieved by noting that the strength of the magnetic current near the short-circuited end of the radiating section is insignificant. Hence, bending this section of the line does not significantly reduce the radiation efficiency despite allowing opposing currents. In Fig. 2.2 the T-top represents a small reduction in the length of the line without affecting the radiation efficiency.

This antenna is fed by an open-ended microstrip line shown in Fig. 2.3. A quarter wavelength line corresponds short-circuit line under the slot, however, using the length of the microstrip line as an adjustable parameter, the reactive part of the antenna input impedance can be compensated for. Figures 2.2 and 2.3, respectively, show the simulated electric current distribution on the microstrip feed and the magnetic current distribution on the slot of the compact UHF antenna designed to operate at 600 MHz. For this design we chose an ordinary FR4 substrate with a thickness of 3 mm (120 mil) and a dielectric constant of  $\epsilon_r = 4$ . A full-wave moment method software was used for the simulations of this antenna [12].

The microstrip feed is constructed from two sections: 1) a  $50\ \Omega$  line section, and 2) an open-ended  $80\ \Omega$  line. The  $80\ \Omega$  line is thinner which allows for compact and

localized feeding of the slot. The length of this line is adjusted to compensate for the reactive component of the slot input impedance. Noting that the slot appears as a series load in the microstrip transmission line, a line length of less than  $\lambda_m/4$  compensates for an inductive reactance, and a line length of longer than  $\lambda_m/4$  compensates for a capacitive reactance, where  $\lambda_m$  is the guided wavelength on the microstrip line.

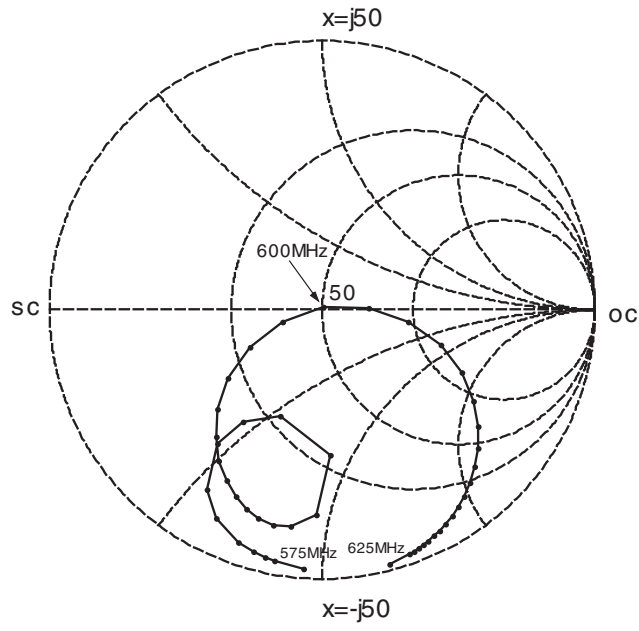
In the process of impedance matching, the length of the microstrip line feeding the slot was first set equal to a quarter-wavelength so that the the characteristic impedance of the slot antenna can be identified. Through this simulation, it was found that the slot antenna fed near the edge is inductive. Therefore, a length less than  $\lambda_m/4$  is chosen for the open-ended microstrip line to compensate for the inductive input impedance. The real part of the input impedance of a slot dipole depends on the feed location along the slot and increases from zero at the short-circuited end to about  $2000\ \Omega$  at the center (quarter wavelength from the short circuit). This property of the slot dipole allows for matching to almost all practical transmission line impedances. The crossing point of the microstrip line over the slot was determined using the full-wave analysis tool by trial-and-error. The uniform current distribution over the  $50\ \Omega$  line section, as shown in Fig. 2.3, indicates no standing wave pattern, which is a result of a very good input impedance match.

Apart from the T-top section, the quarter-wave radiating section of the slot dipole is composed of three slot-line sections, two vertical and one horizontal. Significant radiation emanates from the middle and lower sections. Changing the relative size of these two sections controls the polarization of the proposed antenna. In this design, the relative lengths of the three line sections were chosen in order to minimize the area occupied by the slot structure. The slot width of the first section can as well be varied in order to enhance the impedance matching. When there is a limitation in moving the microstrip and slot-line crossing point, the slot width may be changed. At a given point from the short-circuited end, an impedance match to a lower line

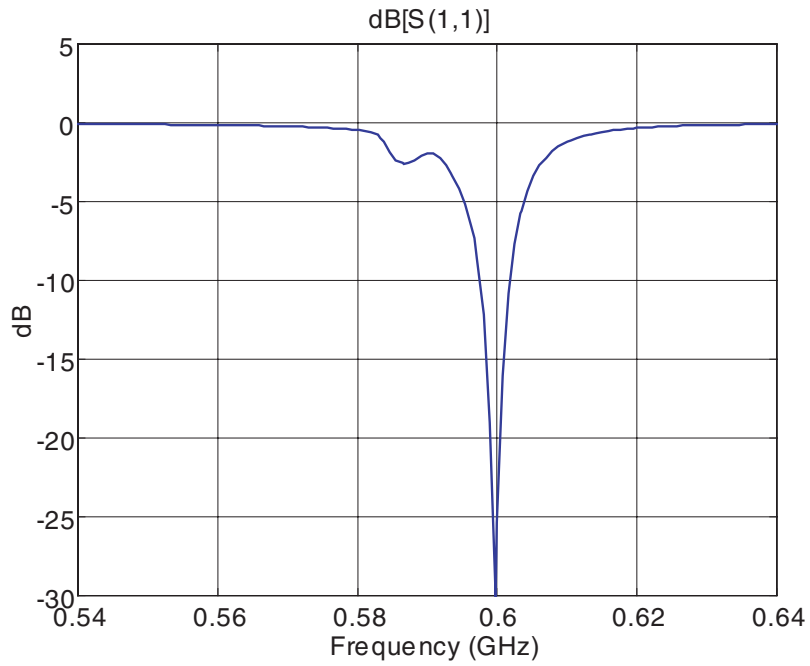
impedance can be achieved when the slot width is narrowed. This was used in this design, where the slot-line width of the top vertical section is narrower than those of the other two sections. It should be pointed out that by narrowing the slot-line width the magnetic current density increases, but the total magnetic current in the line does not. In other words, there is no discontinuity in the magnetic current along the line at points where the slot width is changed, however, there are other consequences. One is the change in the characteristic impedance of the line, and the second is the change in the antenna efficiency considering the finite conductivity of the ground plane. There are two components of electric current flowing on the ground plane; one component flows parallel to the edge and the other is perpendicular. For narrow slots the current density of the parallel component near the edge increases, and as a result, this current sees a higher ohmic resistance. The magnetic current over the T-top section is very low and does not contribute to the radiated field but its length affects the resonant frequency. Half the length of the T-top section originally was part of the first vertical section, which is removed and placed horizontally to lower the vertical extent of the antenna.

The slot-line sections were chosen so that a resonant frequency of 600 MHz was achieved. At this frequency, the slot antenna occupies an area of  $(6.5 \text{ cm} \times 6.5 \text{ cm})$ , which is  $0.12\lambda_0 \times 0.12\lambda_0$  in terms of the free-space wavelength. Figures 2.4(a) and (b), respectively, show the simulated input impedance and return loss of the miniaturized UHF antenna as a function of frequency. It is shown that the 1.2 VSWR (-10 dB return loss) bandwidth of this antenna is around 6 MHz, which corresponds to a 1% fractional bandwidth. This low bandwidth is a characteristic of miniaturized resonant slot dipoles.

The simulated return loss of Fig. 2.4 indicates that a weak resonance is also present at a slightly lower frequency. To understand the nature of such a weak resonance, the magnetic current distribution should be carefully examined. The simulated current



(a)



(b)

Figure 2.4: Simulated reflection coefficient of the miniaturized UHF antenna with an infinite ground plane. (a) Smith chart representation. (b) Magnitude of  $|S_{11}|$  in logarithmic scale.

distribution demonstrates that the double spiral terminations are at resonance at the exact frequency where a weak resonance is observed in the return loss. In this scenario, the radiating section serves as a feed line for the terminating double spirals, and the double spirals turn into a radiating element over this frequency band. This double spiral, which resembles the cornu-spiral of Fig. 2.1(a), is not a very efficient radiator due to its ohmic losses nor can it be matched easily. That is why the return loss at this resonance is poor.

The polarization of this antenna may appear to be rather unpredictable at a first glance due to its convoluted geometry. However, it can be conjectured that the polarization of any miniaturized antenna whose dimensions are much smaller than a wavelength cannot be anything other than linear. This is basically because of the fact that the small electrical size of the antenna does not allow for a phase shift between two orthogonal components of the radiated field required for producing an elliptical polarization. Hence by rotating the antenna a desired linear polarization along a given direction can be obtained.

## 2.4 Realization and Measurements

An antenna based on the layout shown in Figs. 2.2 and 2.3 was made on a FR4 printed-circuit-board. In the first try, the size of the ground plane was chosen to be  $8.5\text{ cm} \times 11.5\text{ cm}$ . The return loss of this antenna was measured with a network analyzer, and the result is shown by the solid line in Fig. 2.5. It is noticed that the resonant frequency of this antenna is at 568 MHz, which is significantly lower than what was predicted by the simulation. Also, the measured return loss for the designed microstrip feed line (not shown here) was around -10 dB. To get a better return loss, the length of the microstrip line had to be extended slightly. The measured return loss of this antenna, after a slight modification, is shown in Fig. 2.5. The gain of

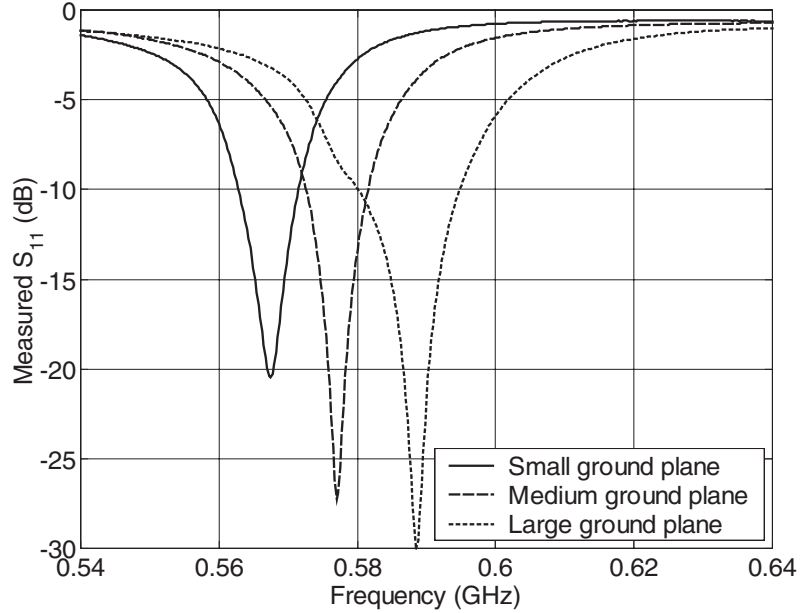


Figure 2.5: Measured reflection coefficient of three miniaturized UHF slot antennas, described in Table 2.1 and shown in Fig. 2.7, all having the same size and geometry, but with different ground plane sizes.

this antenna was also measured against a calibrated antenna. Under polarization matched condition, a gain of  $-5.0$  dBi (gain in dB against an isotropic radiator) is measured. The simulated gain value of this antenna using infinite ground plane and  $\epsilon_r = 4.0 - j0.0$  is found to be 2.2 dBi. The difference in the simulation results and the measured ones can be attributed to the finiteness of the ground plane, finite conductivity of the ground plane, and the loss-tangent of the substrate. The effect of the imaginary part of the substrate dielectric constant ( $\epsilon_r = 4.0 - j\epsilon''$ ) can be quantified using a numerical simulation. Figure 2.6 shows the simulated gain values of this antenna as a function of  $\epsilon''$  with an infinite ground plane. It is shown that, as expected, the gain is decreased when the loss tangent is increased indicating the importance of using substrates with very low loss tangent. The FR4 used for this antenna has a poor loss tangent ( $\tan \delta \approx 0.01$ ) at UHF.

To investigate the effect of ground plane size on the resonance frequency and

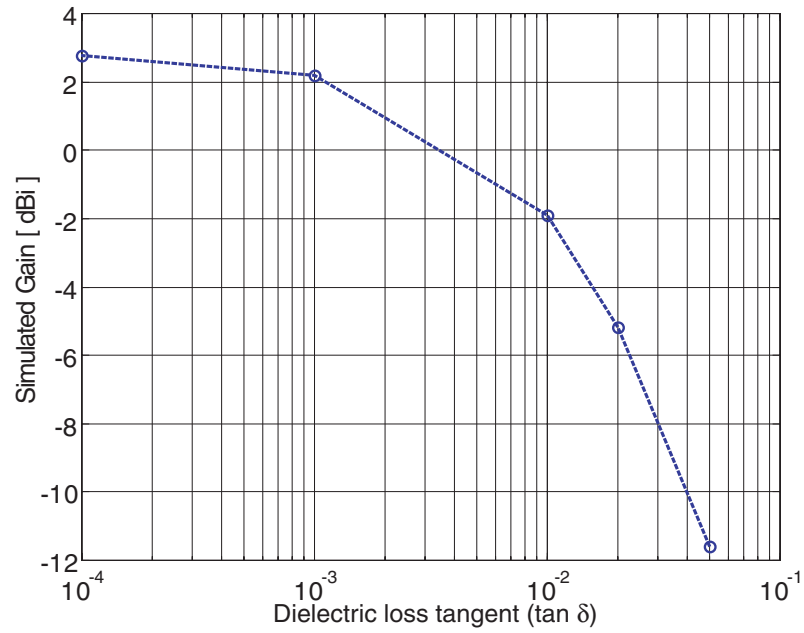


Figure 2.6: Simulated Gain of the UHF miniaturized antenna on an infinite substrate with  $\epsilon_r = 4.0(1 - j \tan \delta)$ .

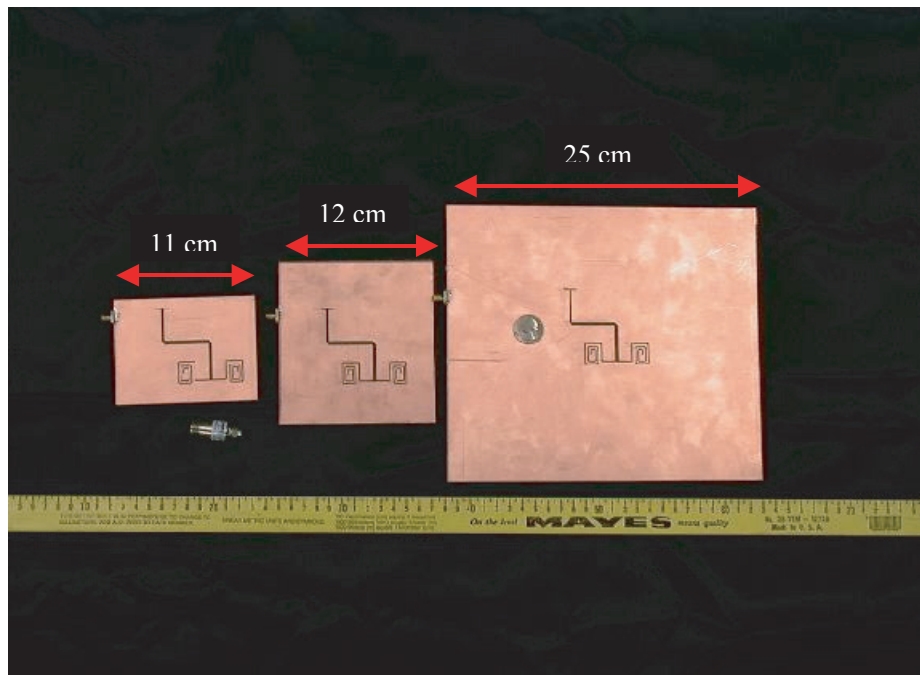


Figure 2.7: A photograph of three miniaturized UHF antennas, all having the same topology and dimensions but with different ground plane sizes.

Table 2.1: Resonant frequencies, gains, and ground plane sizes of the three miniaturized slot antennas of Fig. 2.7.

|           | Ground-plane size[cm] | Resonant frequency [MHz] | Gain [dBi] |
|-----------|-----------------------|--------------------------|------------|
| Antenna 1 | $8.5 \times 11$       | 568                      | -5.0       |
| Antenna 2 | $13 \times 12$        | 577                      | -2.0       |
| Antenna 3 | $22.2 \times 25$      | 592                      | 0.5        |

radiation efficiency, two more antennas having the same geometry and dimensions but with different ground plane sizes were made as photographed in Fig. 2.7. The measured resonant frequencies and return losses of these antennas are also shown in Fig. 2.5. The dimensions of the ground planes and the measured gain of these antennas are reported in Table 2.1. As expected, the resonant frequency and the gain of the antenna approaches the predicted values as the size of the ground plane is increased. The gain of Antenna 3 (with the largest ground plane) is almost as high as the gain of a standard dipole considering the loss-tangent of the substrate used in these experiments.

The gain reduction as a function of the ground plane size can be explained by noting that there are strong edge currents on the periphery of a finite ground, which decreases as the size of the ground plane is increased. The confined currents around the edge experience an ohmic loss which is responsible for the decrease in the antenna gain. Apart from ohmic losses, a decrease in the size of the ground plane reduces the antenna directivity. In the H-plane of a slot antenna, two nulls exists at the ground plane ( $\theta = \pm 90^\circ$ ). These nulls are enforced as the boundary condition requires the tangential electric field to vanish on the ground plane. As the size of the ground plane decreases, these nulls at  $\theta = \pm 90^\circ$  are gradually disappeared, and therefore, the antenna becomes less directive.

Figure 2.8 shows the direction of maximum radiation as well as the direction of the electric and magnetic fields at the bore-sight. As illustrated in this figure, the E

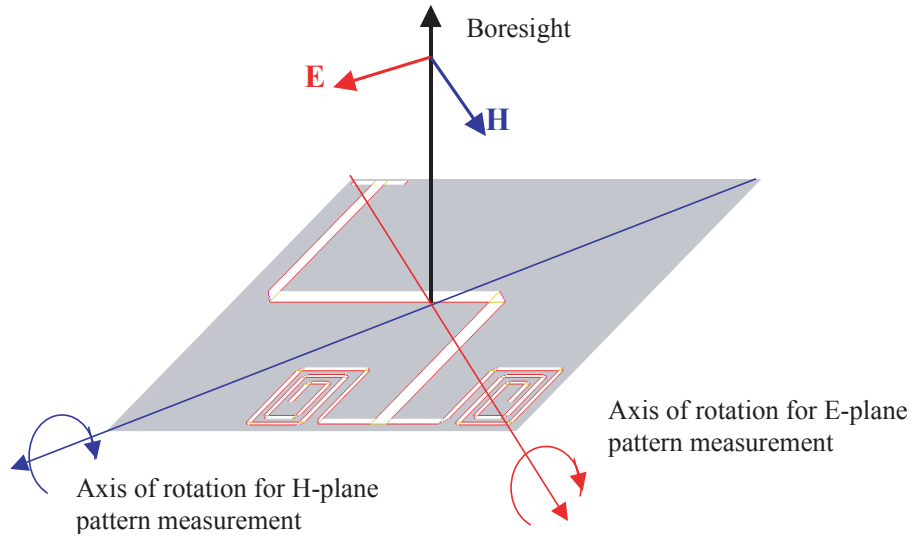


Figure 2.8: Identification of the principle E and H planes of the proposed miniaturized quarter-wave antenna under test.

and H principle planes can be identified as  $E_{\theta}(\theta)$  at  $\phi = 45^{\circ}$ , and  $E_{\phi}(\theta)$  at  $\phi = 135^{\circ}$ , respectively. Figure 2.9 shows the radiation pattern of this antenna in both E and H principle planes for co- and cross-polarized components.

The radiation patterns of this antenna were also measured in the University of Michigan anechoic chamber. A linearly polarized antenna was used as the reference. First, the polarization of the antenna was determined at the direction of maximum radiation (normal to the ground plane). Then, by rotating the antenna under test about the direction of maximum radiation, it was found that, indeed, the polarization of the miniaturized antenna is linear. Figures 2.10(a) and (b) show the co- and cross-polarized measured radiation patterns in the H-plane and E-plane, respectively. It is shown that the antenna polarization remains linear on these principal planes.

As seen in Fig. 2.10, the measured E-plane gain in the plane of the ground, namely ( $\theta = 90^{\circ}$ ), drops because of the finiteness of the ground plane. If the substrate were to be removed, the E-plane gain in the plane of the finite conductor would drop to zero. In this sense, having a thick substrate helps achieving a more uniform pattern in the E-plane, whereas in general, it increases the front-to-back radiation. The level of back-

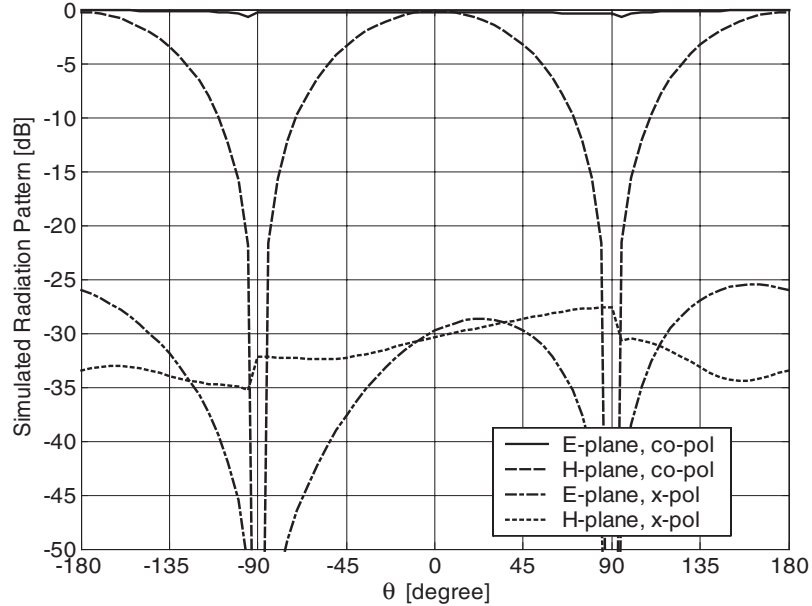


Figure 2.9: Simulated radiation pattern of the miniaturized quarter-wave antenna for both E- and H- planes.

radiation also depends on the size of the ground plane; that is, the smaller the ground plane, the higher is the back-radiation. When no dielectric substrate is present ( $\epsilon_r = 1$ ), the radiation from the upper and lower magnetic currents completely cancel each other in the plane of the perfect conductor, creating a null in the E-plane radiation pattern. However, because of the presence of the substrate and depending on its thickness and relative dielectric constant, a perfect cancellation does not occur. This explains the discrepancies observed between the measured and predicted radiation patterns (for infinite ground plane). Since the thickness of the substrate is only a small fraction of the wavelength, almost similar gain values are measured in the upper and lower half-spaces. A more comprehensive discussion on the effect of finite ground plane will be presented in the next chapter, where a novel approach for miniaturization of resonant slot antennas is proposed.

It is worth mentioning that further miniaturization can easily be accomplished by increasing the dielectric constant of the substrate. In this case, the guide wavelength

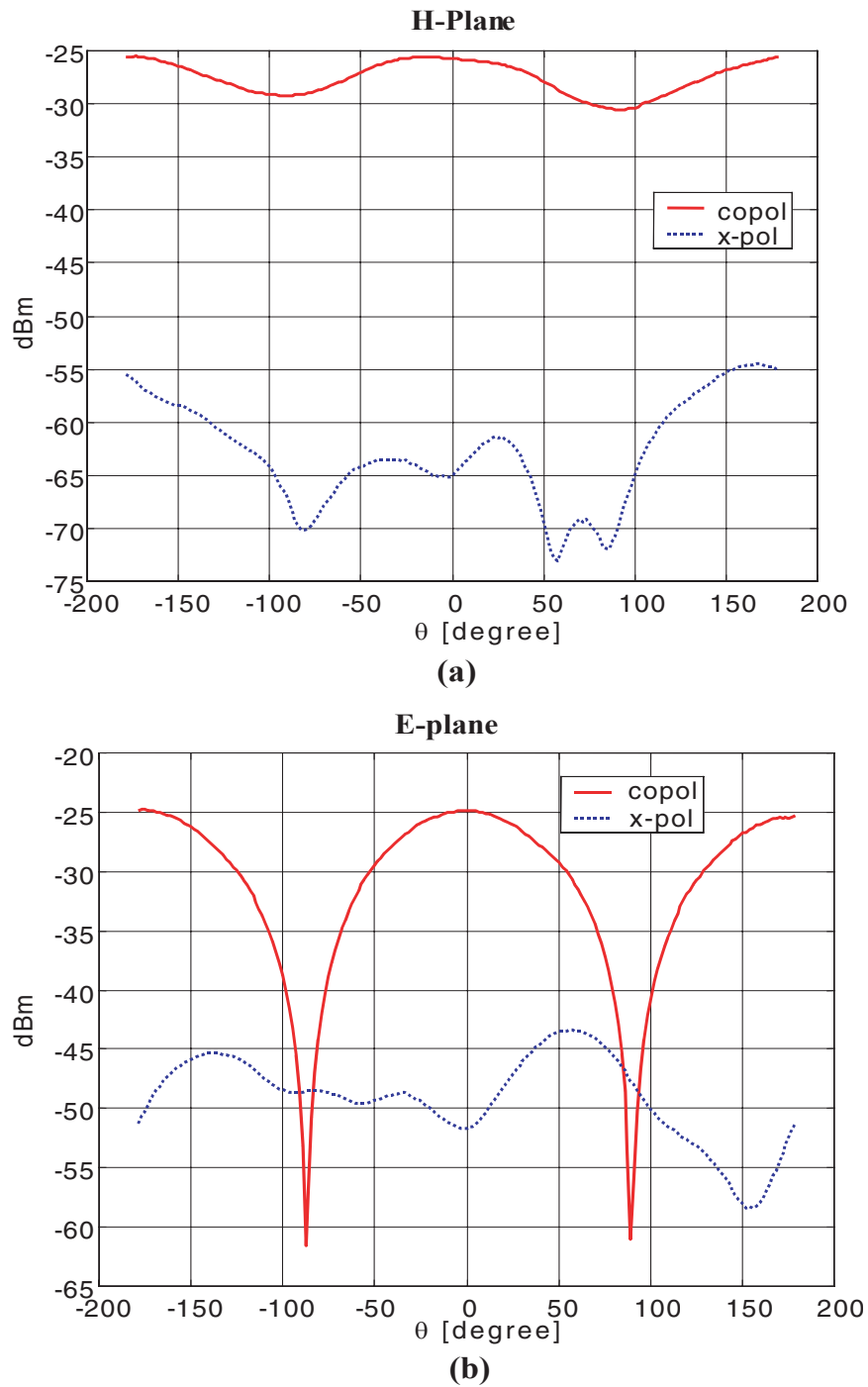


Figure 2.10: The co- and cross-polarized pattern of the miniaturized UHF antenna in (a) E-plane and (b) H-plane.

shortens which renders a smaller antenna. As mentioned earlier, further antenna miniaturization is accompanied by a reduction on the antenna bandwidth. Also confining the electric currents on the ground plane into a smaller area results in a higher ohmic loss, and consequently, a lower antenna efficiency.

## 2.5 Conclusion

A novel topology for designing electrically small resonant slot antenna is demonstrated. A major size reduction was achieved by constructing a  $\lambda_g/4$  resonant slot rather than the traditional  $\lambda_g/2$  antenna. This is accomplished by generating a virtual open circuit at one end of the slot. Further miniaturization was achieved by bending the slot into three pieces in order to use the area of the board more efficiently. The antenna geometry occupies a very small area ( $0.014\lambda_0^2$ ) of a PC board with  $\epsilon_r = 4.0$  and a thickness of 3 mm. The antenna is very efficient and shows a gain as high as that of a dipole antenna and a 1% bandwidth. It is also shown that if the antenna is made on a small ground plane, its gain will be reduced and its radiation pattern will change slightly.

## CHAPTER 3

### Miniaturization of Slot Antennas

#### 3.1 Introduction

##### 3.1.1 Background

The topic of small antennas has been a subject of interest for more than half a century, but in recent years, it has attained significant attention because of an exorbitant demand for mobile wireless communication systems. The need for antenna miniaturization stems from the fact that most mobile platforms have a limited space for all of the required antennas in ever increasing wireless systems. Compact antennas are needed so that more antennas can be closely packed together without the risk of mutual and parasitic coupling between them. For local area networks, there is an emerging interest in making antennas small enough to ultimately fit on a single chip with the rest of the receiving front-end. As part of a general trend in monolithic circuit integration, using the area of substrate more efficiently is another strong motivation. At low frequencies (HF-VHF), miniature antennas are in high demand, since the antenna size often imposes a significant limitation on the overall size of a portable wireless system.

### 3.1.2 Fundamental Limitations of Small Antennas

Earlier studies on small antennas focused on establishing a relationship between the volume occupied by the antenna and its radiation characteristics and bandwidth [1, 2, 3, 8, 9]. In these studies, a relation between the Quality Factor ( $Q$ ) of the antenna and the radius of the smallest fictitious spherical enclosure containing the antenna was derived based on the spherical wave function expansion of the fields radiated from the antenna. Each spherical mode was represented by an equivalent circuit for which a quality factor ( $Q_n$ ) was calculated. Since the spherical eigenfunctions are orthogonal, no energy could be coupled among modes. Therefore, the  $Q$  of the antenna was expressed as a function of the  $Q$  of the individual modes. Finally, it was shown that the quality factor of the lowest order mode is a lower bound for the  $Q$  of a single resonant antenna [1]. A similar approach was adopted by Collin [10] for cylindrical antennas using cylindrical wave functions to provide a tighter lower limit on the  $Q$  of thin antennas with large aspect ratios. Results of these studies have been summarized and referred to as the fundamental limitations of small antennas [2]. However, in the above papers there are no discussions about procedures to design miniaturized antennas.

In addition to high  $Q$ , another direct ramification of antenna miniaturization is reduction in the antenna efficiency owing to the relatively high conduction and/or polarization currents on the conductors or within the dielectric part of the antenna structure. Furthermore, the matching network of a miniaturized antenna is usually complex and lossy. Discussions regarding to the antenna efficiency and impedance matching will be presented in more details in this chapter.

### 3.1.3 Approaches for Antenna Miniaturization

An example of miniaturized antennas is a meandered antenna where a half wavelength dipole is made compact by meandering the wire [13]. A similar approach

can be applied to design a meander type slot antenna [14]. In order to increase the efficiency of these antennas by reducing dissipation, the use of a high-temperature superconductors (HTS) has been proposed [15, 16]. On the other hand, meandered antennas are very hard to match to a  $50\ \Omega$  line. This difficulty is due to the fact that the radiation of almost in-phase electric currents flowing in opposite directions on closely spaced wires tend to cancel each other in the far-field region. This cancellation renders a considerable portion of opposing currents ineffective as far as radiation efficiency is concerned and leads to a very low radiation resistance that might have been increased using a two-strip meandered line [17]. Consequently, these antennas are difficult to match, and yet, require a very low temperature of operation to control material losses [18].

Another approach for antenna miniaturization, reported in the literature, is to use very high dielectric constant materials in dielectric loaded antennas [19, 20]. Obviously, dielectric loading provides a size reduction factor on the order of  $\sqrt{\varepsilon_r}$  for the leaky dielectric and cavity resonator type antennas (e.g. microstrip patch antennas), where  $\varepsilon_r$  is the relative permittivity of the dielectric material. This miniaturization method, however, is less effective for terminated transmission line antennas, such as slot or printed dipole antennas since these antennas see an effective permittivity ( $\varepsilon_{eff}$ ), which is considerably less than  $\varepsilon_r$ . Although this method of miniaturization is susceptible to surface wave excitation, it might be found beneficial, especially when the electrical thickness of the substrate is small compared to the wavelength. It is worth mentioning that this type of antenna miniaturization is not immune to the aforementioned adverse effects such as high  $Q$ , low efficiency, and complexity in the matching network.

There is another important methodology in antenna miniaturization; that is, modifying the antenna geometry. In Chapter 2, a new topology based on an S-shape quarter wavelength resonant slot antenna was introduced using a short-circuit at one

end of the slot and an open-circuit at the other end. The open-circuit was realized by a coiled quarter wavelength slot-line. Using this design, a very efficient miniaturized antenna with dimensions of  $0.12\lambda_0 \times 0.12\lambda_0$  on a substrate having  $\varepsilon_r = 4.0$  was constructed and fed by a microstrip-line. The polarization of the radiated fields by this antenna is frequency dependent, due to the fact that the radiating element is divided into a three S-shape lines. It should also be noted that the size of this antenna cannot be further miniaturized since its design is primarily based on the quarter-wavelength structure.

Nevertheless, further miniaturization of slot antennas can be achieved by the virtual enforcement of the required boundary condition at the end of a slot antenna, whereby the area occupied by the resonant antenna can be reduced. To achieve the required virtual Boundary Condition (BC), the two short-circuit at the end of the standard resonant slot are replaced by some reactive BC, including inductive or capacitive loadings. The application of these loads is shown to reduce the size of the resonant slot antenna for a given resonant frequency without imposing any stringent condition on the impedance matching of the antenna.

In this chapter, a procedure for designing this class of miniaturized slot antennas for any arbitrary size (relative to wavelength) is presented. As will be shown, in order to locate the resonant frequency of this structure, the antenna is first fed by a two-port microstrip line, and then, the location of the null in the insertion loss ( $S_{21}$ ) is found and adjusted. The design procedure is based on an equivalent circuit model for the antenna and its two-port feed structure. The corresponding equivalent circuit parameters are extracted using a full-wave forward model in conjunction with a Genetic Algorithm (GA) optimizer. These parameters are employed to find a proper matching network so that a perfect match to a  $50\ \Omega$  line is obtained.

Finally, a prototype slot antenna with approximate dimensions of  $0.05\lambda_0 \times 0.05\lambda_0$  and a perfect impedance match is obtained, with a fairly high gain of  $-3\ \text{dBi}$ , for a

very small ground plane ( $\approx 0.20\lambda_0$ ).

## 3.2 Miniaturized Antenna Geometry

For a resonant slot antenna, one needs to apply two boundary conditions at both ends of a slot-line to form a resonant standing wave pattern. These two conditions are chosen so as to enforce zero electric current (open-circuit) for a wire antenna or zero voltage (short-circuit) for the slot antenna, and yield a half-wave resonant antenna. On the other hand, alternative boundary conditions may result in a resonant length smaller than a half wavelength antenna [21]. One choice which is conducive to antenna miniaturization is the combination of a short-circuit and an open-circuit, which allows for a shorter resonant length of  $\lambda/4$ , as presented in Chapter 2. The choice of the two boundary conditions, however, is not restricted to the above standard conditions, and alternative boundary conditions such as reactive ones can be used instead. The effect of reactive boundary conditions in reducing the resonant length and antenna miniaturization will be investigated in what follows.

### 3.2.1 Slot Radiator Topology

Starting from a  $\lambda_s/2$  slot and in the view of the transmission line approximation for the slot dipole, the equivalent magnetic current distribution along a linear slot antenna can be expressed as

$$M(z) = M_0 \cos\left(\frac{\pi}{\lambda_s}z\right) \quad (3.1)$$

where  $\lambda_s$  is the guided wavelength in the slot-line. In (3.1)  $M_0$  represents the amplitude of the magnetic current density (electric field across the slot-line). This approximate form of the current distribution satisfies the short-circuit boundary conditions at

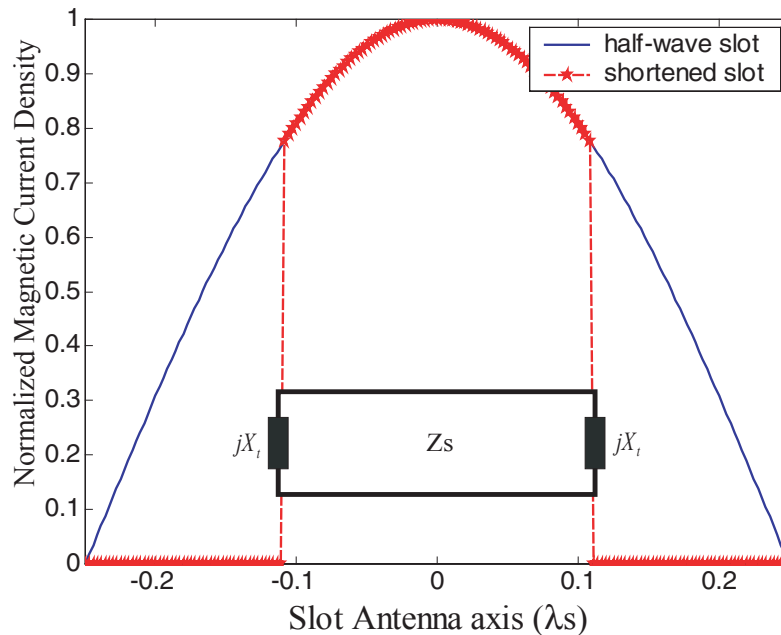


Figure 3.1: Magnetic current distribution on a half wavelength and inductively terminated miniaturized slot antenna.

the end of the slot antenna. If by using an appropriate boundary condition, the magnetic current density at any arbitrary point  $|z'| < \frac{\lambda_s}{4}$  along the length of a modified slot antenna can be maintained the same as the  $\lambda_s/2$  slot antenna, then it is possible to make a smaller slot antenna. Any size reduction of interest can be achieved so long as the appropriate BCs are in place at the proper location on the slot. Figure 3.1 illustrates the idea where it is shown that by imposing a finite voltage at both ends of a slot, the desired magnetic current distribution on a short slot antenna can be established.

To create a voltage discontinuity, one can use a series inductive element at the end of the slot antenna. It should be pointed out that terminating the slot antenna with a lumped inductance or capacitance is not practical since the slot is embedded in a ground plane, which can in fact short-circuit any termination. To circumvent this problem, a lumped inductor could be physically realized by a compact short-circuited slotted spiral. To ensure an inductive loading, the length of the spiral slot must be

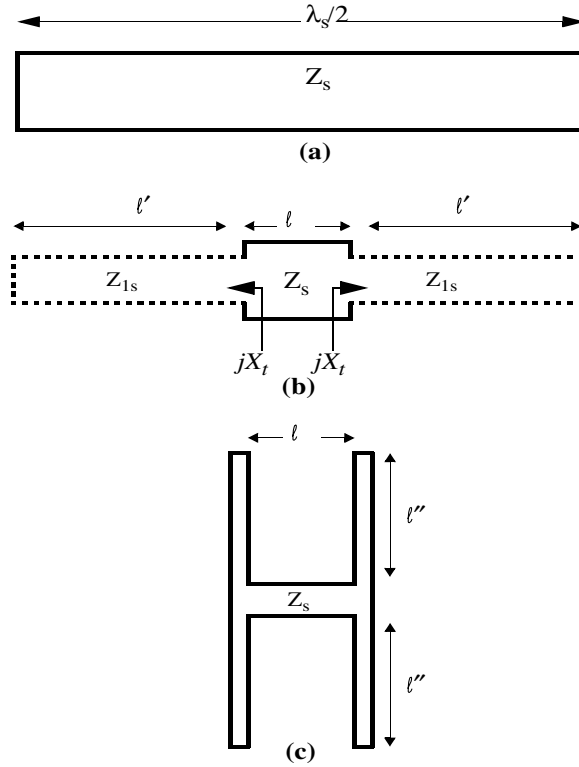


Figure 3.2: Transmission line model of a slot antenna (a) Half wave slot antenna; (b) Inductively terminated slot antenna; (c) Two series inductive terminations.

less than a quarter wavelength. Instead of a single inductive element at each end, it is preferred to use two inductive slot-lines opposite of each other (see Fig. 3.2(c) and Fig. 3.3). Since these two inductors in the slot configuration are in series, a shorter slot-line provides the required inductive load at the end of the slot antenna. Another reason for choosing this configuration is that the magnetic currents flowing in opposite directions cancel each other's fields on the planes of symmetry, and thereby, minimize the near-field coupling effect of the inductive loads on the desired current distribution along the radiating slot.

It should be noted that the mutual coupling within the spiral slot-line reduces the effective inductance, and therefore, a longer spiral length compared with a straight section (Fig. 3.2(c)) is needed to achieve the desired inductance. To alleviate this adverse effect, a narrower slot width must be chosen for the spiral slot-line.

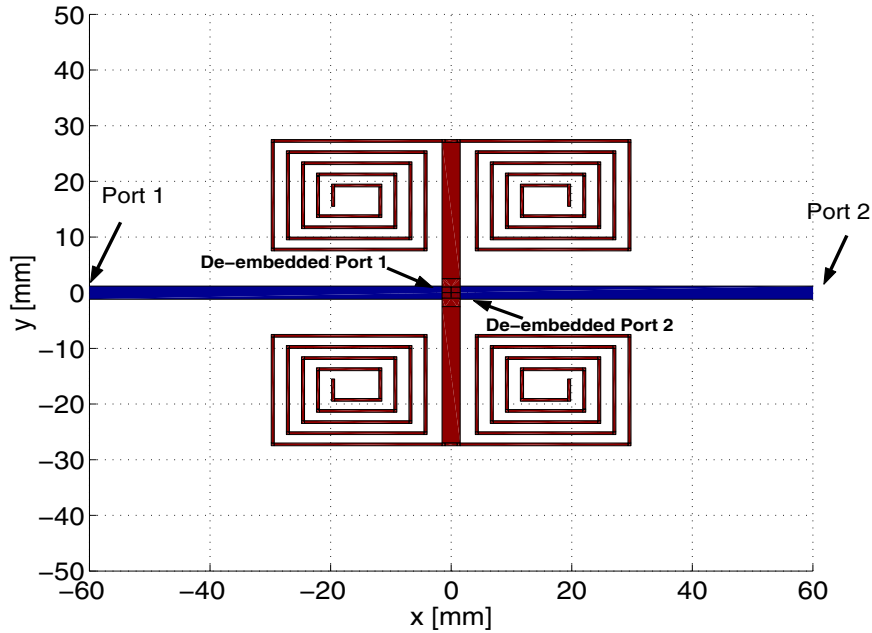


Figure 3.3: Proposed antenna geometry fed by a two-port microstrip feed. This two-port geometry is used to find out the exact resonant frequency of the inductively loaded slot.

### 3.2.2 Antenna Feed

A microstrip transmission line is used to feed this antenna. The choice of the microstrip feed, as opposed to a coaxial line, is based on the ease of fabrication and stability. This feed structure is also more amenable to tuning by providing the designer with an additional parameter. Instead of short-circuiting the microstrip line over the slot, an open-ended microstrip line with an appropriate length extending beyond the microstrip-slot crossing point (additional parameter) can be used.

A Coplanar Waveguide (CPW) can also be used to feed the antenna providing the ease of fabrication, whereas it is more difficult to tune. Usually, a metallic bridge is needed to suppress the odd mode in the CPW. The use of CPW lines also reduces the effective aperture of the slot antenna, especially when a very small antenna is to be matched to a  $50\ \Omega$  line. Typically for a low dielectric constant substrate, the center conductor in the CPW lines at  $50\ \Omega$  is rather wide and the gap between the

center conductor and the ground planes is relatively narrow. Hence, feeding the slot antenna from the center blocks a considerable portion of the miniaturized slot antenna [22]. There are other methods to feed the slot antenna with CPW lines, including an inductively or capacitively fed slot [23].

### 3.3 Design Procedure

In this section, a procedure for designing a novel miniaturized antenna with the topology discussed in the previous section is presented. To illustrate this procedure, a miniaturized slot antenna at 300 MHz is designed. This frequency is the lowest frequency at which we could accurately perform antenna measurements in the anechoic chamber, and yet, the miniature antenna is large enough so that a standard printed circuit technology can be used in the fabrication of the antenna. An RT/duroid substrate with a dielectric constant of  $\epsilon_r = 2.2$ , a loss tangent of  $\tan \delta \approx 10^{-3}$ , and a thickness of 0.787 mm [24] is considered for the antenna prototype.

Table 3.1: Slot-line characteristics for two different values of slot width  $w$ , and the dielectric constant of  $\epsilon_r = 2.2$  and thickness of  $h = 0.787(\text{mm})$  and  $f = 300 \text{ MHz}$ .

| $w(\text{mm})$ | $\lambda_s(\text{mm})$ | $Z_{0s}(\Omega)$ |
|----------------|------------------------|------------------|
| 0.5            | 918                    | 81               |
| 3.0            | 960                    | 107              |

As the first step, the basic transmission line model is employed to design the antenna, and then, a full-wave Moment Method analysis is used for fine tuning. Table 3.1 shows the finite ground plane slot-line characteristic impedance  $Z_{0s}$ , and guided wavelength  $\lambda_s$ , for the above-mentioned substrate and for two slot widths of  $w = 0.5 \text{ mm}$  and  $w = 3.0 \text{ mm}$ , all at 300 MHz. As mentioned before, the antenna size can be chosen as a design parameter, and in this example, we attempt to design a

very small antenna with a length of  $\ell = 55 \text{ mm} \approx 0.05\lambda_0$ . A slot width of  $w = 3 \text{ mm}$  is chosen for the radiating section of the slot antenna. A slot antenna whose radiating slot segment is of a length  $\ell$ , should be terminated by a reactance given by

$$X_t = Z_{0s} \tan \frac{2\pi}{\lambda_s} \ell', \quad (3.2)$$

in order to maintain the magnetic current distribution of a  $\lambda_s/2$  resonant slot antenna (see Fig. 3.2). In (3.2),

$$\ell' = \frac{1}{2} \left( \frac{\lambda_s}{2} - \ell \right), \quad (3.3)$$

and  $Z_{0s}$  and  $\lambda_s$  are the characteristic impedance and the guided wavelength of the slot-line, respectively. As mentioned before, the required terminating reactance of  $X_t$  can be constructed by two smaller series slot-lines. Denoting the length of a terminating slot-line by  $\ell''$ , as shown in Fig. 3.2(c), the relationship between the required reactance and  $\ell''$  is given by

$$\frac{X_t}{2} = Z'_{0s} \tan \frac{2\pi}{\lambda'_{0s}} \ell'', \quad (3.4)$$

where  $Z'_s$  and  $\lambda'_s$  are the characteristic impedance and the guided wavelength of the terminating slot-line. A narrower slot is used to construct the terminating slot-lines so that a more compact configuration can be achieved. As shown in Table 3.1, the narrower slot-line has a smaller characteristic impedance and guided wavelength which results in a slightly shorter length of the termination ( $\ell''$ ). Although  $\ell''$  is smaller than  $\ell'$ , the actual miniaturization is obtained by winding the terminating line into a compact spiral as seen in Fig. 3.3.

According to (3.2), (3.4), and the values for the guided wavelengths,  $\ell''$  is found to be  $\ell'' = 193.7 \text{ mm}$ . Referring to Fig. 3.3, the vertical dimension (along the  $y$  axis) of the rectangular spiral should not exceed half of the length of the radiating slot

segment ( $\ell$ ). This constraint on the inductive rectangular spiral is imposed so that the entire antenna structure can fit into a square area of  $55 \text{ mm} \times 55 \text{ mm}$ , which is about  $0.05\lambda_0 \times 0.05\lambda_0$ . Since the dielectric constant and the thickness of the substrate chosen for this design are very low ( $\epsilon_r = 2.2$ ), the guided wavelength ( $\lambda_s = 96 \text{ cm}$ ) is not very much different from that of the free space ( $\lambda_0 = 100 \text{ cm}$ ). Thus, the miniaturization is mainly achieved by the proper choice of the antenna topology. It is worth mentioning that further size reduction can be obtained once a substrate with higher permittivity is used.

### 3.4 Full-Wave Simulation and Tuning

In the previous section, the transmission line model was employed for designing the proposed miniature antenna. Although this model is not very accurate, it provides the intuition necessary for designing the novel topology. The transmission line model ignores the coupling between the adjacent slot-lines and the microstrip to slot transition. For calculation of the input impedance, and exact determination of the length of different slot-line segments, a full-wave simulation tool is required. IE3D, a commercially available Moment Method code, is used for required numerical simulations [25].

Figure 3.3 shows the proposed antenna geometry fed by a two-port  $50 \Omega$  microstrip line. The two-port structure is constructed to study the resonant frequency of the antenna as well as the transition between the microstrip-line and slot antenna. The microstrip line is extended well beyond the slot transition point so that the port terminals do not couple to the slot antenna. The radiating slot length is chosen to be  $\ell = 55 \text{ mm}$ , and the length of the rectangular spirals are tuned such that the antenna resonates at  $300 \text{ MHz}$ . The resonance at the desired frequency is indicated by a deep null in the frequency response of  $S_{21}$ . The simulated S-parameters of this two-port

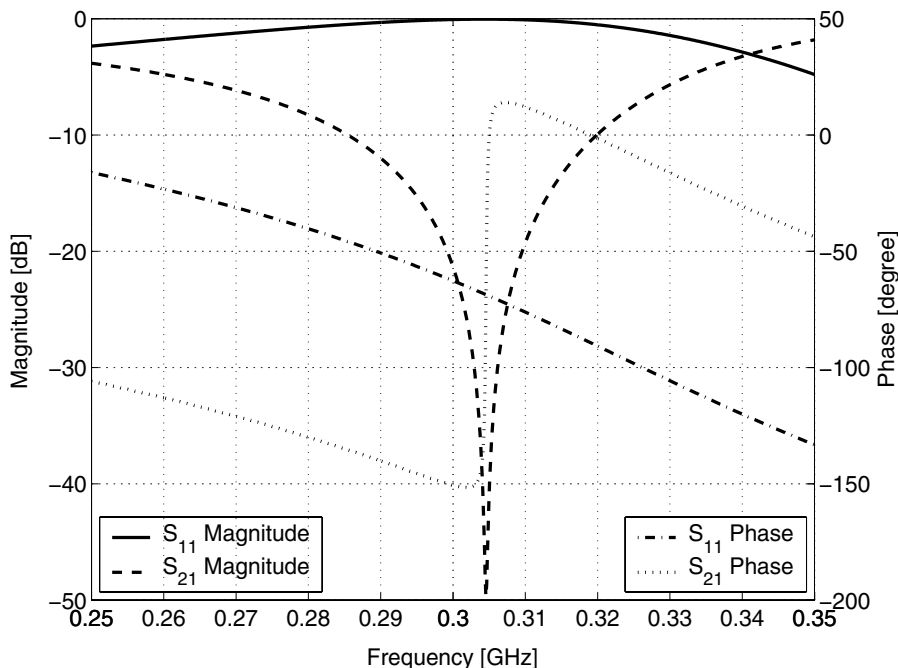


Figure 3.4: S-parameters of the two-port antenna shown in Fig. 3.3.

structure are shown in Fig. 3.4. This figure indicates that the antenna resonates at around 304 MHz, which is close to the desired frequency of 300 MHz. In fact, the resonant frequency of the radiating structure must be chosen at a slightly higher or lower frequency. The reason is that small slot antennas have a low radiation conductance at the first resonance, and therefore, they should be tuned slightly off-resonance if they are to be matched to a  $50\ \Omega$  transmission line. Figure 3.5 shows an equivalent circuit model for the two-port device when the transition between the microstrip and slot-line is represented by an ideal transformer with a frequency dependent turn ratio ( $n$ ) [26], and the slot is modeled by a second order shunt resonant circuit near its resonance [27]. The radiation conductance  $G_s$ , which is also referred to as the slot conductance, attains a low value that corresponds to a very high input impedance at the resonant frequency. However, this impedance would decrease considerably, when the frequency moves off the resonance. The 4 MHz offset in the resonant frequency of the antenna is maintained for this purpose.

Having tuned the resonant frequency of the antenna, coupled to the two-port

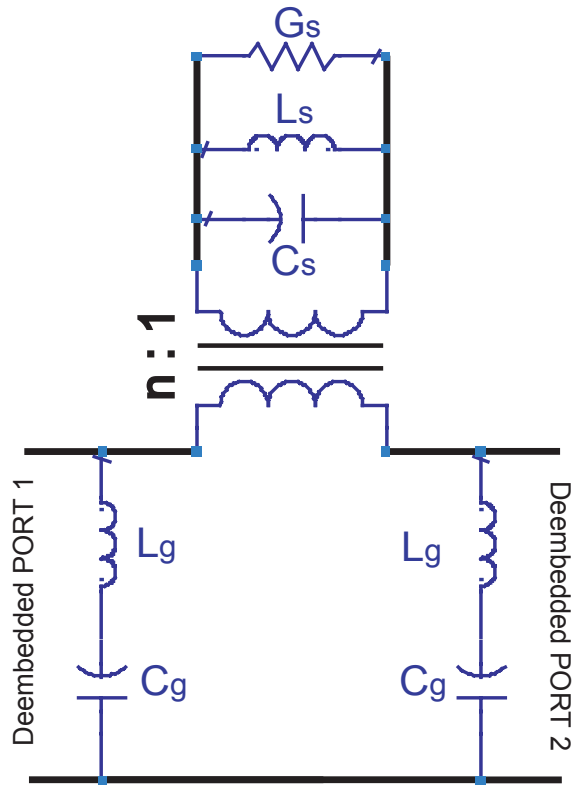


Figure 3.5: Topology of the equivalent circuit for the two-port antenna.

microstrip feed (Fig 3.3), we need to design a loss-less impedance matching network. This can be accomplished by providing a proper impedance to terminate the second port of the microstrip feed line. To fulfill these tasks systematically, we need to extract the equivalent circuit parameters shown in Fig. 3.5. It should be pointed out that for the proposed miniaturized slot antenna, a simplistic model for standard size slots, which treats the slot antenna as an impedance in series with the microstrip line is not sufficient. Essentially, the parasitic effects caused by the coupling between the microstrip feed and rectangular spirals as well as the mutual coupling between the radiator section and the rectangular spirals should also be included in the equivalent circuit.

### 3.4.1 Equivalent-Circuit Model

In this section, an equivalent circuit model for the proposed antenna is developed. This model is capable of predicting the slot radiation conductance and the antenna input impedance near resonance. This approach provides very helpful insight as to how this antenna and its feed network operate. As mentioned before, this model is also needed to find a proper matching network for the antenna.

Near resonant frequencies, the slot antenna can be modeled by a simple second order RLC circuit. Since the voltage across the slot excites the slot antenna at the feed point, it is appropriate to use the shunt resonant model for the radiating slot as shown in Fig. 3.5. The coupling between the microstrip and the slot is modeled by a series ideal transformer with a turn ratio  $n$ .

To model the feeding mechanism right at the cross junction of the microstrip and slot, it is necessary to deembed the effect of the microstrip lines between the terminals and the crossing points. There are different deembedding schemes reported in the literature [28, 29]. The advantage of proper deembedding as opposed to the mere shifting of the reference planes by the corresponding phase factor is to exclude the effect of radiation and other parasitic effects of the line.

To model the parasitic coupling of the microstrip line and the slot (coupling of radiated field from the microstrip line and slot), two additional parasitic parameters, namely,  $L_g$  and  $C_g$  are included in the model. The use of shunt parasitic parameters has previously been suggested to model the effects of fields as perturbed by a wide slot [30]. Figure 3.6 shows the deembedded Y-parameters of the two-port microstrip-fed slot antenna where the location of deembedded ports are shown in Fig. 3.3. Note that these two ports are now defined at the microstrip-slot junction. According to the lumped element model of Fig. 3.5, the Y-parameters are given by:

$$Y_{11} = \frac{-j}{L_g\omega - \frac{1}{C_g\omega}} + \frac{1}{n^2} \left[ G_s + j \left( C_s\omega - \frac{1}{L_s\omega} \right) \right] \quad (3.5)$$

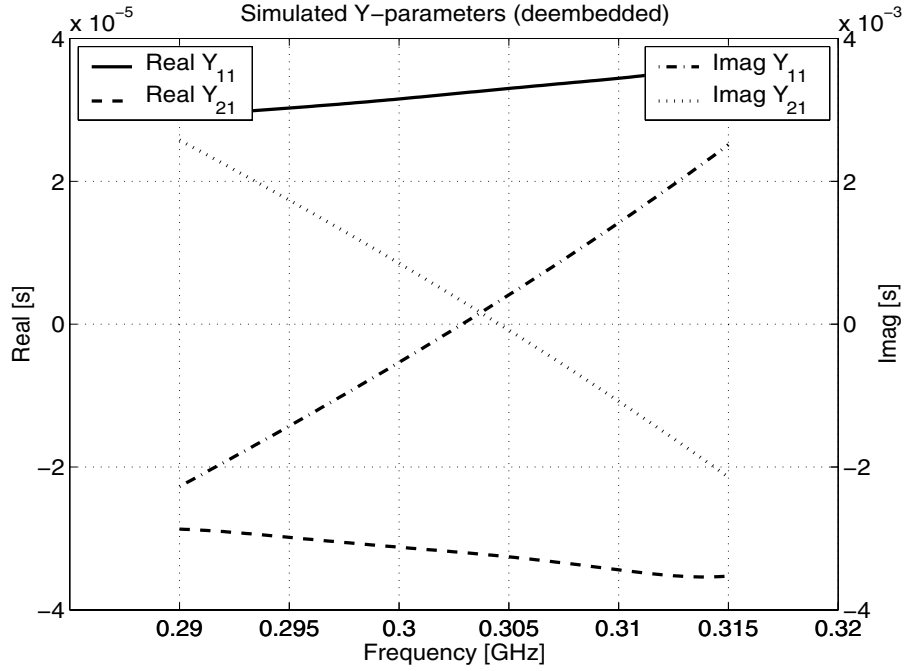


Figure 3.6: Y-parameters of the two-port antenna after deembedding the microstrip feed lines.

$$Y_{21} = -\frac{1}{n^2} \left[ G_s + j \left( C_s \omega - \frac{1}{L_s \omega} \right) \right] \quad (3.6)$$

Using reciprocity and noting the symmetry of the equivalent circuit, it can easily be shown that  $Y_{11} = Y_{22}$  and  $Y_{21} = Y_{12}$ .

In order to extract the equivalent circuit parameters, a Genetic Algorithm optimization code has been developed and implemented [31]. The sum of the squares of relative errors for real and imaginary parts of Y-parameters over 40 frequency points around the resonance is used as the objective (fitness) function of the optimization problem. We ran the program with different random number seeds to ensure the best result over the entire domain of the parameters space. Also, the parameters were constrained only to physical values in the region of interest. The parameters of the GA optimizer are shown in Table 3.2. Table 3.3 shows the extracted equivalent circuit parameters after fifty thousands iterations.

The S-parameters of the equivalent circuit, as well as the S-parameters extracted

Table 3.2: The parameters of the Genetic Algorithm optimizer.

|                     |        |
|---------------------|--------|
| Population Size     | 300    |
| Number of Iteration | 50,000 |
| Chromosome Length   | 128    |
| $P_{Crossover}$     | 0.55   |
| $P_{Mutation}$      | 0.005  |

Table 3.3: The equivalent circuit parameters of the microstrip fed slot antenna.

|                           |          |
|---------------------------|----------|
| <i>Turn Ratio</i> ( $n$ ) | 0.948007 |
| $R_s(\Omega)$             | 33979    |
| $L_s(\mu H)$              | 0.0207   |
| $C_s(pF)$                 | 13.1744  |
| $L_g(\mu H)$              | 0.49997  |
| $C_g(pF)$                 | 0.125    |

from the full-wave analysis, are shown in Fig. 3.7. Excellent agreement is observed between the full-wave results and those of the equivalent circuit.

### 3.4.2 Antenna Matching

Having found the equivalent circuit parameters, the antenna's matching network can readily be designed. For matching networks, especially when efficiency is the main concern, loss-less terminations are usually desired. Therefore, we seek a purely reactive admittance to terminate the feed line, which in fact is the load for the second port of the two-port equivalent circuit model. The explicit expression for a termination admittance ( $Y_t$ ) to be placed at the second terminal of the two-port model in order to match the impedance of the antenna is given by:

$$Y_t = -Y_{11} + \frac{Y_{12}^2}{Y_{11} - Y_0}. \quad (3.7)$$

Fig. 3.8 shows the spectral behavior of  $Y_t$  for a standard  $50\ \Omega$  line ( $Y_0 = 0.02\mathcal{U}$ ).

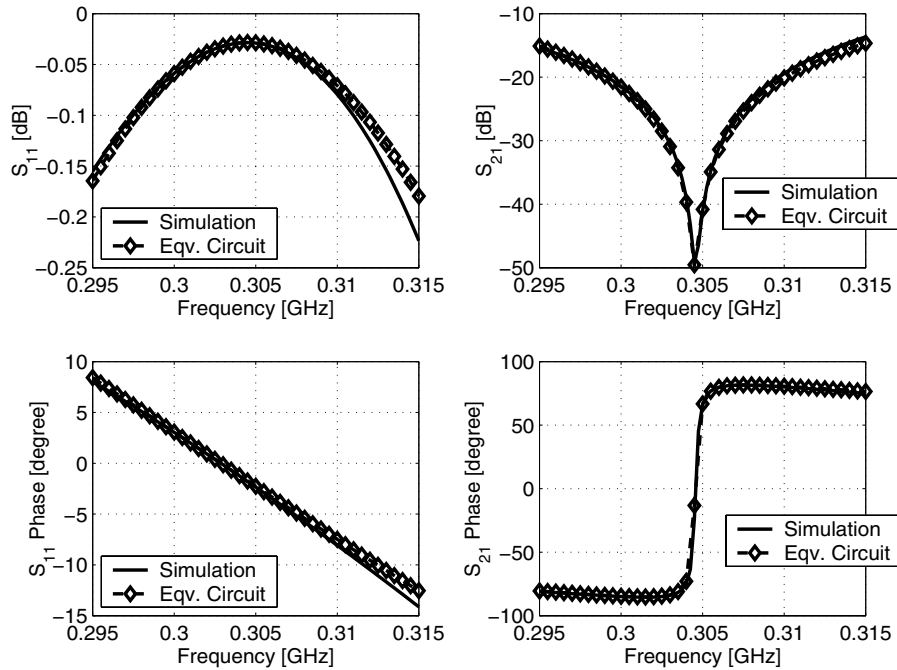


Figure 3.7: Comparison between the full-wave simulated S-parameters of the antenna and that of the equivalent circuit.

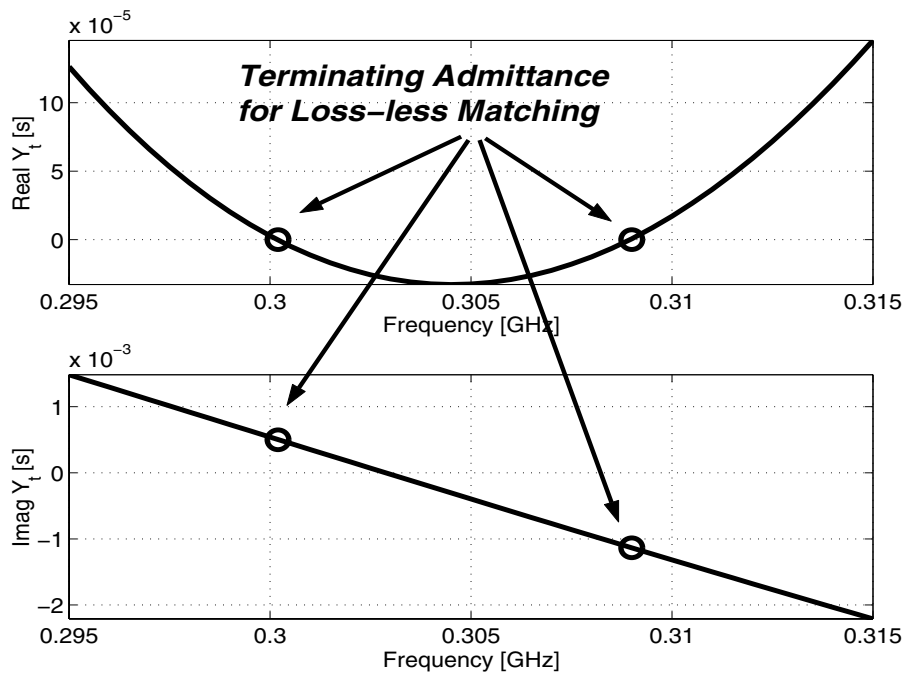


Figure 3.8: The required terminating admittance for the second port of the two-port model in order to match the antenna to a  $50\ \Omega$  line.

Interesting to note are the two distinct frequency points at which the real part of  $Y_t$  vanishes. This implies that we can match this antenna at these two frequency points, namely, 300 MHz and 309 MHz. As mentioned earlier, a small slot antenna has a very low radiation conductance. The value of this low conductance, as shown in Table 3.3, suggests a very high input impedance of the order of  $30\text{ K}\Omega$  at resonance, considering the transformer turn ratio. Thus, in order to match the antenna to a lower impedance transmission line, the matching should be done at a frequency slightly off the resonance. At an off-resonant frequency, the input impedance does not remain a pure real quantity, however, the imaginary part can easily be compensated for by an additional reactive component created by an open-ended microstrip. At each resonance, there are two possibilities. One possibility is to match the antenna slightly below the slot resonance, that is 304 MHz (Fig. 3.4), and terminate the second port capacitively. The second possibility is to tune the antenna slightly above the slot resonance and terminate the second port inductively.

Table 3.4: The physical length of the  $50\ \Omega$  microstrip line needed for realizing the termination susceptance, where the dielectric material properties are as specified in Table 3.1.

|                            |                       |                         |
|----------------------------|-----------------------|-------------------------|
| $f$ (MHz)                  | 300                   | 309                     |
| $Y_t$ (S)                  | $j5.4 \times 10^{-4}$ | $-j1.14 \times 10^{-3}$ |
| $\lambda_g$ (mm)           | 725.57                | 704.52                  |
| $Z_0$ ( $\Omega$ )         | 50                    | 50                      |
| <i>Line Extension</i> (mm) | 3.1514                | 345.80                  |

Based on what is shown in Table 3.4, a very short open-ended microstrip-line extension is required at the second port, in contrast with a quarter wavelength extension for an ordinary half wavelength slot antenna. This short extension introduces a small capacitance, which compensates the additional inductance introduced as a result of operating below resonance. After tuning the antenna, the original slot resonant frequency at 304 MHz shifts down to the desired frequency of 300 MHz as shown in

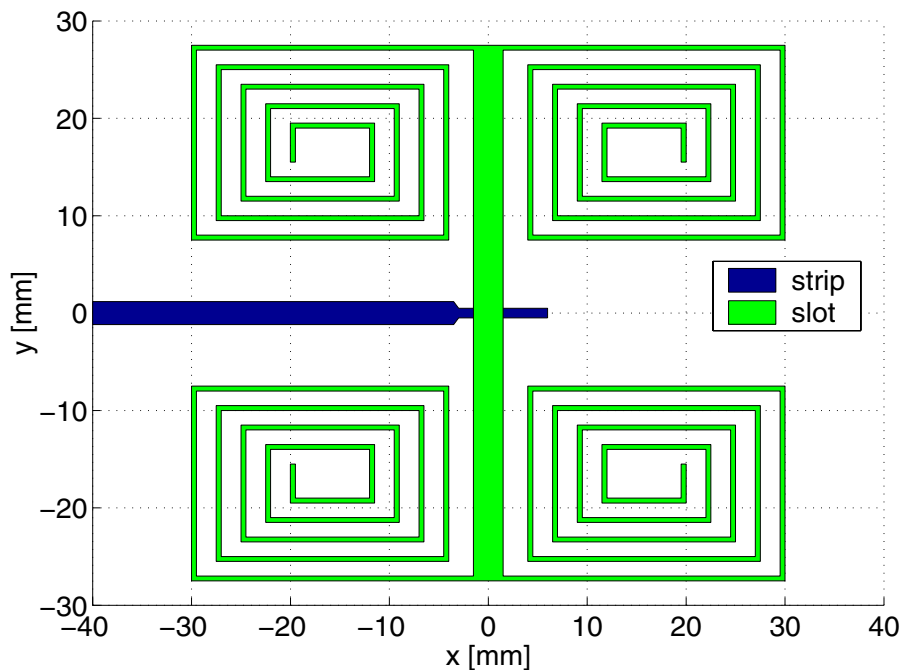


Figure 3.9: The geometry of the antenna and its feed designed to operate at 300 MHz.

Fig. 3.8 and Table 3.4.

### 3.5 Antenna Simulation and Measurements

In this section, simulation results for the proposed antenna are illustrated. Figure 3.9 shows the antenna geometry matched to a  $50\ \Omega$  line. As seen in this figure and suggested by Table 3.4, the feed line has been extended a short distance beyond the slot-line. The width of the microstrip, where it crosses the slot, is reduced so that it may block a smaller portion of the radiating slot. It is worth mentioning that the effect of the feed line width on its coupling to the slot was investigated, and it was found that so long as the line width is much smaller than the radiating slot length, the equivalent circuit parameters do not change considerably.

As mentioned, the antenna has been simulated using a commercial software (IE3D) [25]. Using this software, the return loss ( $S_{11}$ ) of the antenna is calculated and shown in Fig. 3.10. In order to experimentally validate the design procedure, equivalent

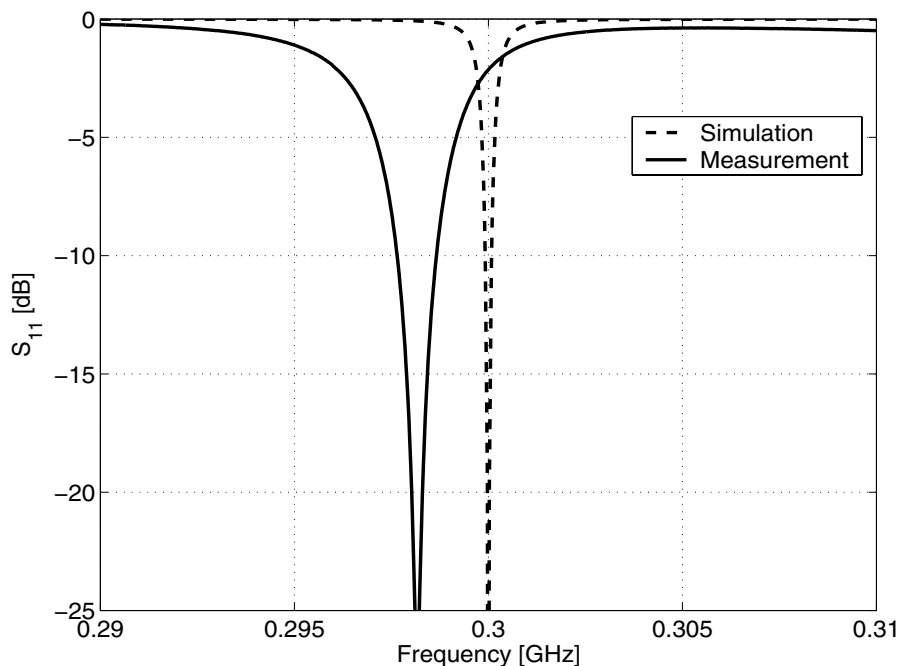


Figure 3.10: Measured and simulated return loss of the miniaturized antenna.

circuit model and simulation results, the antenna was fabricated on a 0.787 mm-thick substrate with  $\epsilon_r = 2.2$  and  $\tan \delta = 0.0009$ .

Figure 3.11 shows a photograph of the fabricated antenna. The return loss ( $S_{11}$ ) of the antenna was measured using a calibrated vector network analyzer and the result is shown in Fig. 3.10. The measured results show a slight shift in the resonant frequency of the antenna ( $\approx 1\%$ ) from what is predicted by the numerical code. The errors associated with the numerical code could have contributed to this frequency shift. This deviation can also be attributed to the finite size of the ground plane,  $0.21\lambda_0 \times 0.18\lambda_0$  for this prototype, knowing that an infinite ground plane is assumed in the numerical simulation. The shift in the resonant frequency resulted from the finite size of the ground plane for slot antennas was briefly discussed in Chapter 2.

The far field radiation patterns of the antenna were measured in the anechoic chamber of The University of Michigan. The gain of the antenna was measured at the bore-sight direction under polarization-matched condition using a standard antenna whose gain is known as a function of frequency. The gain of  $-3$  dBi (relative to an

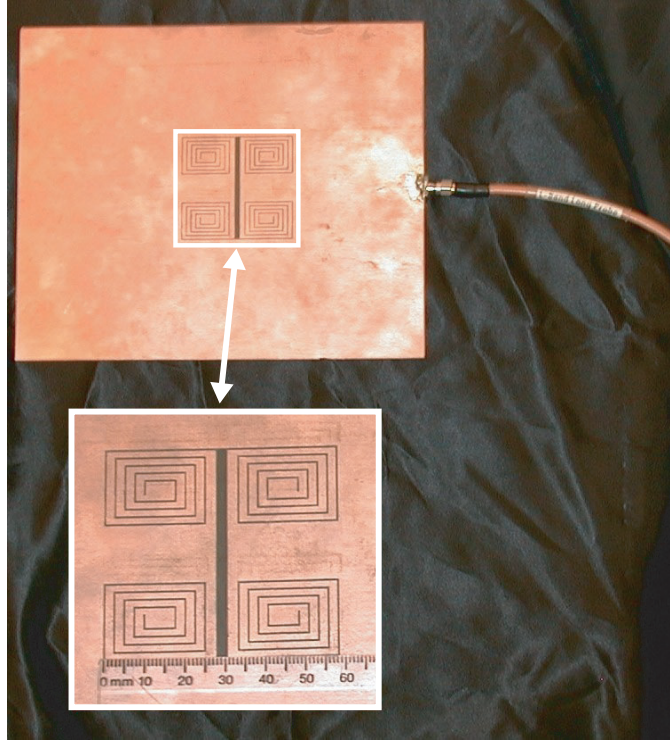


Figure 3.11: A photograph of the fabricated miniaturized slot antenna at 300 MHz.

isotropic radiator) was measured. Having perfectly matched the impedance of the antenna, the simulated efficiency of this antenna is found to be  $\eta = 87\%$  ( $-0.6$  dB), which can be exclusively attributed to the dielectric loss. Obviously, the contribution of the conductor loss, which is the main source of dissipation in slot antennas, is not accounted for in the simulated antenna efficiency. The simulated radiation efficiency is the ratio of the total radiated power to the input power of the antenna. The directivity of this antenna (with infinite ground plane) was computed to be  $D = 2.0$  dB. This value of directivity is very close to that of a dipole antenna. Based on the definition of the antenna gain [21], under the impedance matched condition, one might expect to measure the maximum gain of

$$G = \eta \cdot D = -0.6 \text{ dB} + 2.0 \text{ dB} = 1.4 \text{ dB} \quad (3.8)$$

for this antenna. There is still a considerable difference between the measured and

simulated gains (about 4.4 dB), which stems from two major factors in addition to the ohmic loss of the ground plane. First, in the simulation, an infinite ground plane is assumed, whereas the actual ground plane size for the measured antenna is approximately  $0.2\lambda_0 \times 0.2\lambda_0$ . As the ground plane size decreases, the level of electric current around the edges increases considerably. This increase in the level of the electric current results in an additional ohmic loss compared to the infinite ground plane. Another reason is that as the ground plane size decreases, the directivity of the slot antenna is reduced. Basically, as the ground plane becomes smaller, the null in the pattern diminishes, and the pattern approaches that of an isotropic radiator. The reduction in the directivity of the slot antenna with a finite ground plane can also be attributed to the radiation from the edges and surface wave diffraction [32, 33]. To further study the effect of the size of the ground plane, the same antenna with a slightly larger ground plane ( $0.58\lambda_0 \times 0.43\lambda_0$ ) was fabricated and measured. Table 3.5 shows the comparison between the radiation characteristics of these two antennas and simulated results. As explained, when the size of the antenna ground plane increases, the gain of the antenna increases from  $-3.0$  dBi to  $0.6$  dBi, which is almost equal to the gain of a half wavelength dipole and very close to the simulated value for the antenna gain.

Table 3.5: Antenna characteristics as a function of two different size ground planes compared with the simulated results for the same antenna on an infinite ground plane.

| Ground-Plane size<br>[cm]      | Resonant frequency<br>[MHz] | Return Loss<br>[dB] | Antenna Gain<br>[dBi] |
|--------------------------------|-----------------------------|---------------------|-----------------------|
| $21 \times 18$                 | 298.1                       | -27                 | -3.0                  |
| $58 \times 43$                 | 298.8                       | -30                 | 0.6                   |
| <i>simulation</i> ( $\infty$ ) | 300                         | < -30               | 0.75                  |

Finally, the radiation patterns of the proposed antenna in the principal E- and H-

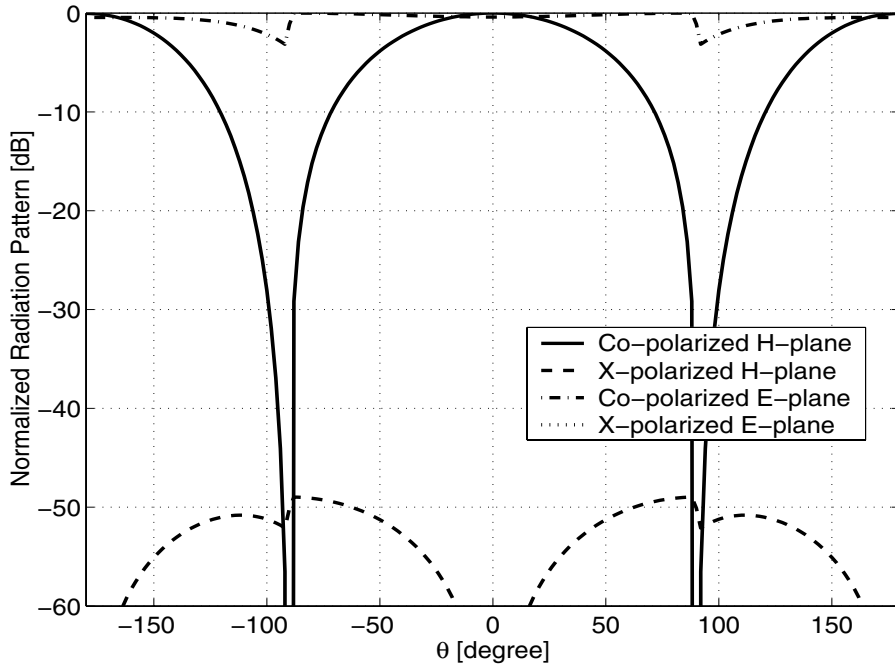
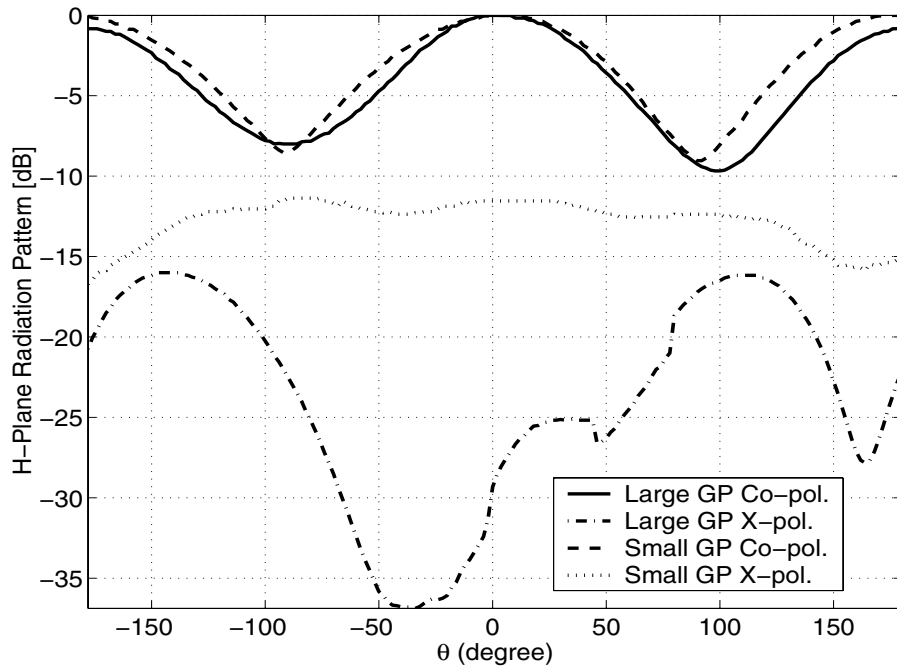


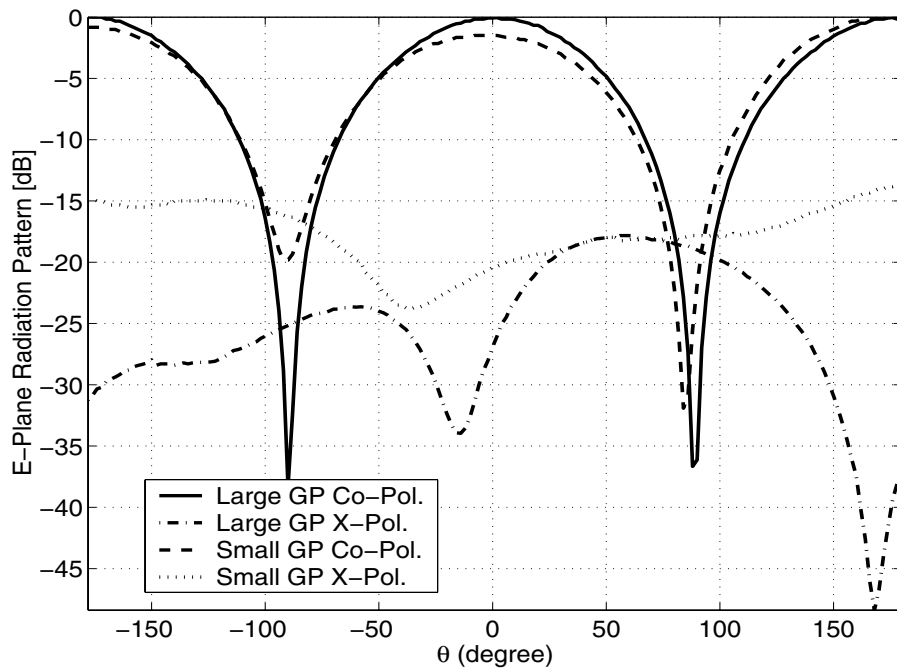
Figure 3.12: Simulated radiation pattern of the miniaturized antenna.

planes were measured and compared with the theoretical ones. For H-plane pattern, we measured  $E_\phi(\theta)$  in the  $\phi = 90^\circ$  plane, and for E-plane pattern,  $E_\theta(\theta)$  was measured in the  $\phi = 0^\circ$ . The simulated radiation patterns of this antenna are shown in Fig. 3.12.

It is seen that the simulated radiation pattern of the proposed antenna with an infinite ground plane is almost the same as that of an infinitesimal slot dipole. Figures 3.13(a) and 3.13(b) show the normalized co- and cross-polarized radiation patterns of the H- and E-planes, respectively, for two different ground planes. As expected, the null in the H-plane radiation pattern is filled considerably, owing to the finite ground plane size. The ground plane enforces the tangential E-field,  $E_\phi(\theta)$ , to vanish along the radiating slot at  $\theta = 90^\circ$ , which in fact creates the null in the H-plane pattern. On the other hand, a deep null in the measured E-plane pattern is observed, whereas in simulation this cut of the pattern is constant except at the dielectric-air interface where the normal E-field is discontinuous. This null in the E-plane is the result of the cancellation of fields, which are radiated by the two opposing



(a)



(b)

Figure 3.13: Measured radiation patterns of the antenna with a small ( $0.2\lambda_0 \times 0.2\lambda_0$ ) and a larger ( $0.5\lambda_0 \times 0.5\lambda_0$ ) Ground Plane (GP): (a) H-plane pattern, (b) E-plane pattern.

magnetic currents. The equivalent magnetic currents, flowing in the upper and lower side of the ground plane, are in opposite directions and consequently, their radiations in the point of symmetry at the E-plane cancel each other. However, in the case of an infinite ground plane, the upper and lower half-spaces are isolated and therefore, the E-plane radiation pattern remains constant. Appendix A will further delineate the effect of the finite ground plane on the radiation pattern of slot antennas.

Moreover, an increase in the measured cross-polarized component is observed as compared with the simulation results. Although it may seem that there is a considerable cross polarization radiation due to the presence of spiral slots at the terminations, there is no such a component in the principal planes as well as the  $\phi = \pm 45^\circ$  planes since the geometry is symmetric with respect to those planes. The cross polarization appeared in these measurements is mainly caused by radiation from the edges as well as the feed cable. The radiated field of the antenna is always capable of inducing currents on the feeding cable, especially when the ground plane size is very small compared to the wavelength. Then, the induced currents re-radiate and give rise to the cross polarization. Moreover, the contribution of the anechoic chamber, giving rise to the cross-polarized component at the low frequency of 300 MHz, is also another factor. Nevertheless, both of the above-mentioned sources for the cross-polarization can be eliminated by increasing the size of the ground plane.

### **3.6 Conformability to Curved Platforms**

Interest in conformal and low profile antennas is in response to mobility, space and airborne requirements. To meet these requirements all at once, the application of slot antennas is a prudent choice. A slotted structure can be mounted on the body of mobile platforms such as airplanes, cars, etc. A slot antenna topology is also desired since it is invisible and does not change the profile of the mobile platform. Knowing

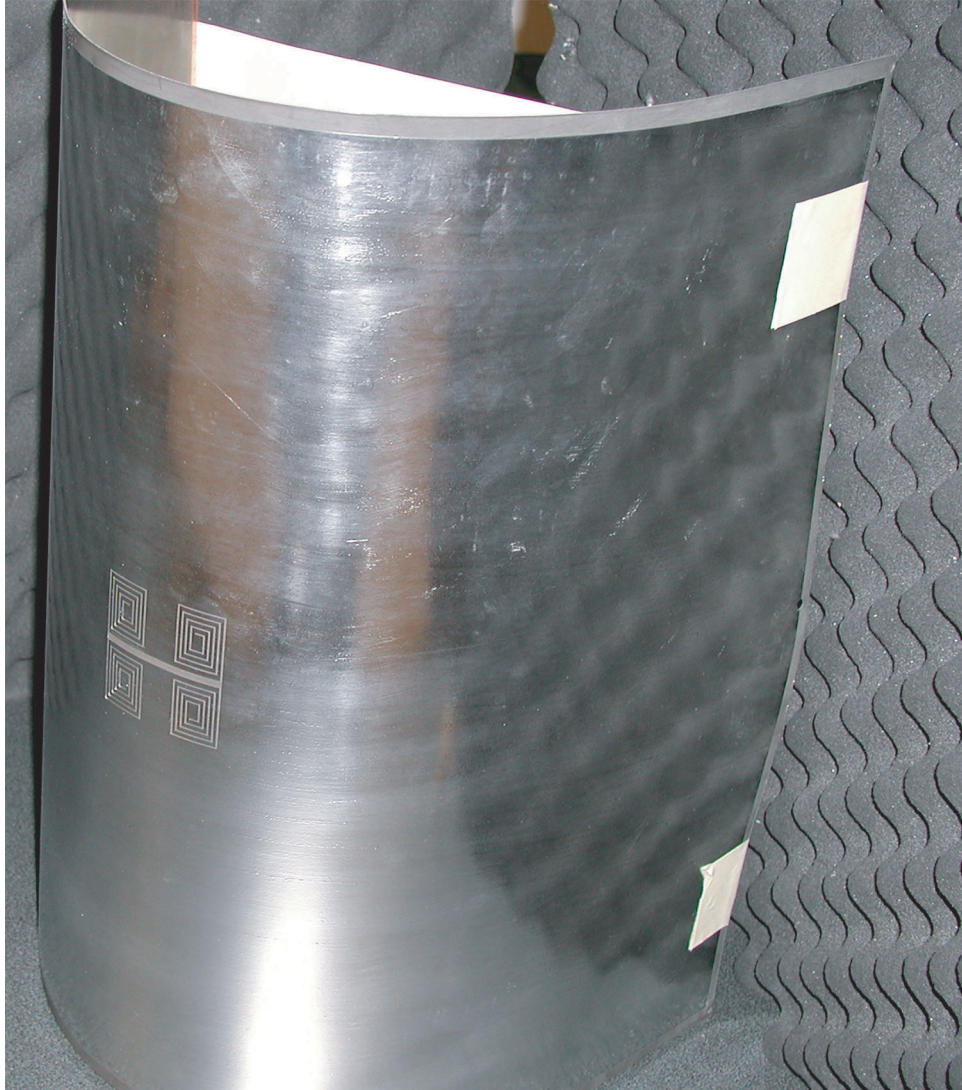


Figure 3.14: A photograph of the miniaturized slot antenna conformed into a curved surface along the H-plane.

that the body of a mobile platform is generally curved, the effect of the ground plane curvature on the radiation property of a slot antenna needs to be investigated.

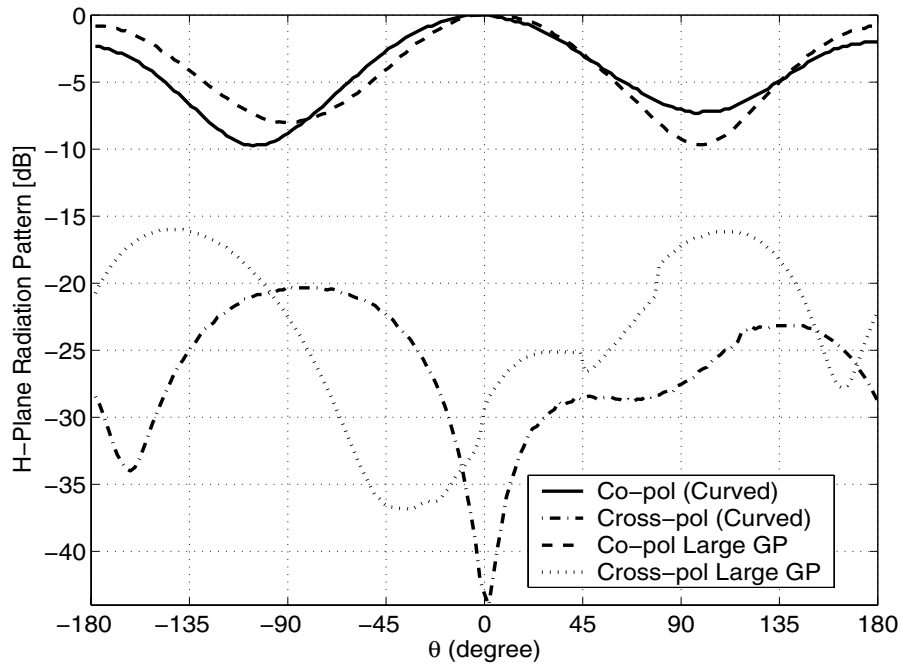
In this section, the conformability of the proposed miniature slot antenna to the curved surfaces is experimentally investigated. The miniaturized antenna of Fig. 3.11 with the large ground is conformed onto two cylindrical surfaces, once along the H-plane, and then, along the E-plane.

Figure 3.14 shows the photograph of the miniaturized slot antenna when con-

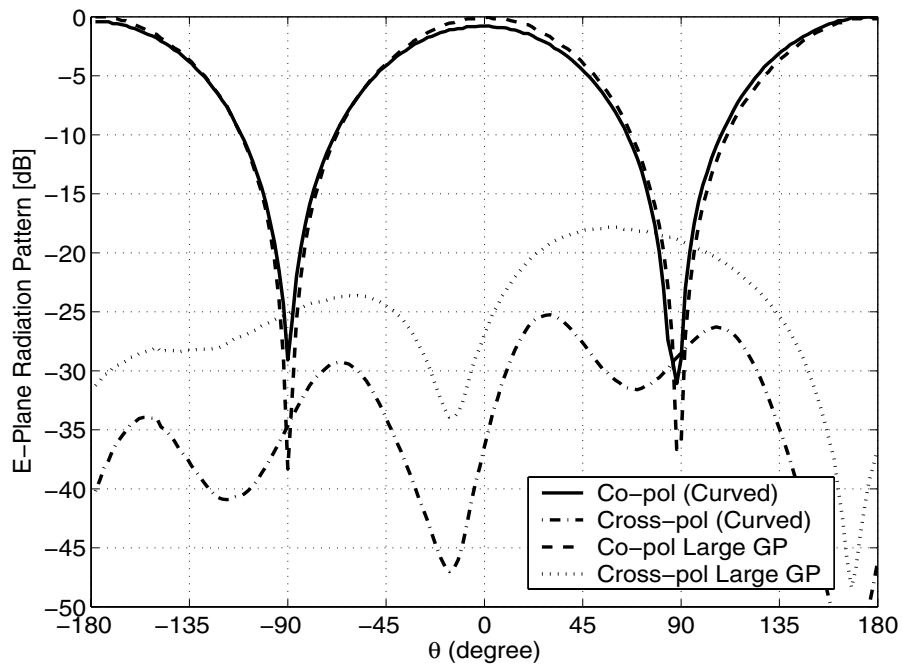
formed to a cylindrical surface along its H-plane. The variation of the input return loss of the conformed antenna is negligible as compared to the planar ground. The radiation pattern of the curved antenna of Fig. 3.14 is measured and plotted in Fig. 3.15. Figure 3.15 also includes the measured radiation pattern of the original miniature antenna without the curvature for comparison. As seen in this figure, the H-plane radiation pattern slightly changes, and it exhibits some asymmetry. Changes in the E-plane pattern are minimal since the curvature does not incur any asymmetry on this plane.

The miniaturized slot antenna is then conformed to a cylindrical surface along the E-plane as depicted in Fig. 3.16. The return loss of the antenna in this configuration does not change either. The radiation pattern of the E-plane conformed antenna was measured for both principle planes of E and H and shown in Figs 3.17(a) and (b), respectively. These patterns are again compared with the radiation pattern on the same antenna without the curvature. As seen in Fig. 3.17, the H-plane pattern of the curved antenna is changed slightly, whereas the E-plane pattern experiences a noteworthy change. As Fig. 3.17(b) shows, the E-plane nulls of the original pattern are filled considerably. As alluded to in earlier discussions and will be elaborated in Appendix A, a simulation with finite ground plane predicts a constant E-plane pattern for the slot antenna. But due to the finite size ground plane, the equivalent magnetic currents flowing in opposite directions, slightly above and below the ground plane, tend to cancel each other's radiated fields and create two nulls. Obviously, the curvature in the E-plane partially blocks the radiation by one of these opposing magnetic currents at  $\theta = \pm 90^\circ$ . That is why the null in the E-plane pattern is filled considerably.

The above study shows that conforming the miniaturized slot antenna to a curved plane does not deteriorate the pattern of the antenna so far as the radius of the curvature is much larger than the dimensions of the antenna. Based on this preliminary



(a)

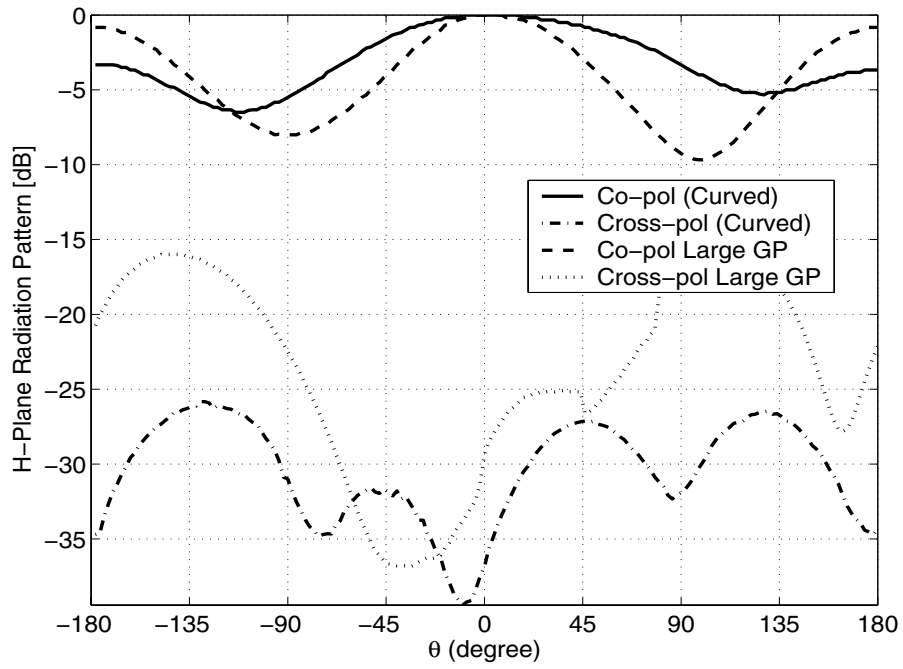


(b)

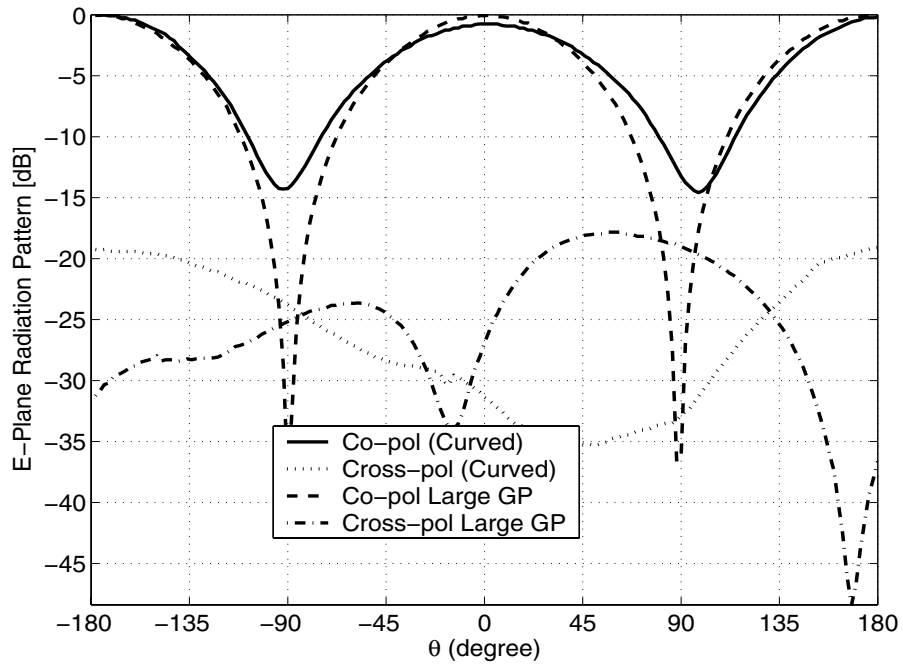
Figure 3.15: Comparison between the measured radiation pattern of the conformed miniaturized slot antenna of Fig. 3.14 with that of its planar counterpart having a large ground plane (GP) with dimensions of  $(0.5\lambda_0 \times 0.5\lambda_0)$ : (a) H-plane pattern, (b) E-plane pattern.



Figure 3.16: A photograph of the miniaturized slot antenna conformed into a curved surface along the E-plane.



(a)



(b)

Figure 3.17: Comparison between the measured radiation pattern of the conformed miniaturized slot antenna of Fig. 3.16 with that of its planar counterpart having a large ground plane (GP) with dimensions of  $(0.5\lambda_0 \times 0.5\lambda_0)$ : (a) H-plane pattern, (b) E-plane pattern.

study, we expect that the effect of the curvature on the cavity backed miniaturized slot antenna to be tolerable.

### 3.7 Conclusion

In this chapter, a procedure for designing a new class of miniaturized slot antennas was proposed. In this design the area occupied by the antenna can be chosen to be arbitrarily small, depending on the applications at hand and the trade-off between the antenna size and the required bandwidth. As an example, an antenna with the dimensions  $0.05\lambda_0 \times 0.05\lambda_0$  was designed at 300 MHz and perfectly matched to a  $50\ \Omega$  transmission line. In this prototype, a substrate with a low dielectric constant of  $\epsilon_r = 2.2$  was used to ensure that the dielectric material would not contribute to the antenna miniaturization. An equivalent circuit for the antenna was developed, which provided the guidelines necessary for designing a compact loss-less matching network for the antenna. To validate the design procedure, a prototype antenna was fabricated and measured at 300 MHz. A perfect match for this very small antenna was demonstrated with a moderate gain of  $-3.0$  dBi when the antenna is fabricated on a very small ground plane with the approximate dimensions of  $0.2\lambda_0 \times 0.2\lambda_0$ . The gain of this antenna can increase to that of a half-wave dipole when a slightly larger ground plane of about  $0.5\lambda_0 \times 0.5\lambda_0$  is used. The fractional bandwidth for this antenna was measured to be 0.34%.

## CHAPTER 4

# Bandwidth Enhancement of Miniaturized Slot Antennas Using Folded, Complementary and Self-Complementary Realizations

### 4.1 Introduction

The notion of antenna miniaturization coincides with the narrow bandwidth and low efficiency. These two adverse impacts of miniaturization make miniaturized antennas very difficult to match. Among the above ramifications, narrow bandwidth has particularly been the subject of additional interests, and been referred to as one of the fundamental limitation of small antennas [1, 2, 3, 8, 9, 10]. Given that a small antenna can be enclosed within a sphere with a certain radius, the above literature introduces a limit on the bandwidth of these antennas. The limit can be approached only if the antenna is occupying the whole spherical volume. If not, which is the case for planar antennas, the fundamental limit gives a very loose upper bound for the bandwidth. Thus, one may attempt to enhance the bandwidth of a planar miniature antenna and still not to exceed the fundamental limit.

Nevertheless, practical aspects of antenna miniaturization have received significant attention in recent years. In Chapter 3, we have proposed a new class of efficient

miniaturized slot antennas which can be easily matched without the need for external matching networks. The topology of a typical miniaturized slot antenna of this class is shown in Fig. 4.1. The miniature design is achieved by introducing symmetric inductive loadings at both ends of a short radiating slot section to create a voltage discontinuity along a resonant slot-line. An important advantage of this topology is that the antenna size, depending on the application at hand, can be chosen almost arbitrarily small at the cost of reduction in bandwidth and efficiency. As an example, the design of a miniaturized antenna with dimensions as small as  $0.05\lambda_0 \times 0.05\lambda_0$  showing a fairly high gain of  $-3$  dBi was demonstrated in Chapter 3.

Resonant antennas in general, and resonant slot antennas in particular, are inherently narrow band. Obviously, further bandwidth reduction is expected for miniature slotted structures. In addition to a narrow bandwidth, another important issue regarding slot antennas is the ground plane size and its impact on antenna gain and efficiency. The effects of a finite size ground plane on the radiation characteristics of the miniaturized slot antennas have been experimentally studied in Chapter 2 and Chapter 3. Additional investigation of the effects of finite size ground plane is presented in Appendix A.

This chapter focuses on two main objectives. First is to introduce methodologies to enhance the bandwidth of the miniaturized slot antenna presented in Chapter 3, and second is to mitigate the drawbacks related to the small size ground plane. The finite size ground becomes a critical issue in cases where a large metallic body is not available to be used for the slot ground plane.

In order to fulfill the first objective of this chapter, namely, the bandwidth enhancement of the miniature antenna, folded and self-complementary configurations are examined. Folded and self-complementary structures are considered as two effective approaches to increase the bandwidth of miniaturized antennas. A folded structure may be introduced to significantly increase the bandwidth of a miniatur-

ized antenna, such as the one shown in Fig. 4.1, without compromising the size and efficiency. Using miniaturized folded slot can result in a more than 100% increase in the bandwidth as compared with that of the miniaturized slot antenna. Another approach for bandwidth improvement is the implementation of self-complementary topologies to moderate the frequency dependence of the antenna input impedance. With regard to this approach, a folded self-complementary miniature antenna is studied, where a noticeable improvement over bandwidth is observed.

In order to alleviate ramifications related to the ground plane size, which is the second objective of this chapter, a complimentary pair of the folded slot topology is introduced, in which the slot is replaced by a metallic strip (printed wire), and the ground plane is eliminated. The duality principle between the two antennas, however, cannot be directly applied because of the presence of the dielectric substrate. It will be shown that folded slots have a much higher radiation efficiency when compared with their complementary folded wire antennas.

In what follows, a miniaturized folded slot, its complementary miniaturized folded printed wire, as well as their self-complementary realization, are fabricated and tested. These antennas do not need complicated external matching circuits and can fit into a very small rectangular area with dimensions as small as  $0.065\lambda_0 \times 0.065\lambda_0$ . Experimental and theoretical data shows that the folded structures exhibit bandwidths twice as wide as their ordinary miniaturized counterparts with similar sizes and gains. The self-complementary version of the folded antenna shows further increase in the bandwidth. In the efficiency/gain comparison, self-complimentary structures fall between the slot and printed wires since they consist of equal proportions of both the slot and printed wire. A self-complementary H-shape antenna is also introduced whereby the required self-complementarity conditions are met at the expense of relaxing miniaturization, and consequently, a very wide bandwidth is achieved. With yet small dimensions of  $0.13\lambda_0 \times 0.24\lambda_0$ , a very wide bandwidth of (2.3:1) can be obtained. For

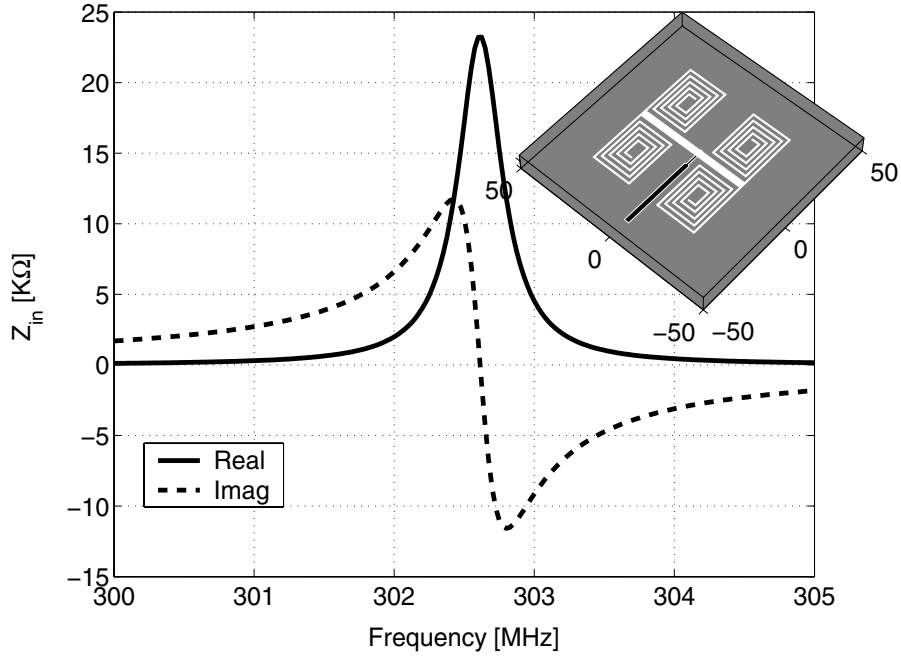


Figure 4.1: The layout and the simulated input impedance of the miniaturized slot antenna around its resonance.

the case of no dielectric substrate, even a wider bandwidth of (3:1) is achieved.

## 4.2 Miniaturized Folded Slot Antenna

The miniaturized slot antenna structure shown in Fig. 4.1 has a relatively narrow bandwidth. The radiating slot segment has a length of  $\ell = 0.05\lambda_0$ , which is 10 times smaller than a standard half-wave resonant slot. Since the physical aperture of this miniature antenna is much smaller than that of a standard slot antenna, its radiation conductance is much lower than a standard  $\lambda/2$  slot. The input impedance of the miniature slot antenna, when fed by a short-circuited microstrip line, is shown to be about  $25K\Omega$  at resonance (see Fig. 4.1). In order to match such a high impedance to a standard transmission-line, impedance matching had to be done off resonance, where the reactance slope is very high. This high spectral variation of the antenna reactance limits the impedance matching to only a narrow band. If the radiation

conductance of the miniaturized slot antenna can be increased without significantly increasing the antenna size, impedance matching over a wider bandwidth can be achieved. Increasing the physical aperture by means of introducing a suitable folded structure seems to be an appropriate approach since the antenna aperture readily increases, while the antenna size can be kept almost the same.

The impedance of a resonant folded dipole antenna is related to that of a dipole antenna by [34, 21]

$$Z_{in}^{folded-dipole} = 4 Z_{in}^{dipole} \quad (4.1)$$

Using Bookers' relation [35], the input impedance of a resonant slot (magnetic) dipole can be obtained from its complementary pair and vice versa as

$$Z_{in}^{folded-slot} = \frac{\eta^2}{4} \frac{1}{Z_{in}^{folded-dipole}} = \frac{Z_{in}^{slot}}{4} \quad (4.2)$$

Equation (4.2) shows that the input impedance of a folded slot is four times smaller than that of the standard slot dipole. Thus, the impedance of a miniaturized folded slot is expected to be much closer to the impedance of standard transmission-lines, and thus easier to match.

Figure 4.2 shows the proposed miniaturized folded slot topology fed by a CPW line. The same figure shows the simulated input impedance as a function of frequency. Dimensions of the folded prototype are chosen to be the same as those of the miniaturized antenna in Fig. 4.1. This antenna occupies an area of  $6\text{cm} \times 6\text{cm}$ . The resonant frequency of this folded antenna, however, is slightly higher than that of the original miniaturized slot. As illustrated, the miniature folded-slot impedance is reduced from about  $25\text{K}\Omega$  for the original design to  $6\text{K}\Omega$ , which is easier to match to a  $50\Omega$  line. Moreover, for the folded antenna, the reactance slope of the input impedance is much lower at the frequency where the real part of the antenna impedance is  $50\Omega$ , indicating the possibility of impedance matching over a wider frequency band.

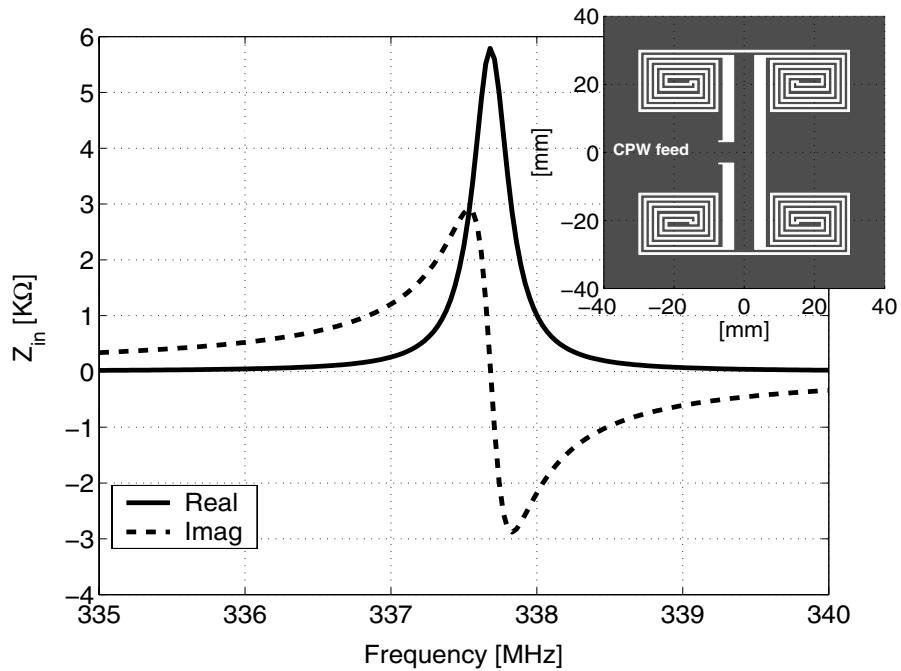


Figure 4.2: The layout and the simulated input impedance of the miniaturized folded slot antenna around its resonance.

Two solutions are available for matching the input impedance of the miniaturized slot antenna to a  $50\ \Omega$ . One solution is to tune the slot antenna below its resonance where the slot is inductive, using a capacitive coupling at the feed, and the other one is to inductively feed the slot and tune it slightly above its resonance. Since the objective is to minimize the antenna size, a capacitively coupled slot antenna is chosen. Figure 4.3 shows the proposed miniaturized folded slot antenna capacitively coupled to a  $50\ \Omega$  CPW line. An interdigital capacitor is placed in between the feed line and the antenna to control the amount of coupling between the line and the miniaturized folded slot in order to achieve the impedance match. The exact value of this capacitance is determined by modeling the miniaturized folded slot with an equivalent second-order resonant circuit model. The equivalent circuit parameters are extracted using a full-wave simulation of the antenna structure similar to what was done for the original miniaturized slot antenna of Chapter 3.

A prototype of the miniaturized folded slot antenna shown in Fig. 4.3 was fab-

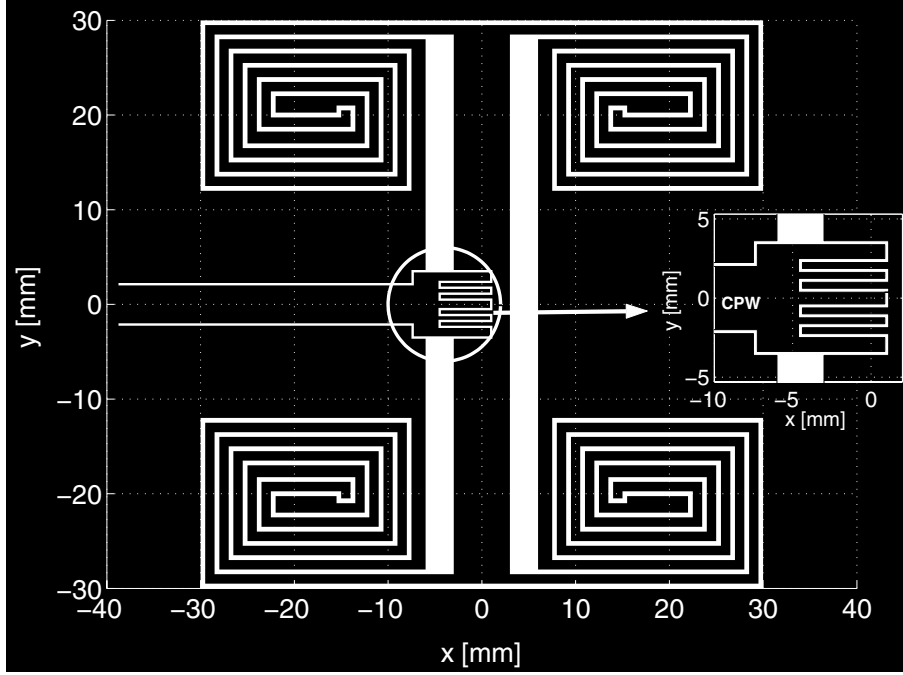


Figure 4.3: Miniaturized folded-slot antenna fed by a capacitively coupled CPW line.

licated on a substrate with a dielectric constant of  $\varepsilon_r = 2.2$  and a loss tangent of  $\tan \delta = 0.0009$ , and a thickness of 0.787mm [24]. Then, the input impedance and far-field co- and cross-polarized radiation patterns of this antenna were simulated and measured. The full-wave simulations were performed using a commercially available Moment Method package [25]. Figure 4.4 shows a comparison between the simulated and measured input return loss values of the antenna depicted in Fig. 4.3. As the simulation shows, the folded antenna occupies an area as small as  $0.065\lambda_0 \times 0.065\lambda_0$  and is perfectly matched at 336.1 MHz. This frequency is lower than the resonant frequency of the folded slot structure (337.7 MHz) shown in Fig. 4.2 because of the insertion of the interdigitated matching capacitance. There is also a 1.8% shift in the measured resonant frequency of the antenna compared to the results obtained from the simulation. This discrepancy can be attributed to the finite size of the ground-plane, numerical errors, and the exclusion of ohmic losses of the ground plane.

For slot-line structures, equivalent magnetic currents are usually used to facilitate efficient implementation of the Method of Moment solution. In this approach, the

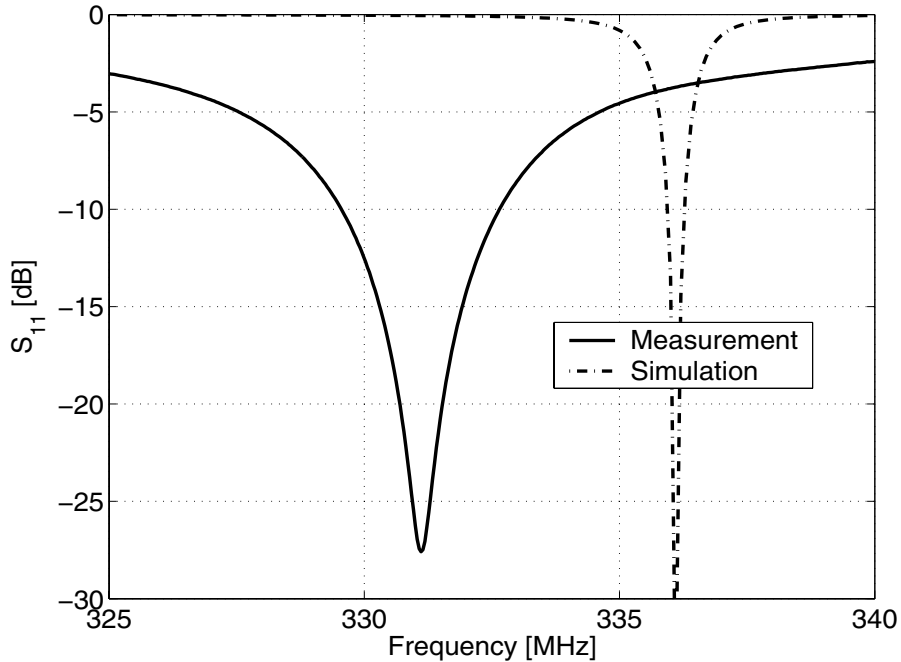


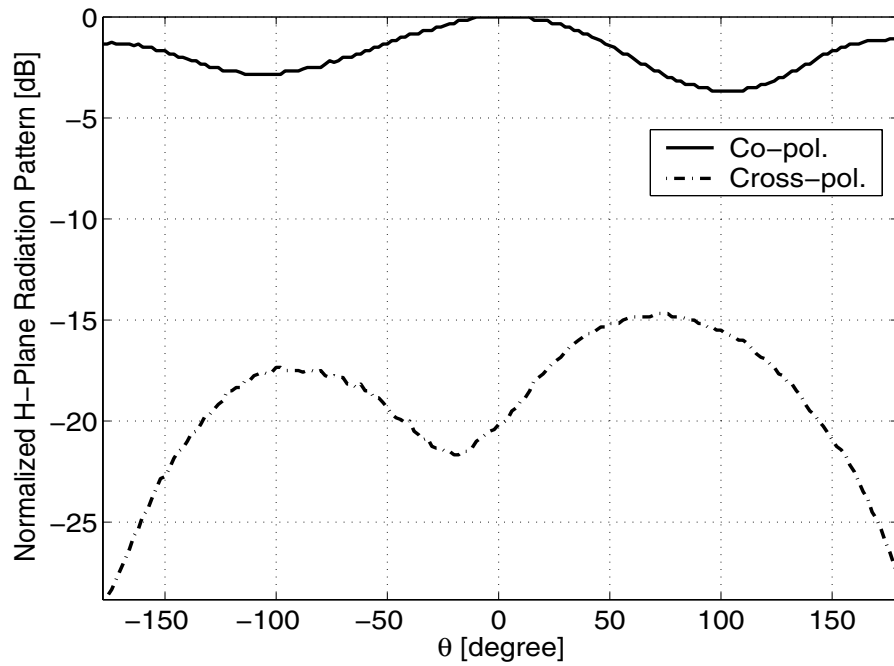
Figure 4.4: Simulated and measured input return loss of the miniaturized folded slot antenna of Fig. 4.3.

tangential electric field over the slot is replaced with an equivalent magnetic current, while the field is assumed to vanish over an infinite ground plane. This assumption implies that the ground plane is modeled by a perfect conductor, and therefore, the ohmic loss cannot be accounted for in this case. In reality, the ground plane of the slot-line structure has finite conductivity and finite size, which leads to the observed discrepancies between the simulation and the measured results. Whereas the finiteness of the ground plane is responsible for the observed disagreement between the measured and simulated antenna center frequency, exclusion of ohmic losses of the ground plane from simulation is responsible for the observed discrepancy in the  $-10$  dB return loss bandwidth of the miniaturized folded slot (see Fig. 4.4).

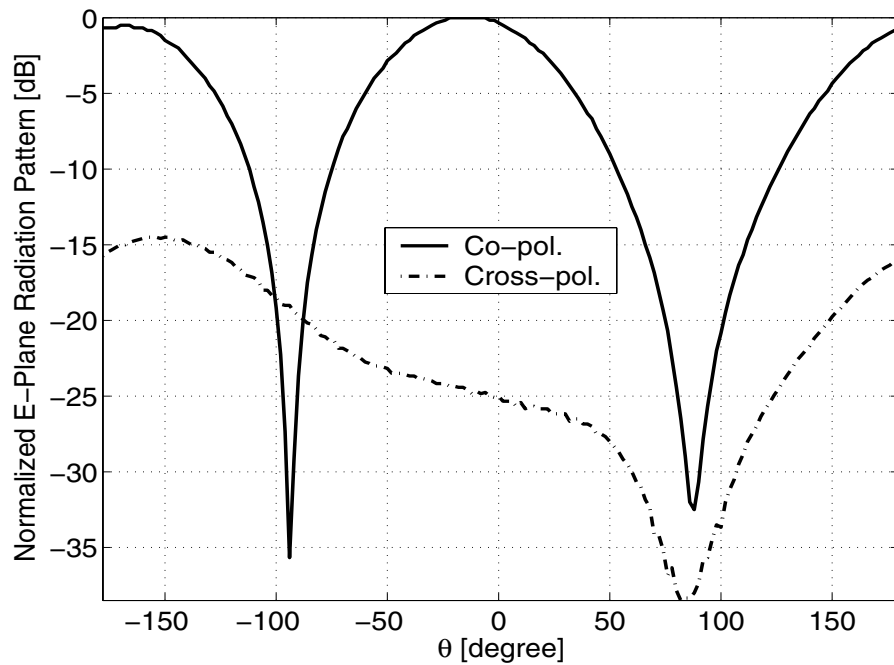
To demonstrate the bandwidth enhancement of the miniaturized folded-slot compared to the original miniaturized antenna, both simulated and measured near-field and far-field characteristics of these antennas are summarized in Table 4.1. Table 4.1 clearly shows an increase in the  $-10$  dB return-loss bandwidth of the folded slot

antenna over the original antenna from 0.34% to 0.93%. The gains of these antennas were measured against a standard half wavelength dipole antenna. The gain of the folded and original miniaturized slot antennas were, respectively, measured to be  $-2.7$  dBi and  $-3.0$  dBi. The measured values of the gains are lower than the simulated results. This again difference can be attributed to the the ohmic loss and finite size of the ground plane which have not been accounted for in the simulation.

Finally, the H-plane and E-plane radiation patterns of the miniaturized folded-slot antenna were measured in the anechoic chamber of the University of Michigan and are shown in Fig. 4.5. For the E-plane pattern,  $E_\theta(\theta)$  was measured in the  $\phi = 0^\circ$  plane. The measurement of  $E_\phi(\theta)$  in the  $\phi = 90^\circ$  plane provides the H-plane pattern of the antenna. In theory, a null should exist in the H-plane pattern of an infinitesimal folded-slot, since the ground plane forces the tangential electric field of  $E_\phi(\theta = 90^\circ) = 0$  at  $\phi = 90^\circ$  to vanish. This deep null, however, is not observed because of the finite dimensions of the ground plane. When the ground is not extended to infinity, the radiation by edges would fill the null. On the other hand, a null is created in the E-plane pattern, whereas the theory predicts a uniform pattern. This phenomenon is also caused by the finite dimensions of the ground plane. Based on the equivalence principle, the magnetic currents on the upper and lower half space flow in two opposite directions and create out of phase normal electric fields on the antenna plane ( $\theta = 0^\circ$ ). When the ground plane is infinite, the lower and upper half spaces are decoupled, and no cancellation occurs. The cross-polarization component of the radiation pattern is small because of the symmetry of the structure in the principal E- and H-planes. The observed minor cross-polarized radiation is caused by the edges of the finite size ground plane and the re-radiation of the near-field of the antenna by the feeding cable.



(a)



(b)

Figure 4.5: Measured radiation pattern of the miniaturized folded slot antenna of Fig. 4.3. (a) H-plane pattern, (b) E-plane pattern.

### 4.3 Miniaturized Folded Printed Wire Antenna

The size of the ground plane was found to be an important parameter in slot antenna gain, bandwidth, and depolarization. In general, the larger the ground plane, the better antenna performance can be expected. In many applications, such as automotive, aviation, and large arrays, metallic platforms of considerable size are already available. Therefore, the ground plane size does not impose a major restriction on the antenna performance. When no large ground plane is available, an alternative miniaturized design may be considered. Basically, printed wire structures, unlike slotted structures, do not need a ground plane. In this section, a printed antenna topology which is the complementary pair of the miniaturized folded-slot of Fig. 4.2 is proposed and tested. This structure is shown in Figure 4.6, where the slot-lines are replaced by metallic strips and vice versa. Two vertical radiating elements at the center of the structure are terminated by distributed capacitive loadings. The electric current distribution attains its maximum on these vertical strips. Although the far-field radiation mainly emanates from the two vertical elements, the contribution of the distributed capacitive loads on the radiation resistance should not be overlooked.

The radiation resistance of an infinitesimal dipole with a constant current distribution can be calculated analytically [34]. This quantity is multiplied by a factor of four in the case of an infinitesimal folded dipole; that is,

$$R_a = 4 \times 80\pi^2 \left(\frac{\ell}{\lambda}\right)^2. \quad (4.3)$$

In the above equation, the antenna is assumed to be radiating in free space. For the miniature folded dipole considered in Fig. 4.6,  $\ell = 0.065\lambda_0$  results in radiation resistance of  $R_a = 13.34\Omega$ . Equation (4.3) only accounts for the contribution of the main radiating arms, and the effects of capacitive loading and the dielectric substrate are not included in the calculation of the input resistance. In order to include all these

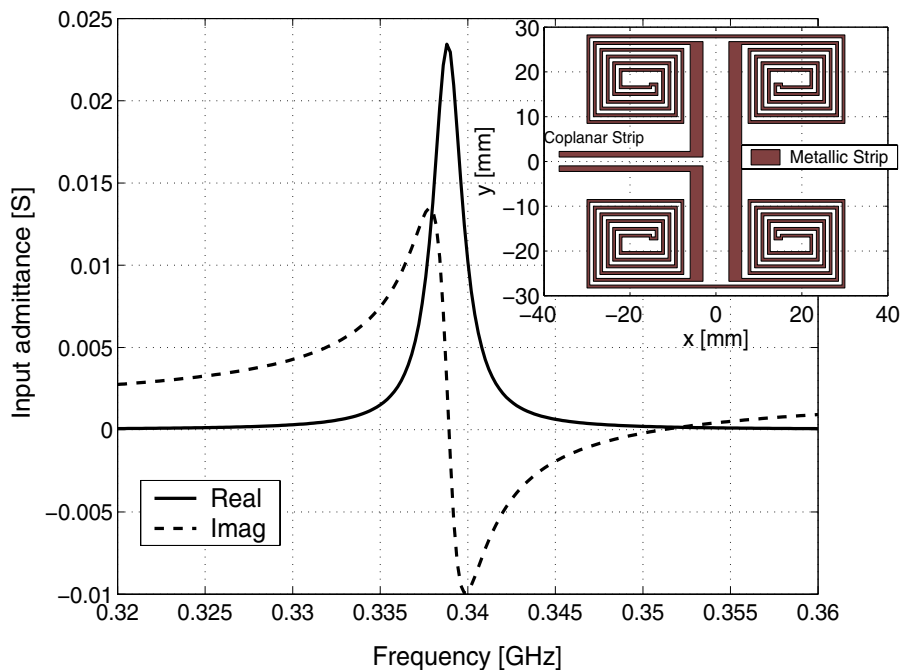


Figure 4.6: Layout of the miniaturized folded printed wire antenna, and the real and imaginary parts of its input admittance.

parameters, the full-wave Moment Method code assuming infinite substrate is used, and the input admittance is calculated and shown in Fig. 4.6. The simulated input impedance of the printed folded dipole at the structure resonance is  $R_a = 43 \Omega$ , which is considerably different from the value predicted by (4.3) for the reasons mentioned earlier.

Similar to its folded-slot counterpart, the folded printed-wire can be directly matched to a  $50 \Omega$  line, without a complicated matching network. The printed dipole antenna requires a balanced input to ensure a symmetric current distribution on the antenna. Both lumped element (RF transformer chips) and distributed baluns can be used to transform the unbalanced feed into balanced co-planar strips (CPS), which feed the miniaturized printed folded-dipole antenna of Fig. 4.6. Figure 4.7 illustrates the layout of a Merchand balun which is an example of a distributed transformer [36]. This transformer is used for a  $50 \Omega$  microstrip line to a CPS transition. Figure 4.8 shows the layout of the printed wire antenna connected to a Merchand balun.

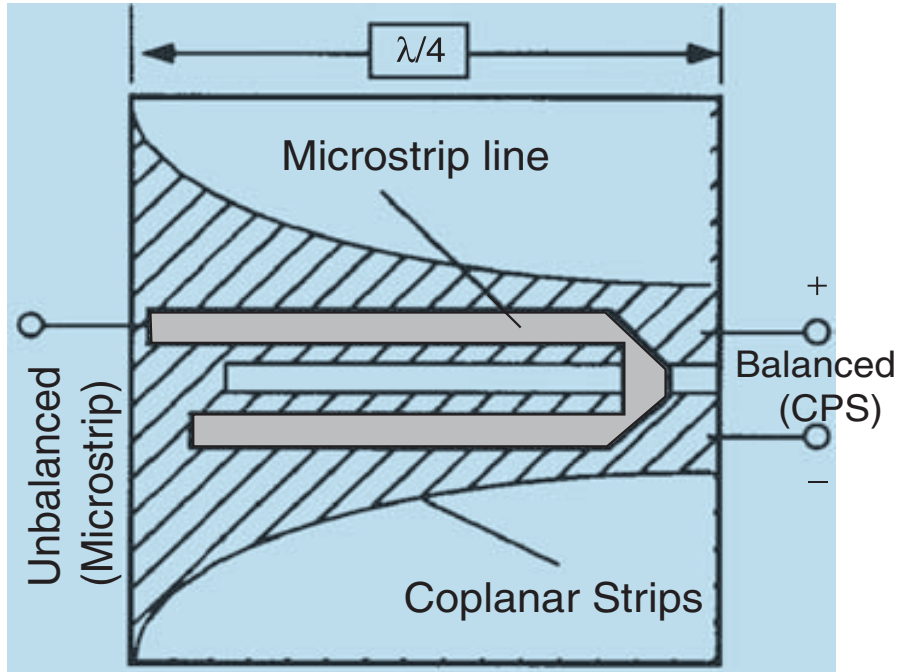


Figure 4.7: Merchand balun architecture [36].

Although the balun is considerably larger than the antenna itself, it should not be considered as a part of the antenna, and it has only been used here to characterize the antenna discretely. When the antenna is integrated with transceiver electronics, balanced circuitry can be utilized instead.

The design procedure for this antennas is similar to the one presented for the miniaturized slot antennas making use of the duality principle. Figure 4.8, shows the miniature antenna fed by a  $50\ \Omega$  microstrip line through a Merchand balun. Note that fine-tuning is accomplished by a small amount of reactive feed generated by having a microstrip line extended slightly less than  $\lambda/4$ . This antenna was fabricated on the same substrate used in the previous examples. Figure 4.9 shows a comparison between the simulated and measured input return loss values of the miniaturized printed folded antenna. This antenna can fit into a rectangular area of  $0.06\lambda_0 \times 0.065\lambda_0$  at 336 MHz. However, there is about 1% shift in the measured operating frequency compared with the simulation, which again can be attributed to numerical errors and the finite dimensions of the dielectric substrate.

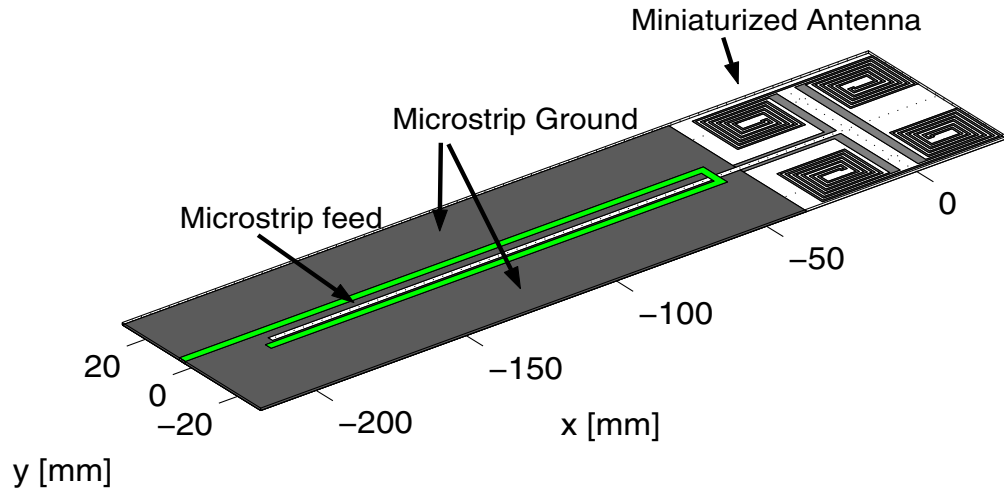


Figure 4.8: The miniaturized folded printed wire antenna with balanced feed and fine tuning setup.

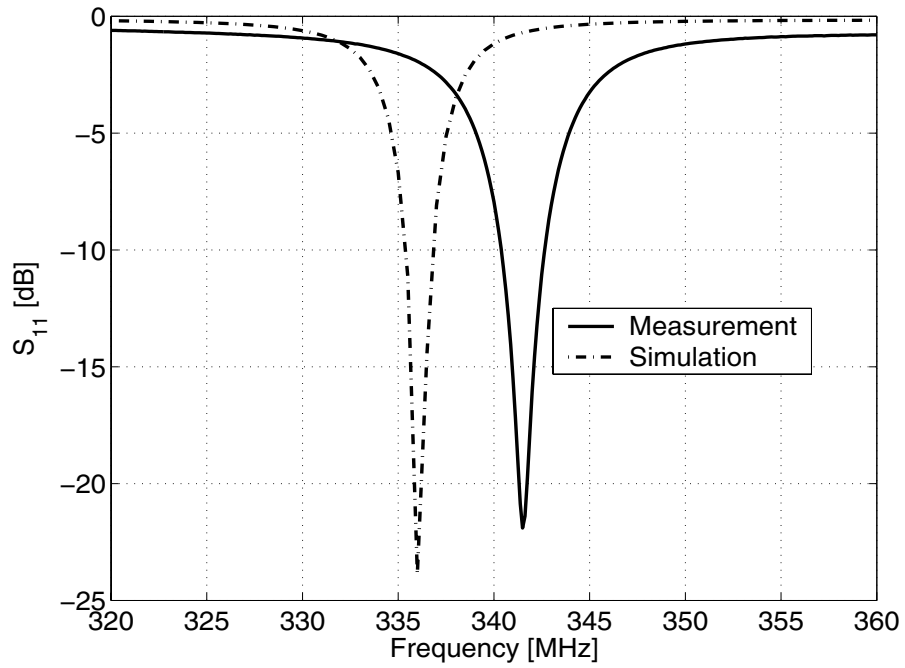


Figure 4.9: Simulated and measured input return loss of the miniaturized antenna in Fig. 4.8.

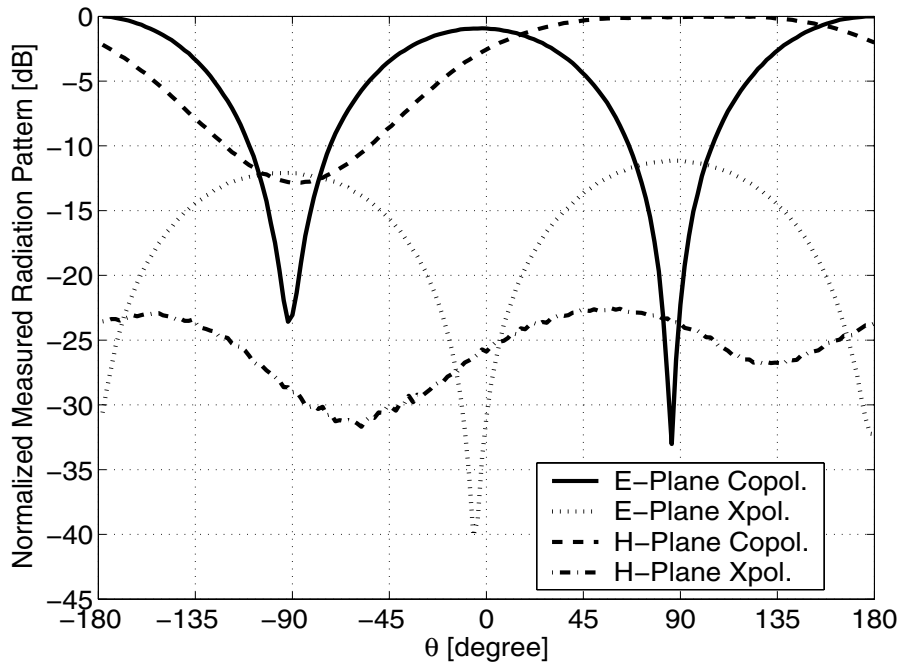


Figure 4.10: E- and H-plane measured radiation patterns of the miniaturized folded printed wire of Fig. 4.8.

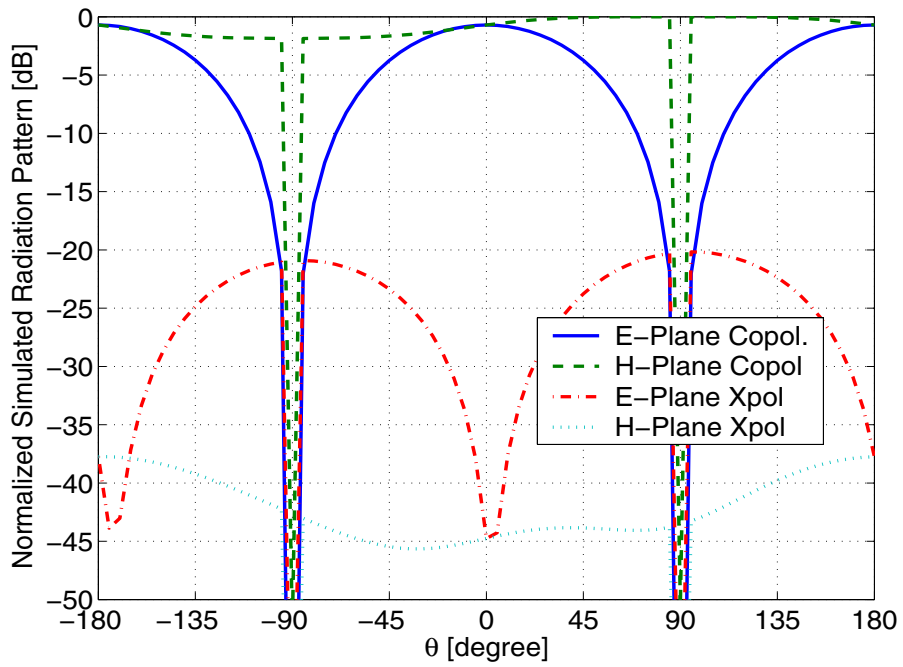


Figure 4.11: The simulated radiation pattern of the miniaturized folded printed wire antenna without a balun.

The measured radiation pattern of this printed antenna for E- and H-planes are plotted in Fig. 4.10. Figure 4.11 illustrates the simulated radiation pattern of the antenna itself in the absence of the balun. The measured radiation pattern in the E-plane agrees with the numerical simulation and the theoretical radiation pattern of an infinitesimal folded dipole. In contrast, an asymmetric null appears in the H-plane pattern at  $\theta = -90^\circ$ , whereas a constant pattern in the H-plane is expected. This asymmetry emerges because of the presence of the balun. The major portion of the observed cross polarized radiation is believed to emanate from the feed cables rather than the antenna structure itself. The far-field gain of this antenna is measured to be  $-6.5$  dBi, which is slightly higher than the value predicted by the simulation. Knowing that the balun creates a null in the H-plane pattern, one should expect the antenna to be more directive when the balun is present. That is why the measured gain is slightly higher than the gain obtained from the simulation (see Table 4.1). The observed difference between the gains of the miniaturized folded-slot and printed dipole is noteworthy. A 3.8 dB gain difference exists between the two antennas which is attributed to conductor ohmic losses. Slot antennas make use of more conductors, and therefore, their ohmic losses are significantly less than the ohmic losses of their printed wire antennas counterpart. Therefore, the use of slotted structures are preferred for the miniaturized designs.

Table 4.1: Comparison among characteristics of miniaturized slot, miniaturized folded slot, and miniaturized printed folded dipole antennas.

| Antenna Type      | Size                                   | Bandwidth [%] |       | Gain [dBi] |       | Directivity [dB] |
|-------------------|--|---------------|-------|------------|-------|------------------|
|                   |  | Sim.          | Meas. | Sim.       | Meas. |                  |
| Miniature slot    | $0.05\lambda_0 \times 0.05\lambda_0$   | 0.058         | 0.34  | 1.0        | -3.0  | 1.9              |
| Folded slot       | $0.065\lambda_0 \times 0.065\lambda_0$ | 0.12          | 0.93  | 1.0        | -2.7  | 1.9              |
| Folded wire       | $0.065\lambda_0 \times 0.065\lambda_0$ | 0.45          | 0.60  | -7.0       | -6.5  | 2.4              |
| Self-comp. folded | $0.065\lambda_0 \times 0.065\lambda_0$ | 1.1           | 1.1   | -5.5       | -4.5  | 2.7              |

## 4.4 Miniaturized Self-Complementary Folded Antenna

The use of self-complementary antennas has been suggested to obtain antennas with frequency-independent input impedances [37]. The basic idea stems from the fact that these structures consist of two sections that are dual of each other. Therefore, the reactive parts of these two subsections tend to cancel each other, which leads to a purely real input impedance over the frequency band. In reality, however, a self-complementary radiating structure needs to be truncated, and this truncation by itself deteriorates the performance of a self-complementary design. The extent of this deterioration depends on the geometry as well as the truncation extent. Truncation becomes even more important when miniaturized antennas are considered. Apparently, miniaturized self-complementary antennas are subject to a very tight truncation whose effect should be closely examined.

Another important assumption in self-complementary structures is that the antenna should radiate in the free space or homogeneous media. Consequently, the introduction of a dielectric medium would violate the required condition for self-complementarity, and thus, the prescribed theoretical results may not be achieved.

Figure 4.12 shows a self-complementary pair of the two previously introduced folded antennas where the top half of the structure is similar to that of the folded printed wire in Fig. 4.6, and the lower half resembles the folded slot of Fig. 4.2. This structure is excited through self-complementary transmission-line which resembles an asymmetric CPW waveguide. The characteristic impedance of this transmission-line is  $Z_c \approx 60\pi/\sqrt{\epsilon_r}$ , given that a dielectric substrate is present. This antenna has the same dimensions as the two previously introduced structures and is fabricated on the same Duroid dielectric substrate. In order to analyze the structure, the two-port antenna structure shown in Fig. 4.12 is simulated using the Method of Moment

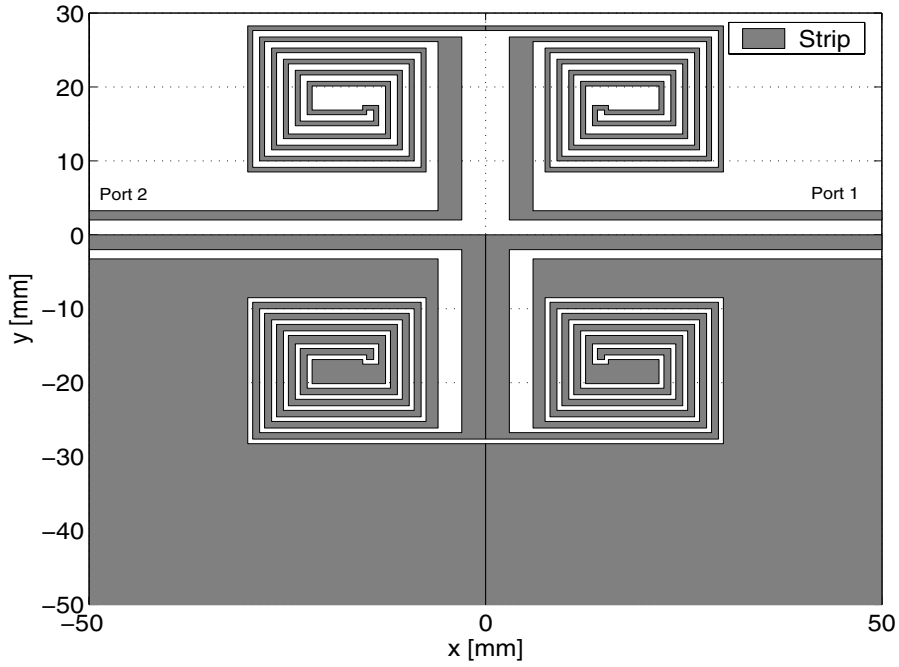


Figure 4.12: The miniaturized self-complementary folded antenna fed by a two-port self-complementary asymmetric CPW-line.

[25], and its S-parameters are presented in Fig. 4.13. Based on the simulated S-parameters, the resonant frequency of the antenna can be determined. Furthermore, the knowledge of the S-parameters provides the information required for designing a matching network for the antenna.

#### 4.4.1 Impedance Matching

In order to match the impedance of the antenna, two parameters should be determined. One parameter is the terminating impedance of the second port, and the other is an appropriate reactive circuit to be placed in series with the antenna at the first port. A trivial choice for the terminating impedance of the second port is the intrinsic impedance of the self-complementary CPW line, which is approximately  $Z_c \approx 60\pi/\sqrt{\epsilon_r} = 125 \Omega$ . This termination ensures no reflection from the line at the second port, but at the same time, the resistive termination reduces the radiation efficiency of the antenna drastically. That is why reactive (loss-less) termination for the

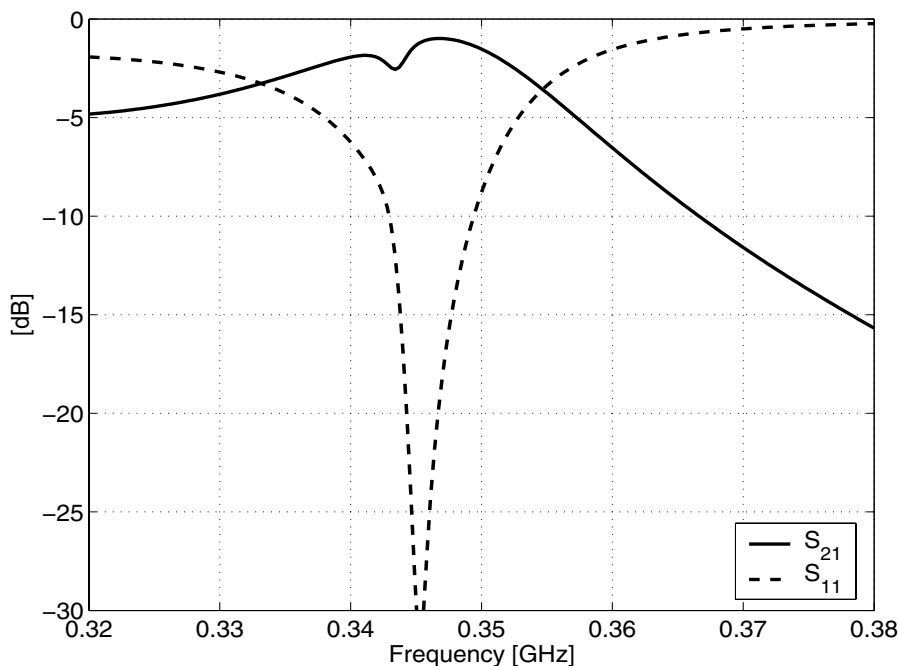


Figure 4.13: The two-port simulated S-parameters of the miniaturized self-complementary folded antenna of Fig. 4.12 to be used for obtaining a proper loss-less matching network.

second port is preferred. In order to minimize ohmic losses, the second port is short circuited, and the matching circuit of Fig. 4.14 is proposed. The matching parameters of this circuit can be found using an optimization algorithm so that a wide band impedance matching may be obtained around the resonant frequency of the structure. The loss-less matching circuit can be realized either by distributed elements or by lumped elements. Figure 4.15 illustrates the antenna with a distributed element realization of the matching network. Obviously, this distributed matching network is not a part of the antenna, and may be replaced with high  $Q$  lumped elements when the antenna is integrated with a transceiver.

The antenna of Fig. 4.15 is fabricated on the same substrate as the previous antennas, and its input return loss is measured and compared with those obtained from the full-wave simulation and the equivalent circuit model. This comparison is shown in Fig. 4.16 where a good agreement is observed. Both simulated and

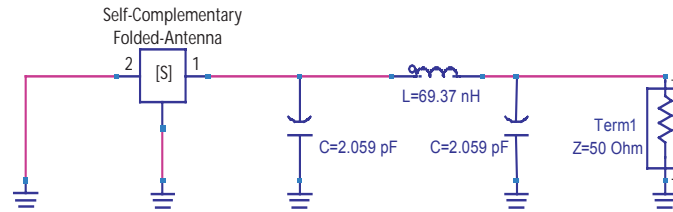


Figure 4.14: The equivalent circuit of the required matching network to a 50  $\Omega$  line.

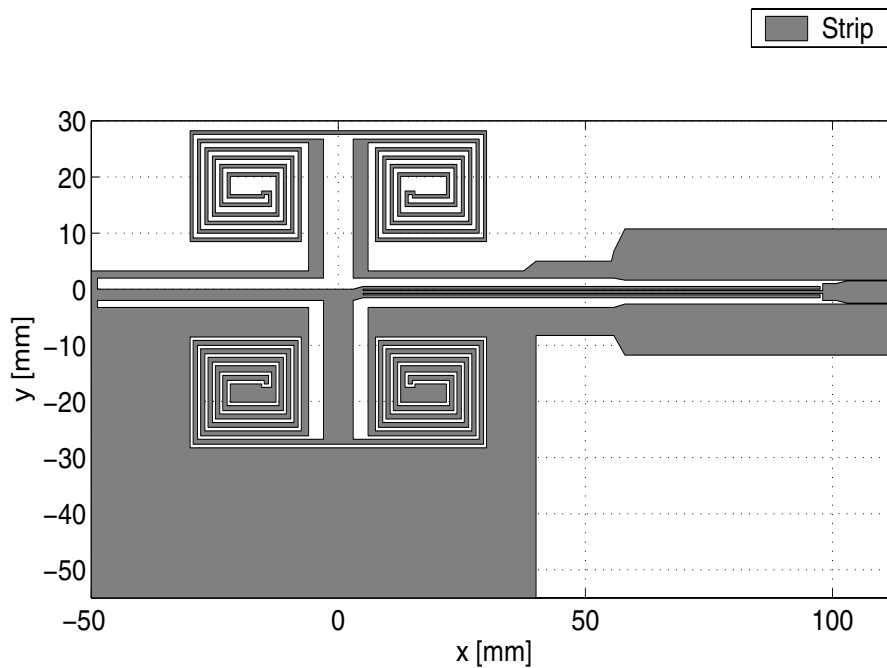


Figure 4.15: The geometry of the miniaturized self-complementary folded antenna along with the distributed-element realization of the matching network of Fig. 4.14.

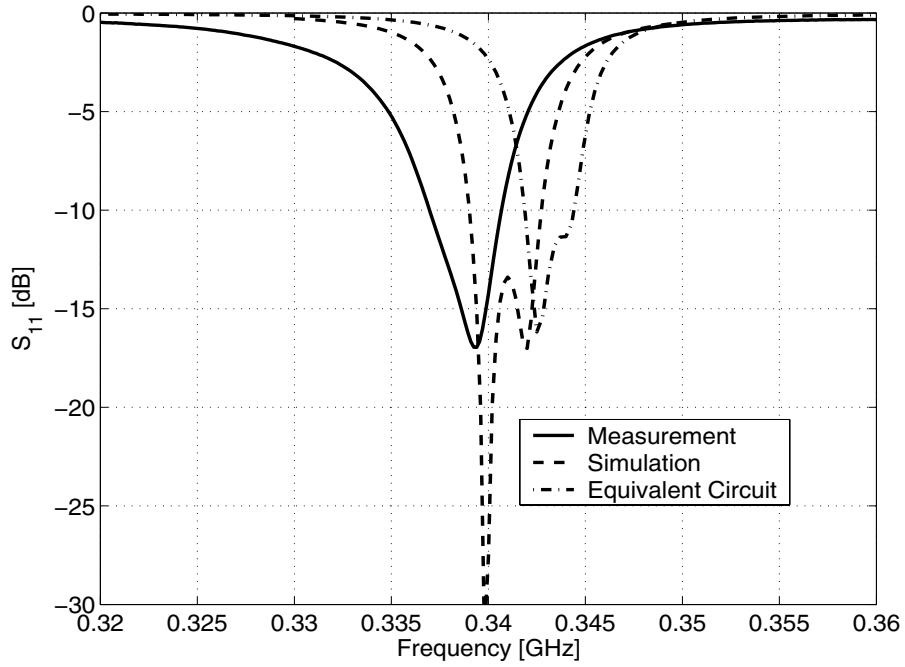


Figure 4.16: The measured, simulated, input return losses of the antenna of Fig. 4.15, as well as that of the equivalent circuit model of Fig. 4.14.

measured fractional bandwidths for this structure are found to be 1.1% which exhibits at least 25% improvement over the measured bandwidth of the miniaturized folded slot antenna in Table 4.1. Unlike miniaturized slot and folded slot antennas, the simulated and measured bandwidth and gain of this antenna agree favorably since in the simulation of the self-complementary antenna, the notion of magnetic currents were not used, and thus, the ohmic losses are accounted for.

The radiation pattern of this antenna might seem to be complicated at the first glance. However, the radiated fields can be considered as the superposition of the field of a small folded dipole and that of a folded slot. Therefore,  $\phi = \pm 45^\circ$  specifies the principle plane of the antenna given that both dipole and slot modes are excited in phase. The radiation pattern of the self-complementary folded antenna is measured in three cuts of  $\phi = 0^\circ$ ,  $\phi = 45^\circ$ , and  $\phi = 90^\circ$ . Fig. 4.17 compares the measured and simulated radiation pattern of this antenna for these three cuts. Pattern measurement of self-complementary antennas with tight truncation is a rather involved procedure

mainly due to the coexistence of both the electric and magnetic radiating elements, which have dual patterns. Therefore, the resultant radiation is symmetric neither with respect to the symmetry planes of the truncated structure nor with respect to the edges. This asymmetry also increases the chance that the near-field of the antenna could excite currents on the feeding cable, and that those excited currents re-radiate, and thus, interfere with the far-fields of the antenna. In order to prevent unwanted radiations, a portion of the feeding cable at the immediate vicinity of the antenna was shielded and grounded.

The gain of this antenna was measured against a calibrated antenna. Under polarization matched condition, a gain of  $-4.5$  dBi was measured, which is slightly higher than the simulated gain for this antenna. The difference may be attributed to the perturbation of the radiation pattern of the antenna owing to the presence of the additional ground plane used in the measurement setup.

Comparing the self-complementary folded antenna with two previously discussed antennas, one can recognize that the self-complementary design has the widest bandwidth among the three though it is still far from being a wide-band antenna. This frequency dependence is caused by the tight truncation of the structure so as not to negate the miniaturization. Furthermore, the presence of the dielectric substrate and feeding network are two factors that tend to violate the self-complementary conditions of the topology. The efficiency/gain of this antenna falls in between the gain of the two previous designs, which is inline with our expectation. Slot antennas are superior with respect to ohmic losses, whereas printed wire antennas have the highest ohmic losses. This self-complementary antenna is half slot and half strip. Thus, the self-complementary design is expected to be better than the printed wire, and worse than the slot, which is consistent with the observations summarized in Table 4.1.

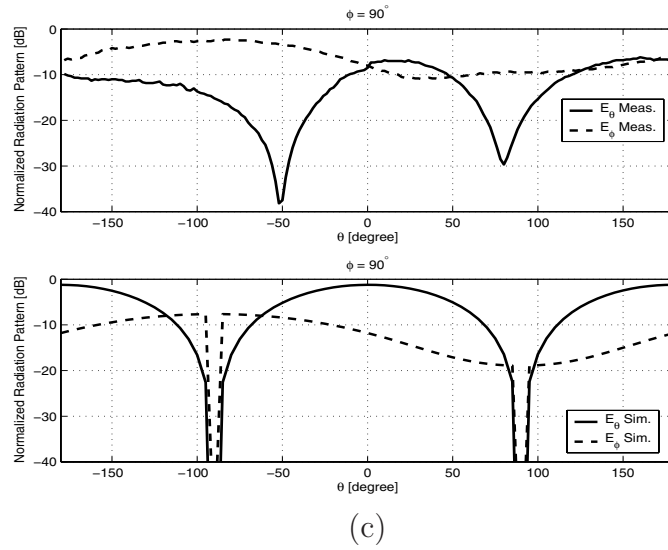
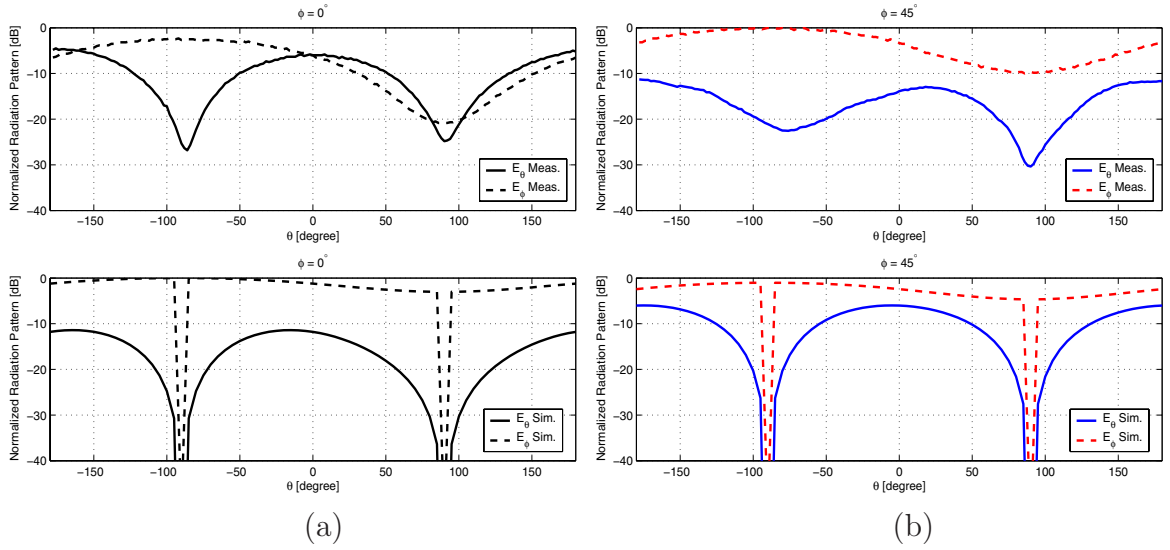


Figure 4.17: Comparison between the measured and simulated radiation patterns of the miniaturized self-complementary antenna on three different planes of (a):  $\phi = 0^\circ$ , (b):  $\phi = 45^\circ$ , and (c):  $\phi = 90^\circ$ .

## 4.5 Self-Complimentary H-Shaped Antenna

In the self-complementary antenna design of the previous section, the main objective was to maintain a very small size, regardless of how adversely the required conditions for self-complementary structures were affected. In this section, a more compatible design with the self-complementary conditions is introduced. In this design, the miniaturization criterion is relaxed by reducing the end-loading. By removing all of the loading spiral arms except for one, an H-antenna is obtained. Figure 4.18 shows the geometry of this structure fed by a short-circuited microstrip line. Note that a via-hole connects the end of the microstrip line of Fig. 4.18 to the right hand side of the ground plane. Again a substrate with  $\epsilon_r = 2.2$  and a thickness of 0.787 mm was used to fabricate this antenna. An impedance step in the microstrip line, as well as two short stubs, was introduced to enhance the impedance matching to a  $50\Omega$  line. The simulated and measured input return losses of this antenna are illustrated in Fig. 4.19. As shown in this figure, a very wide  $-10$  dB bandwidth from 1.35 GHz to 3.2 GHz (2.3:1) is achieved. To demonstrate the effect of the substrate in perturbing the self-complementarity, the same structure is simulated with no dielectric substrate ( $\epsilon_r = 1.0$ ) as well. The simulated return loss of this antenna is also illustrated in Fig. 4.19, where it demonstrates a considerably wider bandwidth from 1.3 GHz to 3.9 GHz (3:1).

Another source of frequency dependence in the response of the antenna structure in Fig. 4.18 is the asymmetry created by the microstrip feed and the corresponding matching network. Comparing this feeding configuration with those of the perfectly self-complementary structures [38, 39], one can recognize that the symmetry can only be preserved when the antenna structure has two ports, and the second port is terminated by a resistance of  $R_L = Z_0/2 = 60\pi\Omega$ . Using this terminated configuration, the input impedance of the antenna becomes  $60\pi = 188\Omega$  over a wide frequency band requiring an additional wide-band matching network, should the antenna be

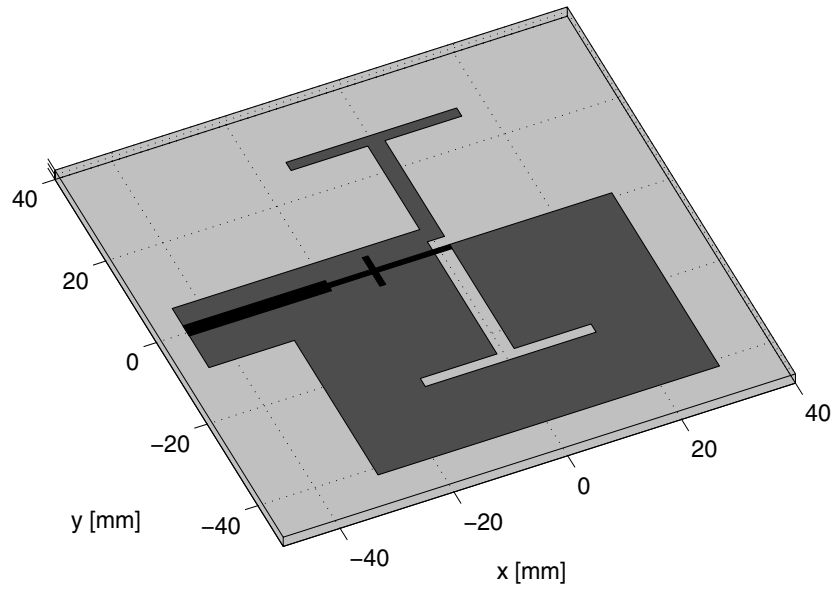


Figure 4.18: The topology of a self-complementary H-antenna fed by a short-circuited microstrip line.

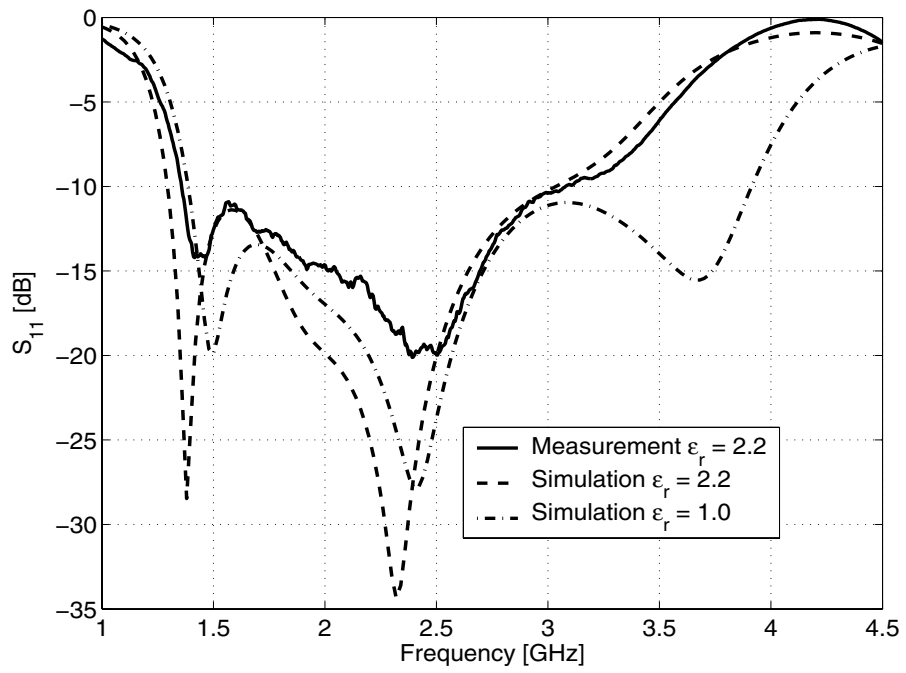


Figure 4.19: Measured and simulated return losses of the H-antenna in Fig. 4.18, as well as that of the same structure without dielectric ( $\epsilon_r = 1.0$ ).

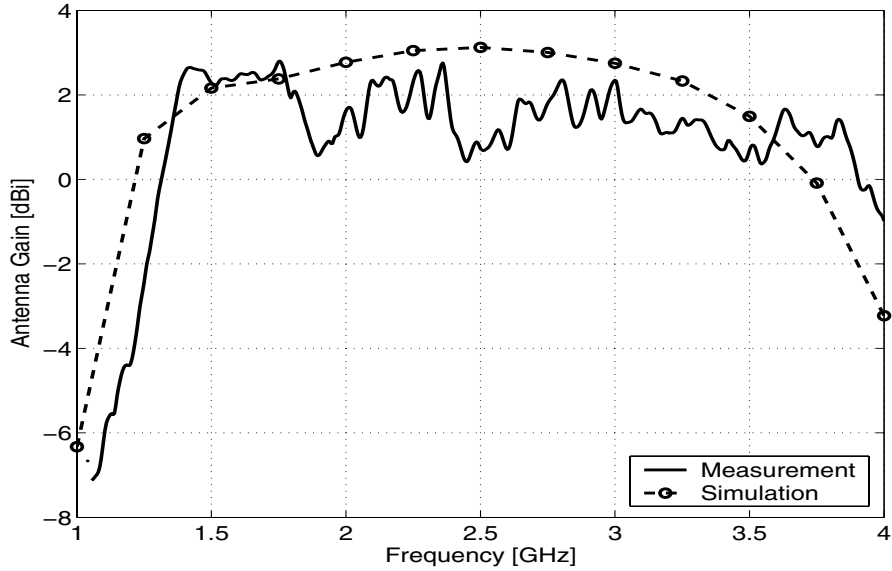


Figure 4.20: Comparison between the measured and simulated gains of the self-complementary H-antenna as a function of frequency.

matched to a standard  $50\ \Omega$  line. Furthermore, introducing a resistive load reduces the antenna efficiency as mentioned earlier. The finite extent of the structure is another inevitable factor that deteriorates the frequency-independent performance of a self-complementary antenna.

The far-field characteristics of this antenna is considered next. The bore-sight gain of this antenna was measured over the spectrum of the operation against that of a wide band calibrated ridged horn<sup>1</sup>. The total measured gain of the antenna at the bore-sight ( $\theta = 0^\circ$ ) is plotted in Fig. 4.20, where good agreement is observed between the simulated and measured values. The slight difference between the simulated and measured gains is mainly due to the response of the anechoic chamber as well as the potential multi-path and unwanted radiation by the feeding cable.

Finally, the radiation pattern of this antenna is measured at four frequency points within the antenna band, namely 1.5 GHz, 2.0 GHz, 2.5 GHz, and 3.0 GHz, in three different planes of  $\phi = 0^\circ$ ,  $\phi = 45^\circ$ , and  $\phi = 90^\circ$ . Both horizontal ( $E_\theta(\theta)$ ) and vertical ( $E_\phi(\theta)$ ) polarizations were measured. Figure 4.21 shows the pattern measurement

<sup>1</sup>EMC Test Systems (ETS), model # 3115

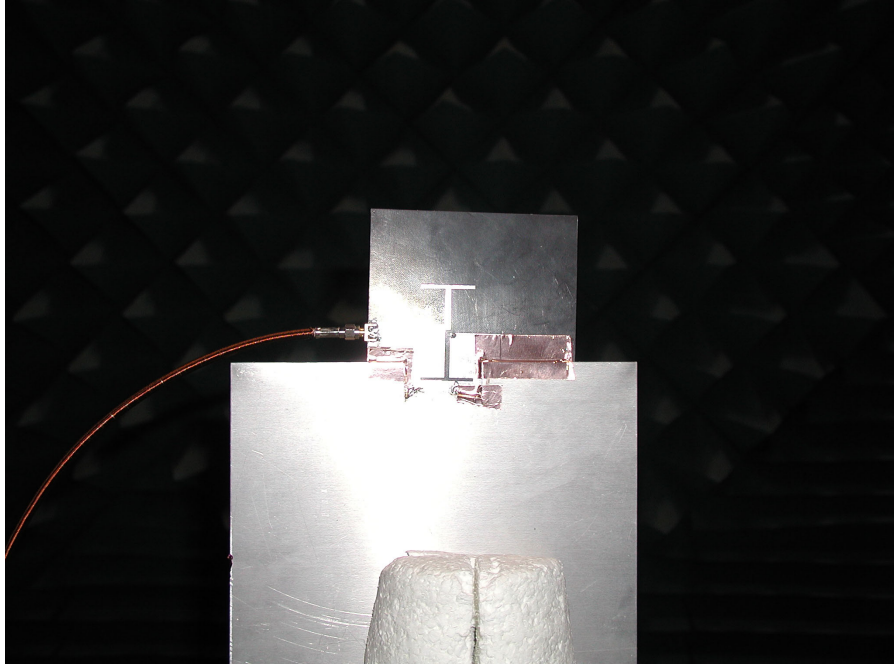


Figure 4.21: Comparison between the measured and simulated gain of the self-complementary H-antenna as a function of frequency.

setup used in the experiment. Figures 4.22, 4.23, 4.24, and 4.25 show the simulated and measured radiation patterns of the self-complementary H-antenna at the above frequencies.

A few points should be explained before comparing the measured patterns with the simulated results. In the simulation, the dielectric substrate is assumed to be of an infinite extent, which explains the presence of a null in the simulated  $E_\phi(\pm 90^\circ)$  patterns at all of the frequency points. This phenomenon has been further discussed in Appendix A. Another factor that accounts for some of the discrepancies is the effect of the antenna mount fixture with a larger half-ground plane. As seen in Fig. 4.21, the effect of this fixture is minimal in the  $\phi = 0^\circ$  plane. Therefore, very good agreement is observed between the simulated and measured patterns at all frequency points. On the other hand, the measurement fixture imposes a null on the  $E_\phi(\theta = -90^\circ)$  pattern at  $\phi = 45^\circ$  plane, which is why a weak null is observed in the  $E_\phi$  at  $\theta = -90^\circ$ . The remaining patterns agree rather favorably with the simulation. By the same token,

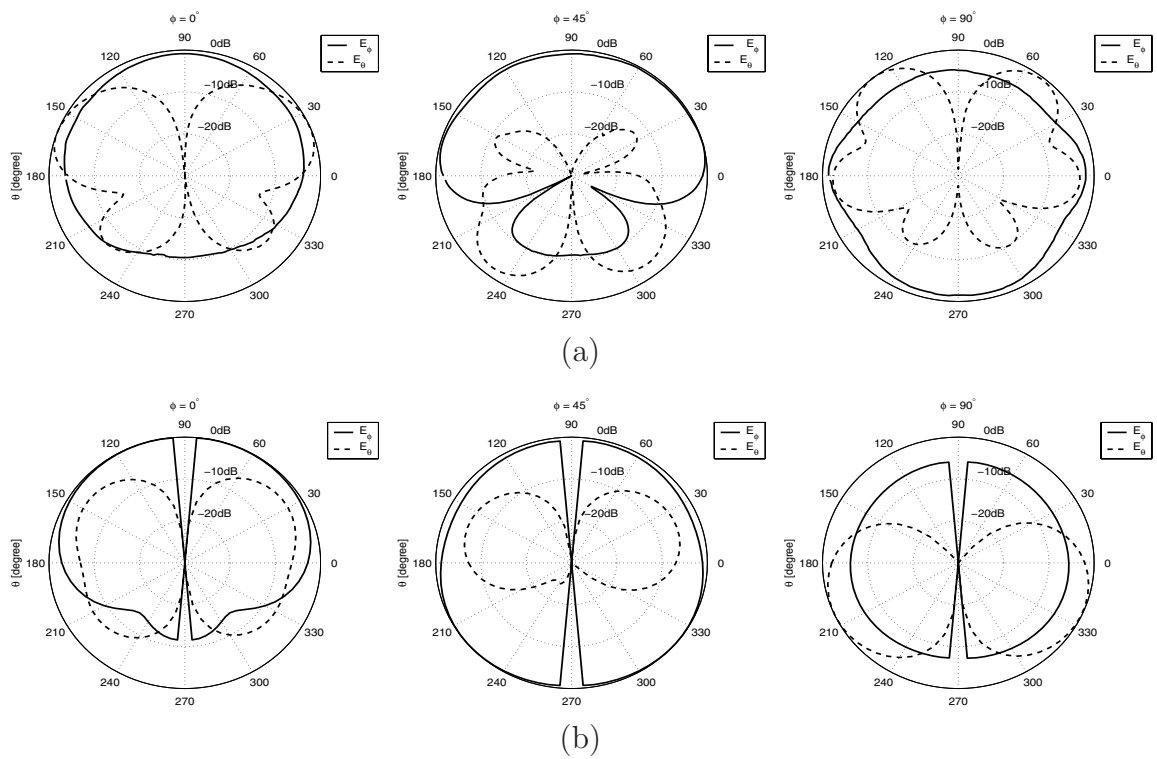


Figure 4.22: Comparison between the measured and simulated radiation patterns of the self-complementary H antenna at 1.5 GHz for three cuts of  $\phi = 0^\circ$ ,  $\phi = 45^\circ$ ,  $\phi = 90^\circ$ ; (a): measurements, (b): simulations.

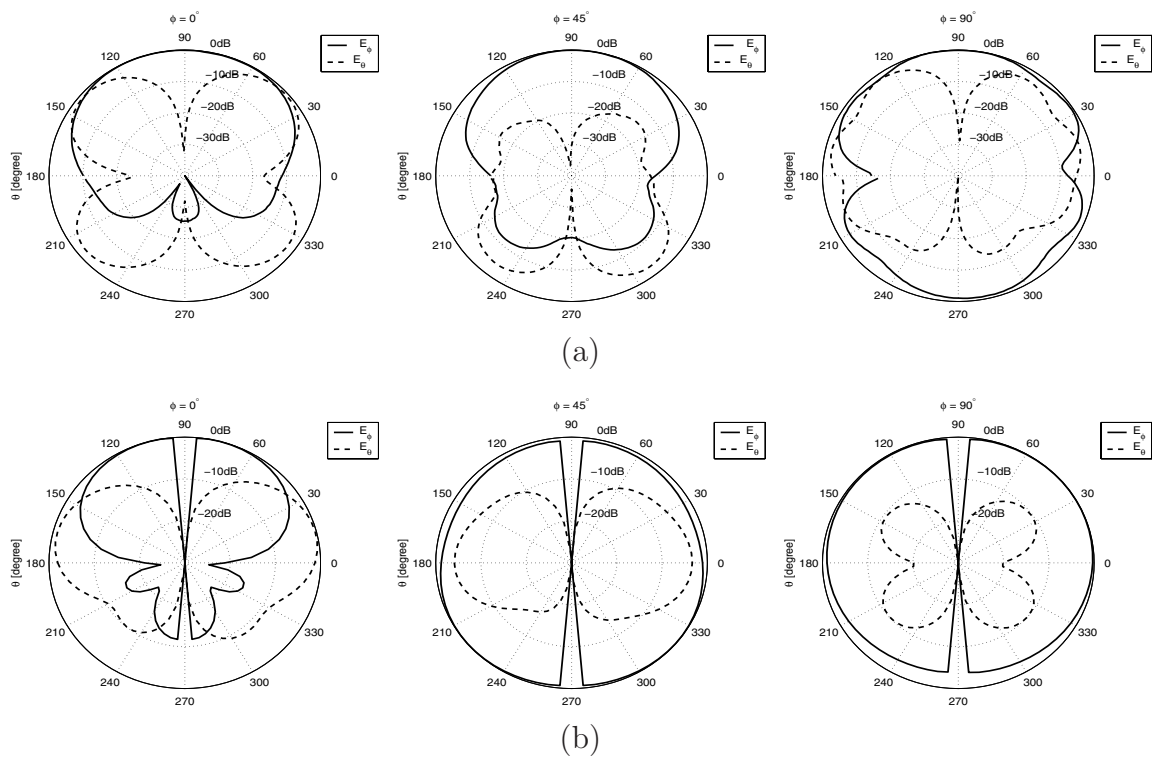


Figure 4.23: Comparison between the measured and simulated radiation patterns of the self-complementary H antenna at 2.0 GHz for three cuts of  $\phi = 0^\circ$ ,  $\phi = 45^\circ$ ,  $\phi = 90^\circ$ ; (a): measurements, (b): simulations.

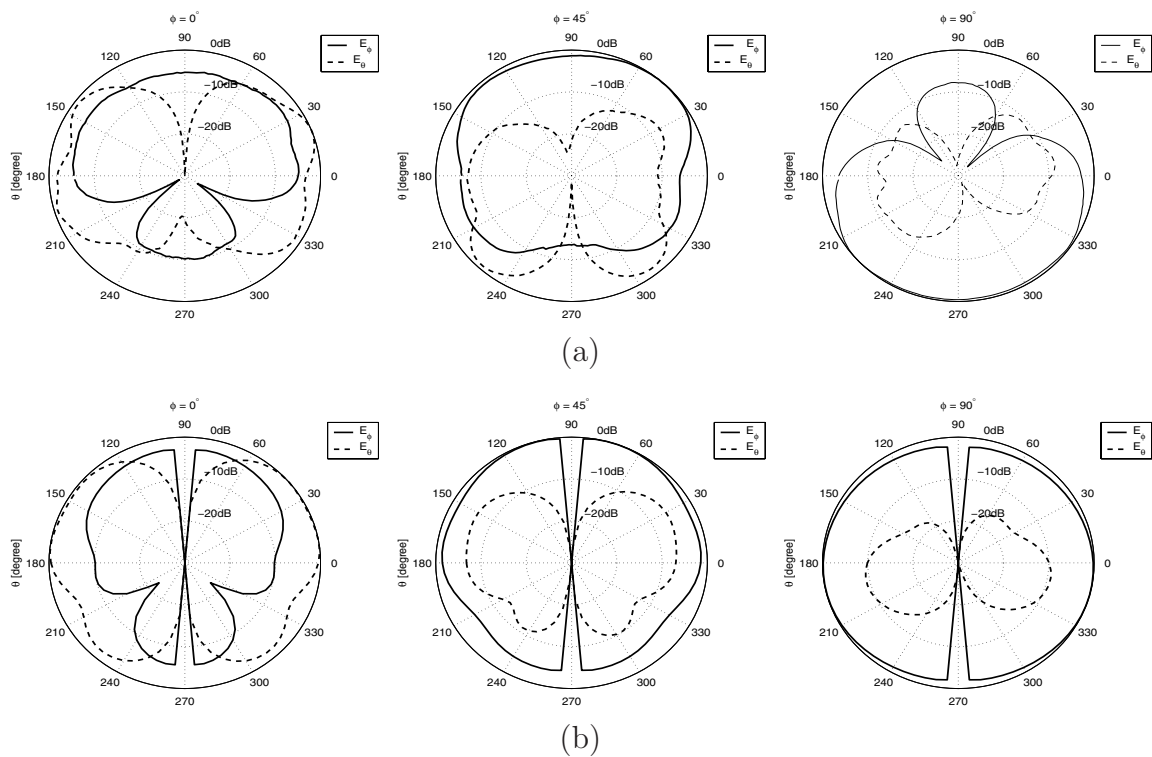


Figure 4.24: Comparison between the measured and simulated radiation patterns of the self-complementary H antenna at 2.5 GHz for three cuts of  $\phi = 0^\circ$ ,  $\phi = 45^\circ$ ,  $\phi = 90^\circ$ ; (a): measurements, (b): simulations.

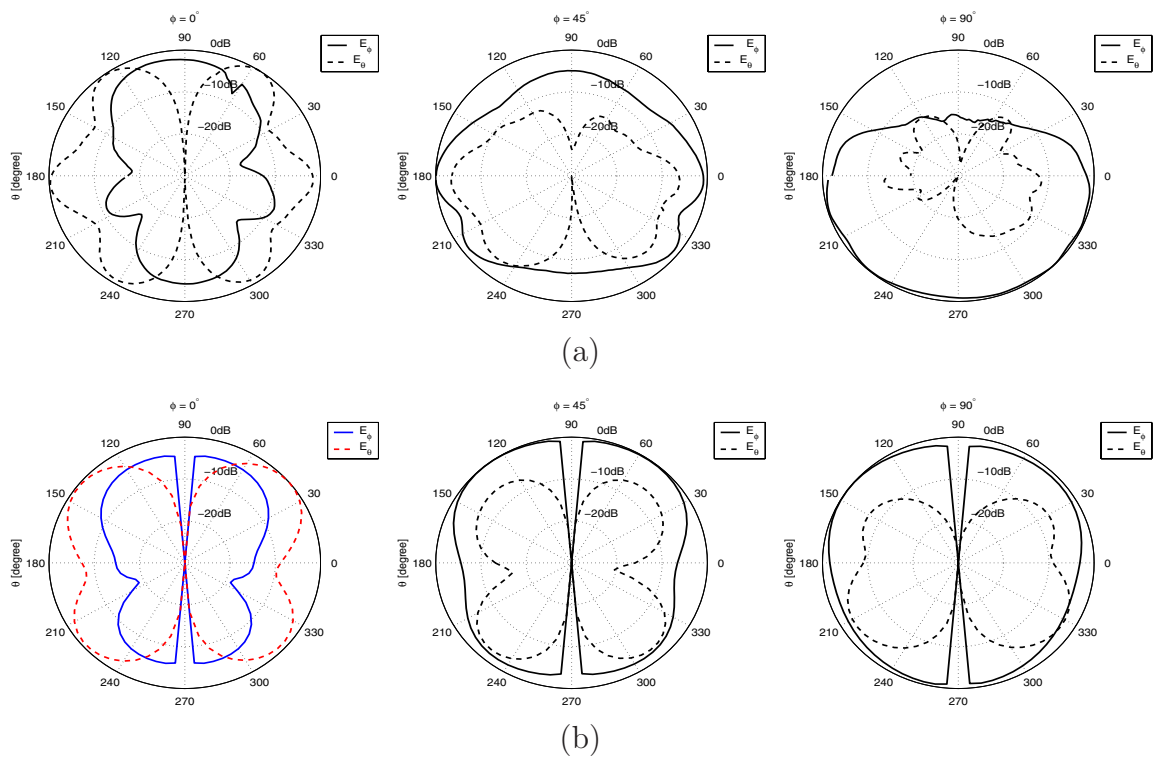


Figure 4.25: Comparison between the measured and simulated radiation patterns of the self-complementary H antenna at 3.0 GHz for three cuts of  $\phi = 0^\circ$ ,  $\phi = 45^\circ$ ,  $\phi = 90^\circ$ ; (a): measurements, (b): simulations.

$E_\phi(\theta = 90^\circ)$  is perturbed due to a weak null at  $\phi = 90^\circ$  plane. Radiation by the edges of the ground plane, dielectric, and the feeding cable are among other reasons for the observed discrepancies. Further discussion about some of these discrepancies can be found in Appendix A.

## 4.6 Conclusion

In this chapter, two methodologies to increase the bandwidth of miniaturized antennas were investigated. The first approach was to introduce the folded miniature antenna which may increase the effective aperture of the miniature antenna without compromising the size drastically, and the second approach was to take advantage of the self-complementary structures to reduce the frequency dependence of the antenna characteristics. The first approach was demonstrated through introducing miniaturized folded slot antenna that occupies a region as small as  $0.65\lambda_0 \times 0.65\lambda_0$  with the measured gain and fractional bandwidth of  $-2.7$  dBi and  $0.93\%$ , respectively. When compared with the original miniaturized topology of Chapter 3, the simulation shows a four-time decrease in the slot impedance, and over  $100\%$  increase in the simulated bandwidth, while its dimensions (relative to the wavelength) are increased by  $13\%$ . The complementary pair of this structure, that is, a miniaturized folded printed wire was also presented with a moderate bandwidth of  $0.7\%$  and a measured gain of  $-6.5$  dBi. This gain is substantially lower (about  $3.8$  dB) than its slotted counterpart. This reduction in gain indicates that slot structures are far more suitable for antenna miniaturization when a metallic platform of adequate size is available to be used as the ground plane.

The self-complementary pair of these two folded antennas is the third design presented in this chapter to exploit the wide-band characteristics of self-complementary structures. Maintaining the same dimensions, the fractional bandwidth of the self-

complementary antenna reaches to 1.1%, which exhibits at least 25% increase over its slotted and printed strip counterparts. The gain/efficiency of this antenna, as expected, falls between those of the folded slot and printed wire antennas. When miniaturization criterion is relaxed in exchange for satisfying more of the self-complementarity conditions, a much wider bandwidth can be obtained, an example of which is an H-antenna. This antenna demonstrates a very wide  $-10$  dB return loss bandwidth of 2.3:1 and a fairly constant gain of slightly above 1 dBi over the entire frequency band of operation. The dimensions of this antenna are  $0.13\lambda_0 \times 0.24\lambda_0$  at the lowest frequency of operation (1.3 GHz).

## CHAPTER 5

# RF Filter Miniaturization Using a High- $Q$ Slot-line Resonator

### 5.1 Introduction

Mobile wireless systems of various kinds, e.g., cellular phones, hand-held GPS units, and palm pilots have become an integral part of everyday life. Future expansion of the wireless market depends on the cost, size, and power efficiency of the wireless systems. These characteristics are the driving force behind substantial research efforts towards miniaturizing the RF frontend of wireless devices. High- $Q$  low insertion loss miniaturized filters, with applications in multiplexer and co-site interference suppression, are important components of the RF frontend. A few approaches in the literature address filter miniaturization, among which are the use of lumped-element filters, high-temperature super-conducting (HTS) filters, bulk acoustic-wave (BAW) filters, and slow-wave distributed resonator filters [5, 6, 7, 40].

Lumped-element filters can be made very small at lower frequencies. At higher frequencies, however, their extremely small size may result in high insertion loss and possibly low power handling capacity. To cope with the insertion loss problem, high-temperature super-conducting filters (HTS) have been proposed. BAW filters also

have exceptionally small size and fairly good performance but may be extremely expensive to develop for any new application. These two classes of filters are not further considered in this chapter, the subject of which is to introduce a new type of high- $Q$  coiled slot-line resonator with comparison to the microstrip. On the other hand, conventional distributed element filters using coupled transmission line resonators exhibit superior performance but are frequently too large.

In order to reach a compromise between size and performance, some compact architectures have been proposed. The size reduction of ordinary microstrip line resonators, for example, was made possible first by employing microstrip stepped impedance resonators (SIR) [41, 42], and then, by using hairpin-line resonators [43]. A more compact hairpin filter using split ring resonators with parallel coupled lines was later proposed [44]. This resonator is a capacitively end-loaded hairpin resonator where the loading is implemented by distributed coupled lines. The loaded hairpin resonator, together with the SIR, resulted in an improved hairpin resonator [45]. Incorporating dissimilar resonators in filter design has also been reported [45].

Another form of resonator which is similar to the above hairpin resonators utilizes square open loops [46]. To further reduce size, the open loop structure can be modified by introducing a narrow capacitive gap at the open end of the loop [47]. The same authors suggested an aperture coupled two-layer filter design using the same type of resonator [48]. Using the two sides of the substrate provides additional miniaturization. In both loaded open loop and loaded hairpin resonators, electric and magnetic coupling can be implemented, which allows for the flexible design of many structures, such as quasi-elliptic filters.

Slot-lines and coplanar waveguides (CPW) are other important configurations for the realization of resonators and filters. In the early 1970s, slot transmission lines were shown to be a practical configuration for the realization of microwave filters and couplers [49], but more attention has been devoted to CPW filters [26, 50, 51].

Also known as uniplanar configurations, slot and CPW lines are fundamental to many microwave and millimeter-wave integrated circuits [52, 53]. With regard to CPW filter miniaturization, the use of quarter-wave transmission line resonators, for example a  $\lambda/4$  CPW hairpin resonator [54], meandered super-conducting CPW filters [55], double surface CPW filters [56], and air bridge capacitive loadings have been proposed. Additionally, the periodic loading of CPW lines has been suggested to construct a slow wave transmission line and used in the fabrication of a miniature low pass filter [57].

In contrast, the literature concerning the use of slot-lines for filter design and filter miniaturization is rather scarce. The  $Q$  of slot-line resonators is higher than that of microstrip resonators of similar dimensions due to the fact that the stored energy in the resonator is confined within a larger volume, and that the electric current flows over a wider area, which translates into lower ohmic losses. Actually, slot-lines are comparable to suspended substrate strip-lines, which also have higher  $Q$  than microstrips due to the larger volume occupied by the stored energy.

In this chapter, a new class of low insertion loss miniaturized filters using slot-line resonators is proposed. Miniaturization is achieved by terminating the slot-line with a double-spiral inductive termination at both ends. Using this miniaturized resonator, both positive and negative couplings may be realized by appropriate geometric layout of the miniaturized resonators, and therefore, both standard coupled-line and cross-coupled quasi-elliptic filters are realizable. The unloaded  $Q$  of these slot-line filters is considerably higher than that of miniaturized microstrip filters of comparable dimensions due to the inherent higher  $Q$  of slot-line. To demonstrate the validity of the design procedures and the performance characteristics, two different types of filters were fabricated and tested. One is a four-pole Chebyshev filter, and the other is a quasi-elliptic filter, where in each case the full-wave simulations show very good agreement with measurements.

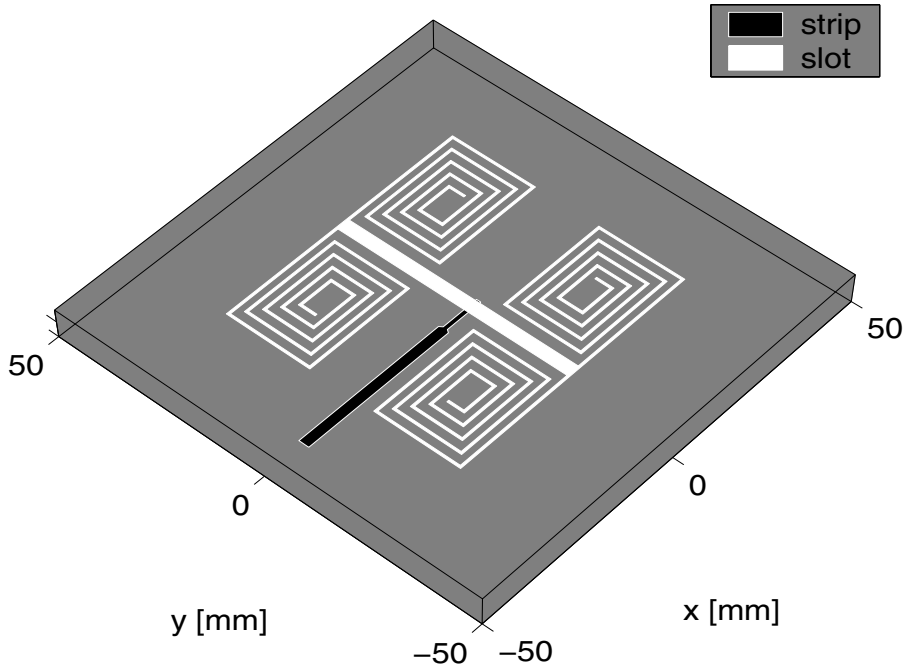


Figure 5.1: A weakly coupled miniaturized slot-line resonator at 300 MHz with symmetrical inductive loadings.

## 5.2 Miniaturized Slot-line Resonator Topology

In Chapter 3, we have demonstrated a novel and highly efficient miniaturized slot antenna using a resonant slot-line geometry for applications at VHF-UHF. The antenna miniaturization was achieved by using two balanced inductive loadings at both ends of a short radiating slot-line segment with a proper impedance matching. Figure 5.1 shows the geometry of the miniaturized slot-line resonator with symmetric inductive terminations. The very compact inductive end-loading was realized by coiling a short-circuited slot-line, with a length smaller than a quarter wavelength. Comparing the slot antenna of Fig. 5.1 with its complementary printed strip counterpart, introduced in Section 4.3, demonstrates a considerable increase in the antenna efficiency mainly due to lower ohmic losses. Thus, miniaturized slot-line resonators may be expected to exhibit higher  $Q$  than their microstrip versions.

Figure 5.2 shows the miniaturized slot-line resonator with asymmetric loading. This resonator exhibits a superior miniaturization factor and is capable of generating

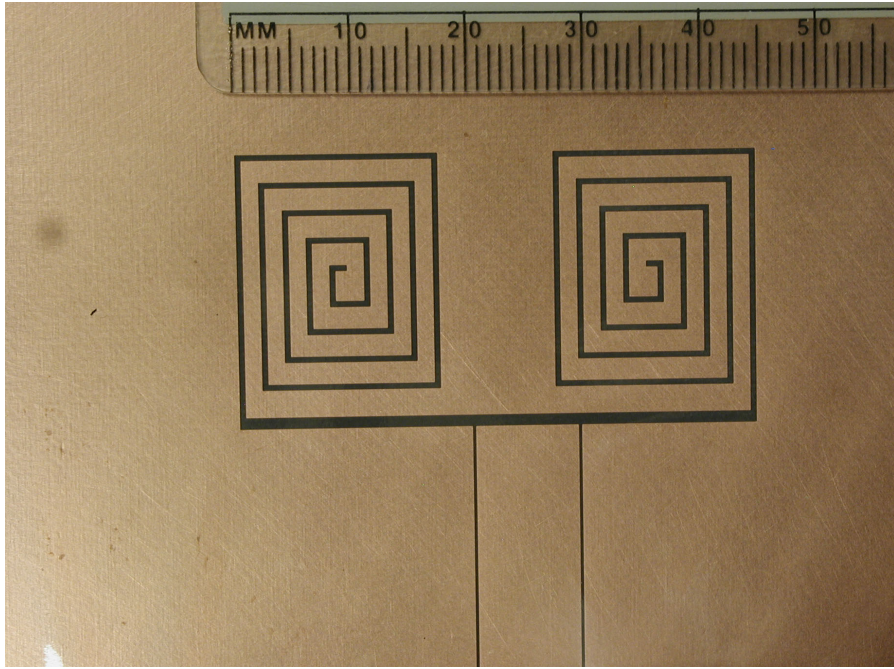


Figure 5.2: Photograph of the proposed miniaturized resonator capacitively coupled at 400 MHz with asymmetric end-loadings.

electric, magnetic, and mixed coupling mechanisms. The balanced end-loading of Fig. 5.1 is more suitable for antenna applications. For miniaturized filter applications, however, asymmetric end-loading similar to that of Fig. 5.2 may be used, leading to even more compact designs.

To assess the performance of the miniature slot-line resonators, a capacitively coupled miniaturized resonator as shown in Fig. 5.2 was fabricated on a 0.787 mm thick Duroid substrate with a dielectric constant of  $\epsilon_r = 2.2$ , and a loss tangent of  $\tan \delta = 0.0009$  [24]. The same substrate is used for the rest of the designs presented in this chapter to give direct comparisons. A low permittivity substrate was used to minimize the effects of dielectric loading on miniaturization. The resonator of Fig. 5.2 is designed to operate at 400 MHz and fits within a rectangular area of  $0.06\lambda_0 \times 0.03\lambda_0$ . The input admittance of this resonator, which is capacitively coupled to a CPW line, is measured and shown in Fig. 5.3. The unloaded  $Q$  of this resonator can be found using a single port impedance/admittance measurement technique referred to as the

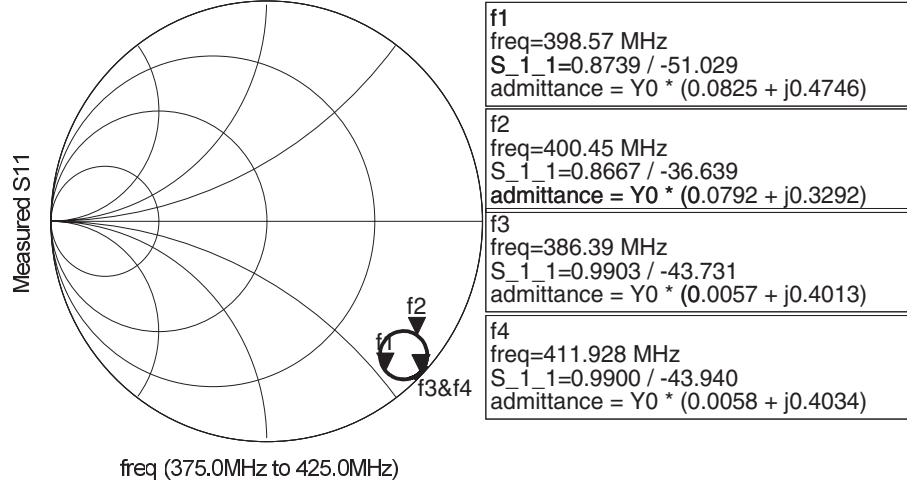


Figure 5.3: Smith chart representation of the measured input admittance of the weakly coupled miniaturized resonator at 400 MHz.

critical-point method [58]. The  $Q_0$  is expressed in terms of two *critical* frequency points,  $f_1$  and  $f_2$ , at which the input susceptance function attains its maximum and minimum, respectively. According to the critical point method, the unloaded  $Q$  can be obtained from

$$Q_0 = \frac{f_1 + f_2}{2|f_1 - f_2|} |x| \quad (5.1)$$

where

$$x^2 = \frac{(b - 2a - 1) + \sqrt{(b - 2a - 1)^2 - 4(a + b)(a - 1)}}{2(a + b)}$$

$$a = 1 + \frac{0.5 ((f_1 + f_2)^2 - 4 f_3 f_4)}{f_1 f_3 + f_2 f_3 + f_1 f_4 + f_2 f_4 + 4 f_3 f_4}$$

$$b = \left( \frac{f_4 - f_3 - \left(\frac{f_1 + f_2}{2}\right)^2 \left(\frac{1}{f_4} - \frac{1}{f_3}\right)}{2(f_1 - f_2)^2} \right)^2$$

In the above expressions for  $a$  and  $b$ ,  $f_3$  and  $f_4$  are *de-tuned crossover* frequencies at which the input admittances are identical (see Fig. 5.3). Using this technique, the unloaded  $Q$  of the miniaturized resonator at 400 MHz was measured to be  $Q_0 \approx 210$ ,

which compares favorably with the  $Q$  of miniaturized hairpin resonators [44], while being about an order of magnitude smaller in area.

Using the relationship [5]

$$Q = K b \sqrt{f} \quad (5.2)$$

where  $b$  is a linear dimension of the resonator, and  $K$  is a constant defined as a figure of merit, a better comparison can be made between miniature slot-line and microstrip resonators. For microstrip resonators,  $b$  is defined as the substrate thickness, while for the slot resonators,  $b$  represents the slot width. Invoking (5.2), the figure of merit constant  $K$  is found to be  $K = 100$  for the miniaturized hairpin resonator [44], and  $K = 330$  for the slot-line resonator of Fig. 5.2.

Table 5.1: The effect of the slot to strip width ( $s/w$ ) on the unloaded  $Q$  of the miniaturized slot-line resonators.

| $s/w$ | <i>Critical frequency</i> |             | <i>Cross-over frequency</i> |             | $f_0$<br>[GHz] | $Q_0$ |
|-------|---------------------------|-------------|-----------------------------|-------------|----------------|-------|
|       | $f_1$ [GHz]               | $f_2$ [GHz] | $f_3$ [GHz]                 | $f_4$ [GHz] |                |       |
| 0.2   | 2.3019                    | 2.2837      | 2.2581                      | 2.3750      | 2.29           | 120   |
| 0.33  | 2.3775                    | 2.3615      | 2.3307                      | 2.4282      | 2.37           | 140   |
| 0.5   | 2.4631                    | 2.4509      | 2.4162                      | 2.5125      | 2.45           | 195   |
| 1.0   | 2.6154                    | 2.6011      | 2.5604                      | 2.6658      | 2.60           | 173   |

The ohmic loss of the CPW lines and slot-lines is drastically affected by the width of the slot, or equivalently, the impedance of the line [49]. At resonance the electric current distribution on the ground plane around the slot has a higher concentration near the edges. By making the slot wider, the peak of the current at the edges is reduced and a smoother current distribution away from the slot edges is obtained. Lower current distribution at the edges translates into lower ohmic losses. In order to obtain the best  $Q_0$ , for a given resonator, the width of the slot-line may be optimized. Table 5.1 compares the unloaded  $Q$  of the proposed miniaturized resonator topology with a number of different slot-line widths (see Fig. 5.4). In this study, the overall size of the resonator is fixed while ( $s/w$ ), i.e., the ratio of the slot width ( $s$ ) to the adjacent

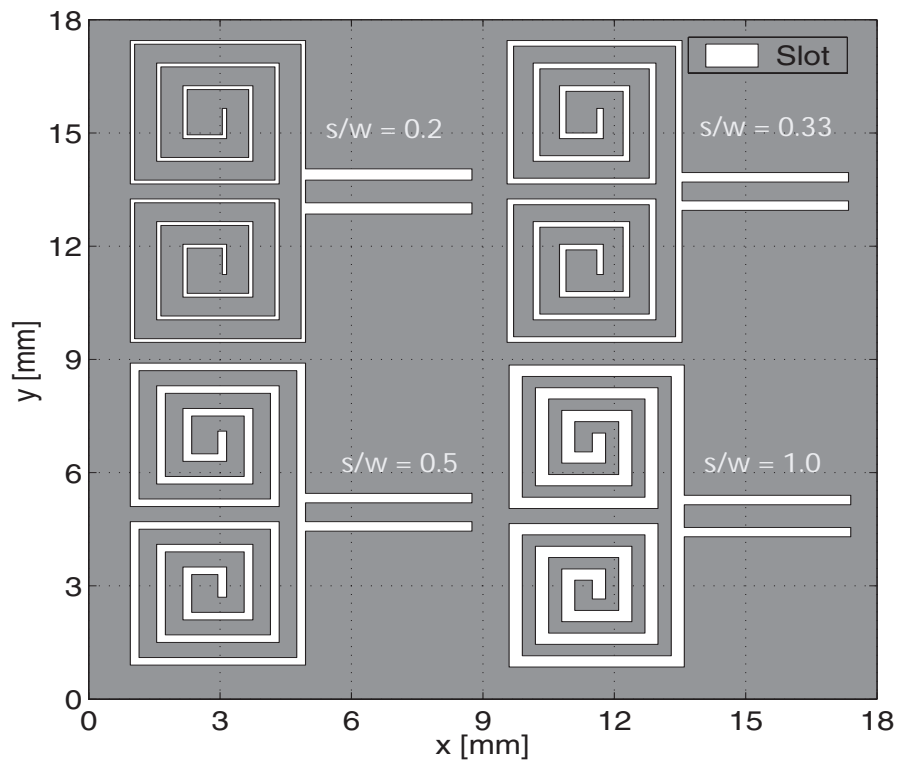


Figure 5.4: The miniaturized slot-line resonator topology with different ratios of slot to stirp width ( $s/w$ ).

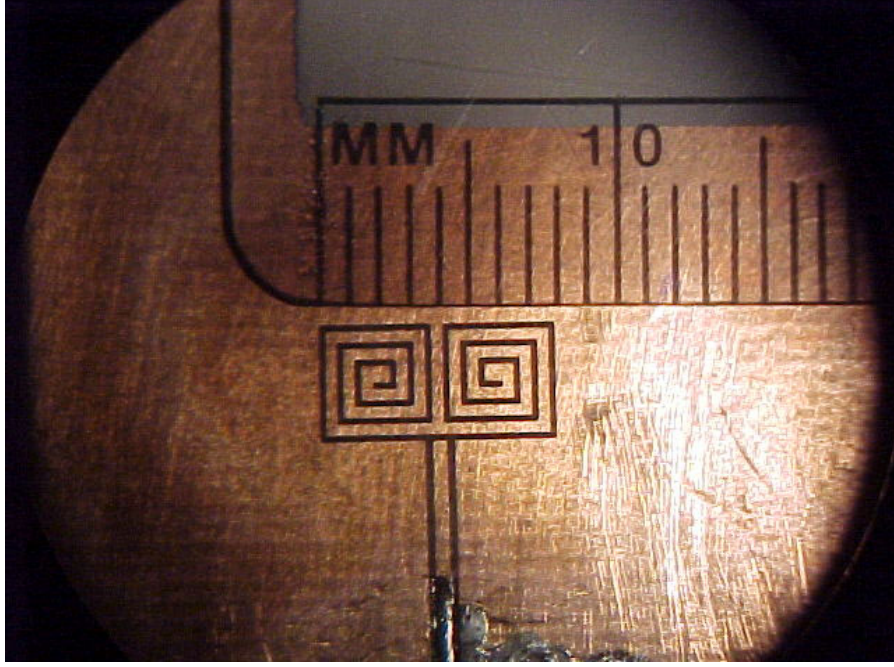


Figure 5.5: Photograph of the optimized miniature resonator at 2.45 GHz.

metallic strip width ( $w$ ), is varied as a parameter. For the proposed miniaturized double-spiral slot resonator, the width of the metallic strips should be approximately twice the width of the adjacent slots ( $s/w = 0.5$ ). Figure 5.5 shows an optimized miniaturized resonator at 2.45 GHz with approximately the same size as the previous resonator relative to the wavelength, namely  $0.03\lambda_0 \times 0.06\lambda_0$ . The unloaded  $Q$  is found to be  $Q_0 \approx 195$ . A comparison of the  $Q_0$  of this resonator with that of the scaled version of the resonator in Fig. 5.2, (shown in Table 5.1 with  $s/w = 0.2$ ), exhibits a considerable improvement due to the effect of slot-line impedance on reducing the ohmic losses of the resonator. The figure of merit constant ( $K$ ) for the optimized miniature resonator with ( $s/w = 0.5$ ) at 2.4 GHz can be obtained from (5.2) as  $K = 600$ , which is four times higher than that of a half-wave microstrip resonator.

It is worth mentioning that (5.2) indicates that the  $Q$  of a given resonator increases as  $\sqrt{f}$ . However, there is a limitation on the maximum value of the linear dimension  $b$ , which is inversely proportional to frequency. Hence, if one compares resonators having the maximum possible values of  $b$ , one can define an available  $Q$ , which decreases by

the square root of frequency.

To measure the radiation loss of the resonator, it was enclosed in a larger metallic cavity and its  $Q$  was measured to be  $Q'_0 = 265$ . Therefore, the  $Q$  due to the radiation loss can be obtained from

$$\frac{1}{Q_{rad}} = \frac{1}{Q_0} - \frac{1}{Q'_0} \quad (5.3)$$

giving  $Q_{rad} \approx 808$ . This result indicates that the  $Q$  of the resonator is dominated by the ohmic and dielectric losses.

In this section, only measurement has been used to identify the quality factor of the proposed resonators since a numerical estimate of  $Q$  for the miniaturized resonators does not provide very accurate results. For example, the finite element method (FEM) requires enormous amounts of memory and extremely small cell sizes due to the very large ratio of fine and coarse features of the structure. On the other hand, full-wave methods based on integral equations (Method of Moments) make use of the Green's Function for multi-layer structures of infinite extent. Hence, ground planes and substrates of finite size cannot be modelled efficiently. The equivalent magnetic current method, however, provides a numerically efficient approach for the simulation of slotted structures. In this approach, the tangential electric field over the slot is replaced with an equivalent magnetic current, while the field is assumed to vanish over the ground plane. This assumption implies that the ground plane is a perfect conductor, and therefore, the ohmic loss cannot be modelled in this case. Obviously, the ground plane of the slot-line resonators under study is neither a perfect conductor nor is it extended to infinity. Despite the aforementioned drawbacks of the integral equation method, such as [25], it can predict the frequency response of the filters very accurately with the exception of the insertion-loss.

## 5.3 Direct-Coupled 4-Pole Filter

To demonstrate the versatility of the proposed miniaturized resonators to design different types of filters, we begin with the design of direct-coupled bandpass filters. A bandpass filter may be characterized by a set of internally coupled resonators (not necessarily identical) all resonating at the same frequency, and an external quality factor denoting the input and output couplings. The couplings between resonator pairs and the input/output coupling are represented by  $k_{ij}$  and  $Q_{ext}$ , respectively. In what follows, the coupling architectures as well as external coupling mechanisms are investigated.

### 5.3.1 Coupling Structures

For the case of capacitively coupled miniaturized slot resonators, the resonators have a series equivalent circuit model. Figure 5.6 illustrates the equivalent circuit of two coupled miniaturized resonators exhibiting electric, magnetic, and mixed couplings all realized by impedance (K) inverter.

In order to realize the desired values for the coupling coefficients, there are different coupling configurations. In each of these configurations, the coupling coefficients may be extracted using the pole splitting method [46] in conjunction with full-wave simulations [25]. In the pole splitting method, a relationship is established between the frequency separation of the poles and the coupling coefficients, as well as the corresponding coupling capacitance or inductance in the impedance inverter. Given that  $f_u$  and  $f_l$  are the frequencies at which the  $S_{21}$  reaches its peak values, the coupling coefficients can be obtained from

$$k = \frac{f_u^2 - f_l^2}{f_u^2 + f_l^2}. \quad (5.4)$$

In the case of the pure electric or magnetic coupling whose appropriate circuit models

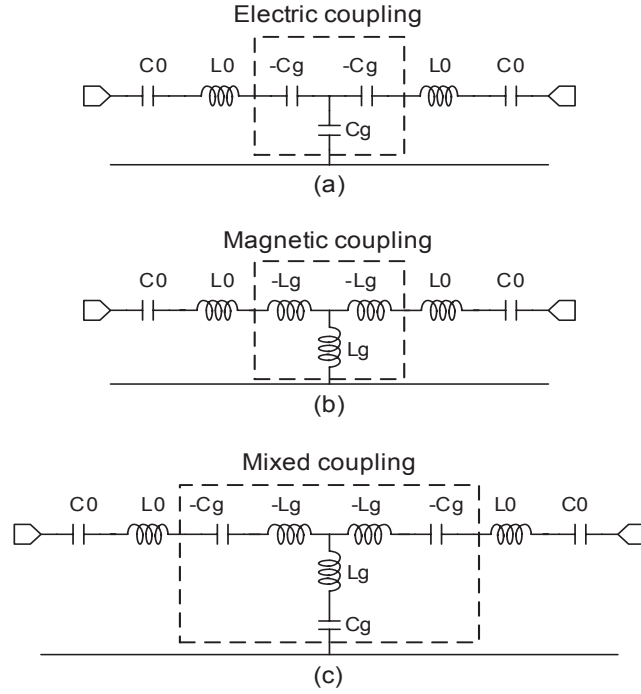


Figure 5.6: Equivalent circuit model of coupled miniaturized resonators exhibiting: (a) Electric coupling, (b) magnetic coupling, and (c) mixed coupling.

are shown in Figs. 5.6(a) and (b)

$$k_e = \frac{C_0}{C_g} \text{ (electric coupling),}$$

$$k_m = \frac{L_g}{L_0} \text{ (magnetic coupling).}$$
(5.5)

Note that in the case of electric coupling, the capacitance to ground  $C_g$  of the impedance inverter is formed by the relatively wide ground plane region of the length  $\Delta x$  between the two resonators shown in Fig. 5.7. Since the inverter impedance is  $K = 1/(\omega_0 C_g)$ , then a larger  $\Delta x$  gives a larger  $C_g$  and the inverter impedance becomes smaller. Noting that the coupling coefficient is proportional to  $K$  in the series representation [4], therefore, this is consistent with the looser coupling requirement as  $C_g$  and  $\Delta x$  increase. Note that  $C_g$  relates only to the  $K$  inverter impedance and

is unrelated to the mutual capacitance between the resonators.

Mixed coupling may also be represented by an impedance inverter as shown in Fig. 5.6(c). Since usually  $C_0 \ll C_g$  and  $L_g \ll L_0$ , the coupling coefficient for the mixed coupling can be simplified as

$$\begin{aligned} k_{em} &= \frac{L_0 C_0 - L_g C_g}{L_g C_0 - L_0 C_g} \approx \frac{L_g}{L_0} - \frac{C_0}{C_g} \\ &= k_m - k_e \end{aligned} \quad (5.6)$$

Equation (5.6) indicates that, for mixed coupling, the electric and magnetic coupling are out of phase and tend to counteract each other. Examining the mixed coupling more closely, it becomes clear that at the frequency of  $\omega_n = 1/\sqrt{L_g C_g}$ , the two resonators in Fig. 5.6(c) become decoupled, and a zero in the pass-band is introduced. For dominant electric coupling where  $k_e > k_m$ ,

$$\frac{1}{C_g \omega_0} > \omega_0 L_g \implies \omega_n > \omega_0 = \frac{1}{\sqrt{L_0 C_0}} \quad (5.7)$$

Likewise, when the magnetic coupling is dominant, the zero appears below the pass-band, that is  $\omega_n < \omega_0$ .

In order to design the first Chebyshev prototype, two different coupling configurations are investigated. These configurations are identified according to the mutual orientation of the two resonators with respect to each other. In the first coupling configuration, henceforth referred to as configuration (A), the resonators are positioned back-to-back as shown in Fig. 5.7. The coupling coefficient ( $k$ ) is calculated from (5.4) and is plotted as a function of the horizontal distance between the resonators ( $\Delta x$ ) for two different values of vertical offsets ( $\Delta y$ ). Figure 5.8 shows a face-to-face coupling arrangement and its calculated coupling coefficients, henceforth referred to as configuration (B).

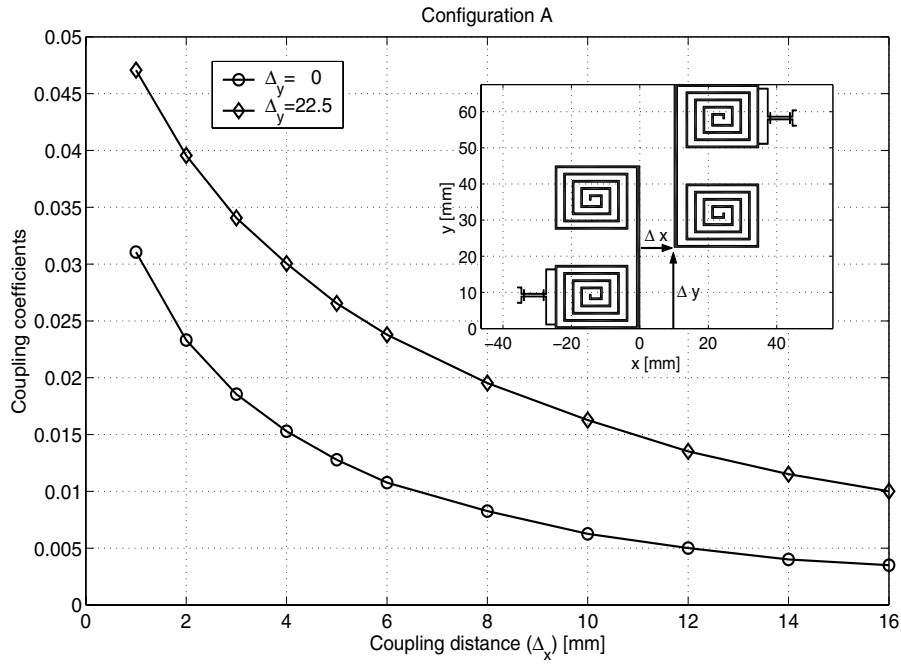


Figure 5.7: Extracted coupling coefficients for a back-to-back coupling configuration (A) as a function of the horizontal separation  $\Delta x$  for two different values of vertical offsets  $\Delta y$ .

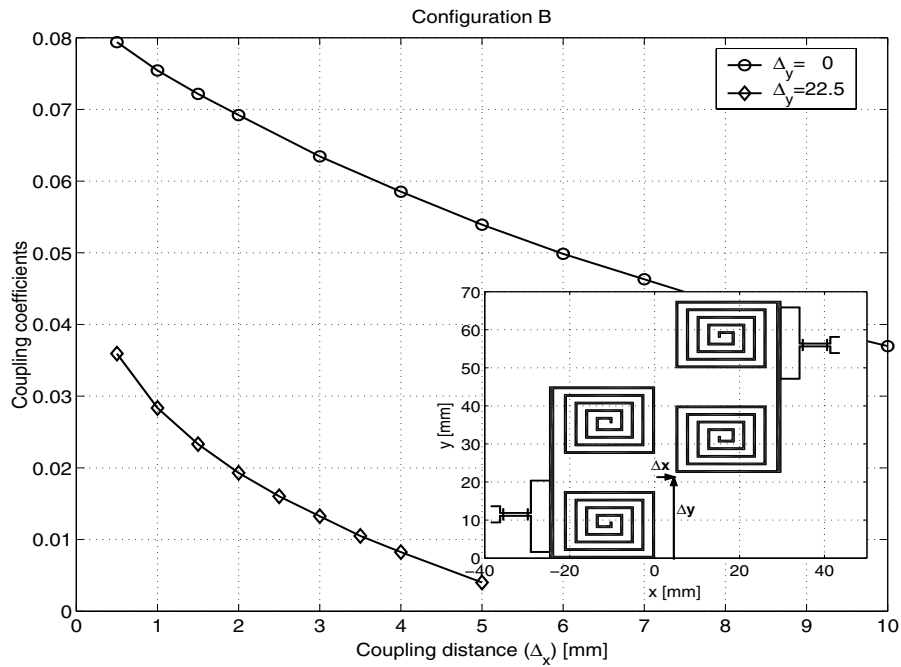


Figure 5.8: Extracted coupling coefficients for configuration (B) (face-to-face arrangement) as a function of horizontal separation  $\Delta x$  for two different values of vertical offsets  $\Delta y$ .

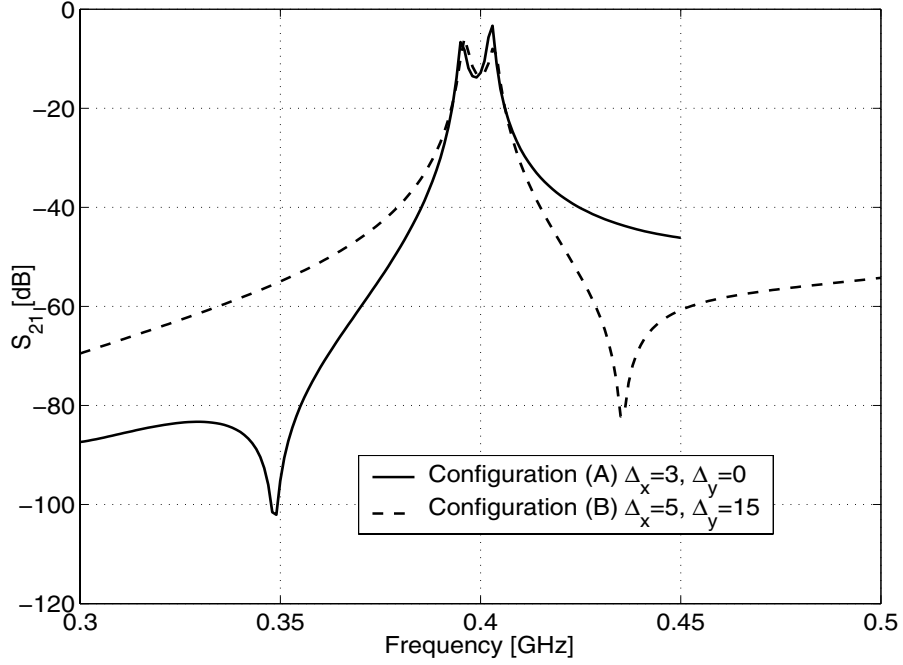


Figure 5.9: Comparison between dominantly magnetic: configuration (A), and dominantly electric: configuration (B), for the same overall coupling coefficient. (Note the locations of zeros.)

Since the proposed resonators are very compact and in close proximity to each other, the coupling mechanism is complex. The external coupling topology also has a significant effect on the nature of the couplings, and thus, each case should be studied separately. Figure 5.9 shows the pole splitting phenomenon in the  $S_{21}$  responses of the two coupling configurations. The coupling parameters for (A) were set to  $\Delta x = 3$  mm,  $\Delta y = 0$ , and for (B) to  $\Delta x = 5$  mm,  $\Delta y = 15$  mm so as to provide approximately the same coupling value. The  $S_{21}$  responses shown in Fig. 5.9 demonstrate that both structures are coupled through a mixed coupling mechanism since there is a zero in the transmission. The locations of the zeros, however, are different. For configuration (A),  $\omega_n < \omega_0$ , and thus, the magnetic coupling is dominant. For configuration (B),  $\omega_n > \omega_0$ , indicating that the electric coupling is dominant.

Considering configuration (A) and recalling the fact that the electric field distribution in a resonant slot-line is maximum at the center, electric coupling is maximized

when there is no vertical offset between the two resonators, namely  $\Delta y = 0$ . However, it is interesting to note that although the electric coupling decreases as  $\Delta y$  increases, the overall coupling increases (See Fig. 5.7.) This behavior indicates that magnetic coupling is dominant and electric coupling counteracts the effect of magnetic coupling in this configuration. This behavior is also consistent with the increasing trend of magnetic coupling as  $\Delta y$  is increased, noting that the electric current linkage (magnetic coupling) from the first resonator to the second one is increased by a factor proportional to  $\Delta y$ .

As for configuration (B), shown in Fig. 5.8, two mechanisms give rise to electric coupling. One is the direct capacitance between the input and output, and the other is obtained from the electric coupling between the adjacent coiled slot arms. Both of these electric coupling components are inversely proportional to distance ( $\Delta x$ ). Similarly, when  $\Delta y$  increases, these coupling components are reduced. Conversely, the electric current linkage (magnetic coupling) between the two resonators is increased. This argument confirms the fact that both types of couplings are present, and since the overall coupling decreases with an increase in  $\Delta y$ , the magnetic coupling is the one subtracted from the dominant electric coupling.

### 5.3.2 External Coupling

For the miniaturized slot-line resonator, both electric and magnetic external couplings can be realized. Figures 5.10 (a) and (b) illustrate input and output electric and magnetic couplings, respectively.

Electric coupling can be controlled by the value of the interdigital capacitor inserted between an input or output CPW line and the slot resonator. By changing the gap size and/or finger length of the interdigital capacitor shown in Fig. 5.10(a), a wide range of electric external coupling values can be realized. However, note that when the finger length of the capacitor is increased, the resonant slot length is in-

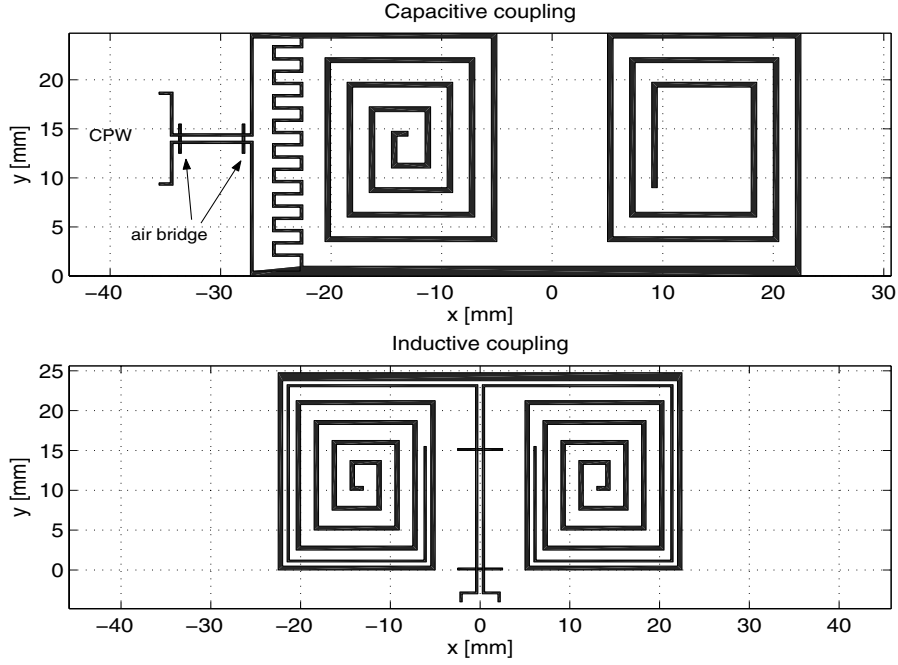


Figure 5.10: Two different methods for external coupling: (a) Electric coupling; (b) Magnetic coupling.

creased, and therefore, the resonant frequency of the structure shifts downward. To alleviate the frequency shift, the size of the resonator must be trimmed in such a way as to maintain the resonance of the structure intact, which is why one of the inductive terminations in Fig. 5.10(a) is shorter. In the case of magnetic external coupling depicted in Fig. 5.10(b), the length of the CPW coupled line extension controls the magnitude of the external coupling.

### 5.3.3 Examples

In order to demonstrate the performance of the proposed miniaturized filters, two examples are considered. In the first example, a four-pole Chebyshev filter with a fractional bandwidth of 5% and 0.25 dB ripple at 400 MHz is designed and shown in Fig. 5.11. The required coupling coefficients are  $k_{12} = k_{34} = 0.0378$ ,  $k_{23} = 0.0310$ , and the external coupling is  $Q_{ext} = 27.565$  [4]. The prescribed coupling coefficients can be realized using the design curves of Figs. 5.7 and 5.8. For this design, a fixed vertical

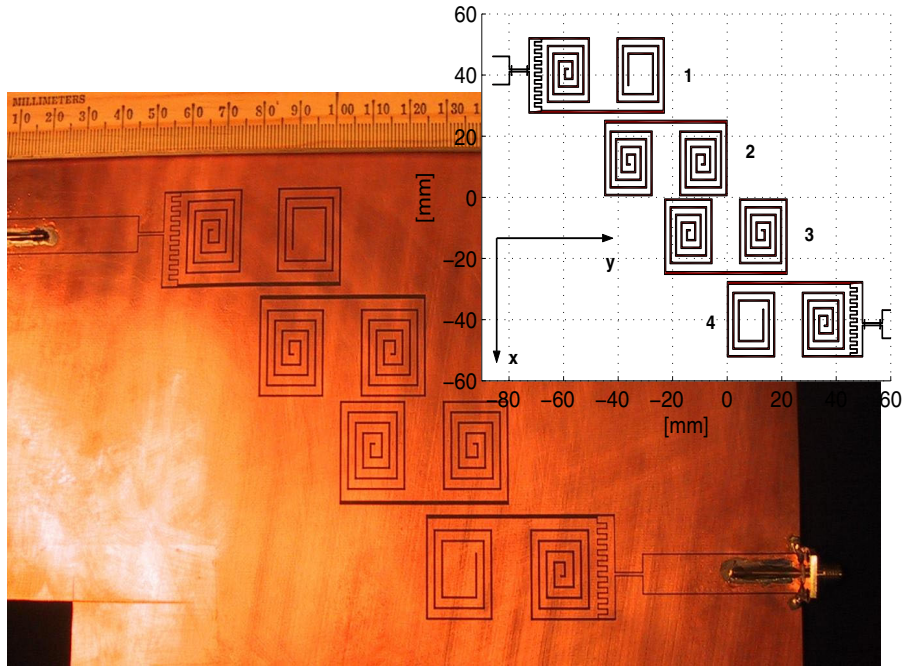


Figure 5.11: The photograph and schematic of the miniaturized four-pole Chebyshev filter at 400 MHz.

offset of  $\Delta y = 22.5$  mm was chosen in order to obtain a more realizable horizontal offset and also to ensure that non adjacent resonators do not couple to each other. The horizontal offsets in the first example are found to be  $\Delta x_{1,2} = \Delta x_{3,4} = 2.25$  mm and  $\Delta x_{2,3} = 0.85$  mm. The area occupied by this filter is  $0.22\lambda_0 \times 0.06\lambda_0 = 0.0132\lambda_0^2$ . As illustrated in Fig. 5.12, the measured response of the filter accurately follows the numerical results obtained by a full-wave Method of Moment (MoM) simulation [25].

A frequency shift of less than 0.5% occurs which can be attributed to the finite size of the ground plane, noting that in the MoM simulation an infinite ground plane is assumed. The minimum measured insertion loss for this filter is about  $-1.7$  dB, corresponding to a  $Q$  of 240. Note that the  $Q$  of a miniature microstrip filter of comparable dimensions is less than 70.

The next example considers an inductive mechanism for the external coupling of a 4-pole Chebyshev bandpass filter with 3% bandwidth. For this example, an inline resonator design ( $\Delta y = 0$ ) is used to further reduce the area occupied by the

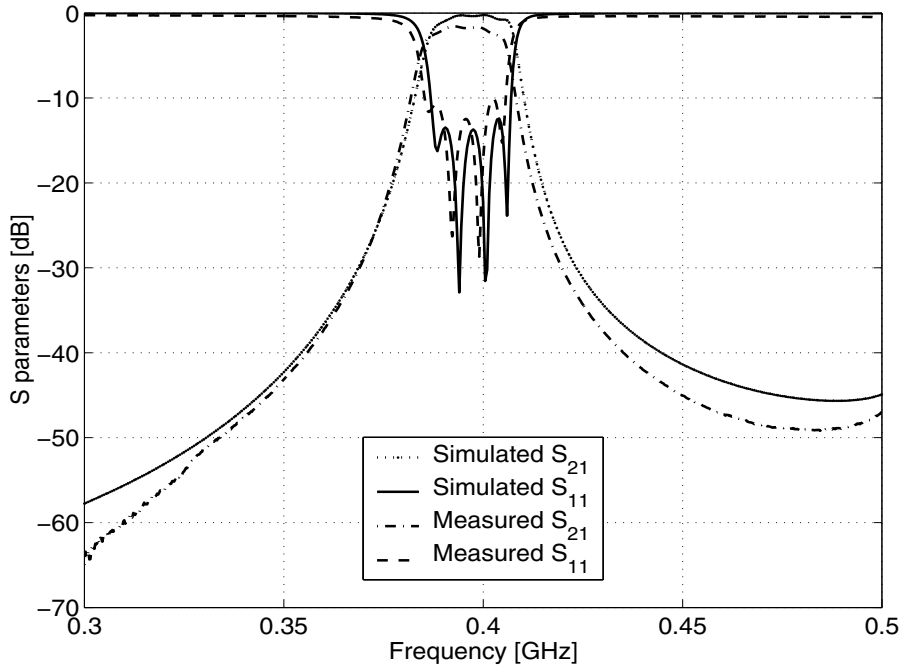


Figure 5.12: Comparison between the simulated and measured S parameters of the filter in Fig. 5.11.

filter. In configuration (B), electric coupling is dominant, thereby producing an excess coupling coefficient. If a short slot-line is inserted between two face-to-face resonators, the electric coupling can be reduced considerably, and therefore, a much smaller  $\Delta x$  is needed to achieve the prescribed coupling coefficient. Figure 5.13 shows the designed filter in which configuration (B) is modified for further compactness.

The dimensions of this filter are  $0.15\lambda_0 \times 0.06\lambda_0 = 0.009\lambda_0^2$ . The comparison between the measured and simulated responses are illustrated in Fig. 5.13. In this example, an insertion loss of  $-3.7$  dB is achieved, which corresponds to the  $Q$  of 220. Obviously, because of the modification to coupling configuration (B), the zero associated with the mixed coupling now becomes closer to the pass-band ( $\omega_n \rightarrow \omega_0$ ) and enhances the rejection in the upper band. This observed zero in the rejection band arises from a mechanism different from that of normal quasi-elliptical filters where the pass-band zeros are the results of the cancellation of multi-path signals through different resonators.

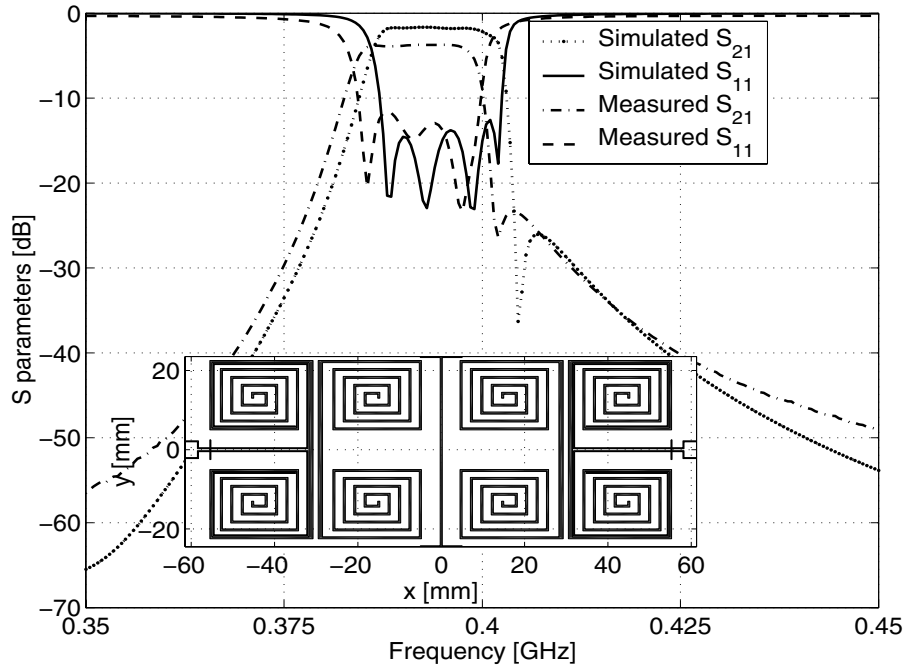


Figure 5.13: Layout of a four-pole miniaturized filter, with inline resonators at 400 MHz, as well as the comparison between its simulated and measured S parameters.

## 5.4 Cross Coupled Miniature Filters

In the RF frontend of many wireless devices, quasi-elliptic filters are commonly used because of their compactness and high selectivity. The enhanced out of band rejection of elliptic filters is due to the presence of zeros in the filter transfer function created by cross couplings [59, 60, 61]. In this section, the synthesis of a lumped-element low-pass prototype of a four-pole quasi elliptic filter is demonstrated, and then, the required coupling coefficients and external couplings are extracted. Different coupling architectures appropriate for the proposed resonator and suitable for realizing the required coupling coefficients, including negative values, will be investigated. Following a procedure similar to the one used in the previous section, a typical four-pole cross coupled filter is designed, fabricated, and tested.

Figure 5.14 shows a low-pass prototype for a four-pole cross-coupled filter with series elements. In the above,  $g_0 = 1$  represents the source and load normalized

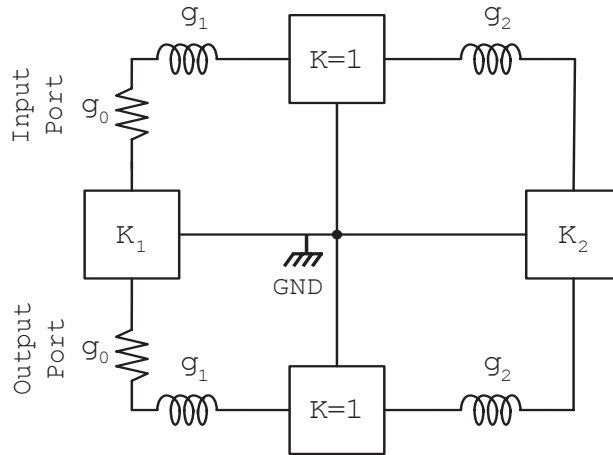


Figure 5.14: Schematic of a low-pass prototype quasi-elliptic filter with series elements.

impedances, and the remaining four unknowns are found following a synthesis procedure outlined in [60]. A low-pass prototype of a quasi elliptic filter can be described by a spectral insertion loss and a return loss function of the form given by

$$A_L = 1 + \alpha^2 f^2(s) \quad (5.8)$$

where  $\alpha$  in the insertion loss function ( $A_L$ ) is a parameter indicating the pass-band ripple, and the function  $f(s)$  can be expressed in terms of Chebyshev functions as

$$f(x) = \frac{(a + \sqrt{a^2 - 1})^2 x T_{n-1}(x) + (a - \sqrt{a^2 - 1})^2 x T_{n-3}(x) - 2a^2 T_{n-2}(x)}{2(a^2 - x^2)} \quad (5.9)$$

In the above equation,  $T_n(x)$  denotes the Chebyshev polynomial of the first kind of order  $n$ . The location of the normalized transmission zeros is characterized by  $a$ , such that the nulls take place at  $\omega_n = \omega_0[1 \pm \frac{\Delta}{2}(1 + \frac{a}{2})]$ . Figure 5.15 shows the schematics of the rational function  $f(x)$  for the case  $n = 4$ , and  $a = 2.0$ . This rational form is

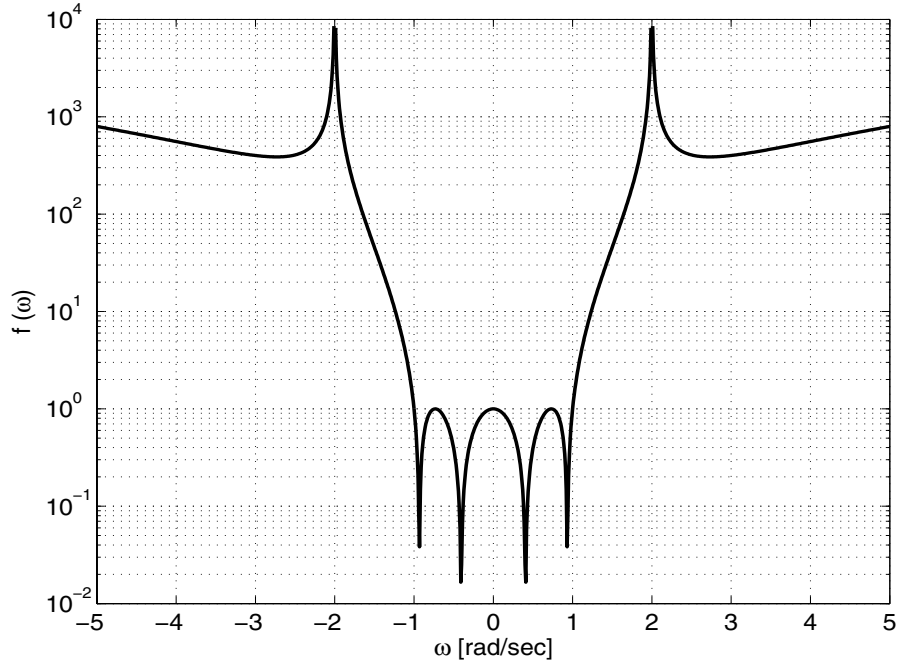


Figure 5.15: Rational function ( $f(\omega)$ ) of the fourth order ( $n = 4$ ) with single attenuation pole corresponding to a transmission zeros. This function is used as a shape function for the synthesis of the quasi elliptic filter of Fig. 5.14.

used in the exact synthesis method for shunt resonators with admittance inverters ( $J$ ) [60]. The input reflection coefficient of the low-pass prototype is derived from (5.9) as

$$\Gamma^2(s) = \frac{\alpha^2 f^2(s)}{1 + \alpha^2 f^2(s)}. \quad (5.10)$$

The driving point impedance is, therefor, given by

$$Z_{in}(s) = \frac{1 + \Gamma(s)}{1 - \Gamma(s)} \quad (5.11)$$

On the other hand, the input impedance of the low-pass prototype of Fig. 5.14 can be written as

$$\begin{aligned}
Z_{in}(s) = & \frac{1 - 2K_1K_2 + K_1^2K_2^2 + (g_2 + g_1K_2^2)s}{K_2^2 + (g_2 + g_1K_2^2)s + g_2^2s^2 + g_1g_2^2s^3} \\
& + \frac{(2g_1g_2 + g_2^2K_1^2 + g_1^2K_2^2)s^2 + g_1g_2^2s^3 + g_1^2g_2^2s^4}{K_2^2 + (g_2 + g_1K_2^2)s + g_2^2s^2 + g_1g_2^2s^3} \quad (5.12)
\end{aligned}$$

By setting the expressions for input impedance in (5.12) equal to  $Z_{in}(j\omega)$  obtained from (5.11), the exact parameters of the low-pass prototype can be found. For the following design example, a filter with a fractional bandwidth of  $\Delta = 5\%$  and pass-band ripple of  $\alpha = 0.1$  dB is considered. The transmission zero parameter is set to  $a = 2j$ , which implies the occurrence of two transmission zeros at  $\omega_n = \omega_0(1 \pm \Delta)$ . Thus, prototype elements in Fig. 5.14 are calculated using the method described in [60, 59] and found to be  $g_1 = 0.9526$ ,  $g_2 = 1.3822$ ,  $K_1 = -0.1629$ , and  $K_2 = 1.0615$ . The corresponding coupling coefficients and external coupling can, therefore, be obtained as

$$\begin{aligned}
k_{12} = k_{34} &= \frac{\Delta}{\sqrt{g_1g_2}} = 0.0436 \\
k_{23} &= K_2 \frac{\Delta}{g_2} = 0.0384 \\
k_{14} &= K_1 \frac{\Delta}{g_1} = -0.0085 \\
Q_{ext} &= \frac{g_1}{\Delta} = 19.05 \quad (5.13)
\end{aligned}$$

A few coupling configurations can be employed to realize the required coupling coefficients. Two such coupling structures, namely, configurations (A) and (B) were discussed in the previous section. Figure 5.16 shows the coupling coefficients of structure (A), computed at 2.4 GHz, as a function of resonator separation  $\Delta x$  when the vertical offset denoted by  $\Delta y$  is varied as a parameter. The nature of this coupling

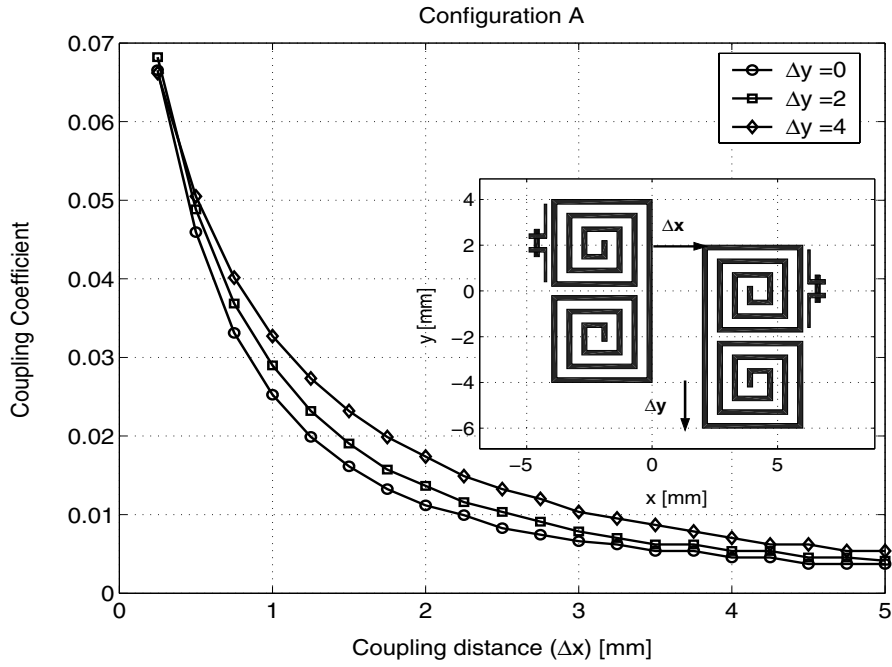


Figure 5.16: Extracted coupling coefficients for configuration (A), as a function of resonators separation  $\Delta x$  for different values of vertical offsets  $\Delta y$  at 2.4 GHz.

is, again, a dominantly magnetic mixed-coupling.

A variation of structure (B), in which a short slot-line is incised between the two resonators, was used in the second example of the previous section. In Fig. 5.9, it was shown that in structure (B) electric coupling is dominant. Again, to reduce the coupling coefficient without increasing the distance between the resonators, a slot incision is introduced between the two resonators as illustrated in Fig. 5.17. This figure also shows the pole splitting in the transfer function with the incision width  $w$  as a free parameter. In these simulations, the length of the incision is  $h = 8$  mm. As the width of the incision increases, the electric coupling between the resonators decreases, and therefore, the net coupling is reduced. In Fig. 5.17, when  $w = 1$  mm, a null appears approximately at the center frequency  $\omega_n \approx \omega_0$  which implies that the electric and magnetic couplings are equal and totally cancel each other. Also, as the incision width is increased, the frequency at which the null occurs falls below the center frequency  $\omega_n < \omega_0$ . This indicates that the dominant coupling becomes

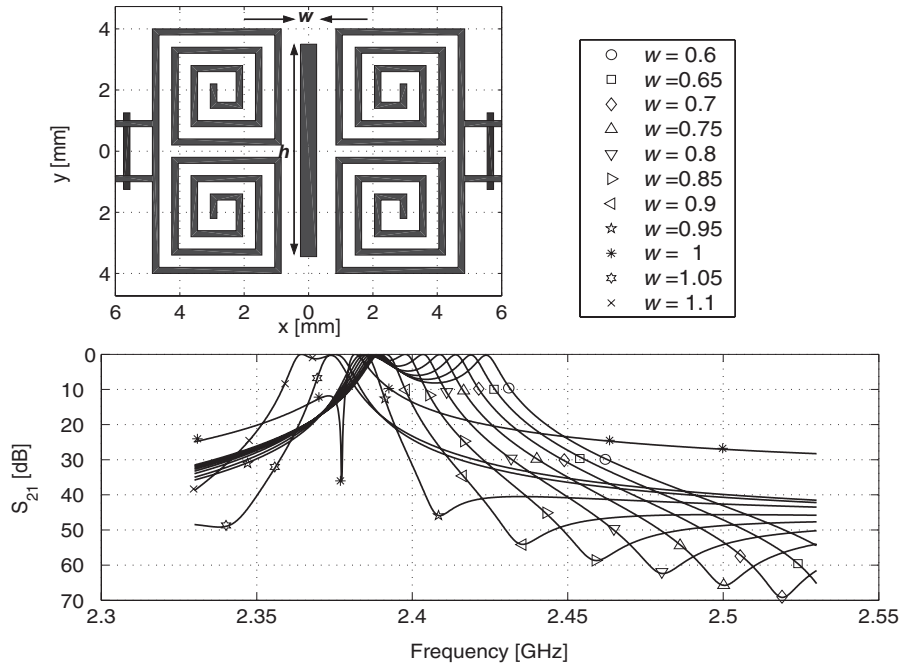


Figure 5.17: Topology of the modified coupling structure B, and the effect of the width of slot incision ( $w$ ) in the type and magnitude of coupling for the case of  $h = 8\text{mm}$ .

magnetic for larger values of incision width. Figure 5.18 illustrates the coupling coefficients of the structure shown in Fig. 5.17 versus the incision width ( $w$ ) when the incision height is varied as a free parameter. This structure, which will be referred to as modified configuration (B), provides rather small values for electric coupling (negative coupling) without sacrificing the compactness of the structure.

Finally, coupling coefficients for configuration (C) are shown in Fig. 5.19 as a function of the horizontal offset ( $\Delta x$ ) with the vertical distance  $\Delta y$  used as a parameter. This configuration is similar to the two previous structures with the exception that the offset parameters are much larger. This structure exhibits a dominantly magnetic coupling. Defining dominantly magnetic coupling by convention as positive coupling, and electric coupling as negative coupling, all the coupling coefficients as required by (5.13) to synthesize a quasi elliptic filter can be realized.

Figure 5.20 shows the layout and a photograph of this filter where the distances between the resonators have been chosen in accordance with the simulated coupling

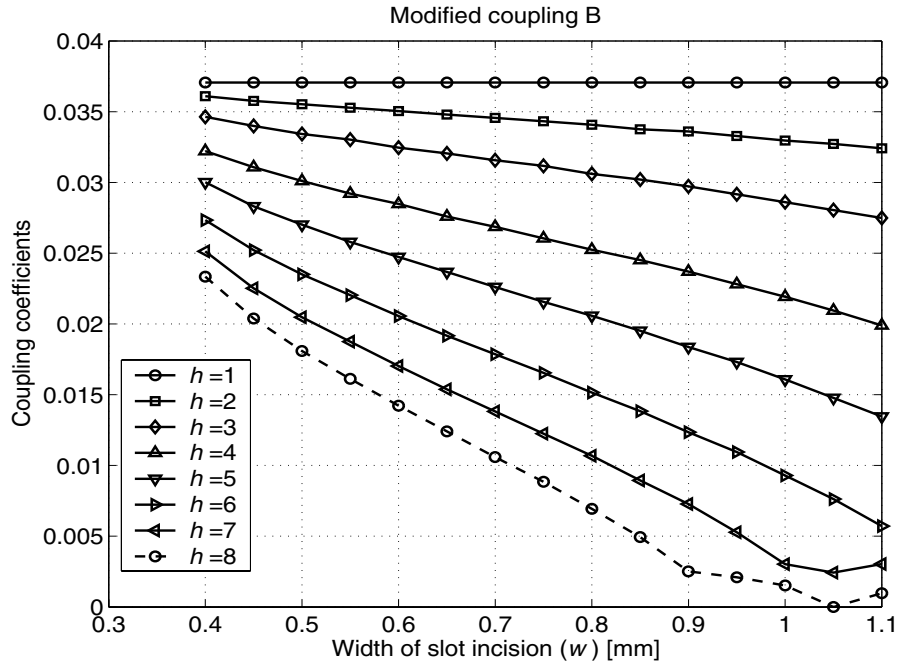


Figure 5.18: Extracted coupling coefficients for the coupling configuration shown in Fig. 5.17, as a function of incision width and height (in millimeter), at 2.4 GHz.

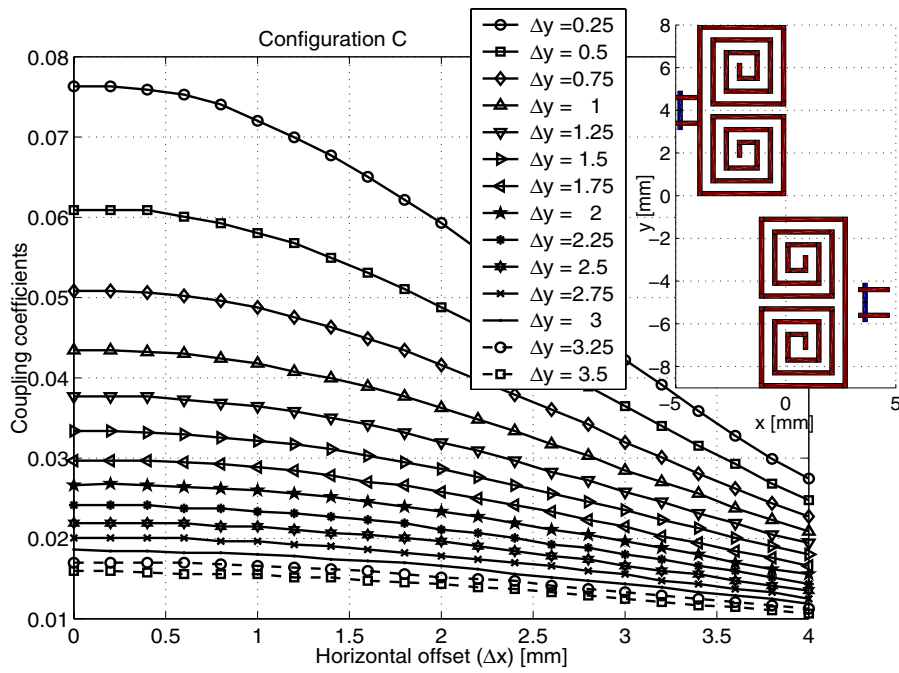


Figure 5.19: Extracted coupling coefficients for coupling configuration (C), as a function of the horizontal offset between the resonators  $\Delta x$  for different values of vertical distances  $\Delta y$  at 2.4 GHz.

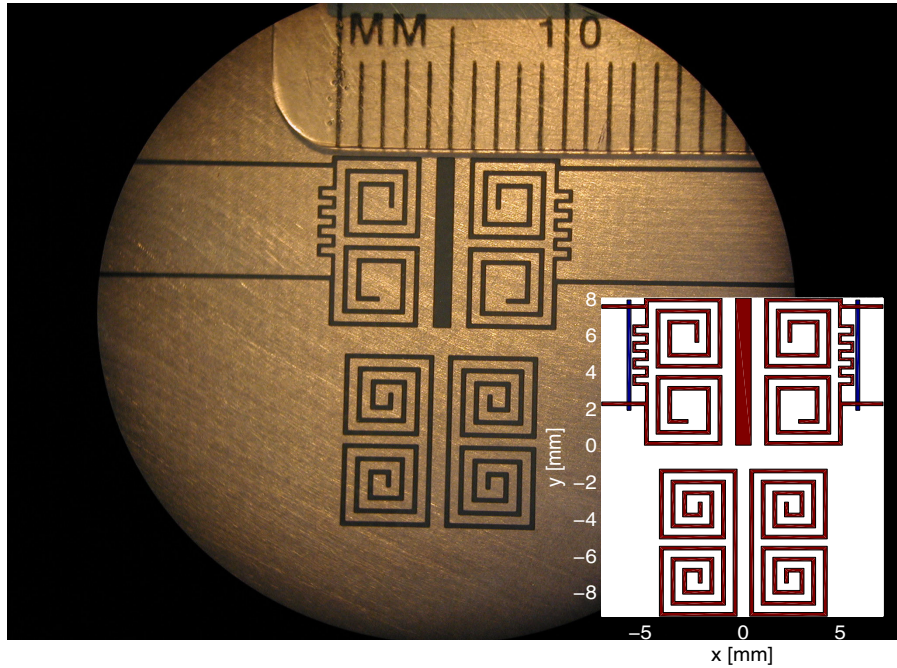


Figure 5.20: Photograph and schematic layout of a miniaturized quasi elliptic filter at 2.4 GHz with dimensions of  $0.09\lambda_0 \times 0.14\lambda_0$ .

coefficients of different coupling configurations. This four-pole filter occupies an area as small as  $0.09\lambda_0 \times 0.14\lambda_0$ , while having an insertion loss of about 2.0 dB corresponding to the  $Q$  of 180. The  $Q$  of a straight half-wave microstrip resonator is about 170 but becomes much smaller when coiled. The simulated and measured responses are illustrated in Fig. 5.21, where very good agreement between the measurement and full-wave simulation is observed.

The locations of transmission zeros in the measurement, however, are not as predicted using the lumped-element prototype of Fig. 5.14. The asymmetry observed in the location of the transmission zeros can be attributed to the frequency dependence of the coupling coefficients [48]. The impedance inverter models, used in the low-pass prototype, assume a frequency independent coupling, whereas the electric and magnetic couplings are frequency dependent in nature. In quasi elliptic filters where both types of electric and magnetic couplings with opposite frequency dependence are present, the location of transmission zeroes can be shifted considerably. More impor-

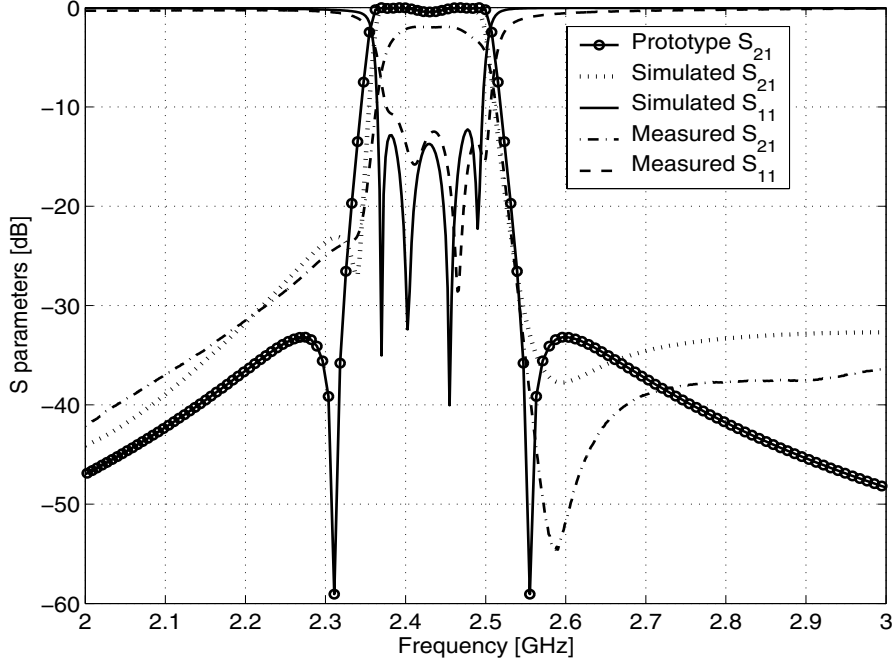


Figure 5.21: Comparison between the lumped-element prototype, full-wave simulated, and measured S parameters of the quasi elliptic filter of Fig.5.20.

tantly, in the proposed miniaturized design, the cross coupling term, which controls the transmission zeros, is realized by subtracting two out-of-phase components of magnetic and electric couplings having different frequency dependence, resulting in an overall cross-coupling with a strong frequency dependence.

Figure 5.22 shows the equivalent circuit of the normalized filter shown in Fig. 5.20, where the cross-coupling is realized by a dominantly electric mixed-coupling. To ensure the proper value for the cross-coupling according to (5.13), the difference between the electric and magnetic coupling has to be equal to  $k_{14}$ , that is,  $k_{14} = k_e - k_m = \frac{1}{C_{14}\omega_0} - L_{14}\omega_0$ . Let  $\eta = \frac{k_m}{k_e} < 1$  be the ratio of the magnetic component of the cross-coupling term to its electric component. Based on this definition, the value of the cross-coupling elements can be defined as  $C_{14} = \frac{1-\eta}{k_{14}}$ ,  $L_{14} = \frac{\eta k_{14}}{1-\eta}$ . Figure 5.23 plots  $S_{21}$  of the equivalent circuit shown in Fig. 5.22 for different values of  $\eta$  while keeping the net magnitude of the cross-coupling constant, namely,  $k_{14} = 0.0085$ . As seen in Fig. 5.23, the location of the transmission zero shifts when  $\eta$  is increased. The

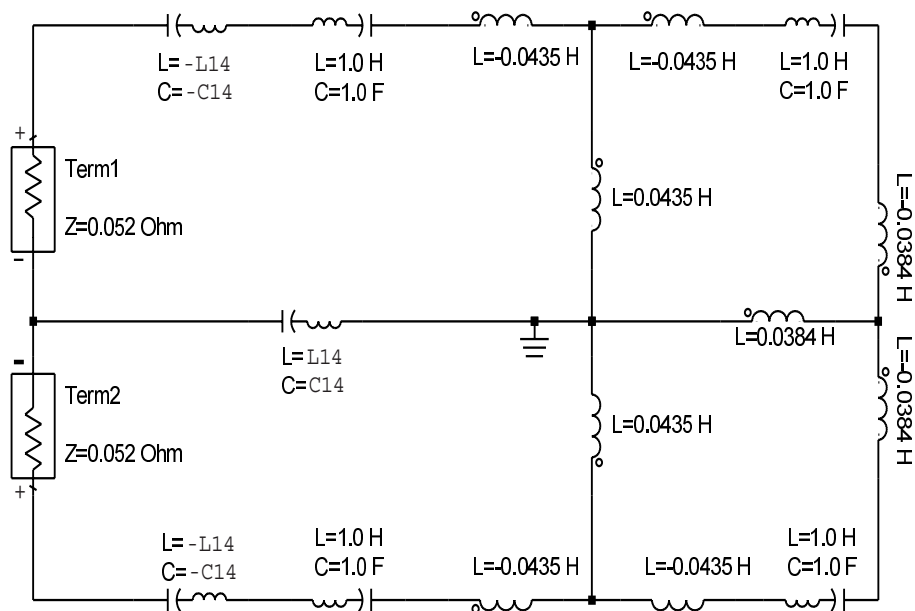


Figure 5.22: The lumped-element prototype of a normalized quasi-elliptic bandpass filter in which, the cross-coupling term  $k_{14}$  is realized by a mixed coupling where the difference between the two electric and magnetic coupling components is constant.

increase in  $\eta$ , while the overall cross-coupling term is fixed, indicates that a larger portion of the electric component of the cross-coupling is cancelled by an out-of-phase magnetic component. Obviously, the proper cancellation only takes place at the center frequency, but since the cross-coupling is frequency dependent, the coupling is more than required at frequencies above the pass-band and less below the pass-band. In order to alleviate the observed asymmetry in the location of transmission zeros and rejection band ripples, one might try to reduce  $\eta$ , which implies a smaller cancellation of the out-of-phase electric and magnetic couplings while maintaining the same value of  $k_{14}$ . As mentioned earlier, the required cross-coupling term needs to be rather small and can be realized by introducing a mixed electric-magnetic coupling in which the electric and magnetic couplings cancel each other out. To reduce the cancellation, and at the same time have the cross-coupling term remain intact, the absolute value of the electric coupling should be reduced using via-holes in the slot incision and/or

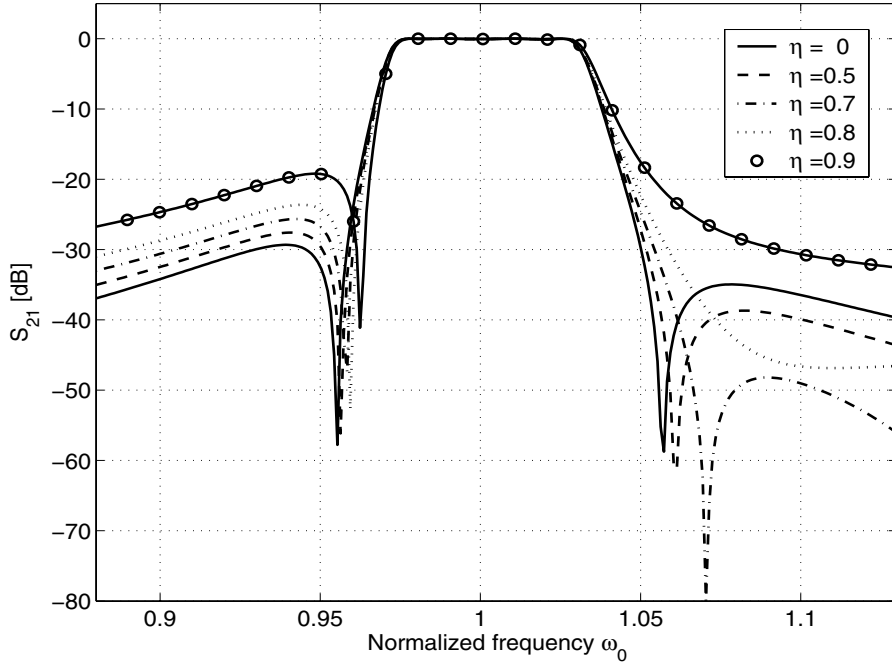


Figure 5.23: The variation of the location of transmission zeroes of a normalized quasi elliptic filter of Fig. 5.20 for different values of the ratio of the magnetic component to the electric component of the cross-coupling term  $\eta = k_m/k_e$ , given that  $k_{14} = k_e - k_m$ .

increasing the vertical offset between the first and last resonators.

## 5.5 Conclusions

A new class of slot-line resonators for applications in miniaturized filter design are demonstrated. The slot-line resonator offers flexibility of different coupling mechanisms facilitating various compact filter designs. It is shown that the resonators may be further miniaturized by increasing the value of the inductive loading through increasing the number of turns in the coiled terminations, with a moderate decrease in the resonator  $Q$  factor. The unloaded  $Q$  is higher than that of miniaturized microstrip filters of similar volume.

Both electric and magnetic couplings were demonstrated simply by positioning two such miniaturized resonators in different arrangements with respect to each other. A

straightforward method was given to determine whether the coupling mechanism is magnetic or electric. A full-wave analysis was used to extract the coupling coefficients used in the filter design.

To demonstrate the validity of the approach, three examples were studied including two four-pole Chebyshev filters, one of which used a mixed coupling structure, and a four-pole quasi elliptic filter. The agreement between the simulated and measured responses of these filters was shown to be excellent.

The prototype Chebyshev filters at 400 MHz with fractional bandwidths of 5% and 3% show insertion loss values of about 1.7 dB, and 3.7 dB, while occupying a very small rectangular area of  $0.22\lambda_0 \times 0.06\lambda_0$ , and  $0.15\lambda_0 \times 0.06\lambda_0$ , respectively. The unloaded  $Q$  of these filters is about three times greater than those of their microstrip counterparts.

A four-pole quasi-elliptic filter with  $\Delta = 5\%$  at 2.4 GHz was also fabricated, and its measured response was compared with numerical simulation. This filter with an improved out of band rejection gives 2 dB insertion loss while occupying a very small area of about  $0.09\lambda_0 \times 0.14\lambda_0$ . The effect of the frequency dependent cross-coupling on the quasi-elliptic filter was also investigated and shown to delineate the asymmetry in the rejection band and transmission zeroes.

## CHAPTER 6

# RCS Measurement Technique to Extract the Input Impedance of High-Impedance Miniaturized Slot Antennas

### 6.1 Introduction

In the wake of recent interests in micro- and nano-technologies, there is an ongoing effort towards the application of these emerging technologies in the fabrication of different devices, components, and circuits. One severe concern in dealing with such devices is their high impedance –due to their extremely small size– rendering them very difficult to test and characterize. The difference between the impedance level of nano-devices and that of standard RF and microwave components is so immense that makes any kind of matching network prohibitively lossy, and thus, impractical.

MEMS resonators/filters are an example of very high-impedance microsystems ( $10\text{ K}\Omega - 20\text{ K}\Omega$ ). Therefore, they require high-impedance antennas and RF circuits to be integrated with in order for them to be utilized for wireless and sensor network applications.

The interest in high-impedance components is not restricted to micro and nano applications. High-impedance components may find some applications in other areas,

such as electronics. Although electronic devices are traditionally sought for operation with  $50\ \Omega$  systems, they can be made high-impedance to reduce the transceiver power. For example, in the MOSFET design, the size of the gate is increased to accommodate for matchable impedances to a  $50\ \Omega$  line. By reducing the gate size, the impedance increases, which in turn reduces the power consumption drastically. Given that a high-impedance antenna is available, the impedance of the electronic devices can be reduced to obtain a minimum power, without any need for additional matching networks.

In response to aforementioned needs, significant effort has been devoted to design a high-impedance miniature antenna by modifying the miniaturized slot antenna presented in Chapter 3. Remembering from Chapters 3, and 4, miniaturization reduces the physical aperture and the radiation conductance of the antenna. This effect can be exploited to yield a high-impedance antenna. One of the main challenges of high-impedance antennas, as well as any other high-impedance RF circuit, is the measurement of very high impedances. High-impedance measurement becomes intractable at higher frequencies using currently available microwave measurement instruments since they are designed for standard  $50\ \Omega$  line. The standard impedance is adopted because it is an optimal point where a low conduction loss with reasonable transmission line dimensions can be achieved. In practice, the impedance of a microwave transmission line cannot go beyond  $80\ \Omega - 90\ \Omega$ ; even so, they become very lossy and start to radiate as the frequency increases.

The main objective of this chapter is to demonstrate that the miniaturized slot antennas, which were presented in this thesis, can exhibit a very high radiation resistance on the order of a few kilo-ohms. At lower region of microwave frequency up to about 3 GHz, high impedances can be measured using the RF Impedance/Material Analyzer.<sup>1</sup> The impedance analyzer is used to measure the input impedance of a

---

<sup>1</sup>Agilent E4991A RF Impedance/Material Analyzer.

prototype miniature slot antenna at UHF. This instrument, however, cannot be used for frequencies higher than 3 GHz, and thus, an alternative technique is required.

For higher frequencies, a novel technique to measure the input impedance of generally high-impedance miniaturized slot/aperture antennas are introduced whereby a relationship is established between the RCS of a slot/aperture antenna to its terminating impedance/conductance. Then, the necessary condition of the RCS that must be satisfied when the receiving antenna is terminated by a matched load is derived and used to identify the corresponding RCS. Examining the RCS of the loaded antenna against the criteria provided by the proposed method can determine whether the receiving antenna is matched or not. If not, one can change the termination resistance till the required conditions on the RCS are met, and then, identify the matched load, which is equal to the impedance of the antenna at resonance.

## 6.2 Methodology

In order to establish a relationship between the RCS of a slot/aperture antenna and its load impedance, first a resonant half-wave slot antenna is considered. Although the center-fed slot antenna is not so high-impedance as of MEMS or nano-devices, its impedance is on around  $500\ \Omega$ , which is still an order of magnitude larger than that of a standard transmission line. Furthermore, its radiated and scattered fields can be analytically calculated using Babinet's principle and Bookers' relation [62, 37].

Consider an infinite perfectly electric conducting (PEC) screen with a narrow half-wavelength aperture, and its complimentary structure consisting of a thin strip of PEC as displayed in Fig. 6.1(a) and (b), respectively. Figure 6.1(c) shows a thin perfectly magnetic conducting (PMC) strip of the same size as the PEC strip of Fig. 6.1(b). The objective of the proposed measurement technique is to infer the impedance of the

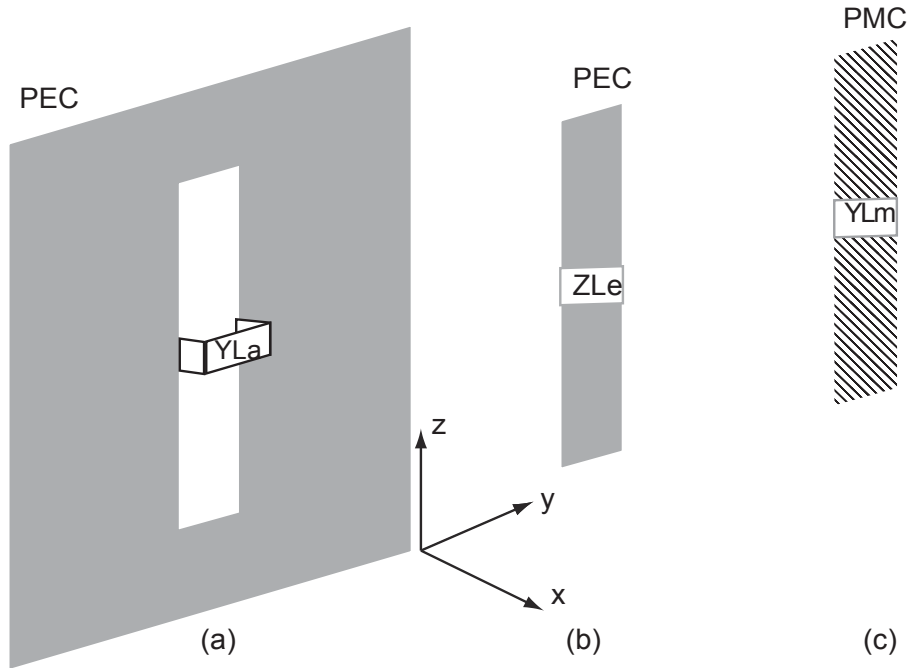


Figure 6.1: Illustration of Babinet's principle for three receiving antennas (a): an aperture antenna in a PEC screen, (b): the complimentary PEC strip, (c): the dual case of PMC strip.

aperture antenna from its measured RCS. First, we need to calculate the RCS of the aperture antenna of Fig. 6.1(a) as a function of the load admittance of the aperture ( $Y_{La}$ ). Note that the scattering from the aperture antenna has two components: 1) the reflection from an often large PEC plate, and 2) the scattering from the aperture itself. The scattering from the plate can be much larger than the perturbation introduced by the slot, and it may supersede the perturbation introduced by the aperture and reduce the sensitivity of the measurements. The effect of the ground plane, however, can be calculated analytically, and then, subtracted from the total scattered fields. This approach resembles the coherent subtraction in the radar measurement experiment.

In the view of duality principle, on one hand the scattered field of an electric dipole is equal to the scattering from a PMC dipole. On the other hand, diffracted fields by a slot/aperture can be related to the scattered fields by an electric dipole through Babinet's principle [63]. This means that the contribution of the slot/aperture in the

total scattered field from a slot antenna can be calculated analytically.

## 6.3 Formulation

In this section, we seek an analytical formulation of electromagnetic scattering from three different receiving antenna structures depicted in Fig. 6.1.

### 6.3.1 Scattering from an Electric-Dipole Antenna

Figure 6.1(b) shows the electric dipole antenna illuminated by a plane wave propagating along the  $-\hat{x}$  direction of the form:

$$\bar{E}^i = \hat{z}E_0e^{jkx} \quad (6.1)$$

Using the reciprocity theorem, the scattered fields of the received antenna is reciprocal to the radiated fields of the same antenna in the transmit mode. Therefore, the formulation for the radiation pattern of a half-wavelength dipole antenna can be used to obtain the scattered field of a resonant electric dipole [34]; that is,

$$E_\theta \simeq j\eta \frac{I_{in}e^{-jkr}}{2\pi r} \frac{\cos(\frac{\pi}{2} \cos \theta)}{\sin \theta} \quad (6.2)$$

An antenna in the receive mode is used to intercept electromagnetic waves and to extract power from them. For any antenna, the effective length can be defined [34]. The effective length is a vector quantity to determine the induced open-circuit voltage of the antenna when antenna is illuminated by electromagnetic waves. This parameter is basically defined in accordance with Faraday's Law, wherein the open-circuit voltage is defined as  $v_{oc} = \oint \bar{E} \cdot d\bar{\ell}$ . Note that the effective length is related to the far-field of the antenna, and given by [34, 64]

$$\bar{E}_a = \hat{a}_\theta E_\theta + \hat{a}_\phi E_\phi = -j\eta \frac{kI_{in}}{4\pi r} \bar{\ell}_{eff} e^{-jkr} \quad (6.3)$$

Based on the definition of the effective length, the open-circuit voltage of an antenna in the receive mode is related to the incident wave and the effective length of the antenna using

$$V_{oc} = \bar{E}^i \cdot \bar{\ell}_{eff}. \quad (6.4)$$

In a case where the incident wave is assumed to impinge on the antenna from the direction of the maximum gain, namely,  $\theta = 90^\circ$ , invoking (6.4) gives the open-circuit voltage of the resonant electric dipole as

$$V_{oc} = 2 \frac{E_0}{k} \quad (6.5)$$

Thus, the current at the input terminal of the antenna as a function of the load is found to be

$$I_{in}(Z_L) = \frac{2E_0/k}{Z_{ant} + Z_L} \quad (6.6)$$

In the above,  $Z_{ant}$  and  $Z_L$  stand for the input impedance of the antenna and the load impedance, respectively. Substituting the input current from (6.6) in (6.2) gives an expression for the scattered field of a resonant electric dipole at the broad side as

$$\bar{E}_e^s = j\eta \frac{2E_0/k}{Z_e + Z_{Le}} \frac{e^{-jkr}}{2\pi r} \quad (6.7)$$

The radar cross-section of the electric dipole in the peak direction ( $\theta = 90^\circ$ ) is, therefore, calculated to be

$$\sigma_e = 4\pi R^2 \left| \frac{E^s}{E^i} \right|^2 = \frac{4\eta^2}{\pi k^2 |Z_e + Z_{Le}|^2} \quad (6.8)$$

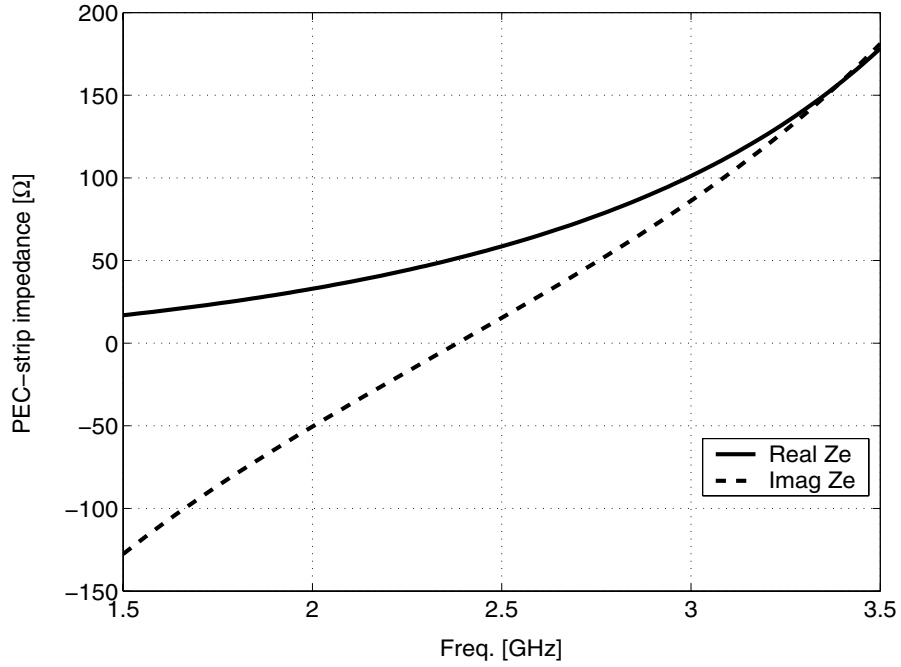


Figure 6.2: The input impedance of the PEC strip ( $Z_e$ ) with  $\ell=55$  mm around its first resonance.

Equation (6.8) suggests that the RCS would be maximum when  $Z_{Le} = 0$ . When the load resistance is equal to the input impedance of the antenna at resonance, the RCS reduces by a factor of four ( $-6$  dB) compared to its peak for the short-circuit load.

Figure 6.2 illustrates the input impedance of the printed electric dipole of Fig. 6.1(b), with a length of  $\ell = 55$  mm. As indicated by Fig. 6.2, this antenna resonates at 2.5 GHz, where the input impedance is a real quantity with the value of  $Z_e = 50 \Omega$ . The radar cross-section of this antenna, in the plane of the maximum gain at  $\theta = 0^\circ$ , has been calculated using (6.8) and plotted in Fig. 6.3 with the terminating impedance as a varying parameter. As seen in this figure, the RCS of the short-circuited antenna has the highest peak at the first resonance, and it gradually decreases when the value of the load impedance increases. When the load and antenna impedances are equal, the maximum RCS is 6 dB lower than that of the maximum RCS corresponding to the short-circuit termination.

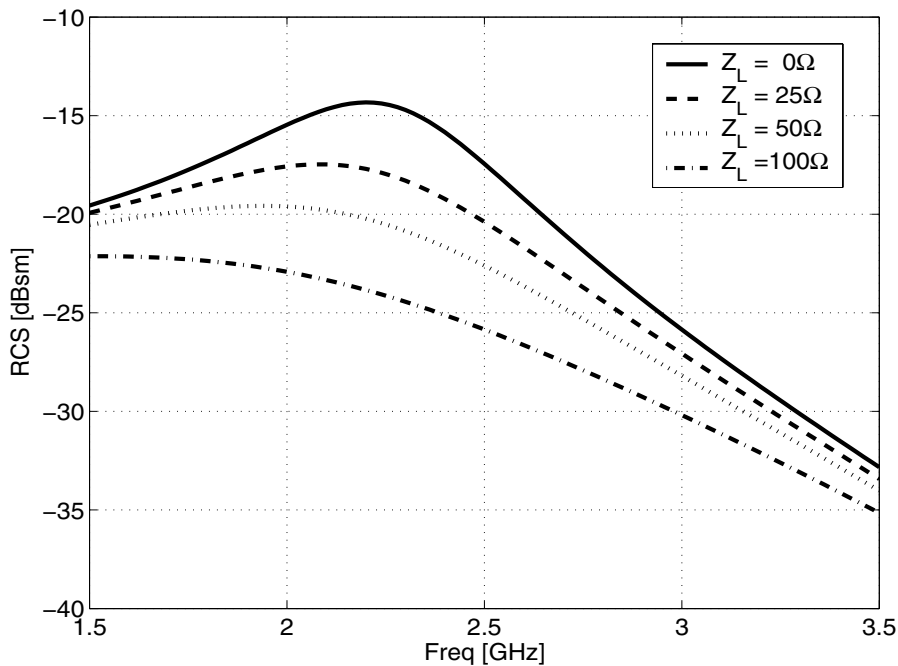


Figure 6.3: the maximum back-scattering cross-section of the printed dipole as a function of load resistance  $Z_{Le}$ .

### 6.3.2 Scattering from a Magnetic Dipole Antenna

The second example is a PMC strip that is shown in Fig. 6.1(c). This structure is also known as a magnetic dipole. Again, an analytical formulation for the RCS of this receiving antenna is presented as a function of the load admittance/impedance. Considering duality in Maxwell equations, a magnetic current  $-\overline{M}$  can be added to Faraday's law, which corresponds to the electric current  $\overline{J}$  in Ampere's law [62, 63]. Adding the magnetic current to the Maxwell equation, makes the differential representation of the Ampere's and Faraday's law dual of each other given the following replacements.

$$\begin{aligned}
\overline{E} &\rightarrow \overline{H} \\
\overline{H} &\rightarrow -\overline{E} \\
\overline{J} &\rightarrow \overline{M} \\
\overline{M} &\rightarrow -\overline{J} \\
\mu &\rightarrow \epsilon \\
\epsilon &\rightarrow \mu \\
\eta &\rightarrow \frac{1}{\eta}
\end{aligned} \tag{6.9}$$

The PMC strip of Fig. 6.1(c) is a dual of the PEC antenna of Fig. 6.1(b) provided that the former is radiating in a medium with an intrinsic impedance of  $1/\eta$ , and is terminated with a load admittance of  $Y_{Lm} = 1/Z_{Le}$ . If so, the RCS of the receiving PMC strip (magnetic dipole), as a function of the load admittance, can be obtained using the following equation.

$$\sigma_m = 4\pi R^2 \left| \frac{H^s}{H^i} \right|^2 = \frac{4}{\pi k^2 \eta^2 |Y_m + Y_{Lm}|^2} \tag{6.10}$$

where  $Y_m$  is the input admittance of a strip of PMC and is related to that of a PEC strip through duality.

### 6.3.3 Radar Cross-Section of an Aperture Antenna

The third structure to be discussed here is an aperture/slot antenna shown in Fig. 6.1(a). This antenna is the complementary pair of the PEC dipole of Fig. 6.1(b). In dealing with complementary structures, another form of duality can be established, wherein the medium does not need to be replaced. This representation of duality is more suitable for antenna and radiation problems. The following replacements again

make the Ampere's and Faraday's laws in the Maxwell equations interchangeable.

$$\begin{aligned}
\overline{E} &\rightarrow \eta \overline{H} \\
\overline{H} &\rightarrow -\frac{\overline{E}}{\eta} \\
\overline{J} &\rightarrow \frac{\overline{M}}{\eta} \\
\overline{M} &\rightarrow -\eta \overline{J}
\end{aligned} \tag{6.11}$$

In the above set of transformations,  $\eta = \sqrt{\mu/\epsilon}$  remains intact, and therefore, the medium does not need to be replaced by a dual medium. In fact, the field quantities in the above duality are normalized to the impedance of the medium, an example of which is the  $S$ -parameters in the microwave network theory [65]. With that in mind, the impedance of the antennas in Figs. 6.1(a) and 6.1(b) are related through the Bookers' relationship; that is

$$Z_e Z_a = \frac{\eta^2}{4} \tag{6.12}$$

Moreover, Babinet's principle asserts that the diffractions by a planar aperture is mathematically dual with the scattered fields by its complementary structure, subject to the substitutions prescribed in (6.11) [62, 63].

As mentioned earlier, two components contribute to the total scattered field from a receiving slot/aperture antenna. First is the diffraction caused by the slot, and second is the reflection by the ground plane. Using duality equations as stated by (6.11) and (6.12), the contribution of the aperture diffraction can be obtained using the same set of equations for the scattered field of an antenna. Invoking duality in equation (6.7) by the following replacements

$$\overline{E}_e^s \rightarrow \eta \overline{H}_a^s, \quad \text{and} \quad Z_e \rightarrow \frac{\eta^2}{4} Y_a \quad (6.13)$$

in equations (6.7), gives the contribution of the slot diffraction to the total scattered field as

$$\overline{H}_a^s = j \frac{8H_0/k}{\eta(Y_a + Y_{La})} \frac{e^{-jkr}}{2\pi r} \quad (6.14)$$

The RCS due to diffraction by the aperture is, then, found to be

$$\sigma_a = \frac{64}{\pi k^2 \eta^2 |Y_a + Y_{La}|^2} \quad (6.15)$$

Comparing the RCS of an aperture with its complementary PEC strip, as well as the PMC strip in (6.8) and (6.10), might seem to indicate an increase in the RCS of the aperture antenna by a factor of 16 (12 dB). However, the impedance of an aperture antenna is four times smaller than that of a PMC strip with the same size, which leads to the same RCS for both cases.

The next component in the total scattered field by a slot antenna is the reflection from the ground plane. This component can be calculated using the physical optics (PO) approximation [64]. Assuming that the structure of Fig. 6.1(a) is illuminated by a normal incident plane-wave of  $\overline{H}^i = \hat{z} H_0 e^{jkx}$ , the back-scattered field at  $\theta = 90^\circ$  is given by

$$\overline{E}_{plate}^s = -j\eta k L_x L_y H_0 \frac{e^{-jkr}}{2\pi r} \hat{a}_z \quad (6.16)$$

Thus, for the total scattered field, we have

$$\overline{E}_{total}^s = \overline{E}_{plate}^s + \overline{E}_{slot}^s = -j\eta H_0 \frac{e^{-jkr}}{2\pi r} \left( k L_x L_y - \frac{8}{k\eta(Y_a + Y_{La})} \right) \hat{a}_z \quad (6.17)$$

which gives the total RCS of

$$\sigma_t = \frac{1}{\pi} \left| kL_xL_y - \frac{8}{k\eta(Y_a + Y_{La})} \right|^2. \quad (6.18)$$

## 6.4 Analytical Results

In reality, the RCS measurement of the slot antennas gives the total RCS, namely,  $\sigma_t$ . As can be seen in equation (6.18), this quantity contains a large background component due to the scattering by a metallic plate. Moreover, this portion of the RCS does not contain any information of the load impedance of the antenna, and consequently, cannot be used to extract the high input impedance of the antenna. Another drawback of having a large background clutter is the reduction of the dynamic range of the radar measurement. To alleviate problems associated with the scattering by the ground of the slot antenna, one may analytically subtract the contribution of the ground to the total scattered power. The same idea can be implemented in the measurement experiment by a method referred to as background subtraction. In background subtraction, another plate with the same size as the slot ground plane is made, and its scattered field is coherently subtracted from that of the slot antenna. As a result, the contribution of the slot diffraction can be obtained with a much higher dynamic range.

Figure 6.4(a) illustrates the total scattered field of the slot antenna evaluated by (6.18) when the load impedance is varied as a parameter. The slot is assumed to have a length of  $\ell = 55$  mm, in a rectangular ground plane with dimensions of  $2\lambda \times 2\lambda$ . Included in this figure is also the RCS of a rectangular plate without an aperture. As seen in Fig. 6.4, the contribution of the ground plane in the RCS is dominant, and the diffraction by the aperture can be viewed as a perturbation. Coherently subtracting the ground reflection term – based on the analytical formulation already presented –

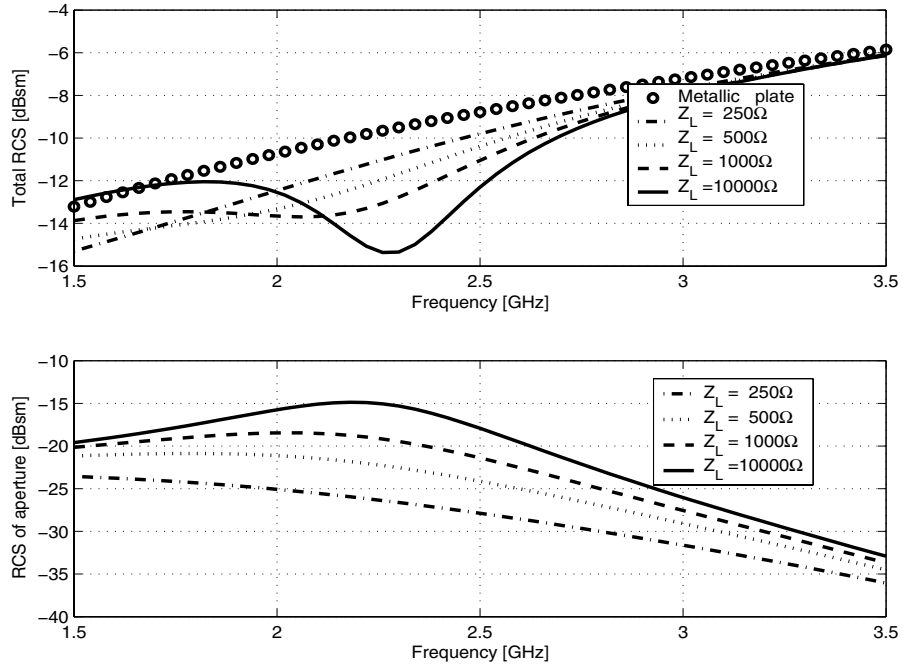


Figure 6.4: The radar cross-section of a slot antenna with the length of  $\ell = 55$  mm, and ground plane size of  $2\lambda \times 2\lambda$ , when the load impedance is changed as a parameter; (a) total RCS, (b) RCS after coherent subtraction.

can drastically improve the accuracy of the measurement. Figure 6.4(b) shows the RCS due to the diffraction by the aperture after the contribution of the ground is removed. Obviously, the calibrated data is more sensitive to the variation of the load impedance.

## 6.5 Numerical Simulation

In this section, numerical results obtained from an MoM simulator [25] is presented to verify the feasibility of the proposed measurement technique for high-impedance antennas.

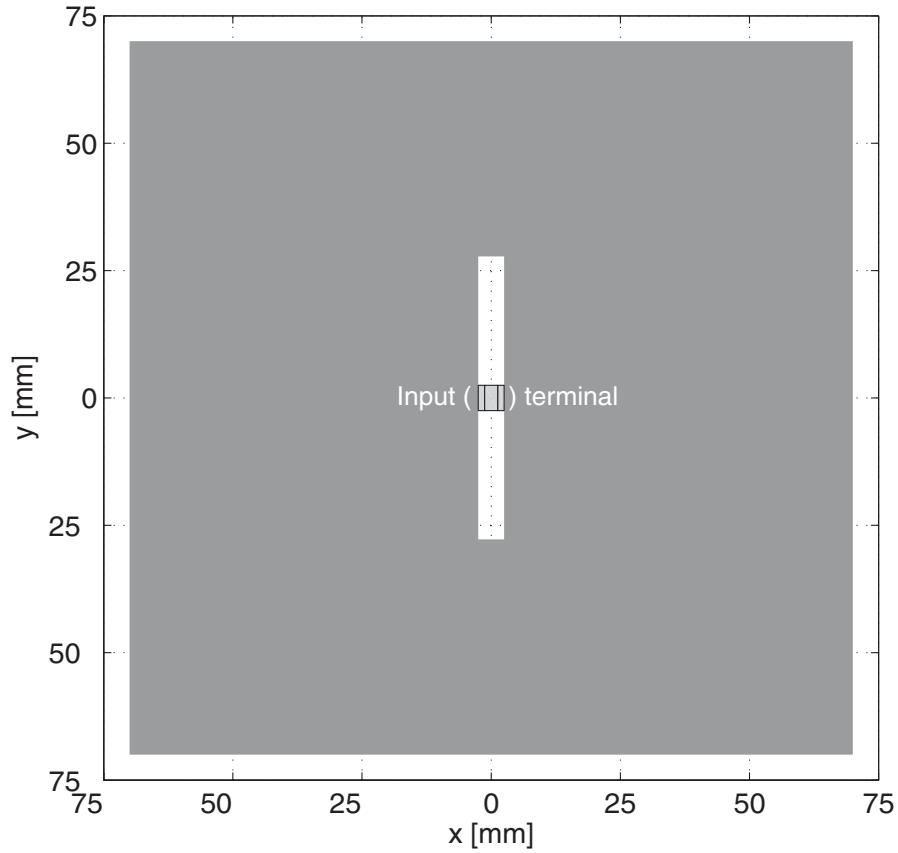


Figure 6.5: The layout of a center-fed slot antenna with  $\ell = 55$  mm, and ground plane size of  $14 \text{ cm} \times 14 \text{ cm}$ .

### 6.5.1 Center-fed Slot Antenna

First, a slot antenna with a length of  $\ell = 55$  mm, and a ground plane of  $14 \text{ cm} \times 14 \text{ cm}$  is considered as shown in Fig. 6.5. This example is similar to the one considered in the previous section and is chosen to compare the analytical formulation with the full-wave simulation.

Figure 6.6 shows the total RCS of the slot antenna of Fig. 6.5, which includes the contribution of both the ground plane and the aperture. The RCS of a similar size rectangular ground plane without an aperture, whose RCS is needed for background subtraction, is also simulated and plotted in Fig. 6.6. As seen in this figure, a strong background is present and needs to be removed. A simple way of doing so is to perform incoherent subtraction, in which, the scattered power of the plate is subtracted from

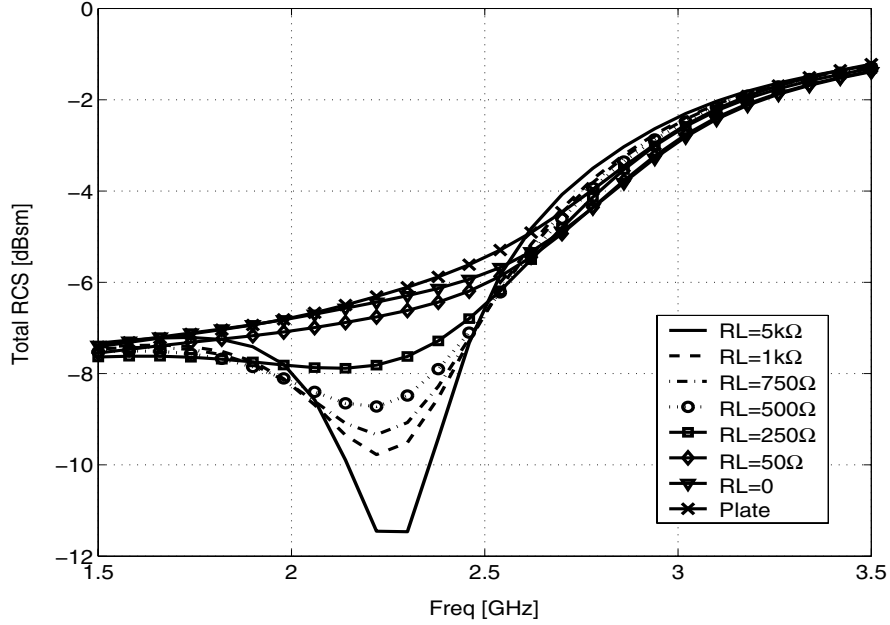


Figure 6.6: The simulated total RCS of the slot antenna of Fig. 6.5 as a function of frequency for different values of load resistance ( $R_{La}$ ).

the total back-scattered power. Figure 6.7 shows the RCS of the aperture after the contribution of the ground plane is removed incoherently. Knowing that the normal incident wave excites both the plate and the aperture in-phase, one can conclude that the scattered fields remain in-phase so far as the admittance of the aperture is a real quantity -which is the case at resonance. Therefore, incoherent subtraction can deembed the effect of the ground plane only at resonant frequency. The clutter in the measurement, however, is not limited to the ground plane, and can come from different sources, including thermal noise, multi-path, edge effects and depolarization. In order to remove all these unwanted contributions, a coherent and perhaps fully polarimetric system is required. Figure. 6.8 shows the RCS of the aperture extracted from the total RCS of Fig. 6.6, when the contribution of the ground plane is subtracted coherently. Comparing Fig. 6.8 and Fig. 6.7 clearly explains the advantage of the coherent system versus the incoherent system, even though both of them provide similar results at the vicinity of the resonant frequency.

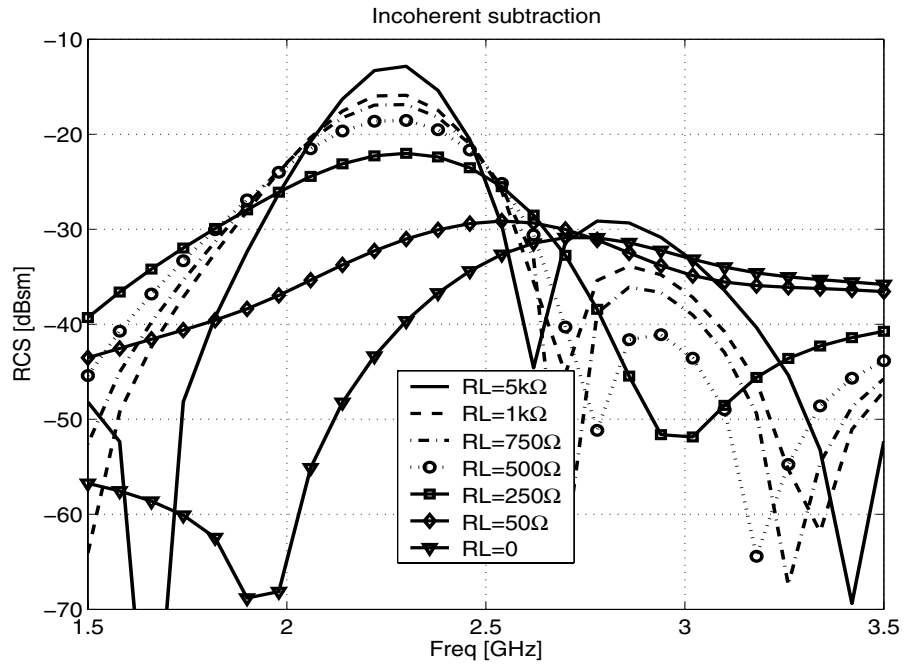


Figure 6.7: Incoherent subtraction of the scattered power of the ground plane (background) from the total back-scattered power shown in Fig. 6.6.

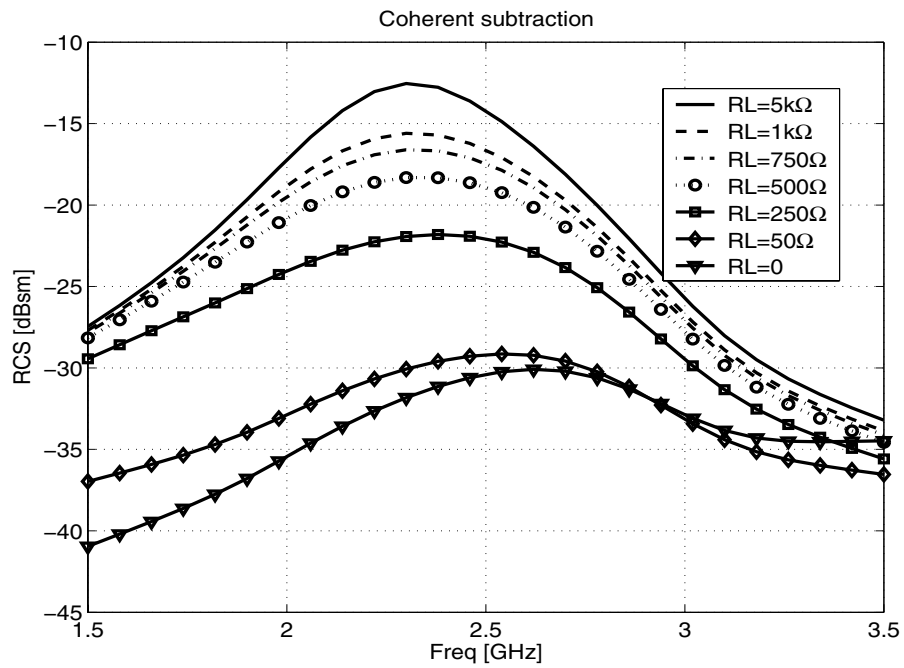


Figure 6.8: Coherent subtraction of the scattered field of the ground plane (background) from the total back-scattered field coming from the aperture and the ground.

Considering the variation of the RCS of a loaded aperture against the terminating load impedance, as illustrated in Fig. 6.8, demonstrates how the RCS can be used to determine the matched load, and consequently, the radiation resistance of the antenna. As expected, the open-circuit load ( $Y_{La} = 0$ ) creates the maximum RCS with a peak at resonance. As the load impedance decreases, the peak value of the RCS decreases up to a point where the peak value of the RCS becomes 6 dB lower than that of the open-circuit load. This particular load impedance designates the radiation resistance of the antenna. In Fig. 6.8, the peak of the RCS for  $Z_{La} = 500 \Omega$  is about 6 dB below the peak corresponding to the open-circuit load, and thus, one can discern that the impedance of this antenna is about  $500 \Omega$  at resonance. The location of the peak also determines the resonant frequency of the antenna under test.

### 6.5.2 High-impedance Miniaturized Slot Antenna

Using the same technique, a high-impedance antenna is chosen as the second example. For this purpose, a center-fed miniaturized slot antenna is considered. The topology of this structure is the same as that of Fig. 3.9 with the exception of the microstrip feed network. Figure 6.9 shows this antenna when made on a ground plane with dimensions of  $35.5 \text{ cm} \times 35.5 \text{ cm}$ . The input impedance of this antenna with a finite ground plane is simulated using an MoM simulator and plotted in Fig. 6.10. As illustrated, this structure has a very high impedance at its resonance; that is on the order of  $15 \text{ K}\Omega$ . Such a high impedance is in accordance with the values reported in Chapter 4 for miniaturized slot and folded-slot antennas having the same dimensions.

The antenna is simulated while being illuminated by a normal incident plane-wave, and its total back-scattered RCS is calculated and shown in Fig. 6.11 for different values of the load impedance,  $R_L$ . The total RCS of Fig. 6.11 is more sensitive to the variation of the termination impedance as compared with the previous example

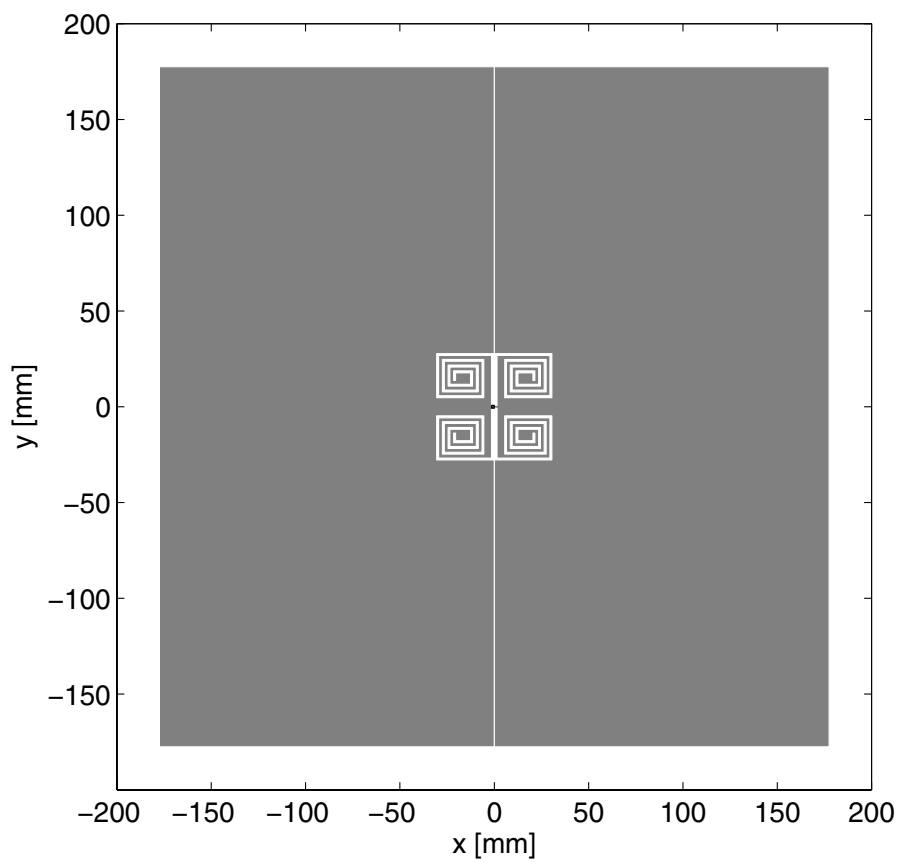


Figure 6.9: The layout of a center-fed miniaturized slot antenna with dimensions of about  $0.05\lambda_0 \times 0.05\lambda_0$ , and ground plane size of  $35.5 \text{ cm} \times 35.5 \text{ cm}$ .

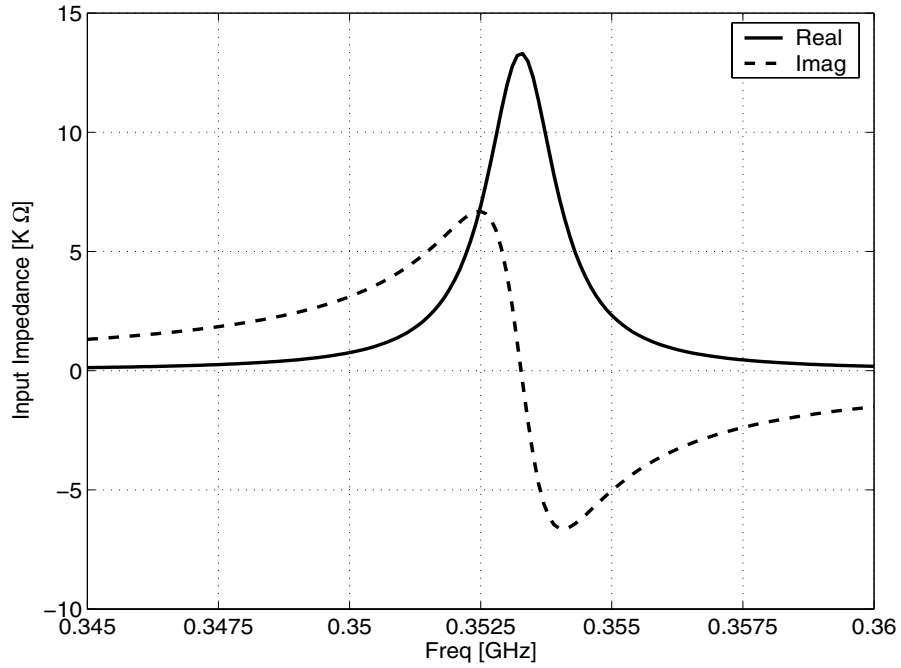


Figure 6.10: The simulated input impedance of the miniature antenna of Fig. 6.9 when fed at the center.

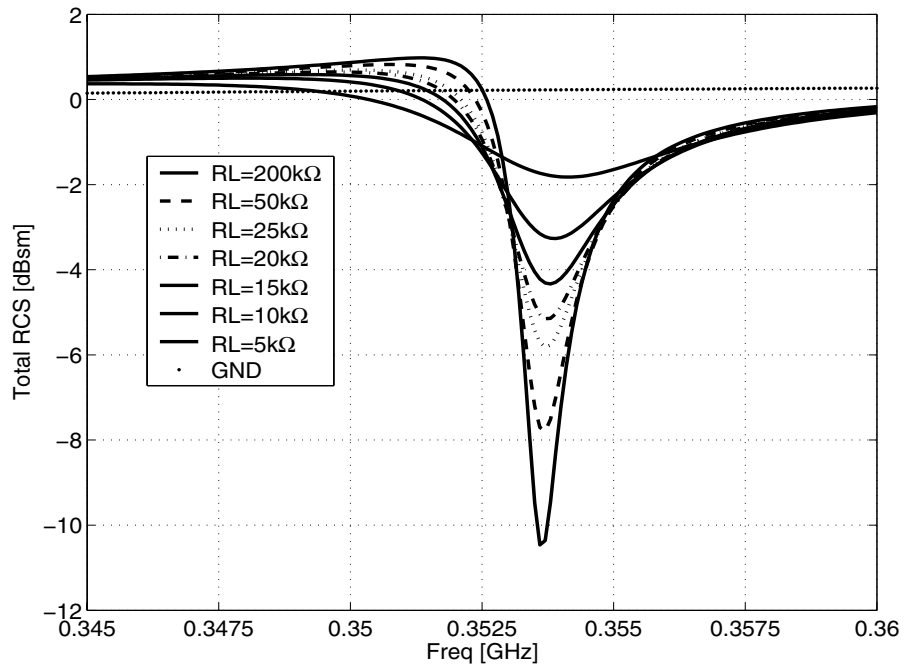


Figure 6.11: The simulated total RCS of the slot antenna of Fig. 6.5 as a function of frequency for different values of load resistance ( $R_{La}$ ).

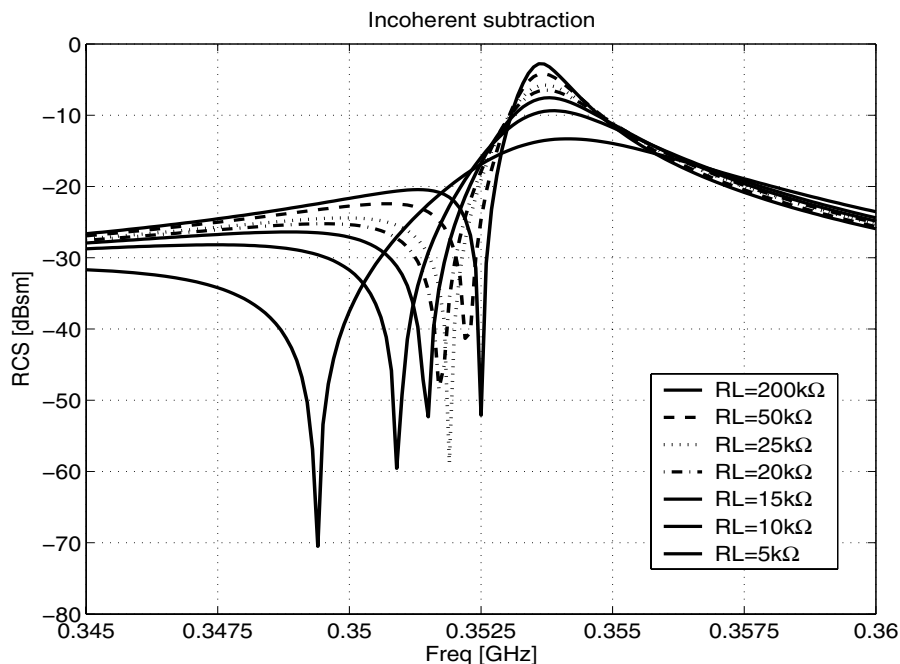


Figure 6.12: Incoherent subtraction of the scattered power of the ground plane (background) from the total back-scattered power shown in Fig. 6.11.

shown in Fig. 6.6. The enhanced sensitivity may seem counter-intuitive knowing that the miniaturized slot antenna is much smaller than a standard slot of the previous example. However, the contribution of the miniaturized slot (aperture diffractions) to the total RCS is comparable to that of a standard half-wavelength slot [66]. That is because small resonant objects produce a much greater back-scattered field than non-resonant objects of the same size. The normalized RCS of the standard slot of the first example is only 5 dB larger than that of the miniaturized slot while being approximately 10 times larger.

Figure 6.12 shows the RCS of the aperture after the contribution of the ground plane has been incoherently subtracted. The RCS of the slot after coherent subtraction is shown in Fig. 6.13. Again, it can be seen that the deembedded RCS resembles the one predicted by the analytical formulation, and its very sensitive to the variation of the load resistance.

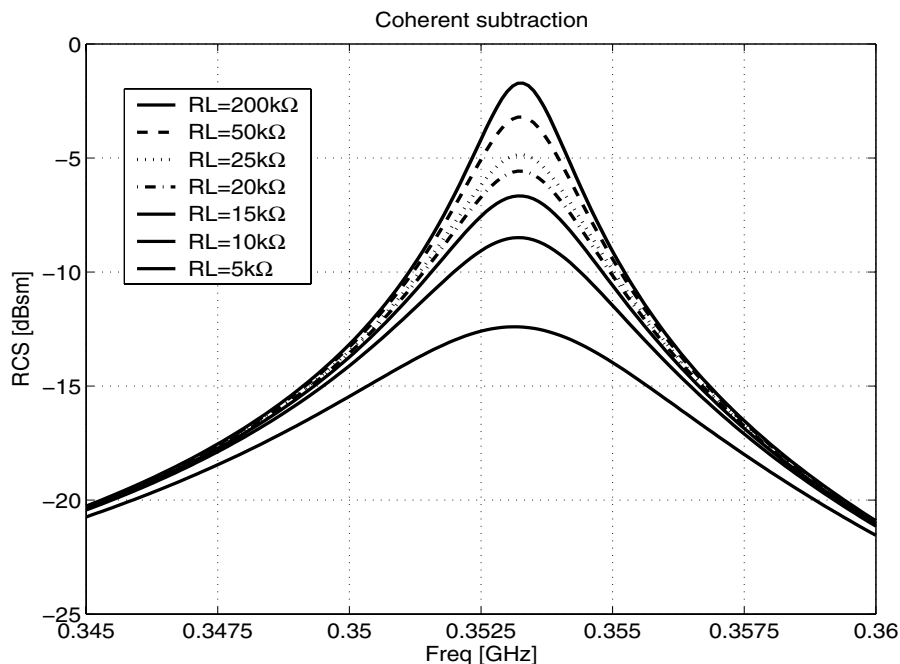


Figure 6.13: Coherent subtraction of the scattered field of the ground plane (background) from the total back-scattered field of the miniaturized antenna of Fig. 6.9.

## 6.6 Measurement of High-Impedance Antenna

The high-impedance miniaturized antenna of Fig. 6.9 is now fed by a short-circuited microstrip-line and connected to the RF Impedance/Material Analyzer. The measurement setup is illustrated in Fig. 6.14. The standard calibration using an open, short and load was done at the input port of the antenna. The input impedance of the antenna is measured and shown in Fig. 6.15. Measured data suggests that the antenna resonates at 205 MHz with very high input impedance of 8 K $\Omega$ . Although the measured impedance of the antenna is still very high, it is considerably different from the simulated input impedance. In addition to the magnitude of the input impedance, a frequency shift greater than 100 MHz is observed in the resonance of the antenna. This discrepancy can be resolved by deembedding the effect of the microstrip line between the impedance analyzer and the center of the slot.

In order to deembed the microstrip-line, first the equivalent circuit parameters of

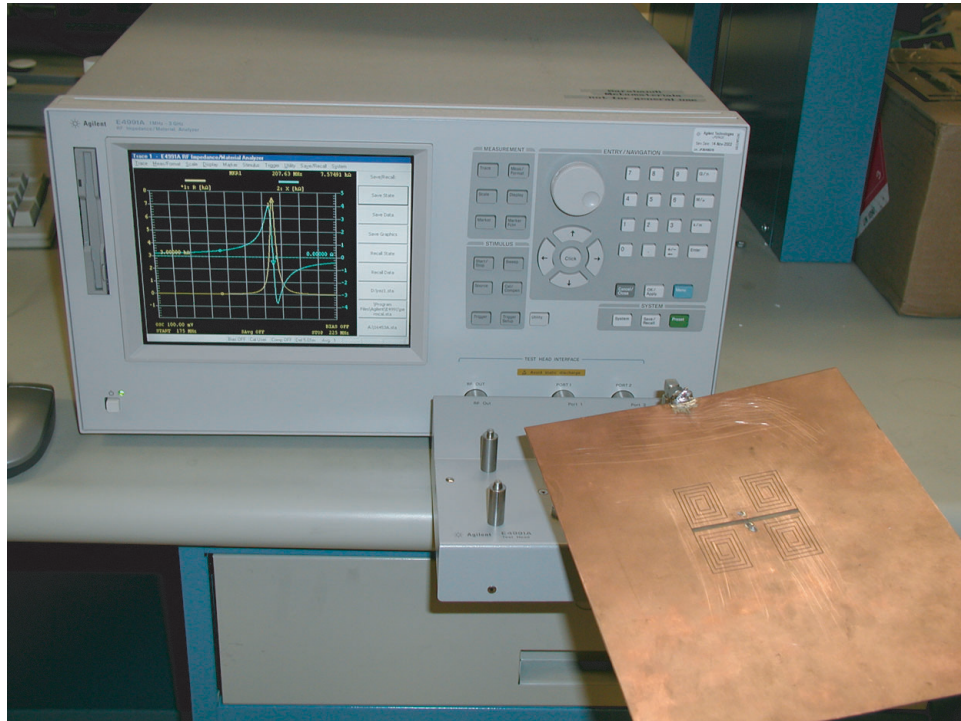


Figure 6.14: High-impedance measurement setup for measuring the input impedance of the miniaturized slot antenna of Fig. 6.9.

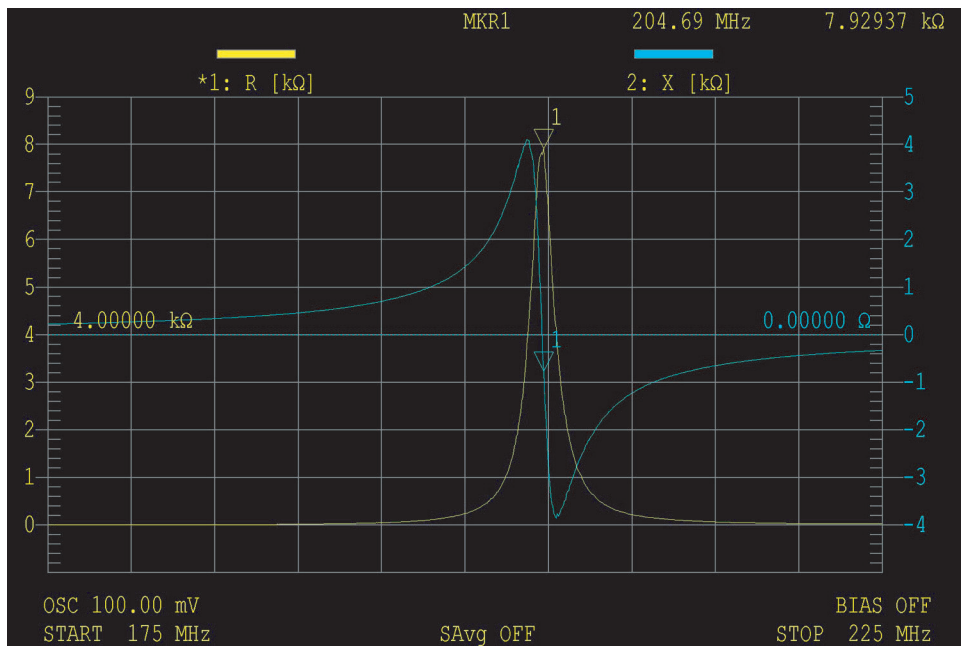


Figure 6.15: The input impedance of the high impedance miniaturized slot antenna of Fig. 6.9 measured using the setup of Fig. 6.14.

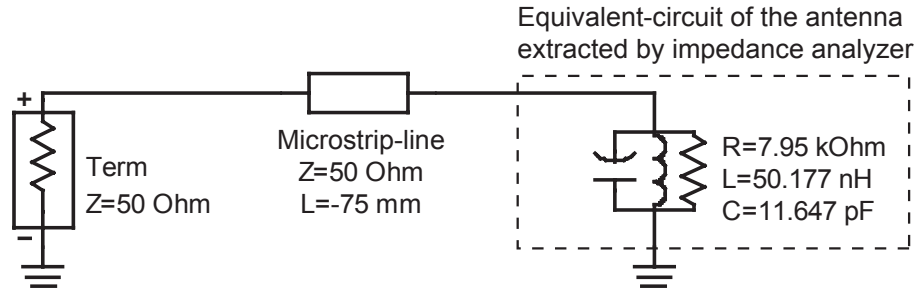


Figure 6.16: Schematics of the equivalent circuit of the high-impedance antenna of Fig. 6.9 extracted by the impedance analyzer along with the line deembedding scheme.

the antenna must be extracted. These parameters are obtained using the impedance analyzer and demonstrated in Fig. 6.16. Noting that these parameters are seen at the calibration plane located at the antenna port, the effect of the microstrip-line is readily embedded in the equivalent circuit parameters. As a result, the effect of the line should be deembedded in order to extract the input impedance at the center of the slot antenna. That is why a microstrip-line with a negative length is inserted in the equivalent circuit of Fig. 6.16. Figure 6.17 shows the input impedance of the miniaturized slot antenna after having deembedded the effect of the transmission-line. The deembedded results compare favorably with those obtained from the full-wave simulation, shown in Fig. 6.10, in both the resonant frequency and the magnitude of the input impedance.

## 6.7 Conclusion

This measurements verifies that the proposed miniaturized slot antenna is extremely high-impedance, and indeed, a suitable candidate for integration into micro-system applications, an example of which is MEMS filter-bank.

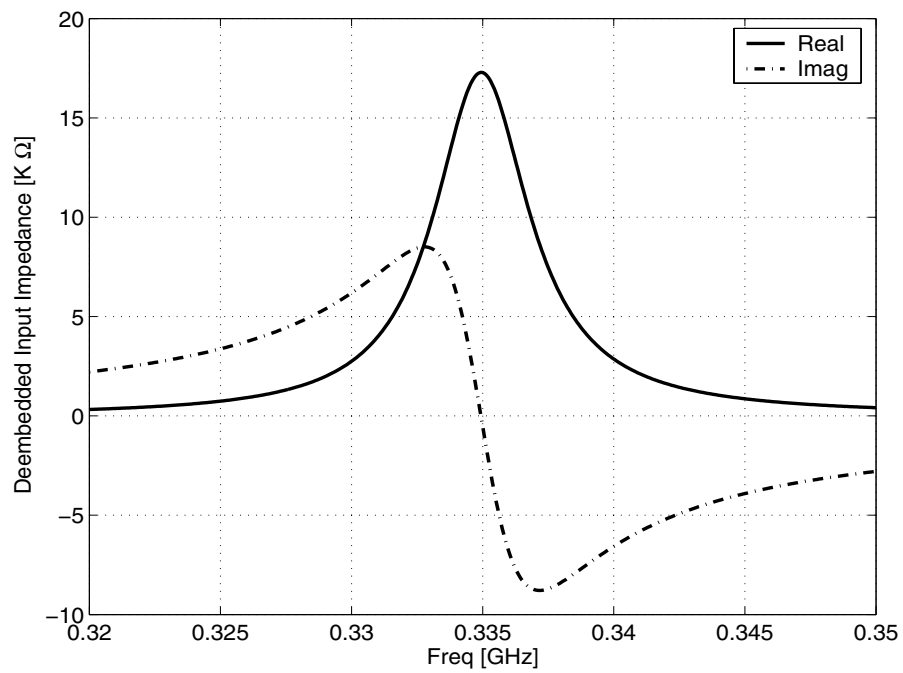


Figure 6.17: The measured input impedance of the high-impedance miniaturized slot antenna of Fig. 6.9 after deembedding the effect of the microstrip-line.

## CHAPTER 7

# Conclusions and Recommendations for Future Work

### 7.1 Summary

The main objective of this thesis was to address the challenging issue of antenna and microwave filter miniaturization in the context of wireless systems. The size of antennas and filters, as well as any other resonant components, is tightly dependant upon the physical dimensions of the structure. In order to establish standing electromagnetic waves, the dimension of the resonant structure needs to be at least half a wavelength, which imposes a size limitation. Furthermore, the size of these components critically affects the power efficiency and ohmic losses. The aforementioned issues have so far precluded antennas and perhaps microwave filters from being integrated monolithically into the rest of the transceiver circuitry.

In response to the above need, a novel approach for miniaturization of antennas and filters have been proposed. In addition to miniaturization, high-impedance matching of the miniaturized antennas was investigated. In fact, high-impedance is another important requirement that must be fulfilled before integrating antennas into high-impedance electronics and microsystems becomes a reality.

## 7.2 Contributions

The major contributions of this thesis fall into three different categories:

### 7.2.1 Antenna Miniaturization

The concept of a new class of efficient miniaturized planar slot antennas with a potential for reconfigurability was demonstrated. This approach takes advantage of the antenna topology to achieve miniaturization. Using this concept, the design of a miniaturized antenna as small as  $0.05\lambda_0 \times 0.05\lambda_0$  with a fairly high gain of  $-3$  dBi was demonstrated. This antenna is an order of magnitude smaller than the standard half-wavelength antennas. Since there are neither polarization nor mismatch losses, the antenna efficiency is limited only by the dielectric and ohmic losses of the substrate on which the antenna is made. The proposed topology can also be made on a high dielectric constant substrate/superstrate providing further size reduction.

### 7.2.2 Bandwidth Enhancement of Miniaturized Antennas

The bandwidth of this new generation of antennas is rather small as is the case for all small antennas. Resonant antennas in general, and slot-dipoles in particular, are inherently narrow-band. By reducing the size of the slot, the physical aperture of the antenna is reduced, and therefore, the radiation conductance of a miniaturized slot antenna becomes very small. One way to match the high impedance of the miniaturized slot antenna to a  $50\Omega$  line is to tune it slightly off resonance, whether capacitively or inductively. A smaller capacitance or larger inductance is needed depending on whether the antenna is tuned below or above the resonance. However, a smaller capacitance, or conversely a larger inductance, results in a narrower bandwidth. To partially improve the bandwidth of miniaturized slot antennas, one can increase the physical aperture without increasing the overall size of the antenna by

introducing folded topology. Some other miniature antenna topologies, such as complementary and self-complementary realizations of the miniature folded slot structure, were explored as suitable candidates for further bandwidth improvement.

### 7.2.3 Microwave Filter Miniaturization

A similar approach to the one used for designing miniaturized antennas can be applied to other passive microwave components, such as resonators, band-pass filters, couplers, and so on. As part of the filter miniaturization efforts, a new class of low insertion loss miniaturized filters using slot-line resonators is proposed. Miniaturization is achieved by terminating the slot-line with a double-spiral inductive termination at both ends. Using these miniaturized resonators, both positive and negative couplings may be realized, and therefore, both standard coupled-line and cross-coupled quasi-elliptic filters are realizable. The unloaded  $Q$  of these slot-line filters is considerably higher than that of miniaturized microstrip filters of comparable dimensions due to the inherent higher  $Q$  of slot-line. The resonators/filters that have been introduced are, again, about an order of magnitude smaller than their standard distributed counterparts, while still having comparable or even higher quality factors.

### 7.2.4 High-Impedance Antenna Measurement

Another aspect of this research is its potential for integration with emerging transceiver designs based on micro-electromechanical systems (MEMS). In order to integrate these miniature antennas with the rest of the transceiver circuitry, impedance matching and interfacing issues must be resolved. Usually, MEMS filters have very high terminating impedance ( $15\text{ K}\Omega$ ) and cannot be connected directly to  $50\ \Omega$  antennas. It is important to note that traditional impedance-matching techniques are not able to overcome this difficulty. Thus, new methodologies should be investigated to make high-impedance miniaturized antennas. One method investigated in this work

is to reduce the physical aperture of the antenna to make its impedance closer to those impedances appropriate for MEMS filters. This step is considered a significant milestone towards the fabrication of the whole transceiver on a single chip knowing that the antenna imposes a stringent bottleneck on the overall size of the wireless subsystems.

### **7.3 Future Work**

In addition to wireless microsystems, which have enormous overlap with the main course of this research, there are some other multidisciplinary areas, such as biotechnology, and nanotechnology that this work can significantly contribute. There are three distinct features in this research that can be applied to the aforementioned areas. First, the need for miniature RF and electromagnetic passive components is inevitable (miniaturization). Second, low-power requirements of these structures demand a great deal of effort to maintain the losses of miniature structures as low as possible, especially at higher frequencies (high  $Q$ , and low loss). Third, the high impedance nature of micro- and nano-scale devices calls for high-impedance miniature antenna/microwave circuit structures for integration. The high-impedance characteristic ensures that the power consumption of the system will be at minimum (high-impedance). The following discussion, more specifically, outlines some of the interesting venues in which this research can be pursued in future.

#### **Fabrication of Miniaturized Antennas on Meta-Materials**

Engineering high-performance magneto-dielectric materials (Meta-Materials) has created a new avenue for RF engineering research. This new generation of materials has great potential to be used as substrates for novel antennas and microwave circuits. Suppressing the surface waves, controlling the near field couplings, manipulating the

permittivity and permeability of substrates, etc. are among advantages of this class of materials, which can uniquely address antenna and RF circuit needs, such as further miniaturization and bandwidth enhancement.

### **Miniature antennas for biomedical applications**

Highly efficient miniaturized components, proposed in this research, can find numerous applications in biomedical field. Having a low-loss miniature electromagnetic probe, capable of transmitting and receiving narrow-band data, is critical in the design of sensors for implantable devices. Particularly, the idea of miniaturized resonators capable of demonstrating both electric and magnetic field couplings with minimal losses can be explored for this class of applications.

### **Sensor Network**

In the wake of global warming, there is an ongoing effort to collect lots of environmental data, such as temperature, humidity, pressure, toxic or pollutant content of the air, etc., by means of low-cost low-power micro-sensors. These sensors will spread over the environment and are sought to be able to communicate with each other, and with the central unit. Micro-technology is adopted for achieving low-power micro-sensors. However, some stringent requirements are to be imposed on the size, power efficiency, and impedance of the antennas sought for micro-sensor applications. The proposed approach of high-impedance miniaturized antennas is a promising start point to come up with new solutions for high-impedance low-power wireless micro-system for sensor network applications.<sup>1</sup>

---

<sup>1</sup>The miniaturized antenna of this thesis is to be used in the micro-power sensor network project of the University of Michigan Engineering Research Center of Wireless Integrated Micro-systems (WIMS)

## **High-Impedance Miniature Antennas and Micro/Nano-scale Devices**

Micro- and nano-scale devices are generally very high-impedance mainly due to their small sizes. A few examples of such devices, including MEMS filter banks and CNT transistors, have already been mentioned in this thesis. In order for micro/nanodevices to be utilized in future wireless systems, it is necessary to resolve the impedance mismatch between them and the antenna system. Introducing the idea of high-impedance miniaturized antennas can be found amenable to the impedance mismatch of these devices.

## APPENDIX

## APPENDIX A

### Effects of the Finite Ground Plane on the Slot Antenna Radiation Pattern

#### A.1 Introduction

A slot antenna element is constructed by cutting slots into a perfectly conducting ground plane of an infinite extent. Figure A.1 illustrates a slot antenna at the resonance fed at the center by a two-wire transmission line. For a narrow slot, the slot itself can be considered as a section of a two-wire transmission line terminated at both ends by short-circuits. A standing wave of voltage can be established across the slot-line such that the electric field in the slot is approximately given by

$$E_y(z) = \frac{V_{ab}}{w} \cos \frac{2\pi}{\lambda_s} z \quad (\text{A.1})$$

where  $V_{ab}$  is the peak voltage at the center. The equivalence principle can be applied to replace the electric field across the slot-line with an equivalent magnetic current. This magnetic current radiates at the presence of the ground. Provided that the ground plane is of an infinite extent, image theory reduces all the sources to a linear

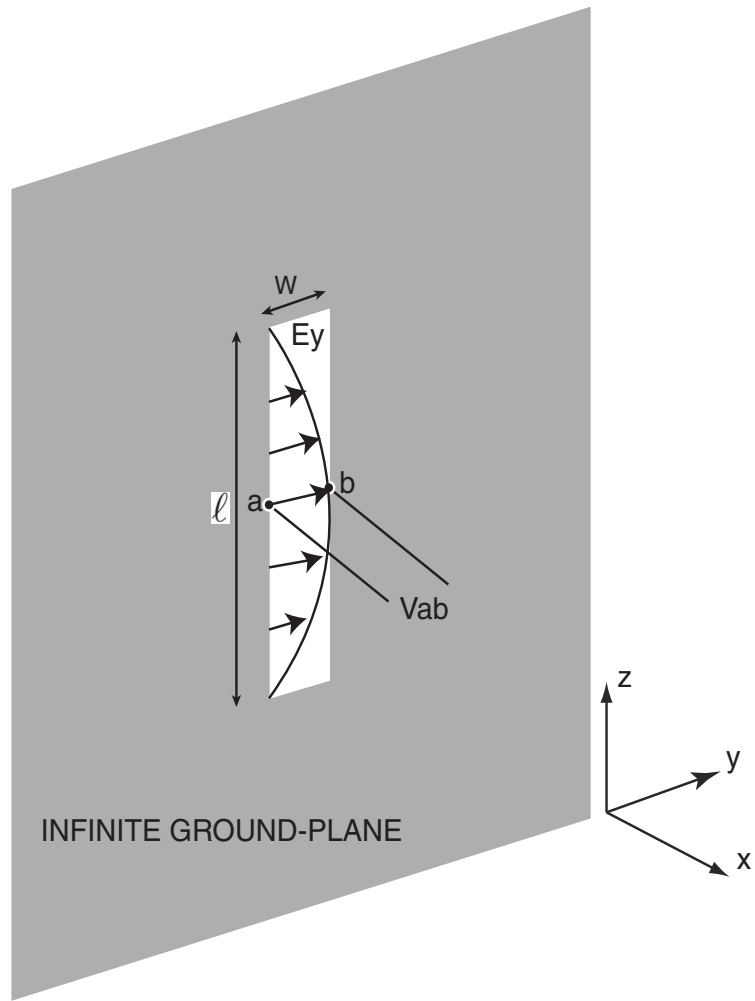


Figure A.1: Slot antenna in a perfectly conducting ground plane center fed by a two-wire transmission line.

magnetic current sheet on the aperture given by [35]

$$M_z = 2E_y \hat{a}_y \times \hat{a}_x = -\hat{a}_z \frac{2V_{ab}}{w} \cos \frac{2\pi}{\lambda_s} z \quad (\text{A.2})$$

Equation A.2 is very similar to the electric current distribution on an electric dipole. Because of this similarity, a narrow center-fed slot in an infinite ground plane is often referred to as a magnetic dipole. These two configurations are indeed dual of each other through Babinet's principle, whereby the analysis of electric dipole can be directly applied to the case of a slot antenna.

## A.2 Numerical Simulation of Slot Antennas

Numerical solutions to the slot antenna can be obtained using both integral equation and differential equation methods. Integral equation methods such as Method of Moments (MoM) are generally preferred for planar and multi-layered structures. In contrast, differential equation methods including finite element (FEM) and finite difference time domain (FDTD) methods are more appropriate for three dimensional and finite structures.

In MoM, two treatments of the slot antenna problem is possible. One is to discretize the unknown electric current on the ground plane, and another is to discretize the electric field (magnetic current) across the slot. Obviously, the latter is more efficient approach since the area of the ground is much larger than that of the aperture. These two problems are not equivalent electromagnetically except when the ground plane is infinite and perfectly conducting. In spite of those idealistic conditions, the magnetic current modeling was utilized to design the miniaturized structures presented throughout this dissertation, and it was proven to be very accurate in predicting the frequency response of the structures.

In FEM method, a physical three-dimensional structure can be meshed and the

fields are solved for. In this approach, there is no restriction on the modeling of a finite ground plane and other physical parameters of the problem. But this approach was shown to be numerically cumbersome for simulating the miniaturized structures having a very large aspect ratio. When the aspect ratio is large, very fine gridding is required which necessitates exorbitant amount of memory. That is why the MoM with magnetic current discretization was adopted in this thesis.

The magnetic current discretization has been implemented in some commercially available MoM softwares such as IE3D [25], in which the magnetic current is treated as an unknown parameter, and it is solved for using the integral equation method. The replacement of the slot with an unknown magnetic current element is based on the presumption that the ground plane should be a perfect conductor and infinite. In addition to the infinite ground, the dielectric substrate of the antenna is assumed to be of an infinite extent. Obviously, the simulated results based on these presumptions do not include ohmic losses of the ground, which is the major source of losses in the slot antenna. As a result, the radiation efficiency obtained by the magnetic current simulation is not accurate, and it includes only the dielectric loss of the antenna. Furthermore, ignoring the ohmic loss of the ground leads to some discrepancies between the simulated and measured bandwidths. In different chapters of this thesis, the issue of ground plane loss and its effect on the discrepancies between the simulated and measured results was discussed in details and is not revisited in this appendix.

The application of magnetic current discretization, however, has another implication, that is the unrealistic presumption of infinite ground plane and substrate. Therefore, some discrepancies might be expected when measured radiation patterns (finite ground) are compared with those obtained by the magnetic current simulation (infinite ground).

The effect of ground plane and dielectric truncations on the radiation pattern of a printed antenna is basically attributed to the near-field and surface-wave diffrac-

tions by the edges of the ground and dielectric. These effects have been studied for microstrip patch structures [33]. It was shown that for certain ground plane dimensions, the radiation efficiency deteriorates considerably due to an increase in the surface-wave loss.

A similar study has been conducted for a slot antenna on a truncated lossy dielectric fed by a rectangular waveguide [67, 32]. This study is similar to the study of the diffraction by a dielectric covered aperture illuminated by a plane wave [34]. In the above studies of the slotted structures, the antennas are radiating only in one half-space, and thus, the obtained results may not be applicable to an omnidirectional slot antenna. The following section, however, deals with a center fed slot antenna radiating into both half-spaces.

### A.3 Simulated Radiation Pattern of a Slot Dipole

In this section, the effect of the finite ground plane on the radiation pattern of a standard slot antenna is investigated. This study includes the comparison between the simulated radiation patterns of a standard half-wavelength slot with finite and infinite ground planes, in both E and H principle cuts. Figure A.2 illustrates the principle E- and H-planes of a standard slot antenna under test. As shown in this figure,  $\phi = 0^\circ$  and  $\phi = 90^\circ$  specify the E- and H-planes of the antenna, respectively. For E-plane pattern,  $E_\theta(\theta)$  is measured in the  $\phi = 0^\circ$  cut, whereas for the H-plane pattern,  $E_\phi(\theta)$  is measured in the  $\phi = 90^\circ$  cut.

Also included in this study, is the comparison between the patterns of antennas with finite and infinite substrates. As mentioned earlier, the numerical simulation of miniature slots with finite ground, using either FEM or MoM (electric current discretization), is very tedious, and thus, a simple slot antenna is used instead for pattern comparison. In the following sets of examples, a slot antenna with a length

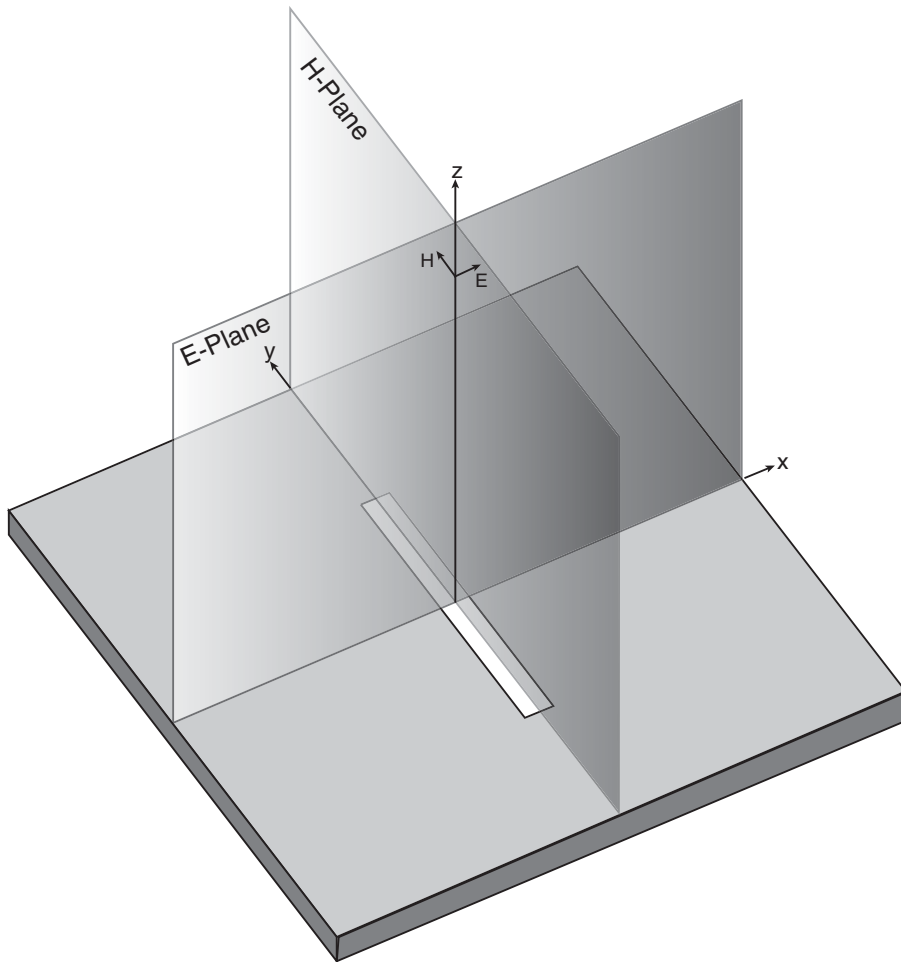


Figure A.2: The geometry of a standard slot antenna along with its principle E- and H-planes.

of  $\ell = 50$  mm is simulated. In the case of finite ground plane, the dimensions of the slot ground plane is set to  $100 \text{ mm} \times 100 \text{ mm}$ . In cases where the antenna is backed by a substrate, the dielectric constant of the substrate is selected to be  $\epsilon_r = 2.2$ , with a thickness of 0.7874 mm.

The first set of examples includes two slot antennas with infinite ground planes, one with a dielectric substrate and the other without a substrate. To simulate these problems, IE3D simulator with the magnetic current discretization is utilized. IE3D can also be used when simulating a finite ground slot but since the moment method makes use of spectral domain Green's function, the substrate still has to be infinite. Therefore, for the case of a slot antenna, with finite ground plane and infinite extent substrate, IE3D with electric current discretization is used. The finite ground slot without dielectric can be perfectly simulated using IE3D with electric current. The same problem can also be solved using a commercially available FEM code, such as HFSS. Finally, the practical case of a slot with a finite ground and a finite substrate is simulated using HFSS [68].

### **Infinite Ground-Plane without Dielectric Substrate**

The first example is a slot antenna with an infinite ground plane. In this configuration, no dielectric substrate is used. An infinite ground plane is impossible to mesh, and therefore, the use of equivalent magnetic currents on the aperture is inevitable. Figure A.3 shows the radiation pattern of this antenna for both principle E- and H-planes. This radiation pattern is similar to that of the electric dipole, with E and H interchanged. That is why the slot on an infinite ground plane is also referred to as a magnetic dipole, which is indeed, the dual of an electric dipole.

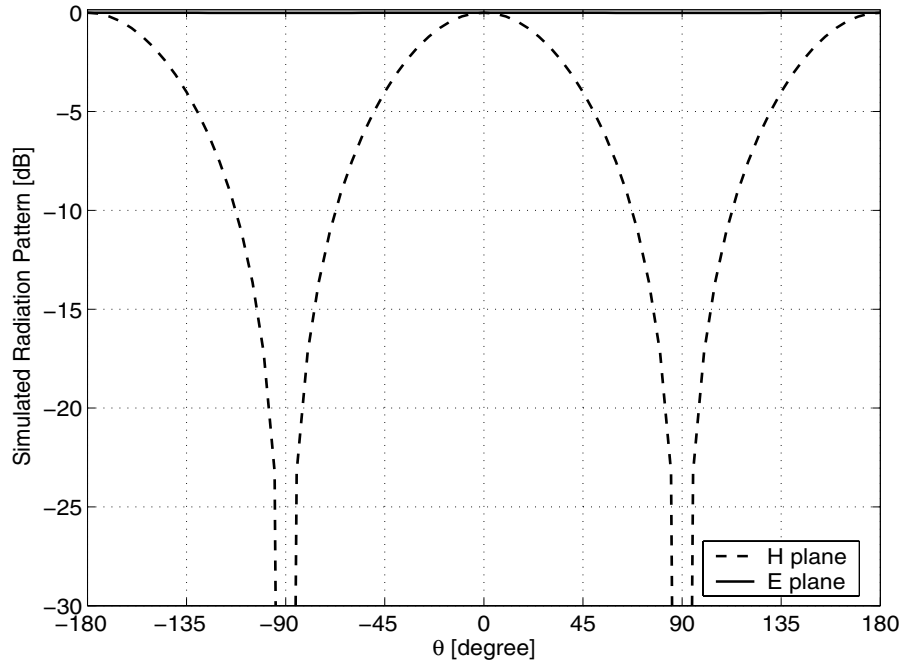


Figure A.3: The simulated radiation pattern of a slot antenna on air with an infinite ground plane using IE3D with magnetic current discretization.

### Infinite Ground-Plane with Infinite Dielectric Substrate

The same structure as previous example, now with a 0.7874 mm thick substrate with  $\epsilon_r = 2.2$  is simulated using IE3D, again with magnetic current discretization. Note that using a Moment Method software (IE3D) implies that the dielectric substrate is also extended to infinity in the x-y plane. The radiation pattern of this antenna is shown in Fig. A.4. This pattern is similar to the one illustrated in Fig. A.3 with an exception of a slight perturbation of the normal E-field at the dielectric-air interface  $-E_\theta(\theta = 90^\circ)$  in the E-plane. This perturbation is due to the fact that the normal electric field is discontinuous at the dielectric interface.

### Finite Ground-Plane without Dielectric Substrate

In the next example, a finite ground slot antenna without a dielectric substrate is considered. This example can be simulated using either MoM with electric current discretization or FEM. Figure A.5 demonstrates the radiation patterns of this

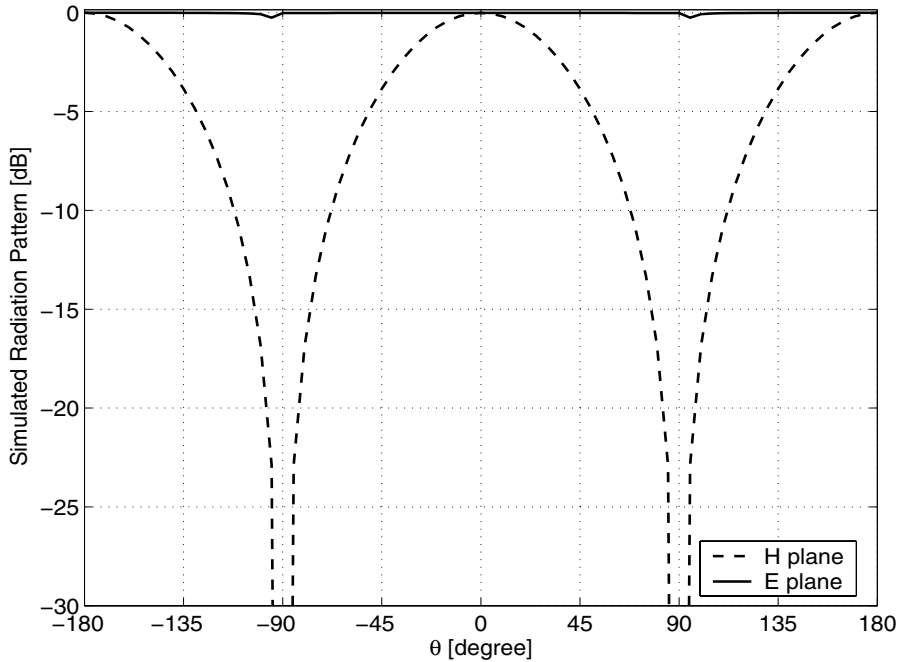


Figure A.4: The simulated radiation pattern of a slot antenna with an infinite ground plane over an infinite extent dielectric substrate with  $\epsilon_r = 2.2$  and thickness of 0.7874 mm using IE3D with magnetic current discretization.

antenna, simulated with both IE3D and HFSS.

Comparing Fig. A.5 with Fig. A.3 exhibits a drastic difference in the radiation pattern of the slot antenna due to the finite ground plane. In the ideal case of Fig. A.3, the radiation pattern is constant in the E-plane, and it has two nulls at  $\theta = \pm 90^\circ$  in the H-plane. Unlike the ideal case, when the ground plane is finite, the radiation pattern demonstrates an opposite behavior in the E- and H-planes. This different behavior is such that two very strong nulls are emerged in the E-plane, whereas the expected nulls at the H-plane of the slot antenna are filled.

In order to explain the reason for these changes in the radiation pattern, one needs to take a closer look at the ramifications of a finite ground plane. For instance, when the ground plane is infinite, no edge current exists, and thus, the edge diffraction does not perturb the radiation pattern. Also, infinite ground plane ensures that the upper and lower half space are decoupled. In this case, the equivalent magnetic currents

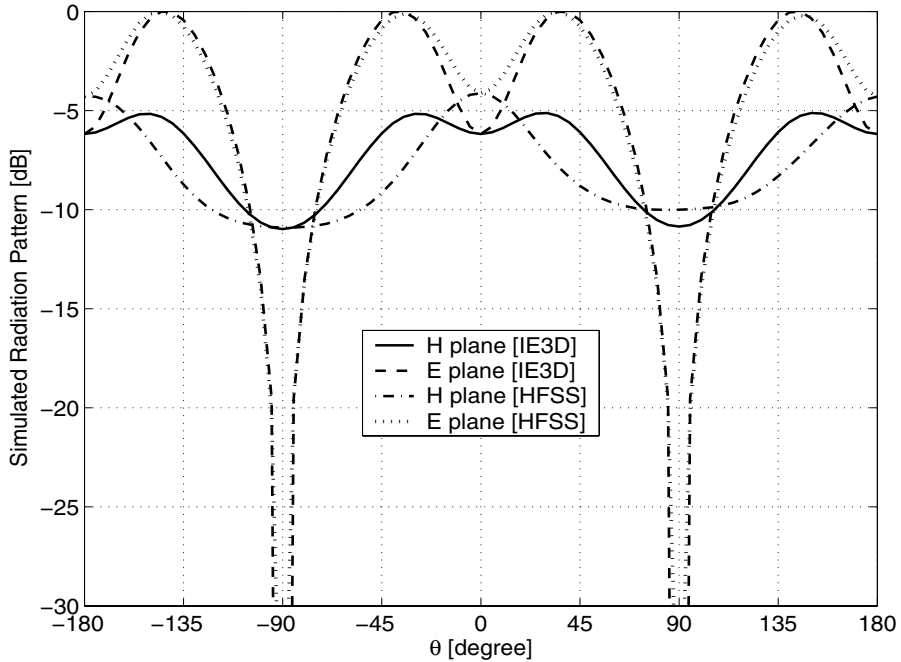


Figure A.5: Comparison between the simulated radiation patterns of a finite ground plane slot with no dielectric substrate, obtained from IE3D (electric current discretization) and HFSS.

that are flowing on opposite directions on the different sides of the ground cannot cancel each other's field along the  $x$ -axis. Conversely, for the finite ground plane, the radiated fields of these two opposing currents cancel each other at  $\theta = \pm 90^\circ$ , and create a null in the E-plane.

In the H-plane pattern, the expected null at  $\theta = \pm 90^\circ$  is filled considerably owing to the finite size ground plane. As alluded earlier, for the H-plane,  $E_\phi(\theta)$  is evaluated at  $\phi = 90^\circ$ . This component of the electric field is tangential to the ground plane at  $\theta = \pm 90^\circ$  and must vanish, provided that the ground plane is extended all the way to the far-field observation point ( $r \rightarrow \infty$ ). In contrast, when the ground plane is finite, there is no ground plane to enforce the nulls on one hand, and on the other hand, the electric currents on the edges of the finite ground plane can contribute to fill the expected null.

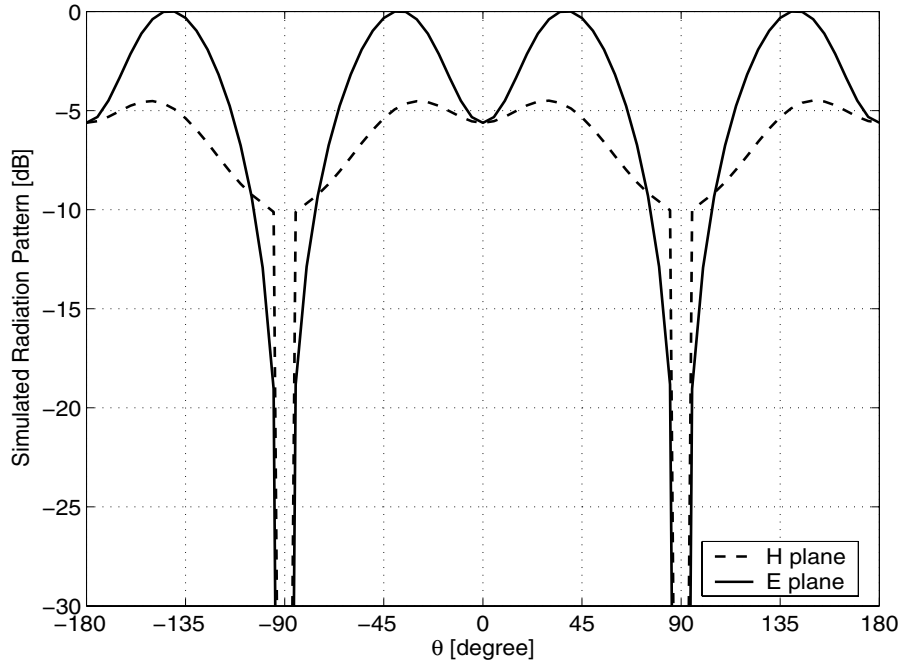


Figure A.6: The simulated radiation pattern of a slot antenna with a finite ground plane on a dielectric substrate using IE3D.

### Finite Ground-Plane with Infinite Dielectric Substrate

The finite ground slot of the previous example is now considered to be on a dielectric substrate with  $\varepsilon_r = 2.2$  and  $t = 0.7874$  mm. The radiation pattern of this antenna is simulated using IE3D and shown in Fig. A.6. Note that in this simulation, the substrate is assumed to be of an infinite extent in the x-y plane. Comparing this example with a similar case without a dielectric, shown in Fig. A.5, indicates that the effect of the dielectric substrate is almost negligible in the radiation pattern. The only difference observed in Fig. A.6 is the occurrence of two nulls in the H-plane of the antenna taking place very abruptly right at the  $\theta = \pm 90^\circ$ . This null might be the result of ignoring the contribution of the surface wave diffraction in the calculated far-field radiation pattern of the antenna [32, 67], and only considering the contribution of the stationary phase points.

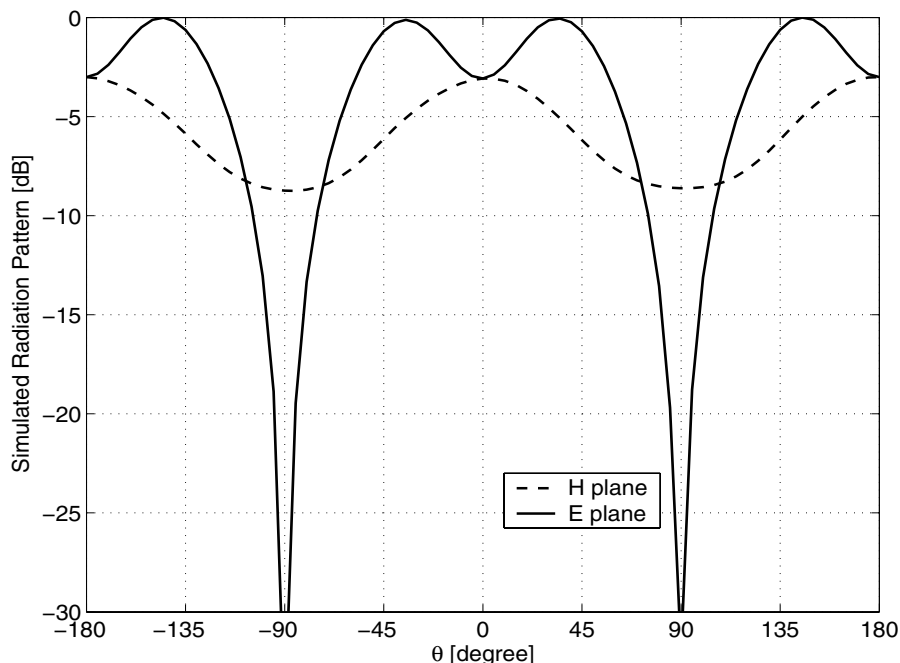


Figure A.7: The simulated radiation pattern of a slot antenna with a finite ground plane and finite dielectric substrate obtained from HFSS.

### Finite Ground-Plane with Finite Dielectric Substrate

Finally, a more common case, that is a finite ground slot antenna with a finite substrate is simulated using HFSS. The calculated radiation pattern of this antenna is plotted in Fig. A.7 for the principle planes of E and H, which is very similar to the one plotted in Fig. A.5.

## A.4 Conclusion

The above examples in this appendix clearly demonstrate how the radiation pattern of a finite ground slot antenna deviates from the predicted patterns by theory, under the assumption of a finite ground plane. For the ideal magnetic dipole, a constant E-plane pattern is expected, whereas in experiment, two nulls exist in this cut. Conversely, the theory predicts an H-plane pattern in the form of  $\sin \theta$  with two nulls at  $\theta = \pm 90^\circ$ , whereas in practice, these nulls are disappeared in the case of finite

ground plane.

Another minor effect in the simulated radiation pattern of a finite ground slot is the presence of two humps around the boresight. This can also be attributed to the radiation by the edges whose radiation is slightly out of phase with that of the main slot, and consequently, the overall radiation pattern resembles beam steering property of a phased array. The features of these humps, as well as their locations change with respect to the ground plane size.

Knowing that the radiation pattern of an infinitesimal dipole is very similar to that of a half-wave dipole, the results of this study hold for the miniaturized antennas, and therefore, explain the discrepancies between the simulated and measured radiation patterns of the antennas of Chapter 2, and Chapter 3.

## BIBLIOGRAPHY

## BIBLIOGRAPHY

- [1] L. J. Chu, “Physical limitations of omni-directional antennas,” *J. Appl. Phys.*, vol. 19, pp. 1163–1175, Dec. 1948.
- [2] R. C. Hansen, “Fundamental limitations in antennas,” *Proceedings of the IEEE*, vol. 69, pp. 170–182, Feb. 1981.
- [3] R. F. Harrington, “Effect of antenna size on gain, bandwidth, and efficiency,” *J. Res. Natl. Bur. Std.*, vol. 64D, pp. 1–12, 1960.
- [4] G. L. Matthaei, L. Young, and E. M. T. Jones, *Microwave Filters, Impedance-Matching Networks and Coupling Structures*, McGraw-Hill, New York, 1964.
- [5] R. Levy, R. V. Snyder, and G. L. Matthaei, “Design of microwave filters,” *IEEE Trans. Microwave Theory Tech.*, vol. 50, pp. 783–793, Mar. 2002.
- [6] R. R. Mansour, “Microwave superconductivity,” *IEEE Trans. Microwave Theory Tech.*, vol. 50, pp. 750–759, Mar. 2002.
- [7] H. T. Su, F. Huang, and M. J. Lancaster, “Highly miniature HTS microwave filters,” *IEEE Trans. Applied Superconductivity.*, vol. 11, pp. 349–352, Mar. 2001.
- [8] H. A. Wheeler, “Fundamental limitations of small antennas,” *Proceedings of the I.R.E.*, vol. 35, pp. 1479–1484, Dec. 1947.
- [9] H. A. Wheeler, “Small antennas,” *IEEE Trans. Antennas Propagat.*, vol. 23, pp. 462–469, Jul. 1975.
- [10] R. E. Collin, “Small antennas,” *IEEE Trans. Antennas Propagat.*, vol. 12, pp. 23–27, Jan. 1966.
- [11] J. A. Kaiser, “The Archimedean two-wire spiral antenna,” *I.R.E. Trans. Antennas Propagat.*, vol. 8, pp. 312–323, May. 1960.
- [12] Em-Picasso, *Electromagnetic Simulation*, EMAG Technologies, Inc., Ann Arbor, MI.
- [13] J. Rashed, and C. T. Tai, “A new class of Resonant antennas,” *IEEE Trans. Antennas Propagat.*, vol. 39, pp. 1428–1430, Sep. 1991.

- [14] J. M. Kim, J. G. Yook, W. Y. Song, Y. J. Yoon, J. Y. Park, and H. K. Park, "Compact meander-type slot antennas," *Proceedings of the IEEE AP-S Symposium*, vol. 2, pp. 724–727, 2001.
- [15] L. P. Ivriissimtzis, M. J. Lancaster, and M. Esa, "Miniature super conducting coplanar strip antennas for microwave and mm-wave applications," *Proceedings of the IEEE AP-S Symposium*, vol. 1, pp. 391–395, Apr. 1995.
- [16] L. P. Ivriissimtzis, M. J. Lancaster, T. S. M. Maclean, and N. Alford, "High-gain series fed printed dipole arrays made of high-T superconductors," *IEEE Trans. Antennas Propagat.*, vol. 42, pp. 1419–1429, Oct. 1994.
- [17] K. Noguchi, N. Yasui, M. Mizusawa, S. Betsudan, and T. Katagi, "Increasing the bandwidth of a two-strip meander-line antenna mounted on a conducting box," *Proceedings of the IEEE AP-S Symposium*, vol. 4, pp. 112–115, 2001.
- [18] H. Chaloupka, N. Klein, M. Peiniger, H. Piel, A. Pischke, and G. Splitt, "Miniaturized high-temperature superconductor microstrip patch antenna," *IEEE Trans. Microwave Theory Tech.*, vol. 39, pp. 1513–1521, Sep. 1991.
- [19] Y.-P. Zhang, T.K.-C. Lo, and Y.-M. Hwang, "A dielectric-loaded miniature antenna for micro-cellular and personal communications," *Proceedings of the IEEE AP-S Symposium*, vol. 2, pp. 1152–1155, 1995.
- [20] Y. Hwang Y.P. Zhang, K.M. Luk, and, E.K.N. Yung, "Gain-enhanced miniaturised rectangular dielectric resonator antenna," *Electronics Letters*, vol. 33, pp. 350–352, Feb. 1997.
- [21] R.E. Collin, *Antennas and Radiowave Propagation*, McGraw-Hill, New York, 1985.
- [22] B. K. Kormanyos, W. Harokopus, L. Katehi, and G. Rebeiz, "CPW-fed active slot antennas," *IEEE Trans. Microwave Theory Tech.*, vol. 42, pp. 541–545, Apr. 1994.
- [23] S. Sierra-Garcia and J. Laurin, "Study of a CPW Inductively Coupled Slot Antenna," *IEEE Trans. Antennas Propagat.*, vol. 47, pp. 58–64, Jan. 1999.
- [24] RT/duroid 5880, *High Frequency Laminate*, Rogers Corporation, Advanced Circuit Materials Division, Chandler, AZ.
- [25] IE3D, *Electromagnetic Simulation and Optimization Package, ver. 10.0*, Zeland Software, Inc., Fremont, CA.
- [26] K.C. Gupta, P. Garg, I. Bahl, and P. Bhartia, *Microstrip Lines and Slotlines*, Artec House, 2nd edition, 1996.
- [27] H.G. Akhavan, and D. Mirshekar-Syahkal, "Approximate model for microstrip fed slot antennas," *Electronics Letters*, vol. 30, pp. 1902–1903, Nov. 1994.

- [28] M. Fariana, and T. Rozzi, “A short-open deembedding technique for method-of-moments-based electromagnetic analyses,” *IEEE Trans. Microwave Theory Tech.*, vol. 49, pp. 624–628, Apr. 2001.
- [29] L. Zhu, and K. Wu, “Unified equivalent-circuit model of planar discontinuities suitable for field theory-based CAD and optimization of M(H)MIC’s,” *IEEE Trans. Microwave Theory Tech.*, vol. 47, pp. 1589–1602, Sep. 1999.
- [30] L. Zhu, and K. Wu, “Complete circuit model of microstrip-fed Slot radiator: Theory and experiments,” *IEEE Microwave and Guided Wave Letters*, vol. 9, pp. 305–307, Aug. 1999.
- [31] J. M. Johnson, and Y. Rahmat-Samii, “Genetic algorithms in engineering electromagnetics,” *IEEE Antennas Propagat. Magazine*, vol. 39, No. 4, pp. 7–21, Aug. 1997.
- [32] B. Stockbroeckx, I. Huynen, and A. Vander Vorst, “Effect of surface wave diffraction on radiation pattern of slot antenna etched in finite ground plane,” *Electronics Letters*, vol. 36, pp. 1444–1446, Aug. 2000.
- [33] A. K. Bhattacharyya, “Effects of ground plane and dielectric truncation on the efficiency of a printed structure,” *IEEE Trans. Antennas Propagat.*, vol. 39, pp. 303–308, Mar. 1991.
- [34] C. A. Balanis, *Antenna Theory: Analysis and Design*, John Wiley & Sons, New York, 1997.
- [35] R. S. Elliott, *Antenna Theory and Design*, John Wiley, New Jersey, 2003.
- [36] K. V. Pugilia, “Application notes: Electromagnetic simulation of some common balun structures,” *IEEE Microwave Mag.*, pp. 56–61, Sep. 2002.
- [37] Y. Mushiake, *Self-Complementary Antennas*, Springer-Verlag, New York.
- [38] T. Ishizone, Y. Mushiake, “A self-complementary antenna composed of unipole and notch antennas,” *Proceedings of the IEEE AP-S Symposium*.
- [39] P. Xu, k. Fujimoto, L. Shiming, “Performance of quasi-self-complementary antenna using a monopole and a slot,” *Proceedings of the IEEE AP-S Symposium*.
- [40] P. Bradley, R. Ruby, J. D. Larson, Y. Oshmyansky, D. Figueredo, “A film bulk acoustic resonator (FBAR) duplexer for USPCS handset applications,” *IEEE MTT-S Int. Microwave Symp. Dig.*, vol. 1, pp. 367–370, May 2001.
- [41] A. Gopinath, A. F. Thomson, and I. M. Stephenson, “Equivalent circuit parameters of microstrip step change in width and cross junction,” *IEEE Trans. Microwave Theory Tech.*, vol. 24, pp. 142–144, Mar. 1976.
- [42] M. Makimoto and S. Yamashita, “Compact bandpass filters using stepped impedance resonators,” *Proceedings of the IEEE*, vol. 67, pp. 16–19, Jan. 1979.

- [43] E. G. Cristal, S. Frankel, "Hairpin-line and hybrid hairpinline/half-wave parallel coupled-line filters," *IEEE Trans. Microwave Theory Tech.*, vol. 20, pp. 719–728, Nov. 1972.
- [44] M. Sagawa, K. Takahashi, and M. Makimoto, "Miniaturized hairpin resonator filters and their application to receiver front-end MIC's," *IEEE Trans. Microwave Theory Tech.*, vol. 37, pp. 1991–1997, Dec. 1989.
- [45] S. Y. Lee, and C. M. Tsai, "New cross-coupled filter design using improved hairpin resonators," *IEEE Trans. Microwave Theory Tech.*, vol. 48, pp. 2482–2490, Dec. 2000.
- [46] J-S. Hong and M. J. Lancaster, "Couplings of microstrip square open-loop resonators for cross-coupled planar microwave filters," *IEEE Trans. Microwave Theory Tech.*, vol. 44, pp. 2099–2109, Dec. 1996.
- [47] J-S. Hong and M. J. Lancaster, "Theory and experiment of novel microstrip slow-wave open-loop resonator filters," *IEEE Trans. Microwave Theory Tech.*, vol. 45, pp. 2358–2365, Dec. 1997.
- [48] J-S. Hong and M. J. Lancaster, "Aperture-coupled microstrip open-loop resonators and their applications to the design of novel microstrip bandpass filters," *IEEE Trans. Microwave Theory Tech.*, vol. 47, pp. 1848–1855, Sep. 1999.
- [49] E. L. Mariani and J. P. Agrios, "Slot-line filters and couplers," *IEEE Trans. Microwave Theory Tech.*, vol. 18, pp. 1089–1095, Dec. 1970.
- [50] D. F. Williams and S. E. Schwarz, "Design and performance of coplanar waveguide bandpass filters," *IEEE Trans. Microwave Theory Tech.*, vol. 31, pp. 558–566, Jul. 1983.
- [51] J. K. A. Everard and K. K. M. Cheng, "High-performance direct coupled bandpass filter on coplanar waveguide," *IEEE Trans. Microwave Theory Tech.*, vol. 41, pp. 1568–1573, Sep. 1993.
- [52] M. Muraguchi, T. Hirota, A. Minakawa, K. Ohwada, and T. Sugeta, "Uniplanar MMIC's and their applications," *IEEE Trans. Microwave Theory Tech.*, vol. 36, pp. 1896–1901, Dec. 1988.
- [53] T. Hirota, Y. Tarusawa and H. Ogawa, "Uniplanar MMIC hybrids: a proposed new MMIC structure," *IEEE Trans. Microwave Theory Tech.*, vol. 35, pp. 576–581, June 1987.
- [54] T. Tsujiguchi, H. Matsumoto, and T. Nishikawa, "A miniaturized end-coupled bandpass filter using  $\lambda/4$  hair-pin coplanar resonators," *IEEE MTT-S Int. Microwave Symp. Dig.*, pp. 829–832, Jun. 1998.

- [55] K. Yoshida, K. Sashiyama, S. Nishioka, H. Shimakage, and Z. Wang, “Design and performance of miniaturized superconducting coplanar waveguide filters,” *IEEE Trans. Applied Superconductivity.*, vol. 9, pp. 3905–3908, Jun. 1999.
- [56] T. Tsujiguchi, H. Matsumoto, and T. Nishikawa, “A miniaturized double-surface CPW bandpass filter improved spurious response,” *IEEE Trans. Microwave Theory Tech.*, vol. 49, pp. 879–885, May 2001.
- [57] J. Sor, Y. Qian, and T. Itoh, “Miniature low-loss CPW periodic structures for filter applications,” *IEEE Trans. Microwave Theory Tech.*, vol. 49, pp. 2336–2341, Dec. 2001.
- [58] E. Yuan, and S. H. Chao, “Unloaded  $Q$  measurement: the critical-point method,” *IEEE Trans. Microwave Theory Tech.*, vol. 43, pp. 1983–1986, Aug. 1995.
- [59] A. E. Atia, A. E. Williams, “Narrow-bandpass waveguide filters,” *IEEE Trans. Microwave Theory Tech.*, vol. 20, pp. 258–265, Apr. 1972.
- [60] R. L. Levy, “Filters with single transmission zeroes at real or imaginary frequencies,” *IEEE Trans. Microwave Theory Tech.*, vol. 24, pp. 172–181, Apr. 1976.
- [61] K. T. Jokella, “Narrow-band stripline or microstrip filters with transmission zeroes at real and imaginary frequencies,” *IEEE Trans. Microwave Theory Tech.*, vol. 28, pp. 542–547, Jun. 1980.
- [62] R. F. Harrington, *Time-Harmonic Electromagnetic Fields*, John Wiley & Sons, New York, 2001.
- [63] J. A. Kong, *Electromagnetic Wave Theory*, EMW Pub, Cambridge, MA, 2000.
- [64] C. A. Balanis, *Advanced Engineering Electromagnetics*, J. W. Wiley & Sons, New York, 1989.
- [65] D. M. Pozar, *Microwave Engineering*, J. W. Wiley & Sons, New York, 1998.
- [66] R. F. Harrington, “Small resonant scatterers and their use for field measurements,” *I.R.E. Trans. Microwave Theory Tech.*, vol. MTT-10, pp. 165–174, May 1962.
- [67] B. Stockbroeckx, and A. Vander Vorst, “Asymptotic Green’s function of a surface magnetic current element on a perfect electric conductor plane covered by a lossy dielectric substrate,” *IEEE Trans. Antennas Propagat.*, vol. 47, pp. 309–316, Feb. 1999.
- [68] HFSS, *High Frequency Structure Simulator, ver. 9.0*, Ansoft Corporation, Pittsburgh, PA.